Control, Manipulation and Exploitation of Electromagnetic Radiation using Complex Electrodynamic Structures

Amy Jane MacLachlan

(201186556)

SUPA Department of Physics

University of Strathclyde

Thesis submitted for the degree of Doctor of Philosophy

December 2015

This thesis is the result of the author's original research. It has been composed by the author and has not been previously submitted for examination which has led to the award of a degree.

Abstract

The coupling of volume and surface fields facilitated by two-dimensional (2D) periodic surface lattices (PSLs) of both cylindrical and planar topology is considered. All the PSLs presented in this work have shallow corrugation allowing the lattice to be described as an effective metadielectric. An analytical dispersion equation describing the hybrid eigenfield of a PSL based on a cylindrical waveguide is derived. The cylindrical structures are designed to have a large diameter, enhancing their potential for use as the interaction region of an active device when combined with an appropriate electron beam. Due to the structure's large diameter, a theoretical model describing some of the possible scattering processes, is developed for planar geometry. Coupled wave equations and an analytical expression for the coupling coefficient are presented. A dispersion study, based on this theory, shows that the properties of the structure are tailored by varying the lattice parameters, and the PSL's capability of supporting a Cherenkov interaction is demonstrated.

Experimental measurements of planar PSLs resembling mesh structures, carried out at 140-220 GHz, show sharp resonances corresponding to the PSL's surface field. When mounted on a suitable metal-backed dielectric substrate, the PSLs exhibit coherent cavity eigenmode formation. The individual lattice elements are coherently synchronised by the surface field and volume field confined within the dielectric, demonstrating the principle of mode selection. Measurements of a planar PSL designed to operate at the 325-500 GHz frequency band are presented, demonstrating the scalability of the PSLs. Dispersion plots, obtained by modelling the planar PSLs using CST Microwave Studio, indicate the frequency positions of the expected cavity eigenmodes. When compared to the experimental results and theoretical dispersions, some correlation is observed.

Acknowledgements

I would like to thank my supervisors Prof. Adrian Cross and Dr. Craig Robertson for their support and guidance throughout this PhD. I am particularly grateful to Dr. Craig Robertson for his invaluable help with the fabrication of structures and experimental measurements presented in this work.

I would like to express my gratitude to Prof. Alan Phelps for his time, encouragement and assistance over the course of this research.

A special thanks to Dr. Ivan Konoplev whose detailed explanations have contributed greatly to the theory developed in this work.

I would also like to acknowledge the Engineering and Physical Sciences Research council for financially supporting this research.

Finally, I wish to thank my Mum and Dad for their patience, support and encouragement over the years.

Table of Contents

5. Experimental Results for 2D Planar PSLs

6. Numerical Dispersions of Planar PSLs

List of Symbols

A = amplitude constant associated with the electric vector potential of the surface field inside the effective metadielectric.

A_1^e, A_2^e = constants associated with electric field components of surface field inside smooth cylindrical waveguide, partially loaded with dielectric

A_1^h, A_2^h= constants associated with magnetic field components of surface field inside smooth cylindrical waveguide, partially loaded with dielectric.

$A_{n_v}(z)$= slowly-varying amplitude along the z-coordinate for the n_v harmonic of the volume field.

$A_{\pm}(z)$= amplitude of forwards and backwards scattered waves for the fundamental harmonic of the near cut-off volume field

a = radius of effective dielectric

a_{wg}=rectangular waveguide dimension

B = amplitude constant associated with the electric vector potential of the surface field inside the effective metadielectric.

$\bar{B}$= magnetic flux density

$B_{n_s}(z)$= slowly-varying amplitude along the z-coordinate for the n_s harmonic of the surface field.

$\bar{B}_D$= magnetic flux vector in dielectric

$\bar{B}_V$= magnetic flux vector in vacuum

b= radius of metal for cylindrical dielectric-lined

b_{wg}=rectangular waveguide dimension

c= speed of light in vacuum (ms^{-1})

C_j^e= slowly varying amplitude of the electric field harmonics for surface field under effective metamaterial approximation

C_j^h= slowly varying amplitude of the magnetic field harmonics for surface field under effective metamaterial approximation

$C_q(z)$= slowly varying amplitude describing the field evolution along the z-coordinate

$C_q^v(z)$= slowly varying amplitude describing the volume field

$C_q^s(z)$= slowly varying amplitude describing the surface field

D= (superscript) used to denote vacuum region in the field derivation of the effective metadielectric

D_{horn}=largest dimension of antennae

D_{wg}= diameter of cylindrical waveguide

$\overline{D}$= electric flux density

$\overline{D}_D$= electric flux vector in dielectric

$\overline{D}_V$= electric flux vector in vacuum

d_z=lattice period (mm)

$\bar{E}$ = electric field vector (Vm^{-1})

E_φ= azimuthal (or tangential) electric field component (Vm^{-1})

$\bar{E}_D$= electric field vector in dielectric (Vm^{-1})

$\bar{E}_V$= electric field vector in vacuum (Vm^{-1})

E_z=longitudinal electric field component (Vm^{-1})

E_n=normal electric field component (Vm^{-1})

$\bar{E}_q^*$= complex conjugate of the transverse electric field for the q^{th}mode of the unperturbed waveguide

$\bar{E}_{q,n}^*$ =complex conjugate structure of the normal electric field for mode, q

$F_{\bar{m}}(x)$= cylindrical function describing the surface field with $m_s = \bar{m}$ inside a partially loaded cylindrical waveguide of finite length

$F_{m_s}^{e,h}$= cylindrical functions of order m_s describing the electric (superscript e) and magnetic (superscript h) fields.

$F_z^{e,h}$= vector potential defining longitudinal field components inside the effective dielectric region of the partially loaded cylindrical waveguide

f= frequency (Hz)

$f_{e,h}$= cylindrical functions used to define the dispersion of the hybrid field inside a cylindrical waveguide partially loaded with an effective metadielectric

$\tilde{f}$= cylindrical function used to define the dispersion of the hybrid field inside a cylindrical waveguide partially loaded with an effective metadielectric

$G_z^{e,h}$= vector potential defining longitudinal field components outside the effective dielectric region of the partially loaded cylindrical waveguide

g= transverse wavenumber of surface field inside dielectric

$\bar{H}$= magnetic field vector (Am^{-1})

$\bar{H}_D$= magnetic field vector in dielectric

$\bar{H}_V$= magnetic field vector in vacuum

H_z= longitudinal magnetic field component

H_z^D= longitudinal magnetic field in dielectric

H_z^V= longitudinal magnetic field in vacuum

H_φ= azimuthal magnetic field component

H_{φ}^{D}= azimuthal magnetic field in dielectric

H_{φ}^{V}= azimuthal magnetic field in vacuum

$\overline{H}_{q}$=transverse magnetic field for the q^{th}mode of the unperturbed cylindrical waveguide

$\overline{H}_{q'}$=transverse magnetic field for the cut-off mode (q) of the unperturbed cylindrical waveguide

$\overline{H}_{q'}^{*}$= complex conjugate of the transverse magnetic field for the cut-off mode of the unperturbed cylindrical waveguide

$\overline{H}_{\tau}$ = the tangential magnetic field component

$H_{q,\tau}^{v}$=tangential magnetic field component for mode q of volume field inside cylindrical waveguide

$\overline{H}_{q,\tau}^{*}$ =the complex conjugate of the tangential mangetic field

$I_m(x)$ = m^{th} order modified Bessel function

$I'_m(x)$ =derivative of m^{th} order modified Bessel function with respect to its argument, x

$J_m(x)$ = m^{th} order of Bessel function of the first kind

$J'_m(x)$ =derivative of m^{th} order of Bessel function of the first kind with respect to its argument, x

j= integer spatial harmonic number of the surface field when describing the case of an infinite cylindrical waveguide lined with an effective metadielectric ($j = \pm 1$)

$\bar{J}_m$=magnetic surface current (fictitious)

$\bar{J}_e$= electric current density

k=wavenumber, $k = \sqrt{k_{\perp}^2 + k_z^2}$ (m^{-1})

$k_{\perp}^{v,s}$=transverse wavenumber of volume (superscript v) and surface (superscript s) fields (m^{-1})

k_z= longitudinal wavenumber (m^{-1})

$k_z^{v,s}$=longitudinal wavenumber of volume (superscript v) and surface (superscript s) fields (m^{-1})

$\bar{k}$= Bragg wavenumber, $\bar{k} = \frac{\omega}{c} + \sqrt{\left(\frac{\omega}{c}\right)^2 - k_{\perp(s)}^2}$ (m^{-1})

$\bar{k}_z$= longitudinal wavenumber of lattice $\bar{k}_z = 2\pi/d_z$ (m^{-1})

$\overline{K}$= mean wavenumber of coupled volume and surface fields $\overline{K} = \Omega/c$ (m^{-1})

$l(z, \varphi)$= function describing the two-dimensional sinusoidal lattice corrugation

L= length

L_x=arbitrary periodic function

m_s=number of azimuthal variations of surface field

m_v=number of azimuthal variations of volume field

$\overline{m}$ =the number of azimuthal variations of the corrugated cylindrical waveguide

N= normalisation parameter, wave norm

N_v=wave norm of volume field

N_v'= wave norm of volume field N_v multiplied by $i\omega$

N_s=wave norm of surface field

N_s'=wave norm of surface field N_s multiplied by $i\omega$

$N_{\overline{m}}(x)$= $\overline{m}^{\text{th}}$ order Neumann function

$N'_{\overline{m}}(x)$= derivative of $N_{\overline{m}}(x)$ with respect to argument, x

n_s=surface field harmonic number

n_v=volume field harmonic number

$\tilde{n}$=refractive index

n_d=refractive index of dielectric

$\tilde{n}_B$=effective refractive index close to the Bragg frequency

$\bar{n}$= normal unit vector component

p=transverse wavenumber of surface field in the vacuum region when considering effective metadielectric model

Q =constant defined as $Q = i\omega\varepsilon$

q= integer number of allowed modes in unperturbed waveguide

q'= integer number of waveguide cut-off mode

Δr = corrugation depth

r_0= mean radius of corrugated cylindrical waveguide

R_{far}=farfield radius

$S_\perp$= perpendicular surface describing the cylindrical cross section of the unperturbed waveguide

s= subscript or superscript used to denote surface mode

t_d= dielectric thickness

t_δ= loss tangent

T= radial mode index used to describe near cut-off volume waves

U= integrand

V= (superscript) used to denote vacuum region in the field derivation of the effective metadielectric

v= subscript or superscript used to denote volume mode

v_z=electron beam velocity

w=arbitrary integer number

X= arbitrary amplitude constant

Y= arbitrary amplitude constant

$\tilde{\alpha}$=coupling coefficient describing field coupling in effective metadielectric approximation

$\alpha_{v,s}$= coupling coefficient defining the coupling from the volume field to the surface field

$\alpha_{s,v}$= coupling coefficient defining the coupling from the surface field to the volume field

α= Combined, normalised coupling coefficient describing coupling between volume and surface fields

γ=relativistic factor

Δ = detuning of the angular cut-off frequencies of the volume and surface waves

$\widetilde{\Delta}$= normalised detuning between the cut-off frequencies of the volume and surface waves $\left(\widetilde{\Delta} = \Phi/\Omega\right)$

$\hat{\delta}$ =the detuning parameter describing the difference between ω and $\overline{\omega}_0$

δ = normalised detuning parameter, $\delta = (\omega - \Omega)/\Omega$

ε_0=permittivity of free space ($\cong 8.85 \times 10^{-12} Fm^{-1}$)

ε= relative permittivity of dielectric

θ_B= Brewster angle (degrees)

θ_i= incident angle (degrees)

θ_i= transmitted angle (degrees)

θ_{air}= phase in air (degrees)

θ_{diel}= phase in dielectric (degrees)

Δθ=change in phase (degrees)

λ= wavelength

λ_c=cut-off wavelength

λ_{op}=operating wavelength of cylindrical PSL

λ_z=longitudinal wavelength

μ=relative permeability

μ_0= permeability of free space (Hm^{-1})

φ=azimuthal coordinate (degrees)

ω= angular operating frequency of structure.

$\bar{\omega}_0$ = mean angular cut-off frequency of the volume and surface waves

ω_0= angular cut-off frequency

ω_0^v= angular cut-off frequency of volume field

ω_0^s= angular cut-off frequency of surface field

ω_B= angular Bragg resonance frequency

ω_b= angular plasma frequency of the electron beam

ω_{ce}= angular electron cyclotron frequency

ω_e= variable angular frequency of coupled dispersion equation

Γ=dimensionless detuning parameter $\Gamma = \bar{k}_z/\overline{K} = 2\bar{k}_z c/((\omega_0^v)^2 + (\omega_0^s)^2)$

Γ_{ref}=reflection coefficient

Λ=normalised wave vector of coupled dispersion equation

Υ= function describing electric vector potential inside the effective dielectric region of the partially loaded cylindrical waveguide, $\Upsilon = N_{\bar{m}}(gb)\ J_{\bar{m}}(gr) - J_{\bar{m}}(gb)\ N_{\bar{m}}(gr)$

$\widehat{\Upsilon}$= function describing electric vector potential outside the effective dielectric region of the partially loaded cylindrical waveguide, $\widehat{\Upsilon} = \widehat{\Psi} = I_{\bar{m}}(pr)$

Ψ= function describing magnetic vector potential inside the effective dielectric region of the partially loaded cylindrical waveguide $\Psi = N'_{\bar{m}}(gb)\ J_{\bar{m}}(gr) - J'_{\bar{m}}(gb)\ N_{\bar{m}}(gr)$

$\widehat{\Psi}$= function describing magnetic vector potential outside the effective dielectric region of the partially loaded cylindrical waveguide $\widehat{\Psi} = \widehat{\Upsilon} = I_{\bar{m}}(pr)$

Ω= mean angular frequency defined as $\Omega = \sqrt{((\omega_0^v)^2 + (\omega_0^s)^2)/2}$

Φ= function describing the detuning in angular cut-off frequency of the volume and surface fields, defined $\Phi = \sqrt{((\omega_0^s)^2 - (\omega_0^v)^2)/2}$

Chapter 1- Introduction and Background Theory

1.1 Introduction

In 1913, Sir William Henry Bragg and Sir William Laurence Bragg demonstrated the periodicity of crystals by successfully diffracting X-rays off a crystal lattice. Similar diffraction behaviour was subsequently observed at microwave frequencies through the use of periodic lattices, sometimes known as Bragg structures. The idea of using a structure with one-dimensional (1D) periodic corrugations to achieve mode transformation at microwave frequencies was first proposed by Kovalev *et al*. (Kovalev, Orlova et al. 1972). More recently, both 1D and 2D lattices were used to provide distributed feedback in the interaction region of lasers (Kogelnik and Shank 1972, Yariv and Nakamura 1977) and masers (Bratman, Denisov et al. 1983, Ginzburg, Peskov et al. 1999, Konoplev, Cross et al. 2000, Cross, Konoplev et al. 2002).

The electromagnetic (EM) field excitation and evolution inside and on the surface of periodic structures has led to breakthroughs in plasma physics and vacuum electronic sources (Glass 1987, Booske, Dobbs et al. 2001, Sirigiri, Kreischer et al. 2003, Korbly, Kesar et al. 2005), as well as optics and photonics (Pendry, Holden et al. 1996, Worthing and Barnes 2001, Barnes, Dereux et al. 2003, Bergman and Stockman 2003, Maier, Andrews et al. 2006, Renger, Grafström et al., 2007 Ishizaki and Noda 2009, Urzhumov and Smith 2010), where the lattices are known as photonic band-gap (PBG) structures, first described by (Yablonovitch, Gmitter 1991). Research relating to particle acceleration (Smirnova, Kesar et al. 2005, Mizrahi and Schächter 2006, Shapiro, Samokhvalova et al. 2008, York, Milchberg et al. 2008) has also benefited from the use of periodic structures.

In recent years, studies of periodic lattices involving both volume and surface fields have been carried out. However, the localised surface fields which exist in such structures are detrimental to the efficient operation of many conventional active and passive devices due to their rapid exponential decay from the surface. This

strong localisation can result in weak coupling with active media, leading to large thermal losses, signal distortion and heating of the device. In spite of this, it has been suggested that surface fields can be used to drive certain high-power active devices (Konoplev, Fisher et al. 2010, Ginzburg, Zaslavskii et al. 2012, Ginzburg, Malkin et al. 2013) or nano-oscillators(Luo, Ibanescu et al. 2003,Noginov, Zhu et al. 2009) which can now be developed due to modern manufacturing capabilities. The utilisation and understanding of surface fields is necessary for the realisation of compact sources of coherent radiation (CSCR) such as the surface plasmon amplifier (SPASAR) (Bergman and Stockman 2003, Stockman 2008, Noginov Zhu et al. 2009, Stockman 2010). This area of research is driven by a desire to bridge the terahertz (THz) gap and achieve high power sources operating in the GHz-THz(Schächter and Ron 1989) and x-ray frequency ranges. Surface fields have been further exploited as a means of profiling femtosecond electron bunches (Doucas, Blackmore et al. 2006) using a slow-wave structure (SWS).

Slow wave (periodic) structures are suitable for use as the interaction region of a high power Cherenkov device (Konoplev, Cross et al 2000, Cook, Tikhoplav et al. 2009, Ginzburg, Zaslavskii et al. 2011). Difficulties (including manufacturing challenges and limited output power) may arise when attempting to increase the operating frequency, thereby reducing the interaction region's size. Another problem associated with the structure's small size is the build-up of charge density, leading to breakdown of the electron beam inside the interaction area.

Overcoming these issues by scaling up the dimensions of the interaction region (such that it becomes oversized in comparison with the operating wavelength) may disrupt the spatial and temporal coherence of the radiation (Konoplev 2001). For this reason, structures are typically designed with their transverse dimensions comparable to the operating wavelength. A method of resolving this problem (for structures with large D_{wg}/λ) involves providing feedback in an arrangement similar to a Fabry-Perot cavity with a periodic surface lattice (PSL) acting as one of the mirrors (Bratman, Dumesh et al. 2010)). This provides synchronisation of the individual scatterers that form the lattice.

Theoretical and experimental studies of Cherenkov oscillators with 2D distributed feedback are the subject of ongoing research (Ginzburg, Malkin et al. 2013, Ginzburg, Malkin et al. 2014, MacLachlan, Phipps et al. 2015) The synchronisation and coupling of fields inside 2D PSLs in a large area ($Vol \gg \lambda^3$) structure is discussed in this work.

Attaining synchronisation in an oversized structure is particularly important for applications where high power, coherent radiation is required for example in communications (Lier, Werner et al. 2011) security, devices for monitoring pollution (atmospheric dust clouds and space debris) and the quality control of pharmaceutical products. Techniques in spectroscopy (Benabid, Knight et al. 2002, Grishin, Fuchs et al. 2004) and THz imaging (Carr et al. 2002) including the study of historical artefacts (Seco-Martorell et al. 2013, Abraham et al. 2009) also rely on the development of coherent sources, capable of producing multi-watt output power at high frequencies.

Another challenge associated with having large D_{wg}/λ is achieving mode selection in the oversized structure to avoid the decrease in efficiency that usually comes with multi-mode operation. The method proposed in this work entails coupling the volume and surface fields to form a cavity eigenmode at a desired frequency, determined by the parameters of the structure. When studying the eigenmodes of the structure with a shallow corrugation, it is convenient to describe the lattice in terms of an effective metadielectric (or high impedance surface)(Sievenpiper, Zhang et al. 1999).

An EM metamaterial, described by an effective permittivity and permeability, is created by introducing a periodic topological defect at a metal surface (such as an array of holes, perturbations or dipoles) which are very small in comparison to the operating wavelength. The observation of a high impedance surface (metadielectric) consisting of a periodic arrangement of metal plates was demonstrated by Sievenpiper (Sievenpiper, Zhang et al., 1999) while numerical modelling has reported close agreement between a wire grid mesh and an

equivalent homogeneous effective dielectric(Lier, Werner et al. 2011). Other examples of EM metamaterials include split ring resonators (Fedatov, Rose et al. 2007) which can exhibit an effective negative permittivity (Shelby, Smith et al. 2001) or nanoparticles covered with dielectrics, while metamaterials based on a fishnet-like structure (Shchegolkov, Azad et al. 2010) have been previously designed for use as terahertz absorbers. Although the study of metamaterials is a relatively new field of research, boosted by recent advances in nanofabrication, related work has been carried out as early as the 1940s, when artificial dielectrics constructed from metals were used to construct lightweight microwave components.

The properties of a metamaterial are defined by its subwavelength structure rather than its chemical composition, allowing the material to be tailored to suit a specific purpose (Mittleman 2008, Shen, Catrysse et al. 2005). Metamaterials are designed to exhibit properties which are rare, or do not occur in nature (for example negative refractive index (Shelby, Smith et al. 2001, Pendry, Holden et al. 1998) or negative permeability (Grigorenko, Geim et al. 2005) and have led to the realisation of new phenomena including perfect lensing (Pendry 2000) and cloaking (Schurig, Mock et al. 2006). Negative phase and group velocity has also been reported (Dolling, Enkrich et al. 2006) at optical frequencies. Another attractive feature of metamaterials is their scalability, and all the theory developed in this thesis is applicable over a broad range of frequencies.

Although the PSLs considered in this work do not fit the true definition of a metadielectric (in that their period is comparable with the operating wavelength) they can still be described as effective metadielectrics in the plane of incidence, whilst appearing more like diffractive surfaces in the transverse plane. Previous research at Strathclyde has laid the foundations for this work. A Free Electron Maser (FEM) experiment with 2D distributed feedback, capable of producing up to 65MW of pulsed output power (Konoplev, Cross et al. 2008) at a frequency of 37.2GHz was successfully demonstrated. At the present stage, experiments involving a W-band Cherenkov Maser (incorporating a cylindrical 2D PSL) are underway.

This chapter begins with a description of the cylindrical 2D PSLs previously designed at Strathclyde and a brief overview of how these structures have been fabricated. The individual volume and surface fields, which exist inside the structures and provide synchronisation of the individual cells, are discussed. Following from this, the necessary conditions for resonant coupling between the volume and surface fields are provided, and the appearance of transmission and reflection zones associated with cavity eigenmode formation is demonstrated via the use of Brillouin diagrams. An introduction to the planar PSLs considered in this work is then given, noting that these structures can be converted to cylindrical geometry using conformal mapping. Finally, the structure's interaction with an electron beam leading to the realisation of a Cherenkov device is discussed before stating the layout of this thesis.

1.2 Cylindrical 2D Periodic Surface Lattices

The two-dimensional (2D) PSL of cylindrical topology can be obtained by introducing shallow periodic perturbations at the inner wall of a cylindrical waveguide. The 2D corrugation at the waveguide surface is defined by:

$$r = r_0 + \Delta r cos(\bar{k}_z z)\, cos(\bar{m}\varphi)$$

where r_0 is the mean radius of the unperturbed cylindrical waveguide, Δr is the amplitude of the perturbations, $\bar{m}$ is the number of lattice azimuthal variations and $\bar{k}_z = 2\pi/d_z$ is the longitudinal wavenumber of the lattice with longitudinal period, d_z. The cylindrical PSL pictured in figure 1.2.1a (Konoplev, Fisher et al. 2010) was obtained through a process of electroforming involving copper deposition on an aluminium mandrel with a 2D sinusoidal corrugation on its outer surface. The aluminium former was later dissolved to give the cylindrical PSL with the lattice corrugation on its inner wall. The Ka-band structure (figure 1.2.1.a) has an operating frequency of approximately 37.6 GHz and has the following parameters: r_0 =39.5mm, Δr =1mm, $\bar{m} = 28$ and $d_z = 8$mm

Figure 1.2.1b shows a smaller, W-band structure with r_0= 10mm, fabricated using the same electroforming technique as figure 1.2.1.a, and designed to operate at

95GHz. The parameters of the W-band structure photographed in figure 1.2.1b are: r_0 =10mm, Δr =0.6mm, $\bar{m}$ = 20 and d_z = 3mm.

The dimensions of these structures (figure 1.2.1a,b) are such that the near cut-off volume field (of the unperturbed waveguide) has a longitudinal wavelength close to the structure's length L, and much greater than d_z ($\lambda_z \sim L$, $\lambda_z \gg d_z$). This means that, despite d_z being comparable with the structure's operating wavelength λ_{op}, the volume field is unable to propagate through the lattice, thereby allowing a modal approximation to be made – where it is assumed that the transverse structure of the excited eigenfield is a superposition of the transverse structures of the eigenmodes that exist inside a smooth waveguide lined with an effective metadielectric (or high-impedance surface).

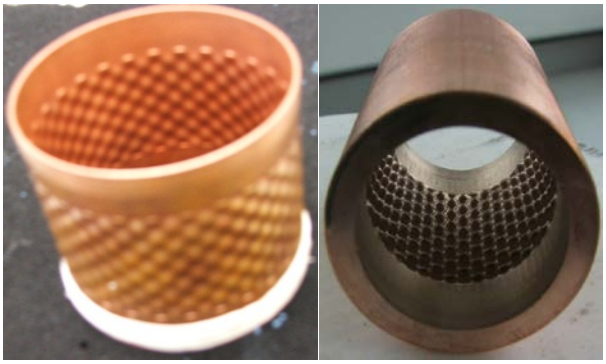

Figure 1.2.1.a (left) Photograph of Ka-band copper cylindrical 2D PSL with an operating frequency of ~37.6 GHz, obtained by copper deposition on an aluminium mandrel. The parameters of the structure are as follows: r_0=39.5mm, Δr =1mm, $\bar{m}$ =28 and d_z =8mm

Figure 1.2.1.b (right) Photograph of W-band copper cylindrical 2D PSL with an operating frequency of ~95 GHz, obtained by copper deposition on an aluminium mandrel. The parameters of the structure are as follows: r_0=10mm, Δr =0.6mm, $\bar{m}$ =20 and d_z =3mm

More recently, silver alloy cylindrical PSLs were constructed for use as the interaction region of the Cherenkov Maser built at Strathclyde(Phipps, MacLachlan et al. 2014). The PSLs were manufactured via high resolution 3D printing technology, using a silver (92.5%) – chromium (7.5%) alloy material which has the advantage of being stronger than pure silver, whilst still maintaining excellent

conductivity. Due to experimental constraints, the structure photographed in figure 1.2.2 has a reduced D_{wg}/λ compared to figures 1.2.1a,b and increased corrugation depth which should lead to stronger coupling between fields. The dispersion of this structure is studied analytically in chapter 3 of this thesis. All the photographed structures are capable of supporting both volume and surface fields.

Figure 1.2.2. Photograph of W-band silver (92.5%) – chromium (7.5%) alloy PSL obtained using high resolution 3D printing.

1.3 Surface and Volume Waves

The 2D PSLs are known to support both volume and surface fields at the corrugated boundary. The volume field occupies the bulk of the structure and is described by the relation:

$$(k^v)^2 = (k_\perp^v)^2 + (k_z^v)^2 \tag{1.3.1}$$

Surface waves are propagating EM waves that are bound to the surface of any metal. If the metal is smooth and flat, then the surface fields will not couple with external fields. However, if scattered by discontinuities, bends or a surface corrugation, the surface fields will radiate allowing, the possibility for coupling with a suitable volume wave. If the longitudinal wavelength of the surface field λ_z^s is much longer than the lattice period $\lambda_z^s \gg d_z$ then the surface waves are not affected by the corrugation. In certain cases, it is advantageous to suppress the propagation of surface fields (or surface plasmons at optical frequencies (Barnes, Priest et al. 1966, Kitson, Barnes et al. 1996)) which can be achieved by choosing

the lattice period such that $d_z \approx \lambda_z^s/2$ and creating a surface wave band-gap through destructive interference (Sievenpiper 1999).

The properties of surface waves are partly determined by their frequency. For example, at optical frequencies, surface plasmons are tightly bound to the dielectric-metal interface, whereas at microwave or radio frequencies (where they are widely known as surface currents) the EM fields extend many wavelengths into the surrounding space. One of the defining characteristics of a surface field, is its rapid exponential decay, resulting in an imaginary transverse wavenumber. The volume wave expression of equation (1.3.1) is adapted to take this property into account

$$(k^s)^2 = (ik_\perp^s)^2 + (k_z^s)^2$$

The dispersion of a surface wave is therefore defined:

$$(k^s)^2 = (k_z^s)^2 - (k_\perp^s)^2$$

(1.3.2)

The difference between volume and surface fields is observed by plotting their fundamental dispersions using equations (1.3.1) and (1.3.2). A dispersion relation (describing the wave propagation k_z with varying angular frequency ω) for the uncoupled volume and surface waves in an unperturbed, cylindrical waveguide is presented in figure 1.3.1.

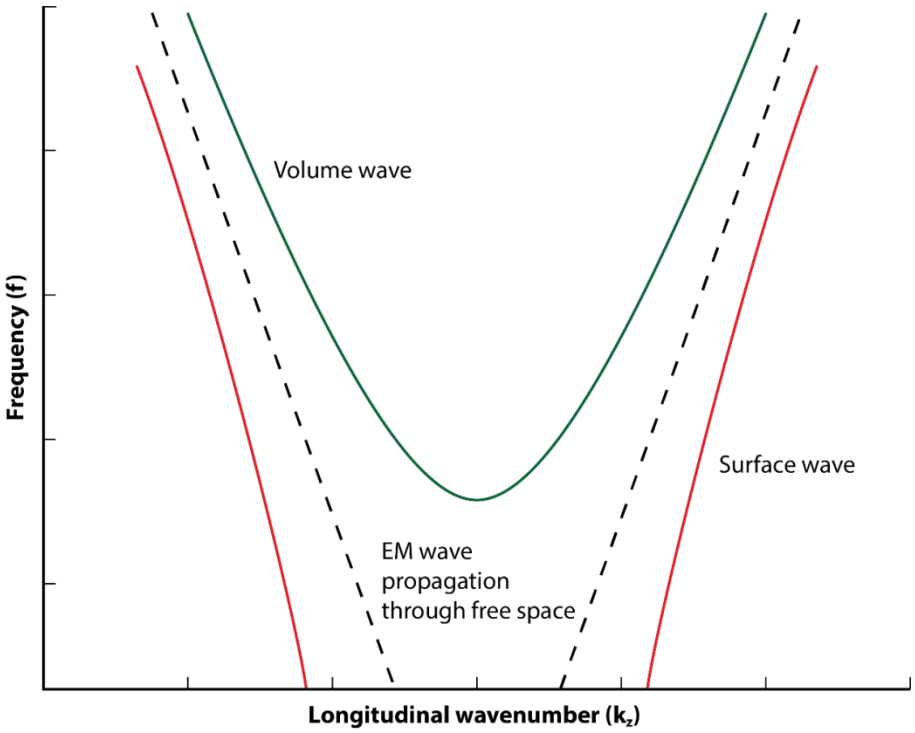

Figure 1.3.1 Schematic dispersion diagram illustrating volume (green) and surface (red) wave propagation through an unperturbed, hollow cylindrical waveguide. The dispersion of a wave propagating through free space (blue dashed line) has been included for comparison.

It can be noted that the volume wave has a parabolic dispersion while the surface field exhibits hyperbolic behaviour. Both dispersion curves tend asymptotically towards the dispersion of an electromagnetic wave propagating through free space. For this reason, it becomes difficult to distinguish between the different fields far above the cut-off frequency of the volume wave. Although the surface field does not have a cut-off frequency, it will not exist if $|k_z| < |k_\perp|$.

Both the volume and surface fields are important for providing synchronisation of the oversized PSL. Each fundamental cell of the lattice acts as an individual scatterer that supports its own localised surface field. When these individual lattice elements are synchronised, the oversized structure (with area $S = 2\pi r_0 L \gg \lambda^2$) behaves like a single cavity. This occurs on the condition that the PSL is irradiated with an azimuthally symmetric, near-cut-off volume field. When a volume field of this description is launched through the structure, it will oscillate back and forth

between the walls of the structure, inducing a surface current at the edges of each scatterer.

Previous experimental findings (Konoplev, Fisher et al. 2010) have shown that the oversized cylindrical structure photographed in figure 1.2.1.a is not synchronised when the volume field is above the cut-off frequency, and propagates through the structure. Mutual resonant scattering will occur between the volume and surface fields, only in the presence of the near cut-off volume field, which couples to the localised surface field at the corrugated boundary, and acts as a "global oscillator", synchronising all the cells throughout the structure. The surface current, which flows around the edges of each cell, allows “cross-talk” between neighbouring cells, providing the role of a “local oscillator”.

For the cylindrical PSLs, the desired coupling takes place between the hybrid $HE_{\overline{m},1}$ surface field and the $TM_{0,T}$ volume field, where T denotes the radial index corresponding to the near cut-off mode. Since this work is related to the construction of a Cherenkov device, only TM volume modes, which have a longitudinal electric field, are of interest. The eigenfield inside the lattice can be written as a superposition of partial volume and surface fields $E = A_v + B_s$ only if the individual scatterers are synchronised and providing the Bragg resonance conditions are satisfied.

1.4 Bragg Scattering in 2D PSLs

Only waves which satisfy the Bragg resonance conditions (Cross, Konoplev et al. 2003, Burt, Samsonov et al. 2004) can be effectively coupled at the corrugated surface. The Bragg conditions in the azimuthal (1.4.1a) and longitudinal (1.4.1b) directions for a PSL of cylindrical topology are as follows:

$$\overline{m} = m_v + m_s \tag{1.4.1a}$$

$$\overline{k}_z = k_z^s - k_z^v \tag{1.4.1.b}$$

where $\overline{k}_z$ is the longitudinal lattice wavenumber and $m_{v,s}$ is the azimuthal number of the volume and surface fields respectively. Coupling is possible in the case where $m_v = 0$ and $\overline{m} = m_s$ as discussed in chapter 2. The coupling coefficient is proportional to the corrugation depth Δr and no coupling exists when $\Delta r \to 0$. Increasing the corrugation height results in strong coupling which causes the structure's dispersion to split into separate branches at the points where the fields intersect. This can sometimes lead to the formation of a band gap (reflection zone). The resonant Bragg scattering, which facilitates coupling between the otherwise independent fields, can be illustrated using Brillouin diagrams.

Figures 1.4.1.a,b show the simplest case of coupling between volume fields. The harmonics of the volume field are shifted along the k_z coordinate by $k_j = 2\pi j/d_z$ where j is an integer. The Brillouin diagram in figure 1.4.1.a shows the case where the corrugation height tends to zero, and the volume field harmonics do not interact with each other. Increasing the corrugation leads to strong coupling between the harmonics (figure 1.4.1.b) at the points of intersection, resulting in the appearance of transmission and reflection zones (band gap). In these regions, the coupled harmonics cannot propagate through the structure and are said to be evanescent. The width of the band gap is directly related to the strength of the coupling between the harmonics.

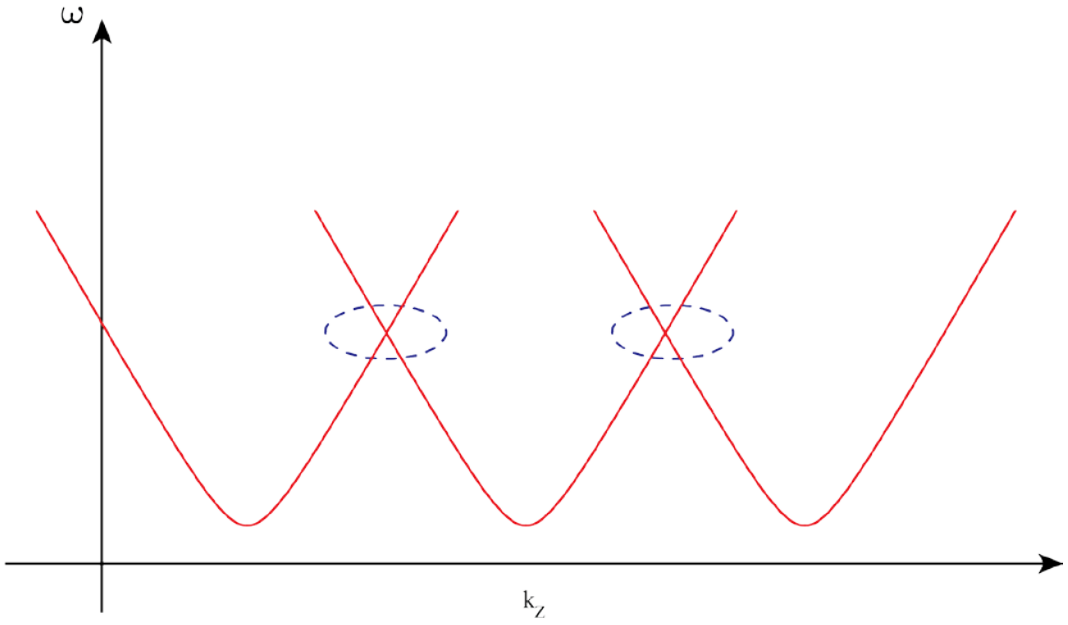

Figure 1.4.1.a.Brillouin diagram illustrating that when the corrugation height tends to zero, coupling of modes does not take place.

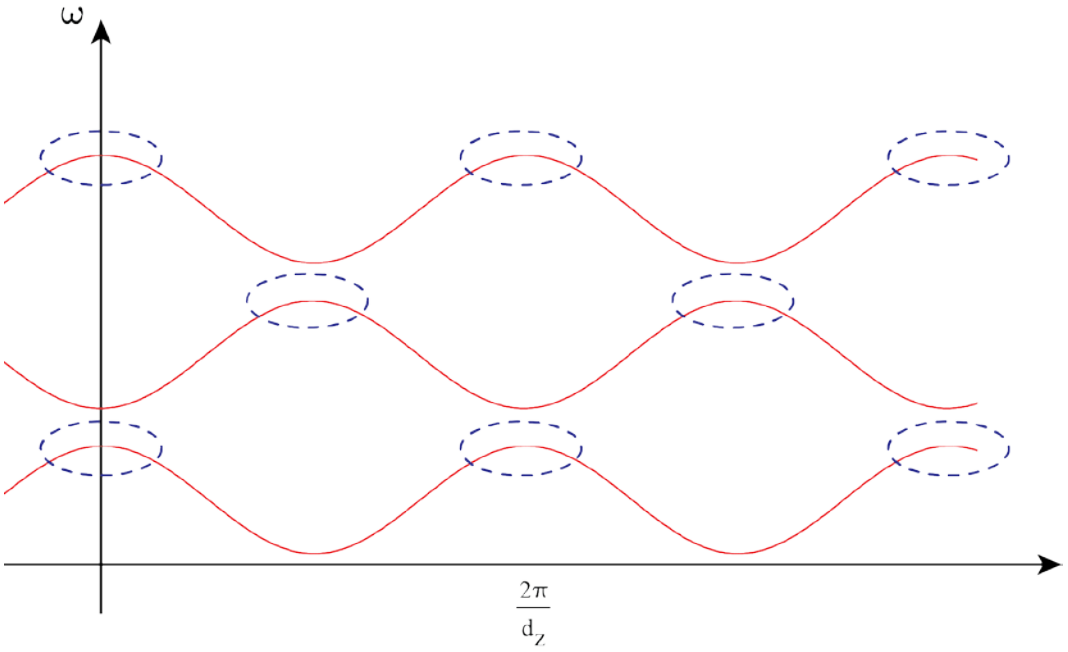

Figure 1.4.1.b Brillouin diagram illustrating mode coupling for a finite corrugation. The coupled mode regions are highlighted by the blue dashed circle

Similar behaviour occurs in the more complicated case of coupling between volume and surface fields. Dispersion diagrams presented in chapter 3, demonstrate the

coupled and uncoupled volume and surface field dispersions, and illustrate splitting at the points where the fields intersect, in a structure with finite corrugation.

1.5 2D PSL of Planar Topology

To understand the possible scattering mechanisms and coupling that can occur inside the cylindrical PSL, the structure is unfolded to study a PSL with planar geometry. The planar PSL can be converted to cylindrical coordinates via conformal mapping (see figure 1.5.1). Due to its geometry, the planar structure is easier to tailor and provides a more convenient means of studying the complex EM behaviour at higher frequencies. Although it is possible to combine a planar PSL with a sheet beam to obtain a novel high power source (Ginzburg, Peskov et al. 1999), the purpose of this study is to gain greater insight into the coupling of volume and surface fields which can be applied to the ongoing research into sources using the cylindrical PSL cavity with an appropriate electron beam, at the University of Strathclyde.

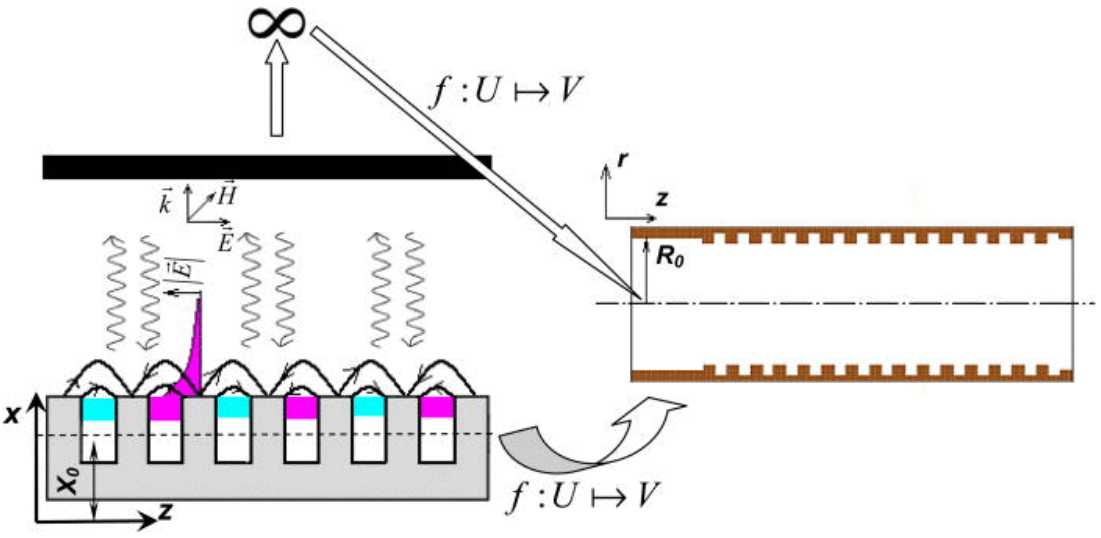

Figure 1.5.1. Schematic showing a planar Fabry-Perot like cavity with one of the mirrors having a high-impedance surface which allows coupling of surface fields and volume fields. The arrows indicate the mathematical steps required to move from planar geometry to a cylindrical cavity with a high-impedance surface similar to a dielectric layer.

The planar PSL with shallow corrugation is arranged in a set-up similar to a Fabry-Perot cavity with the PSL acting as one of the mirrors. The mirrors are separated by

a dielectric substrate as shown in figure 1.5.2 which helps to confine the volume field and facilitate coupling at the lattice-dielectric interface. The structures studied in this thesis were made using chemical etching techniques, described in chapter 4.

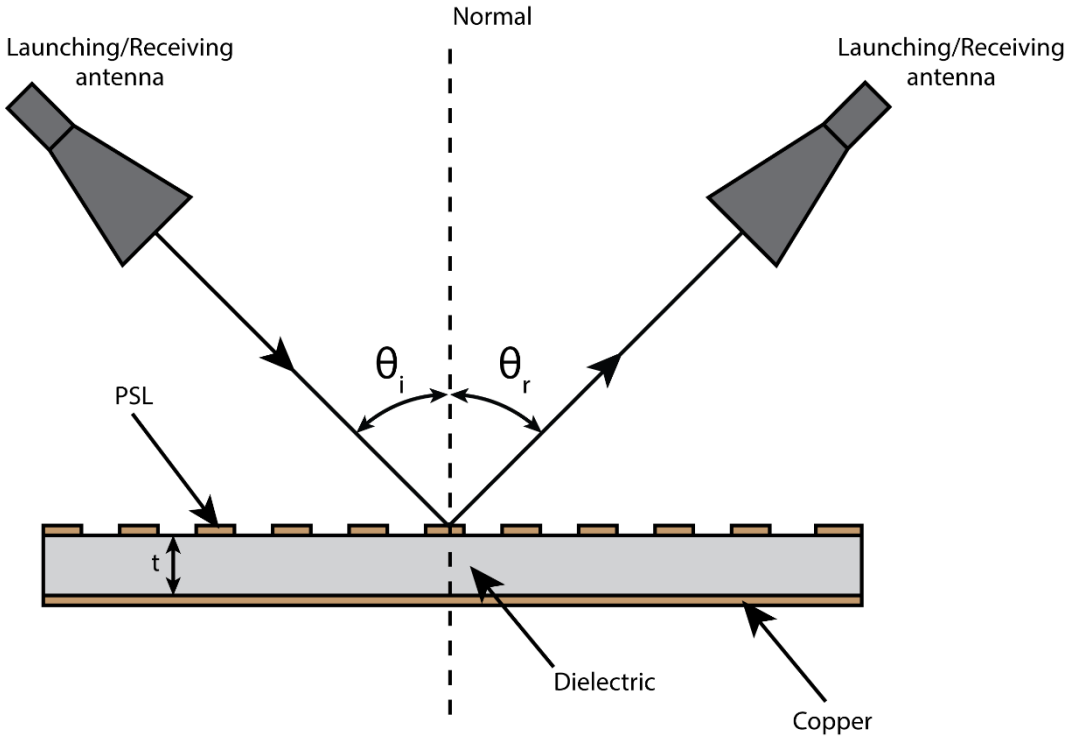

Figure 1.5.2. Schematic diagram illustrating the 2D PSL of planar geometry. The PSL is arranged on a dielectric substrate of thickness t with the copper backing acting as a second mirror, in a set-up similar to a Fabry-Perot cavity. Lattice synchronisation is achieved by standing wave formation within the dielectric.

The standing wave formed inside the dielectric fulfils the role of "global oscillator" (similar to the near cut off wave of the cylindrical structure) while the induced surface current synchronises adjacent cells. In addition to a volume mode (which is less well defined than in the cylindrical structure) the planar PSL can support a TEM mode. The Bragg conditions which must be satisfied for resonant coupling between the volume and surface fields to take place are:

$$\left(\overline{k}_{\perp}\right)^2 = (k_{\perp}^{v})^2 + (k_{\perp}^{s})^2 \qquad (1.5.1.a)$$

$$\overline{k}_z = k_z^s - k_z^v$$

(1.5.1.b)

For the planar PSLs with a chessboard corrugation, $\overline{k}_z = \overline{k}_\perp$. Assuming that coupling between the volume and surface fields occurs in the region where $k_\perp^v \cong k_\perp^s$, and provided the volume field is behaving like a standing wave ($k_z^v \cong 0$), the Bragg conditions can be expressed in the form:

$$\overline{k}_z \cong \sqrt{2} k_\perp^v \tag{1.5.2.a}$$

$$\overline{k}_z \cong k_z^s \tag{1.5.2.b}$$

.

Note that equations (1.5.2a) and (1.5.2b) are approximations since, in practice, some detuning will exist between the uncoupled volume and surface fields.

1.6 Interaction with an Electron Beam

A high power source can be generated by transferring energy from an electron beam to the EM field inside the 2D PSL. The frequency and spatial distribution of the cavity eigenmode can be tailored by varying the structure's parameters. Wave-beam interactions occur only when the appropriate synchronism conditions are satisfied at the points where the dispersion of the beam and EM field intersect. Taking into account the phase velocity $v_{ph} = \omega/k$, the EM field dispersion is written:

$$\omega = v_{ph}\sqrt{k_z^2 + k_\perp^2} \tag{1.6.1}$$

and the dispersion of the electron beam is expressed:

$$\omega = k_z v_z \pm \frac{\omega_b}{\gamma_0} \tag{1.6.2}$$

where v_z is the longitudinal beam velocity, ω_b is the plasma frequency of the electron beam, k_z is the longitudinal wavenumber and γ_0 is the relativistic factor, defined as:

$$\gamma_0 = (1 - {v_z}^2/c^2)^{-1/2}$$

It is important to note that the phase velocity of the wave (v_{ph}) always exceeds c (the speed of light in vacuum) in an unperturbed waveguide. However, when a corrugation is introduced at the inner wall, or in the presence of a dielectric lining, $v_{ph} < c$. This forms the basis of slow wave structures (SWS) which are known to facilitate Cherenkov interactions. The interaction points of equations (1.6.1) and (1.6.2) are illustrated schematically in figure 1.6.1 below.

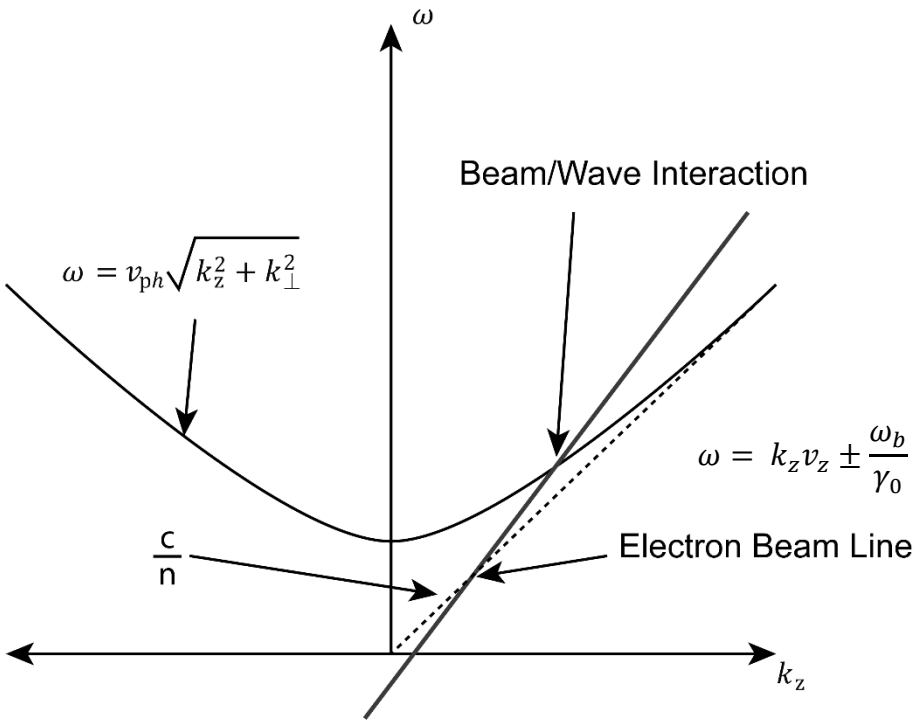

Figure 1.6.1. Schematic of the synchronisation condition, illustrating an interaction between an electron beam and a waveguide cavity mode.

Cherenkov radiation occurs when electrons move in a medium which has a refractive index ($\bar{n}$) greater than 1 and $v_z \geq v_{ph}$ where $v_{ph} = c/\bar{n}$. Assuming $\bar{n}$ is sufficiently large (such that $v_z > v_{ph}$) resonant energy exchange from the electrons to the wave can occur. An electron beam can interact with the partial

surface field of the localised cavity eigenmode when the following condition is satisified:

$$\omega = k_z v_z + \frac{2\pi}{d_z} v_z \tag{1.6.3}$$

where d_z is the longitudinal lattice period. The $k_z v_z$ term describes the Doppler shift associated with the moving beam while the oscillation induced in the electrons by the surface field (when $k_z^s = \overline{k}_z$) is described by $\frac{2\pi}{d_z} v_z$. Taking into account that the electrons interact with the localised eigenmode ($k_z \cong 0$) equation (1.6.3) is written

$$f = \frac{v_z}{d_z} = \frac{c}{d_z}\frac{v_z}{c}$$

The definition of γ_0 is rearranged to give $\frac{v_z}{c} = \sqrt{1 - \gamma_0^{-2}}$ and when $k_z \cong 0$ equation (1.6.3) becomes

$$f = \frac{c}{d_z}\sqrt{1 - \gamma_0^{-2}} \tag{1.6.4}$$

The relativistic Lorentz factor can then be expressed in terms of the electron beam accelerating voltage, U:

$$\gamma_0 = 1 + \frac{eU}{m_0 c^2} \cong 1 + \frac{W(keV)}{511(keV)} \tag{1.6.5}$$

An equation relating U and d_z to the operating wavelength of the structure can be obtained by rearranging (1.6.5) (Konoplev, MacLachlan et al. 2011).

$$U(kV) \cong 511(kV)\left[\frac{\lambda}{\sqrt{\lambda^2 - d_z^2}} - 1\right] \tag{1.6.6}$$

In order to achieve an interaction between an electron beam and the eigenmode of a PSL, the electron beam must be located outside the lattice to avoid its interception with the structure, whilst still remaining inside the strong EM field

region. If a metamaterial model is considered, the beam must pass close to the effective dielectric and couple to the decaying EM surface field as shown (figure 1.6.2.).

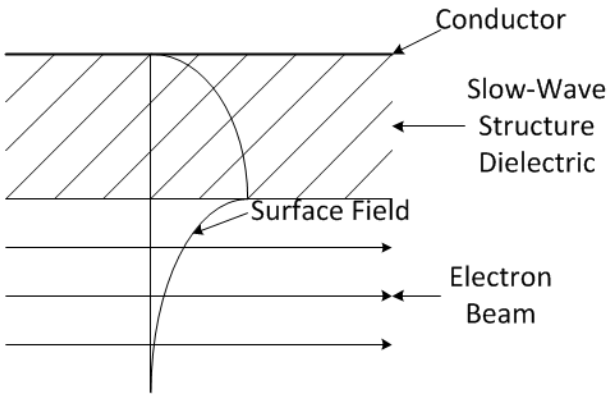

Figure 1.6.2. Schematic diagram showing coupling between an electron beam and the surface field in a slow-wave structure, lined with dielectric.

1.7 Aims and Layout of Thesis

The background theory and concepts behind this work have been introduced in chapter 1. A theoretical study of the 2D PSL of cylindrical topology is presented in chapter 2, where the PSL is described as a metadielectric with an effective refractive index. The field structure within the PSL is defined analytically by matching known boundary conditions at the air-dielectric interface. A second approach, where the lattice corrugation is mathematically approximated to an equivalent magnetic surface current, is carried out in order to obtain coupled wave equations.

Chapter 3 is devoted to the study of the structure's dispersion using an analytical expression derived from the coupled wave equations of chapter 2. It is shown that the electromagnetic characteristics of the structure are tailored by varying the lattice parameters. For the different lattice parameters, dispersion diagrams relating to the cases of strong and weak coupling are presented, and under certain conditions, the PSL's ability to support a Cherenkov instability when coupled with a suitable electron beam, is demonstrated.

Chapter 4 concerns the fabrication and experimental set-up of the planar PSLs, constructed from printed circuit board (PCB) using chemical etching techniques. High resolution images are provided using a 3D imager and the experimental equipment used in the measurements of the PSLs is discussed. Also in this chapter, the refractive index of the PCB dielectric (FR-4) has been measured for the different samples.

Experimental results are provided in chapter 5 where it is demonstrated that the results are dependent on factors such as the lattice period, the refractive index and thickness of the dielectric substrate, and whether or not the PSL and substrate are assembled with a copper backing, which enhances the synchronisation of the structure. Mode selection due to the coupling of volume and surface fields is observed when suitable parameter values are chosen.

The complex EM behaviour observed in chapter 5 is analysed in greater depth in chapter 6, where theoretical and numerical models are used to interpret the experimental findings. Dispersion relations for the planar PSLs, obtained using the Eigenmode solver of CST Microwave Studio, are discussed and compared with the analytical, cylindrical PSL dispersion diagrams of chapter 3. Finally, the key results and conclusions of this work, as well as possible topics of future work, are summarised in chapter 7.

Chapter 2- Theoretical Study of the 2D PSLs of Cylindrical Geometry

2.1. Introduction

Two separate ways of describing the eigenfield formed by the coupling of volume and surface fields are presented in this chapter. In §2.2, the field structure inside the cylindrical PSL is described by substituting the lattice at the inner wall with an effective metadielectric, while in the second method detailed in (§2.3), the corrugation is replaced with an equivalent magnetic surface current acting as an excitation source for the allowed waveguide modes. Using the magnetic surface current method leads to an expression defining the coupling between the volume and surface fields. The coupled wave equations derived in this approach are used later in Chapter 3 to obtain a dispersion relation and study the EM properties of the structure. Both techniques discussed in this chapter are valid only under the assumption of shallow corrugation. The conclusions of this theoretical study are summarised in §2.4.

2.2. Surface Field inside Smooth Cylindrical Waveguide Lined with an Effective Metadielectric

In this section, the effective metadielectric approximation is used to describe the field structure within the cylindrical 2D PSL. The corrugated inner waveguide wall is substituted with a thin dielectric layer, or high impedance surface, allowing the structure to be described as a regular cylindrical waveguide with a partial dielectric load (Sievenpiper, Zhang et al. 1999, Lier, Werner et al. 2011). The field structure is derived by defining the field in each distinct region and applying known boundary conditions at the air-dielectric interface. This approximation is only valid under the assumption of shallow corrugation, and the smaller the perturbation depth, the more reliable this method becomes (Clarricoats, Oliver 1984). The cylindrical PSLs considered in this work have been designed such that $\Delta r \ll D_{wg}$ (where D_{wg} is the

diameter of the cylindrical waveguide) and likewise, the planar PSLs which are the focus of chapters 4, 5 and 6, have $\Delta r \ll \lambda_{op}$.

The accuracy of this approach may be affected to some extent by the PSL not entirely satisfying the metamaterial criteria (on account of its period being comparable with the intended operating wavelength, $\lambda_{op} \approx d_z$). However, for the near cut-off volume waves, $\lambda_z \sim L$ (where *L* is the length of the lattice) and therefore $\lambda_z \gg d_z$. The transverse field structure of the near cut-off volume field is therefore unaffected by the thin dielectric insert, or lattice corrugation. When an azimuthally symmetric ($m = 0$), near-cut off mode is launched into the structure, the cylindrical dielectric-lined waveguide's hybrid *EH* eigenmode is similar to the *TM* mode of a regular cylindrical waveguide ($\Delta r = 0$).

It is important to note that the effective dielectric boundary does not coincide with the mean radius of the perturbed structure (Konoplev, MacLachlan et al. 2011). The effective boundary has a smaller inner radius than that of the lattice corrugation, enhancing the structure's suitability for use as the interaction region of an active device. When combined in a suitable configuration with an electron beam, the structure's eigenfield outside the corrugation should be sufficient to facilitate coupling with the beam, avoiding damage to the inner wall of the structure through over-heating, which may occur in a regular waveguide lined with dielectric (Cook, Tikhoplav et al. 2009).

The cylindrical waveguide lined with a high-impedance dielectric layer, defined by its effective refractive index, $\tilde{n}$ and inner and outer radii a and b respectively, is illustrated schematically in figure 2.2.1. The surface field is localised inside the dielectric ($r \geq a$) where it has a real wavenumber, and decays outside the dielectric ($r \leq a$) towards the centre of the waveguide.

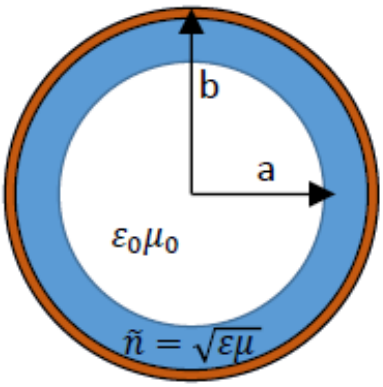

Figure 2.2.1 . Schematic of cylindrical waveguide, partially loaded with an effective meta-dielectric, or high-impedance surface. The blue region is the dielectric with refractive index $\tilde{n} = \sqrt{\varepsilon\mu}$ *and the white area in the centre of the waveguide represents vacuum with* $\tilde{n} = \sqrt{\varepsilon\mu} = 1$

Let us consider the stationary regime (i.e. when the cavity's eigenmode is established). In this case, the azimuthally nonsymmetric $(m_s \neq 0)$ *EH* surface field can be described as a superposition of the *E* and *H* modes of the dielectric-lined cylindrical waveguide. More specifically, in the present study, the cavity eigenmode is described as a superposition of the partial volume$\left(TM_{0,T}\right)$ and surface $\left(EH_{\bar{m},1}\right)$ fields (where T is chosen to ensure a near cut-off wave and the surface field has just one radial variation). By taking into account the periodicities along the azimuthal (φ) and longitudinal (z) coordinates, the Fourier decomposition of the surface field can be applied to describe its E_z and H_z components. These longitudinal field components are written in terms of a "slow" wave envelope $C_j^{e,h}$ (filled with a fast varying term) and a cylindrical function $F_{m_s}^{e,h}$ of order m_s describing the field oscillation in the transverse directions. The longitudinal E_z and H_z field components describing the hybrid surface field are written:

$$E_z = \sum_{m_s=0}^{\infty} F_{m_s}^{e}\left(k_{\perp(s)}r\right)\sin m_s\,\varphi \sum_{j=-\infty}^{\infty} C_j^{e}\,(z)e^{ij\bar{k}_z z} \qquad (2.2.1a)$$

$$H_z = \sum_{m_s=0}^{\infty} F_{m_s}^{h}\left(k_{\perp(s)}r\right)\cos m_s\,\varphi \sum_{j=-\infty}^{\infty} C_j^{h}\,(z)e^{ij\bar{k}_z z} \qquad (2.2.1b)$$

where j is the integer spatial harmonic number and C_j^e, C_j^h are the slowly varying amplitudes of the field harmonics. In the present study, coupling of the fundamental volume field harmonic with the surface field's ± 1 spatial harmonics is of interest. For simplicity, the treatment of higher order harmonics is ignored in this analysis, which focuses solely on the case where $j = \pm 1$ and $m_s = \bar{m}$. The requirement that $m_s = \bar{m}$ originates from the Bragg resonance condition, and is justified mathematically in §2.3. To further reduce the complexity of the problem, the study has been simplified to assume an infinite structure, allowing the slowly changing amplitudes of the finite structure to be treated as constants. This, along with the requirements that $j = 1$ and $m_s = \bar{m}$ reduces Eq.(2.2.1a,b) to the form:

$$E_z = F_{\bar{m}}\left(k_{\perp(s)} r\right) E(z) \cos \bar{k}_z z \ \sin \bar{m}\varphi \qquad (2.2.2a)$$

$$H_z = F_{\bar{m}}\left(k_{\perp(s)} r\right) H(z) \cos \bar{k}_z z \ \cos \bar{m}\varphi \qquad (2.2.2b)$$

Using this approximation, the E_z and H_z components of the hybrid surface field of the infinite cylindrical PSL (or effective metadielectric) are defined separately in the two distinct regions (inside and outside the effective dielectric) using the vector potentials $\mathrm{F}_z^{e,h}$ and $\mathrm{G}_z^{e,h}$ for the dielectric and vacuum regions respectively.

Starting with the dielectric region, we can write:

$$E_z = \left(\frac{\partial^2}{\partial z^2} + \ k^2 \varepsilon \mu\right) \mathrm{F}_z^e \qquad (2.2.3a)$$

$$H_z = \left(\frac{\partial^2}{\partial z^2} + \ k^2 \varepsilon \mu\right) \mathrm{F}_z^h \qquad (2.2.3b)$$

It is well known (Jackson 1999) that the vector potential of an EM field inside a cylindrical waveguide is defined in terms of Bessel functions of the first $\left(J_{\bar{m}}(gr)\right)$ and second kind $\left(N_{\bar{m}}(gr)\right)$ Bessel functions of the second kind, alternatively known as Neumann functions, are infinite at the centre of the waveguide $(r = 0)$ and thus neglected when dealing with a uniform waveguide. However, since we are

concentrating only on the dielectric insert around the circumference of the waveguide, and in this instance ignoring $r = 0$, the Neumann function must be included for a complete description of the field structure in this region. The vector potential must also have a sine or cosine dependence to define the electric and magnetic fields along the azimuthal direction. The vector potentials for the longitudinal electric (F_z^e) and magnetic (F_z^h) fields can be expressed in the form:

$$\mathrm{F}_z^e = [A_1^e J_{\bar{m}}(gr) + A_2^e N_{\bar{m}}(gr)] \sin \bar{m}\varphi \; e^{i\bar{k}_z z} \qquad (2.2.4a)$$

$$\mathrm{F}_z^h = [A_1^h J_{\bar{m}}(gr) + A_2^h N_{\bar{m}}(gr)] \cos \bar{m}\varphi \; e^{i\bar{k}_z z} \qquad (2.2.4b)$$

where A_1^e, A_2^e, A_1^h and A_2^h are constants associated with the electric (superscript *e*) and magnetic field (superscript *h*) components respectively and $g = \sqrt{k^2\tilde{n}^2 - \bar{k}_z^2}$ is the real transverse wavenumber for the field inside the dielectric. As with the case of a hollow cylindrical waveguide, the longitudinal electric field E_z must vanish at the metal wall ($r = b$),forcing F_z^e to zero.

$$A_1^e J_{\bar{m}}(gb) + A_2^e N_{\bar{m}}(gb) = 0 \qquad (2.2.5)$$

Eq.(2.2.5) is then be rearranged to define the constant, A_1^e .

$$A_1^e = -A_2^e \frac{N_{\bar{m}}(gb)}{J_{\bar{m}}(gb)} \qquad (2.2.6)$$

Substituting the current definition of A_1^e back into the original expression (Eq. 2.2.4a) gives a more precise description of the electric vector potential, F_z^e .

$$\mathrm{F}_z^e = \left[-A_2^e \frac{N_{\bar{m}}(gb)}{J_{\bar{m}}(gb)} \; J_{\bar{m}}(gr) + A_2^e \, N_{\bar{m}}(gr) \right] \sin \bar{m}\varphi \; e^{i\bar{k}_z z} \qquad (2.2.7)$$

This can be written in a more convenient form by taking the factor $-A_2^e / J_{\bar{m}}(gb)$ outside the brackets, and introducing a new constant, A.

$$\mathrm{F}_z^e = \frac{-A_2^e}{J_{\bar{m}}(gb)}\left[N_{\bar{m}}(gb)\ J_{\bar{m}}(gr) - J_{\bar{m}}(gb)\ N_{\bar{m}}(gr)\right]\sin\bar{m}\varphi\ e^{i\bar{k}_z z}$$

$$= A\Upsilon(gr)\ \sin\bar{m}\varphi\ e^{i\bar{k}_z z} \qquad (2.2.8)$$

Here, $A = -A_2^e/J_{\bar{m}}(gb)$ and $\Upsilon = N_{\bar{m}}(gb)\ J_{\bar{m}}(gr) - J_{\bar{m}}(gb)\ N_{\bar{m}}(gr)$. A similar approach is used to derive an expression for the magnetic vector potential inside the dielectric. Enforcing the boundary constraint at the metal wall such that:

$$\frac{\partial H_z}{\partial r} = 0 \ \Rightarrow\ \left.\frac{\partial A_z^h}{\partial r}\right|_{r=b} = 0 \qquad (2.2.9)$$

leads to the following expression:

$$A_1^h\, J'_{\bar{m}}(gb) + A_2^h\, N'_{\bar{m}}(gb) = 0 \qquad (2.2.10)$$

where $J'_{\bar{m}}(gb)$ and $N'_{\bar{m}}(gb)$ are the derivatives of the ordinary and Neumann Bessel functions with respect to their arguments. In this case, the constant A_1^h is described by:

$$A_1^h = -A_2^h \frac{N'_{\bar{m}}(gb)}{J_{\bar{m}}(gb)} \qquad (2.2.11)$$

The magnetic vector potential inside the dielectric region is therefore written in the form below:

$$\mathrm{F}_z^h = B\Psi(gr)\ \cos\bar{m}\varphi\ e^{i\bar{k}_z z} \qquad (2.2.12)$$

where $B = -A_2^h/J'_{\bar{m}}(gb)$ and $\Psi = [N'_{\bar{m}}(gb)\ J_{\bar{m}}(gr) - J'_{\bar{m}}(gb)\ N_{\bar{m}}(gr)]$.

Following the same steps outlined above, expressions for the electric and magnetic vector potentials inside the vacuum region, $\mathrm{G}_z^e; \mathrm{G}_z^h$ are obtained. Starting with the fundamental definition of the vector potential, we can write:

$$(E_z; H_z) = \left(\frac{\partial^2}{\partial z^2} + k^2\varepsilon\mu\right)(\mathrm{G}_z^e; \mathrm{G}_z^h) \qquad (2.2.13)$$

Outside the dielectric (in the vacuum region) the transverse wavenumber (p) is purely imaginary i.e. $k^2 = \bar{k}_z^2 + (ip)^2 = \bar{k}_z^2 - p^2$ where $p = \sqrt{\bar{k}_z^2 - k^2}$. Modified Bessel functions are required to describe the exponentially decaying surface field in this region. Since this area encompasses the centre of the waveguide where $r = 0$, the field structure is solely dependent on a modified Bessel function of the first kind $\left(I_{\bar{m}}(pr)\right)$ with no the need to include the Neumann function as before. The vector potentials for the longitudinal electric (G_z^e) and magnetic (G_z^h) fields in vacuum are:

$$\mathrm{G}_z^e = X\widehat{\Upsilon}(\mathrm{pr})\ \sin\bar{m}\varphi\ e^{i\bar{k}_z z} \tag{2.2.14a}$$

$$\mathrm{G}_z^h = Y\widehat{\Psi}(\mathrm{pr})\ \cos\bar{m}\varphi\ e^{i\bar{k}_z z} \tag{2.2.14b}$$

where X and Y are amplitude constants and $\widehat{\Upsilon} = \widehat{\Psi} = I_{\bar{m}}(pr)$

At the current stage, general equations describing the E_φ and H_φ tangential field components applicable to both (dielectric and vacuum) regions are obtained by employing Maxwell's curl equations for a source-free waveguide, $\nabla \times \bar{E} = -i\omega\mu\bar{H}$ and $\nabla \times \bar{H} = i\omega\varepsilon\bar{E}$. Taking the curl of the electric and magnetic fields, and solving for the transverse field components using the method detailed in (Pozar, 2007) yields:

$$E_\varphi = \frac{-i}{{k_\perp}^2}\left(\frac{\bar{k}_z}{r}\frac{\partial E_z}{\partial\varphi} - \omega\mu\frac{\partial H_z}{\partial r}\right) \tag{2.2.15a}$$

$$H_\varphi = \frac{-i}{{k_\perp}^2}\left(\omega\varepsilon\frac{\partial E_z}{\partial r} + \frac{\bar{k}_z}{r}\frac{\partial H_z}{\partial\varphi}\right) \tag{2.2.15b}$$

Equations (2.2.15a,b) can be expressed in terms of the vector potentials in the dielectric and vacuum regions. Starting with the dielectric region, we substitute the electric and magnetic vector potentials of Eq. (2.2.8) and Eq. (2.2.12) into the general

expressions provided in Eq. (2.2.3a,b). Evaluating the second order partial differential of Eq.(2.2.3.a,b) gives

$$\frac{\partial^2}{\partial z^2}\,\mathrm{F}_z^{e,h} = -\bar{k}_z^2\mathrm{F}_z^{e,h} \tag{2.2.16}$$

which, when substituted back into Eq.(2.1.3a,b), leads to

$$E_z = (k^2\tilde{n}^2 - \bar{k}_z^2)\mathrm{F}_z^e$$

$$H_z = (k^2\tilde{n}^2 - \bar{k}_z^2)\mathrm{F}_z^h$$

assuming $\mu = 1$ and $\tilde{n}^2 = \varepsilon\mu = \varepsilon$. Within the dielectric region, the transverse wavenumber g is defined as $g^2 = k^2n^2 - \bar{k}_z^2$ and from this it follows that:

$$(E_z; H_z) = g^2(\mathrm{F}_z^e; \mathrm{F}_z^h)$$

Substituting $(E_z; H_z) = g^2(\mathrm{F}_z^e; \mathrm{F}_z^h)$ into the tangential field component of Eq. (2.2.15a) gives

$$E_\varphi = -i\frac{\bar{k}_z}{r}\frac{\partial \mathrm{F}_z^e}{\partial \varphi} + i\omega\mu\frac{\partial \mathrm{F}_z^h}{\partial r}$$

The first order partial differential $i\bar{k}_z\mathrm{F}_z^e = \frac{\partial}{\partial z}\mathrm{F}_z^e$ is used to obtain

$$E_\varphi = -\frac{1}{r}\frac{\partial^2}{\partial \varphi \partial z}\mathrm{F}_z^e + i\omega\mu\frac{\partial \mathrm{F}_z^h}{\partial r} \tag{2.2.17a}$$

which defines the E_φ tangential field component. The H_φ tangential field component is written in the same way.

$$H_\varphi = -i\omega\varepsilon\,\frac{\partial \mathrm{F}_z^e}{\partial r} - \frac{1}{r}\,\frac{\partial^2 \mathrm{F}_z^h}{\partial \varphi \partial z} \tag{2.2.17b}$$

Deriving the tangential field components laid out in Eq.(2.2.17a) and (2.2.1.7.b) involves evaluating the partial derivatives using the definitions of F_z^e and F_z^h provided in Eq. (2.2.8) and Eq.(2.2.12). This leads to the following equations, defining the

tangential electric and magnetic field components within the effective dielectric region:

$$E_{\varphi} = i\cos\bar{m}\varphi\, e^{i\bar{k}_z z}\left(\omega\mu g B\, \Psi'(gr) - \frac{\bar{k}_z \bar{m} A}{r}\, \Upsilon(gr)\right) \qquad (2.2.18a)$$

$$H_{\varphi} = i\sin\bar{m}\varphi\, e^{i\bar{k}_z z}\left(\omega g\varepsilon A\, \Upsilon'(gr) - \frac{\bar{k}_z \bar{m} B}{r}\Psi(gr)\right) \qquad (2.2.18b)$$

Similarly, the longitudinal electric and magnetic fields outside the dielectric (in the vacuum region) where $k_{\perp}^{s} = p$ and $(E_z; H_z) = -p^2(\mathrm{G}_z^e; \mathrm{G}_z^h)$, are described below.

$$E_z = -p^2 X I_{\bar{m}}(pr)\sin\bar{m}\varphi\, e^{i\bar{k}_z z} \qquad (2.2.19a)$$

$$H_z = -p^2 Y I_{\bar{m}}(pr)\cos\bar{m}\varphi\, e^{i\bar{k}_z z} \qquad (2.2.19b)$$

Once again, the tangential field components are determined. The azimuthal surface fields E_{φ} and H_{φ} within the vacuum are given by:

$$E_{\varphi} = \frac{1}{r}\frac{\partial^2 \mathrm{G}_z^e}{\partial\varphi\partial z} - i\omega\mu\, \frac{\partial \mathrm{G}_z^h}{\partial r} \qquad (2.2.20a)$$

$$H_{\varphi} = i\omega\varepsilon\, \frac{\partial \mathrm{G}_z^e}{\partial r} + \frac{1}{r}\frac{\partial^2 \mathrm{G}_z^h}{\partial\varphi\partial z} \qquad (2.2.40b)$$

which corresponds to the following results:

$$E_{\varphi} = \left(\frac{\bar{m}\bar{k}_z}{r} X I_{\bar{m}}(pr) - \omega p Y I'_{\bar{m}}(pr)\right) i\cos\bar{m}\varphi\; e^{i\bar{k}_z z} \qquad (2.2.41a)$$

$$H_{\varphi} = \left(\omega p\, X I'_{\bar{m}}(pr) - \frac{\bar{m}\bar{k}_z}{r} Y I_{\bar{m}}(pr)\right) i\, sin\,\bar{m}\varphi\; e^{i\bar{k}_z z} \qquad (2.2.41b)$$

To ensure continuity of the tangential field components and impedance matching at the dielectric-vacuum interface (where $r = r_d = a$) the following boundary conditions must be satisfied:

$$E_z^V = E_z^D \tag{2.2.22a}$$

$$E_\varphi^V = E_\varphi^D \tag{2.2.22b}$$

$$H_z^V = H_z^D \tag{2.2.22c}$$

$$H_\varphi^V = H_\varphi^D \tag{2.2.22d}$$

where the superscripts V and D denote the field in a vacuum region and dielectric medium respectively. Applying these four boundary conditions leads to the following set of equations:

$$g^2 A\Upsilon(ga) = -p^2 X\, I_{\bar{m}}(pa) \tag{2.2.23a}$$

$$\mu\omega gaB\Psi'(ga) - \bar{m}\bar{k}_z A\Upsilon(ga) = \bar{m}\bar{k}_z X\, I_{\bar{m}}(pa) - Y\omega pa\, I'_{\bar{m}}(pa) \tag{2.2.23b}$$

$$g^2 B\Psi(ga) = -p^2 Y I_{\bar{m}}(pa) \tag{2.2.23c}$$

$$\varepsilon\omega gaA\Upsilon'(ga) - \bar{m}\bar{k}_z B\Psi(ga) = \omega paXI'_{\bar{m}}(pa) - \bar{m}\bar{k}_z Y I_{\bar{m}}(pa) \tag{2.2.23d}$$

Constants A and B can be expressed in terms of X and Y from equations (2.2.23a) and (2.2.23c). Equations (2.2.23b) and (2.2.23d) become:

$$X\left(\frac{\bar{m}\bar{k}_z p^2 I_{\bar{m}}(pa)}{g^2\Upsilon(ga)} - \bar{m}\bar{k}_z I_{\bar{m}}(pa)\right) = Y\left(\mu\omega ga\frac{p^2 I_{\bar{m}}(pa)}{g^2\Psi(ga)}\Psi'(ga) - \omega pa I'_{\bar{m}}(pa)\right) \tag{2.2.24a}$$

$$-X\left(\frac{\varepsilon\omega a\, p^2 I_{\bar{m}}(pa)}{g\Upsilon(ga)}\Upsilon'(ga) + \omega pa\, I'_{\bar{m}}(pa)\right) = -Y\left(\bar{m}\bar{k}_z\frac{p^2 I_{\bar{m}}(pa)}{g^2} + \bar{m}\bar{k}_z I'_{\bar{m}}(pa)\right) \tag{2.2.24b}$$

At this stage, constants X and Y are eliminated by dividing (2.2.24a) by (2.2.24b). Finally, by rearranging and introducing functions f_e, f_h and $\tilde{f}$, the dispersion equation describing the hybrid surface field is obtained (Konoplev, MacLachlan et al. 2011).

$$p^4 k^4 \tilde{\alpha}^4 \left(\varepsilon f_e - \tilde{f}\right)\left(f_h - \tilde{f}\right) = \bar{m}^2 \bar{k}_z^2 k^2 (\varepsilon - 1)^2 \qquad (2.2.25)$$

where $\tilde{\alpha}$ is the coupling coefficient describing the coupling between the volume and surface fields. The cylindrical functions $\tilde{f}$, f_e and f_h are defined below.

$$\tilde{f} = -\frac{I'_{\bar{m}}(pa)}{pa\, I_{\bar{m}}(pa)}$$

$$f_e = \frac{1}{ga} \frac{J'_{\bar{m}}(ga)N_{\bar{m}}(gb) - J_{\bar{m}}(gb)N'_{\bar{m}}(ga)}{J_{\bar{m}}(ga)N_{\bar{m}}(gb) - J_{\bar{m}}(gb)N_{\bar{m}}(ga)}$$

$$f_h = \frac{1}{ga} \frac{J'_{\bar{m}}(ga)N'_{\bar{m}}(gb) - J'_{\bar{m}}(gb)N'_{\bar{m}}(ga)}{J_{\bar{m}}(ga)N'_{\bar{m}}(gb) - J'_{\bar{m}}(gb)N_{\bar{m}}(ga)}$$

The dispersion relation provided in Eq.(2.2.25) confirms that the surface field with $m_s = \bar{m}$ has both E_z and H_z components (defined implicitly by the f_e and f_h cylindrical functions) as characteristic of a hybrid mode. The eigenfield dispersion theoretically proves that, for the case of an azimuthally symmetric surface field ($m_s = 0$), Eq. (2.2.25) reduces to give: $\left(\varepsilon f_e - \tilde{f}\right) = 0$ or $\left(f_h - \tilde{f}\right) = 0$ and consequently, $E_z = 0$ or $H_z = 0$ corresponding to either *TE* or *TM* waves.

Throughout this derivation it was assumed that $\mu = 1$ and $\tilde{n}^2 = \varepsilon\mu = \varepsilon$ for the effective metadielectric layer. At frequencies far from the PSL's resonant frequency, the electromagnetic field is unaffected by the presence of the metadielectric (or lattice) and no interaction will occur. At such frequencies, the refractive index is effectively $\tilde{n} = 1$ and the structure is equivalent to a hollow, unperturbed, cylindrical waveguide. As expected, when $\tilde{n}^2 = 1$ is substituted into Eq. (2.2.25), the right-hand side term goes to zero, indicating that either *TE* or *TM* waves will propagate, instead of the hybrid cavity eigenmode.

On the other hand, the metadielectric's effective refractive index close to the Bragg resonance frequency $\tilde{n}_B$, where the PSL can facilitate the mutual resonant scattering of volume and surface fields, can be defined in terms of $\bar{k}_z$ and k by phase-matching the coupled volume and surface fields constituting the cavity eigenmode. Within the effective dielectric region, the transverse surface field wavenumber (g) must equal the volume field's transverse wavenumber $(k_{\perp v})$ i.e. $k_{\perp v} \cong g$. For the near cut-off volume mode, $k_{\perp v} \cong k$ and hence $g \cong k$. Taking into account that $k^2\tilde{n}^2 = g^2 + (j\bar{k}_z)^2$ where j is the spatial harmonic of the surface field we obtain the expression:

$$k^2\tilde{n}^2 = k^2 + (j\bar{k}_z)^2 \tag{2.2.26}$$

Which, in the case of coupling with the $j = \pm 1$ surface field harmonics, reduces to:

$$k^2{\tilde{n}_B}^2 = k^2 + {\bar{k}_z}^2 \tag{2.2.27}$$

Finally, rearranging for $\tilde{n}_B$ gives:

$$\tilde{n}_B = \sqrt{1 + \frac{\bar{k}_z^2}{k^2}} \tag{2.2.28}$$

The metadielectric's effective refractive index $\tilde{n}_B$ when the Bragg resonance conditions are met determines the effective inner dielectric radius (Konoplev, MacLachlan et al. 2011). This is important when considering the structure's interaction with an electron beam which should intercept the metadielectric region whilst avoiding the PSL at the waveguide's inner wall.

Finally, impedance matching at the air-dielectric boundary is considered. According to the two-stage scattering model, the incident $TM_{0,T}$ wave (with E_z and H_φ components) excites a surface current (stage 1) which in turn excites the secondary, scattered $EH_{\bar{m},1}$ wave (stage 2). As this is a reversible process $(TM \leftrightarrow EH)$ the incident and scattered waves excite the same surface currents and consequently their impedances at the boundary must be equal. To satisfy this impedance matching condition, the following relationship must hold true:

$$\frac{E_z}{H_\varphi}\left(EH_{\bar{m},1}\right) = \frac{E_z}{H_\varphi}\left(TM_{0,T}\right)$$

Therefore, at the dielectric boundary

$$p\,\frac{I_m(pa)}{I'_m(pa)} = k_\perp^v\,\frac{J_0(k_\perp^v a)}{J'_0(k_\perp^v a)}$$

In the next section, the eigenfield inside a PSL of finite length is described by considering a fictitious magnetic surface current to describe the lattice corrugation.

2.3-Derivation of Coupling Coefficient by Magnetic Surface Current Method

In this section an analytical model of the PSL's possible scattering mechanisms is presented. Using coupled wave equations derived from Maxwell's equations, a definition of the coupling coefficient α determining the strength of the coupling between volume and surface fields is established by the method of fictitious magnetic sources (Kogelnik and Shank 1972, Kovalev, Orlova et al. 1972, Cooke and Denisov 1998). This provides analytic expressions assuming the corrugation at the inner wall is shallow. It is shown that the extent of the coupling depends on parameters such as the corrugation depth, and the structure's mean radius and operating frequency. Evaluation of the coupling coefficient α involves solving an integral mode coupling calculation which is a topic of possible future work. Although this study is pertinent to the case of a finite, cylindrical structure, it is also relevant when studying an equivalent PSL with planar geometry, due to the assumption that $r_0 \gg \lambda$ which has been made throughout this analysis. As mentioned earlier in this work, it is possible to convert between planar and cylindrical geometries through a process of conformal mapping.

2.3.1. Derivation of the Wave Equation for Volume and Surface Modes

The PSL of cylindrical topology can be simplified by instead considering a regular cylindrical waveguide with an equivalent (fictitious) magnetic surface current induced in its walls to account for the corrugation. To begin this theoretical study, a wave equation defining the transmitted power of the cylindrical waveguide modes, is derived from Maxwell's curl equations (where an $e^{i\omega t}$dependence has been assumed).

$$\overline{\nabla} \times \bar{E} = -\frac{\partial \bar{B}}{\partial t} - \bar{J}_m = -i\omega\mu\bar{H} - \bar{J}_m \tag{2.3.1}$$

$$\overline{\nabla} \times \bar{H} = -\frac{\partial \bar{D}}{\partial t} - \bar{J}_e = i\omega\varepsilon\bar{E} \tag{2.3.2}$$

The (fictitious) magnetic surface current, required to describe the coupled modes, is denoted by $\bar{J}_m$. Though both magnetic and electric surface currents are introduced in place of the lattice corrugation, the electric surface currents ($\bar{J}_e$) are effectively short circuited at the metal wall, and are therefore neglected in this analysis. Let us begin by taking the curl of Eq.(2.3.2).

$$\overline{\nabla} \times (\overline{\nabla} \times \bar{H}) = i\omega\varepsilon(\overline{\nabla} \times \bar{E}) = i\omega\varepsilon(-i\omega\mu\bar{H} - \bar{J}_m) \tag{2.3.3}$$

Applying the vector identity $\overline{\nabla} \times (\overline{\nabla} \times \bar{A}) = -\overline{\nabla}^2\bar{A}$ then gives

$$\overline{\nabla}^2\bar{H} = -\omega^2\varepsilon\mu\,\bar{H} + i\omega\varepsilon\bar{J}_m \tag{2.3.4}$$

The $\overline{\nabla}^2$ operator is the gradient defined in Cartesian coordinates: $\overline{\nabla}^2 = \bar{x}_0\nabla_x + \bar{y}_0\nabla_y + \bar{z}_0\nabla_z$. This approximation is valid for a cylindrical waveguide when the radius is large in comparison to the operating wavelength $(r_0 \gg \lambda_{op})$. Provided the lattice corrugation is shallow $(\Delta r \ll \lambda)$ the field inside the structure can be described by a superposition of the eigenmodes inside an unperturbed cylindrical waveguide (where the volume and surface modes have real and imaginary transverse

wavenumbers respectively). This involves defining an arbitrary field distribution over the cross-section of the cylinder. The transverse electric and magnetic fields when $z > 0$ are expanded as a sum of the allowed waveguide modes (Mahmoud 1991). In this approach, we are describing the field inside the cylindrical structure of finite length as a slow wave envelope, filled with fast varying terms. Using $C_q(z)$ to denote the slowly varying amplitude describing the field evolution along the z coordinate, the transverse magnetic and electric fields are written:

$$\bar{H} = \sum_q C_q(z)\bar{H}_q$$

$$\bar{E} = \sum_q C_q(z)\bar{E}_q.$$

This description of the transverse magnetic field is then substituted into Eq.(2.3.4) to give the full and orthogonal set of eigenmodes:

$$\bar{H} = \sum_q \bar{\nabla}^2(C_q(z)\bar{H}_q) = -\omega^2\varepsilon\mu\sum_q C_q(z)\bar{H}_q + i\omega\varepsilon\bar{J}_m \qquad (2.3.5)$$

When a waveguide is excited by an external source (in this case the magnetic surface current) (Jackson 1999) the total power transmitted through the structure is given by integrating the Poynting vector $^1/_2\,(E_t \times H_t^*)$ over the waveguide aperture (in this case the cylindrical cross section). This treatment is restricted to consider only the near cut-off volume mode ($\omega \approx \omega_0^v$) for which $k_z \to 0$ and $\lambda_z \to \infty$, ensuring a uniform field along the length of the cylindrical waveguide and allowing the PSL to be described as a single cavity. In practice, however, some detuning from the ideal situation where $\omega = \omega_0^v$ will arise due to the structure's finite length, resulting in the slowly varying amplitude term $C_q(z)$. The magnetic surface current ($\bar{J}_m$) determines the transverse electric field ($\bar{E}$) allowing $E_t \times H_t^*$ to be implicitly expressed by multiplying both sides of Eq.(2.3.5) by the complex conjugate of the transverse magnetic cut-off mode ($\bar{H}_{q'}^*$) and rearranging to obtain:

$$\bar{H}_{q'}^*\bar{\nabla}^2\sum_q C_q(z)\bar{H}_q + \omega^2\bar{H}_{q'}^*\sum_q C_q(z)\bar{H}_q = i\omega\varepsilon\bar{J}_m\bar{H}_{q'}^* \qquad (2.3.6)$$

Separating the gradient operator $\overline{\nabla}^2$ into its transverse and longitudinal components gives the following result:

$$\overline{H}_{q'}^{*}\overline{\nabla}_z^2\sum_q C_q(z)\overline{H}_q + \overline{H}_{q'}^{*}\overline{\nabla}_\perp^2\sum_q C_q(z)\overline{H}_q + \omega^2\overline{H}_{q'}^{*}\sum_q C_q(z)\overline{H}_q = i\omega\varepsilon\bar{J}_m\overline{H}_{q'}^{*} \tag{2.3.7}$$

The localised volume and surface modes with angular cut-off frequency ω_0^q are described by the Helmholtz equation $\overline{\nabla}_\perp^2\overline{H}_q \pm \frac{(\omega_0^q)^2}{c^2}\overline{H}_q = 0$ where "+" corresponds to the volume modes and "−" corresponds to the surface modes. This sign difference comes from the fact that the surface field is defined by an imaginary transverse wavenumber ($ik_\perp$) i.e. $k_{z,s}^2 = k^2 + k_{\perp,s}^2$.

For the near-cut off volume mode, where $\omega_{q'}^0 = \omega_0^v \cong \omega_0^s = \omega_0$ (and ω_0 is the angular cut-off frequency of the structure's cavity eigenmode) the Helmholtz equation $\overline{\nabla}_\perp^2\overline{H}_{q'} + \frac{{\omega_0}^2}{c^2}\overline{H}_{q'} = 0$ is rearranged and substituted into the second term of Eq.(2.3.7) which then becomes

$$-\frac{{\omega_0}^2}{c^2}\overline{H}_{q'}^{*}\sum_q C_q(z)\overline{H}_q$$

Eq.(2.3.7) is brought to the form:

$$\overline{H}_{q'}^{*}\sum_q \overline{\nabla}_z^2 C_q(z)\overline{H}_q + \overline{H}_{q'}^{*}\sum_q C_q(z)\left(-\frac{{\omega_0}^2}{c^2}\right)\overline{H}_q + \omega^2\overline{H}_{q'}^{*}\overline{H}_q = Q\bar{J}_m\overline{H}_{q'}^{*} \tag{2.3.8}$$

where Q is a constant, defined as $Q = i\omega\varepsilon$. Eq.(2.3.8) is then rearranged and written in the form below, where $\frac{(c^2\omega^2-\omega_0^2)}{c^2}$ describes the detuning between the angular cut-off frequency of the volume mode and the cavity eigenmode's angular frequency.

$$\overline{H}_{q'}^{*}\sum_q \overline{\nabla}_z^2 C_q(z)\overline{H}_q + \overline{H}_{q'}^{*}\sum_q C_q(z)\frac{(c^2\omega^2-\omega_0^2)}{c^2}\ \overline{H}_q = Q\bar{J}_m\overline{H}_{q'}^{*}$$

(2.3.9)

The wave equation defining the average power flow along the structure is obtained by integrating Eq.(2.3.9) around the azimuthal cross-section of the waveguide. At this stage, the orthogonality condition is considered.

$\int_{S\perp=\varphi} \overline{H}_q \overline{H}^*_{q'} = 0$ if $q \neq q'$

When the orthogonality of modes is taken into account, the left-hand side of Eq.(2.3.9) is reduced to describe the field amplitude . Both sides of this expression are then divided by $\overline{H}_q{}^2$ to obtain the final normalised wave equation.

$$\overline{\nabla}_z^2 C_q(z) + \frac{(c^2\omega^2 \mp \omega_0^2)}{c^2} C_q(z) = N \oint \bar{J}_m \overline{H}^*_{q'} \, d\sigma$$

(2.3.10)

The wave norm N is defined:

$$N = \frac{i\omega\varepsilon}{\oint_{S\perp} \overline{H}_q \overline{H}^*_{q'} \, d\varphi}$$

where $\oint_{S\perp} \overline{H}_q \overline{H}^*_{q'}$ is the surface integral of the waveguide modes around the perturbed cylindrical waveguide. It is important to note that the derived wave equation is applicable to both volume and surface fields depending on the $\mp$ sign variation, where " $-$ " corresponds to the volume waves and " $+$ " is used to describe the localised surface waves. We can therefore separate Eq.(2.3.10) into its individual volume and surface wave components where N_v and N_s correspond to the wave norms for the volume and surface waves respectively.

Volume Field:

$$\overline{\nabla}_z^2 C_q^v(z) + \frac{(c^2\omega^2 - (\omega_0^v)^2)}{c^2} C_q^v(z) = N_v \oint \bar{J}_m \overline{H}^*_{q'} \, d\sigma$$

(2.3.10a)

Surface Field:

$$\overline{\nabla}_z^2 C_q^s(z) + \frac{(c^2\omega^2 + (\omega_0^s)^2)}{c^2} C_q^s(z) = N_s \oint \bar{J}_m \overline{H}_q^*, d\sigma$$

(2.3.10b)

2.3.2- Detuning of Bragg Resonance

In §(2.3.1), the detuning between the cut-off frequency of the volume field and operating frequency of the structure $\frac{(c^2\omega^2-(\omega_0^v)^2)}{c^2}$ was introduced. Here, this concept is extended to account for the detuning between the Bragg frequency ω_B and the cut-off frequency of the surface field ω_0^s. An additional detuning parameter ($\Delta = \omega_0^v - \omega_0^s$ where $k_z^v \cong \Delta$ and $\Delta \propto \pi/L$) comes from the assumption that $\omega_0^v \cong \omega_0^s$ when the volume and surface fields are coupled. For simplicity, it has been assumed that $\Delta = 0$ for the theory presented in this work.

To achieve mode selection by coupling volume and surface fields, it is essential that the Bragg resonance conditions are met. The longitudinal condition states that: $\bar{k}_z = k_z^s - k_z^v$ and since we are dealing with the case where $k_z^v \cong 0$ it is required that $\omega_B = \omega_0^s$. From this it is evident that the Bragg frequency defines the scattering of the surface field.

Possible sources of detuning of the surface field from the Bragg frequency include small ohmic and radiation losses in the cavity. In the slow-varying amplitude description, boundary conditions impose that $E_z = 0$ at both ends of the structure ($z = 0, L$) and enforcing these constraints will predict the location of the cavity eigenmodes. However, this is only true for an ideal cavity, and in practice some radiation is leaked out the ends, mostly due to diffraction. In the derivation of the coupled mode equations, it is assumed that the diffractive and ohmic losses are very small, and will be accounted for by the structure's detuning.

To consider the detuning caused by these factors, we define the Bragg detuning $\hat{\delta}$ for both the volume and surface fields in terms of the mean angular cut-off frequency, $\bar{\omega}_0$ where:

$$\bar{\omega}_0 = \frac{\omega_0^v + \omega_0^s}{2}$$

$$\hat{\delta} = \frac{c^2\omega_B - \bar{\omega}_0}{c^2}$$

Using this notation, for the specific case of the fundamental harmonic of the near cut-off volume field which is of particular interest in this work, the slowly varying amplitude $C_q^v(z)$ is written in the form $C_q^v(z) = A_+e^{-i\hat{\delta}z} + A_-e^{+i\hat{\delta}z}$ where $A_{+,-}$ represents the amplitudes of the forwards and backwards scattered volume waves. From this point onwards, $A(z)$ and $B(z)$ (which differ from the constants introduced in §2.2) are used in various notations to denote the volume and surface field amplitudes respectively. Eq.(2.3.10) can now be revised to include the Bragg detuning parameter. Under the assumption that $\omega_0^v \cong \omega_0^s$ we can write:

$$\frac{(\omega_0^v)^2 + (\omega_0^s)^2}{2c^2} \cong \frac{(\omega_0^v)^2}{c^2}$$

$$\frac{(\omega_0^v)^2 - (\omega_0^s)^2}{2c^2} \cong 0$$

and the detuning term of the volume field is expressed:

$$\frac{(c^2\omega^2 - (\omega_0^v)^2)}{c^2} = \omega^2 - \frac{(\omega_0^v)^2}{c^2} = \omega^2 - \left[\left(\frac{(\omega_0^v)^2 + (\omega_0^s)^2}{2c^2}\right) - \left(\frac{(\omega_0^v)^2 - (\omega_0^s)^2}{2c^2}\right)\right]$$

$$= \left[\omega^2 - \left(\frac{(\omega_0^v)^2 + (\omega_0^s)^2}{2c^2}\right)\right] + \left(\frac{(\omega_0^v)^2 - (\omega_0^s)^2}{2c^2}\right)$$

This can be written in terms of the mean angular cut-off frequency $\bar{\omega}_0$ and detuning parameters $\hat{\delta}$ and Δ where $\omega^2 - \left(\frac{(\omega_0^v)^2+(\omega_0^s)^2}{2c^2}\right) \cong \frac{\omega\hat{\delta}}{c}$ and $\left(\frac{(\omega_0^v)^2-(\omega_0^s)^2}{2c^2}\right) \cong \frac{\bar{\omega}_0\Delta}{c^2}$ provided that the detuning is small.

$$\frac{(c^2\omega^2 - (\omega_0^v)^2)}{c^2} \cong \frac{\omega\hat{\delta}}{c} + \frac{\bar{\omega}_0\Delta}{c^2}$$

Similarly, for the surface field:

$$\frac{(c^2\omega^2 + (\omega_0^s)^2)}{c^2} \cong \frac{\bar{\omega}_0\Delta}{c^2} - \frac{\omega\hat{\delta}}{c}$$

Substituting these results into equations (2.3.10a) and (2.3.10b) gives the following volume and surface wave equations:

$$\bar{\nabla}_z^2 C_q^v(z) + \frac{\omega\hat{\delta}}{c} C_q^v(z) + \frac{\bar{\omega}_0\Delta}{c^2} C_q^v(z) = N_v \oint \bar{J}_m \bar{H}_{q'}^* \, d\sigma$$

(2.3.11a)

$$\bar{\nabla}_z^2 C_q^s(z) - \frac{\omega\hat{\delta}}{c} C_q^s(z) + \frac{\bar{\omega}_0\Delta}{c^2} C_q^s(z) = N_s \oint \bar{J}_m \bar{H}_{q'}^* \, d\sigma$$

(2.3.11b)

Having defined the detuning parameter $\hat{\delta}$, the next step in the derivation of the coupled mode equations involves giving consideration to the longitudinal Laplacian operator, $\bar{\nabla}_z^2$.

2.3.3 Descriptions of Volume and Surface Fields using Fourier Expansions

When considering the fundamental harmonic of the volume field, the first term of Eq.(2.3.11a) can be expressed in the form: $\bar{\nabla}_z^2\left(A_\pm(z)e^{\mp i\hat{\delta}z}\right)$. Partially differentiating with respect to z gives the result

$$\frac{\partial}{\partial z}\left(\mp i\hat{\delta}A_\pm(z)e^{\mp i\hat{\delta}z} + e^{\mp i\hat{\delta}z}\frac{\partial A_\pm}{\partial z}\right)$$

and taking the second order differential yields:

$$-\hat{\delta}^2 A_\pm(z)e^{\mp i\hat{\delta}z} \mp 2i\hat{\delta}e^{\mp i\hat{\delta}z}\frac{\partial A_\pm}{\partial z} + e^{\mp i\hat{\delta}z}\frac{\partial^2 A_\pm}{\partial z^2}$$

(2.3.12)

A similar approach is used to study the surface field excited at the periodic boundary along z. Since any periodic function can be expanded into a Fourier series, it is

possible to express the slowly varying $C_q^s(z)$ term of Eq.(2.3.11b) as a sum of sine and cosine functions using a complex Fourier series of the general form (Riley 2006)

$$f(x) = \sum_{r=-\infty}^{r=\infty} c_w exp\left(\frac{2\pi i w x}{L_x}\right)$$

Where w is an integer number which corresponds to the harmonic number of the surface field, n_s. The arbitrary periodic function L_x is replaced with the lattice period, d_z where $\bar{k}_z = 2\pi/d_z$. Following on from this, the harmonic expansion of the slowly varying surface field along the z-coordinate is presented in the form

$$C_q^s(z) = \sum_{n_s=-\infty}^{\infty} B_{n_s}(z) e^{i n_s \bar{k}_z z}$$

(2.3.13)

where B_{n_s} is the Fourier coefficient determined by the amplitude of the surface field with harmonic n_s and is used throughout this analysis to represent the surface field. The wave equation for the surface field is expanded by implementing Eq.(2.3.13)

$$\bar{\nabla}_z^2\left(\sum_n B_n(z)\, e^{in\bar{k}_z z}\right) - \frac{\omega\hat{\delta}}{c}\left(\sum_n B_n(z)\, e^{in\bar{k}_z z}\right) + \frac{\bar{\omega}_0\Delta}{c^2}\left(\sum_n B_n(z) e^{in\bar{k}_z z}\right) = N_s \oint \bar{J}_m \bar{H}_q^*\, d\sigma$$

(2.3.14)

Taking the second order partial differential, the first term of Eq.(2.3.14) becomes

$$\bar{\nabla}_z^2\left(\sum_n B_n(z)\, e^{in\bar{k}_z z}\right) = \sum_n \frac{\partial}{\partial z}\left(in\bar{k}_z B_n(z) e^{in\bar{k}_z z} + e^{in\bar{k}_z z}\frac{\partial B_n(z)}{\partial z}\right)$$

$$= \sum_n \left(2in\bar{k}_z e^{in\bar{k}_z z}\frac{\partial B_n(z)}{\partial z} - n^2 \bar{k}_z{}^2 B_n(z) e^{in\bar{k}_z z} + e^{in\bar{k}_z z}\frac{\partial^2 B_n(z)}{\partial z^2}\right)$$

(2.3.15)

Finally, substituting Eq.(2.3.12) into Eq.(2.3.11a) and Eq.(2.3.15) into Eq.(2.3.11b) yields expressions describing the volume and surface fields.

Volume field:

$$\left(-\hat{\delta}^2 A_{\pm}(z)e^{\mp i\hat{\delta}z} \mp 2i\hat{\delta}e^{\mp i\hat{\delta}z}\frac{\partial A_{\pm}}{\partial z} + e^{\mp i\hat{\delta}z}\frac{\partial^2 A_{\pm}}{\partial z^2}\right)$$

$$+\frac{\omega\hat{\delta}}{c}\left(\bar{A}_{+}(z)e^{-i\hat{\delta}z} + \bar{A}_{-}(z)e^{+i\hat{\delta}z}\right)\frac{\overline{\omega}_0\Delta}{c^2}\left(\bar{A}_{+}(z)e^{-i\hat{\delta}z} + \bar{A}_{-}(z)e^{+i\hat{\delta}z}\right)$$

$$= N_v \oint \bar{J}_m \overline{H}_q^* \, d\sigma$$

(2.3.16)

Eq.(2.3.16) describes the volume field in terms of the detuning parameter, $\hat{\delta}$, and only considers the forwards and backwards scattered volume wave. The slowly varying amplitude term $C_q^v(z)$ of Eq.(2.3.10a) may also be expressed as a complex Fourier expansion, similar to that of the surface field, by taking the periodicity of the structure into account and making the approximation that $k_{z,v} = \bar{k}_z = 2\pi/d_z$. Under this assumption the volume field's longitudinal wavenumber is equivalent to that of the structure, corresponding to the case of coherent, coupled eigenmode formation in the presence of minimal detuning.

$$C_q^v(z) = \sum_{n_v=-\infty}^{\infty} A_{n_v}(z)e^{in_v\bar{k}_z z}$$

(2.3.17)

Eq.(2.3.17) can be written in terms of n_v and $\bar{k}_z$ where $A_{n_v}(z)$ is the Fourier coefficient.

$$\sum_{n_v}\left(e^{in_v\bar{k}_z z}\frac{\partial^2 A_{n_v}(z)}{\partial z^2}-2in_v\bar{k}_z e^{in_v\bar{k}_z z}\frac{\partial A_{n_v}(z)}{\partial z}-{n_v}^2{\bar{k}_z}^2 A_{n_v}(z)e^{in_v\bar{k}_z z}\right)$$
$$+\frac{\omega\hat{\delta}}{c}\left(\sum_{n_v}A_{n_v}(z)\,e^{in_v\bar{k}_z z}\right)\frac{\bar{\omega}_0\Delta}{c^2}\left(\sum_{n_v}A_{n_v}(z)e^{in_v\bar{k}_z z}\right)$$
$$=N_v\oint\bar{J}_m\bar{H}_q^*\,d\sigma$$

(2.3.18)

The surface field is written in the same form.

Surface Field:

$$\sum_{n}\left(2in\bar{k}_z e^{in\bar{k}_z z}\frac{\partial B_n(z)}{\partial z}-n^2{\bar{k}_z}^2 B_n(z)e^{in\bar{k}_z z}+e^{in\bar{k}_z z}\frac{\partial^2 B_n(z)}{\partial z^2}\right)$$
$$-\frac{\omega\hat{\delta}}{c}\left(\sum_{n}B_n(z)\,e^{in\bar{k}_z z}\right)+\frac{\bar{\omega}_0\Delta}{c^2}\left(\sum_{n}B_n(z)e^{in\bar{k}_z z}\right)=N_s\oint\bar{J}_m\bar{H}_q^*\,d\sigma$$

(2.3.19)

2.3.4 The Magnetic Surface Current Boundary Condition

To evaluate the right-hand side of the wave-equation we must first define the term $\bar{J}_m\bar{H}_{q'}^*$. Provided the corrugation depth is suitably shallow ($\Delta r \ll \lambda$) the perturbed waveguide wall can be described as a smooth cylindrical surface with mean radius r_0 subject to the boundary condition (Kovalev, Orlova et al. 1972, Katsenelenbaum 1998, Cross, Konoplev et al. 2003, Burt, Samsonov et al. 2004, Ginzburg, Malkin et al. 2009) :

$$\bar{J}_m=\bar{n}\times\left[\bar{\nabla}(l\bar{E}\bar{n})+i\omega l[\bar{n}\times\bar{\mathrm{H}}]\right]$$

(2.3.20)

where $\bar{n}$ is the unit vector of the normal to the unperturbed waveguide wall and $\bar{E}\bar{n}=E_n$ is the electric field component normal to the waveguide wall. The shallow, sinusoidal corrugation on the inner surface of the waveguide is described by the function, l.

$$\bar{J}_m = \bar{n} \times \left(\overline{\nabla}(l\bar{E}\bar{n})\right) + i\omega l\bar{n} \times [\bar{n} \times \overline{\mathrm{H}}] = I_1 + I_2$$

(2.3.21)

In order to solve the wave equation, it is convenient to separate $\bar{J}_m$ into two components $I_1 = \bar{n} \times \left(\overline{\nabla}(l\bar{E}\bar{n})\right)$ and $I_2 = i\omega l\bar{n} \times [\bar{n} \times \overline{\mathrm{H}}]$ which can be integrated independently. Multiplying the first term by $\bar{H}_q^*$ yields the following expression:

$$\bar{H}_q^* I_1 = \left[\bar{n} \times \left(\overline{\nabla}(l\bar{E}\bar{n})\right)\right]\bar{H}_q^* = \left[\bar{H}_q^* \times \left(\overline{\nabla}(lE_n)\right)\right]\bar{n}$$

(2.3.22)

By rearranging the vector identity $\overline{\nabla} \times (f\bar{A}) = (\overline{\nabla}f \times \bar{A}) + f \cdot (\overline{\nabla} \times \bar{A})$ such that $\bar{A} \times \overline{\nabla}f = f \cdot (\overline{\nabla} \times \bar{A}) - \overline{\nabla} \times (f\bar{A})$ and substituting $\bar{A} = \bar{H}_q^*$ and $f = l\bar{E}\bar{n}$ we find that:

$$\bar{H}_q^* \times \overline{\nabla}(l\bar{E}\bar{n}) = lE_n\left(\overline{\nabla} \times \bar{H}_q^*\right) - \overline{\nabla} \times \left((lE_n)\bar{H}_q^*\right)$$

(2.3.23)

The complex conjugate of the electric field, $\bar{E}_q^*$ is introduced by considering the relation $\overline{\nabla} \times \bar{H}_q^* = i\omega\varepsilon\bar{E}_q^*$ which comes from Eq.(2.3.2).

$$\bar{H}_q^* \times \overline{\nabla}(lE_n) = i\omega\varepsilon lE_n\bar{E}_q^* - \overline{\nabla} \times \left(lE_n\bar{H}_q^*\right)$$

(2.3.24)

Assuming that $\varepsilon = 1$ inside the cylindrical waveguide and taking equations (2.3.22) and (2.3.24) into account gives the following result.

$$\bar{H}_q^* I_1 = i\omega lE_n\left(\bar{E}_q^*\bar{n}\right) - \overline{\nabla} \times \left(lE_n\bar{H}_q^*\right)\bar{n}$$

(2.3.25)

This is simplified by neglecting the $\overline{\nabla} \times \left(lE_n\bar{H}_q^*\right)\bar{n}$ term since $\overline{\nabla} \times E_n\bar{n} = 0$.

$$\bar{H}_q^* I_1 = i\omega lE_n\left(\bar{E}_q^*\bar{n}\right)$$

(2.3.26)

Similarly, for $\bar{H}_q^* I_2$ we can write:

$$\bar{H}_q^* I_2 = i\omega l \bar{n} \times [\bar{n} \times \bar{H}] \bar{H}_q^* = i\omega l \bar{H}_\tau \bar{H}_{q,\tau}^*$$

(2.3.27)

where $\bar{H}_\tau$ is the tangential magnetic field component, which comes from taking the cross product of the normal unit vector $\bar{n}$ and $\bar{n} \times \bar{H}$ such that $\bar{n} \times [\bar{n} \times \bar{H}] = \bar{H}_\tau$. Having defined I_1 and I_2, the $\bar{J}_m \bar{H}_q^*$ term of the right-hand side of the wave equation is brought to the form:

$$\bar{J}_m \bar{H}_q^* = \bar{H}_q^* I_1 + \bar{H}_q^* I_2 = i\omega l(z, \varphi)\left(E_{q,n} \bar{E}_{q,n}^* + \bar{H}_{q,\tau} \bar{H}_{q,\tau}^*\right)$$

(2.3.28)

where $\bar{E}_{q,n}^*$ is the complex conjugate structure of the normal electric field and $\bar{H}_{q,\tau}^*$ is the complex conjugate of the tangential electric field, both for a given mode, q . The components $E_{q,n}$ and $\bar{H}_{q,\tau}$ are the normal electric and tangential magnetic fields of the near-cut off (q^{th}) mode incident at the corrugated surface, l, where $l(z, \varphi)$ describes the lattice corrugation in the z and φ directions. Expanding Eq.(2.3.28) to encompass the full set of eigenmodes gives:

$$\bar{J}_m \bar{H}_q^* = i\omega l(z, \varphi)\left(\sum_q C_q(z)\, E_{q,n} \bar{E}_{q,n}^* + \sum_q C_q(z)\, \bar{H}_{q,\tau} \bar{H}_{q,\tau}^*\right)$$

(2.3.29)

However, the $TM_{0,T}$ near cut-off volume mode, providing synchronisation of the individual lattice perturbations and coupling with the localised surface field at the corrugated boundary, has no normal electric field component ($k_z \cong 0$) thus reducing Eq.(2.3.29) to give the following result:

$$\bar{J}_m \bar{H}_q^* = i\omega l(z, \varphi) \sum_q C_q(z)\, \bar{H}_{q,\tau} \bar{H}_{q,\tau}^*$$

(2.3.30)

The next stage in defining $\bar{J}_m \overline{H}_q^*$ involves considering the two-dimensional lattice corrugation, $l(z, \varphi)$.

2.3.5 Description of 2D Lattice Corrugation

It is evident from the previous expression Eq.(2.3.30) that the lattice corrugation l is required to evaluate the right-hand side of the wave equation and thus determine the coupling coefficient. The two-dimensional lattice perturbations are defined by cosine functions along the azimuthal and radial directions:

$$l(z, \varphi) = r_0 + \Delta r cos\bar{m}\varphi cos\bar{k}_z z \tag{2.3.31}$$

where r_0 is the mean radius of the cylinder, Δr is the perturbation height and $\bar{m}$ is the number of azimuthal variations of the perturbed structure. Using the trigonometric identity $cos\bar{m}\varphi = \frac{1}{2}\left(e^{i\bar{m}\varphi} + e^{-i\bar{m}\varphi}\right)$, we can express the corrugation in the following form:

$$l(z, \varphi) = r_0 + \frac{\Delta r}{4}\left(e^{i\bar{m}\varphi} + e^{-i\bar{m}\varphi}\right)\left(e^{i\bar{k}_z z} + e^{-i\bar{k}_z z}\right) \tag{2.3.32}$$

Referring back to Eq.(2.3.28) it is observed that, in addition to l, the tangential magnetic field component $\left(\overline{H}_{q,\tau}\right)$ is fundamental to evaluating the right-hand side term, $\bar{J}_m \overline{H}_q^*$. The component $\overline{H}_{q,\tau}$ is the superposition of all the allowed eigenmodes' tangential magnetic fields, and can thus be separated into its tangential magnetic volume and surface field components in the following way:

$$\overline{H}_{q,\tau} = \overline{H}_{q,\tau}^{v}(r, \varphi) + \overline{H}_{q,\tau}^{s}(r, \varphi)$$

We can then write:

$$\overline{H}_{q,\tau} = H_{q,\tau}^{v}(r) C_q^{v}(z) + H_{q,\tau}^{s}(r, \varphi) C_q^{s}(z) \tag{2.3.33}$$

Substituting in the fundamental volume field description for $C_q^v(z)$ (considering only the forwards and backwards scattered waves since $n = 0$) and surface field expansion for $C_q^s(z)$ yields:

$$\bar{H}_{q,\tau} = H_{q,\tau}^v(r)\left(A_+(z)e^{-i\hat{\delta}z} + A_-(z)e^{+i\hat{\delta}z}\right) + H_{q,\tau}^s(r)cos(m_s\varphi)\sum_{n_s} B_{n_s}(z)e^{in_s\bar{k}_z z}$$

(2.3.34)

As the structure is behaving like a Fabry-Perot cavity, standing wave formation resulting from the the incident and reflected travelling waves, is considered. When these two waves interfere with one another, the volume field is said to be coupled into itself. For completeness, the theory developed in this section considers not only the coupling between volume and surface fields, but also the "self-scattering" of volume and surface fields. Due to the fact that the near cut-off volume mode is reflected between the walls of the structure i.e. non-propagating, the fast oscillation terms $e^{-i\hat{\delta}z}$ and $e^{+i\hat{\delta}z}$ associated with the volume field's evolution along z disappear. The previous result is now reduced to the form:

$$\bar{H}_{q,\tau} = H_{q,\tau}^v(r)\sum_2 C_q^v(z) + H_{q,\tau}^s(r)cosm_s\varphi\sum_n B_n(z)e^{in\bar{k}_z z}$$

(2.3.35)

Expanding Eq.(2.3.30) to incorporate the sinusoidal corrugation of the lattice (defined in Eq.(2.3.31)) as well as the most recent definition of $\bar{H}_{q,\tau}$ (provided in Eq.(2.3.34)) gives:

$$\bar{J}_m\bar{H}_q^* = i\omega\left[r_0 + \frac{\Delta r}{4}\left(e^{i\bar{m}\varphi} + e^{-i\bar{m}\varphi}\right)\left(e^{i\bar{k}_z z} + e^{-i\bar{k}_z z}\right)\right]\bar{H}_{q,\tau}^{*,v}\left(H_{q,\tau}^v(r)\sum_2 C_q^v(z)\right.$$
$$\left. + H_{q,\tau}^s(r)cosm_s\varphi\sum_n B_n(z)e^{in\bar{k}_z z}\right)$$

(2.3.36)

Finally, the evaluation of $\bar{J}_m \overline{H}_q^*$ requires taking the contour integral over the cylindrical cross section $d\sigma$ illustrated schematically in figure 2.3.5.1.

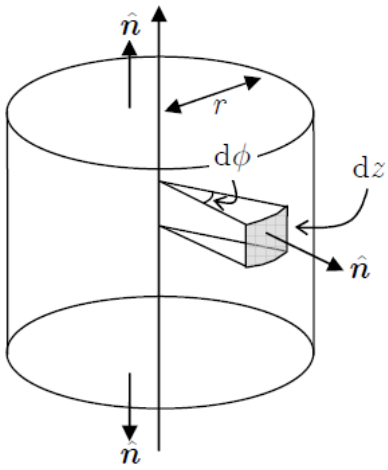

Figure 2.3.5.1 Schematic diagram of integration surfaces of cylinder.

The closed surface integral taken over the full circumference of the cross section (from 0 to 2π) is defined below. The integrand (U) is the wave equation's right-hand term i.e. $U = \bar{J}_m \overline{H}_q^*$ and φ represents the azimuthal coordinate.

$$\oint U(r,\varphi) d\,\sigma = \int_0^{2\pi} rU(r,\varphi)\, d\varphi$$

This leads to a general expression for the right-hand side of the wave equation which is adapted to describe the volume (superscript v) or surface (superscript s) fields by multiplying by the complex conjugate of the specified field, $\overline{H}_{q,\tau}^{*(v,s)}$.

$$N'_{v,s} \oint \bar{J}_m \overline{H}_q^*\, d\sigma = \int_0^{2\pi} r\left(\bar{J}_m \overline{H}_q^*\right)\Big|_{r=r_0} d\varphi$$

leads to the expression:

$$N'_{v,s}\int_0^{2\pi} r\left[r_0+\frac{\Delta r}{4}\left(e^{i\bar{m}\varphi}+e^{-i\bar{m}\varphi}\right)\left(e^{i\bar{k}_z z}+e^{-i\bar{k}_z z}\right)\right]\bar{H}^{*(v,s)}_{q,\tau}(r,\varphi)\left(H^{v}_{q,\tau}(r)\sum_{2}C^{v}_{q}(z)+H^{s}_{q,\tau}(r)cosm_s\varphi\sum_{n_s}B_{n_s}(z)e^{in_s\bar{k}_z z}\right)\Bigg|_{r=r_0}d\varphi \tag{2.3.37}$$

The updated wave norms $N_v{}'$ and N'_s are defined below:

$$N_v{}' = i\omega N_v = i\omega\frac{i\omega\varepsilon}{\oint_{S\perp}\bar{H}_{q,v}\bar{H}^{*}_{q,v}\,d\varphi} = \frac{-\omega^2\varepsilon}{\oint_{S\perp}\bar{H}_{q,v}\bar{H}^{*}_{q,v}\,d\varphi}$$

$$N'_s = \frac{-\omega^2\varepsilon}{\oint_{S\perp}\bar{H}_{q,s}\bar{H}^{*}_{q,s}\,d\varphi}$$

Having obtained a suitable integral equation for the volume and surface fields, we must now average over the period of fast oscillations to reach a non-trivial solution for $\oint \bar{J}_m\bar{H}^{*}_{q}\,d\sigma$.

2.3.6- Averaging over Fast Oscillation Terms

One of the requirements for coupling between the volume and surface fields is that the right-hand side of equations (2.3.16) and (2.3.19) must be non-zero, i.e. $N_{v,s}\oint \bar{J}_m\bar{H}^{*}_{q}\,d\sigma \neq 0$. Satisfying this condition involves averaging over the period of fast oscillations from 0 to 2π, in order to neglect the exponential terms that would otherwise integrate to zero. This section is devoted to the description of the fundamental harmonics of the individual volume (§2.3.6.1) and surface fields (§2.3.6.2). The analysis will later be extended to consider some of the higher order

harmonics (§2.3.7) although a full description requires carrying out a Bloch expansion which is beyond the scope of this study.

2.3.6.1. Fundamental Harmonic of Volume Field

To begin, the brackets of Eq.(2.3.37) are expanded to describe the volume field.

$$N_v{}' \int_0^{2\pi} r \Bigg(r_0 \bar{H}^{*v}_{q,\tau}(r) H^{v}_{q,\tau}(r) \sum_2 C^v_q\,(z) + r_0 \bar{H}^{*v}_{q,\tau} H^{s}_{q,\tau}(r) cosm_s\varphi \sum_{n_s} B_{n_s}(z) e^{i n_s \bar{k}_z z} + \frac{\Delta r}{4}\left(e^{i\bar{m}\varphi} + e^{-i\bar{m}\varphi}\right)\left(e^{i\bar{k}_z z} + e^{-i\bar{k}_z z}\right)\bar{H}^{*v}_{q,\tau} H^{v}_{q,\tau}(r) \sum_2 C^v_q\,(z) + \frac{\Delta r}{4}\left(e^{i\bar{m}\varphi} + e^{-i\bar{m}\varphi}\right)\Big(e^{i\bar{k}_z z} + e^{-i\bar{k}_z z}\Big)\bar{H}^{*v}_{q,\tau} H^{s}_{q,\tau}(r) cosm_s\varphi \sum_{n_s} B_{n_s}(z) e^{i n_s \bar{k}_z z} \Bigg)\Bigg|_{r=r_0} d\varphi \tag{2.3.38}$$

For clarity, the four terms inside the brackets of Eq.(2.3.38) are labelled as follows:

$$r_0 \bar{H}^{*v}_{q,\tau}(r) H^{v}_{q,\tau}(r) \sum_2 C^v_q\,(z) \tag{term 1}$$

$$r_0 \bar{H}^{*v}_{q,\tau} H^{s}_{q,\tau}(r) cosm_s\varphi \sum_{n_s} B_{n_s}(z) e^{i n_s \bar{k}_z z} \tag{term 2}$$

$$\frac{\Delta r}{4}\left(e^{i\bar{m}\varphi} + e^{-i\bar{m}\varphi}\right)\Big(e^{i\bar{k}_z z} + e^{-i\bar{k}_z z}\Big)\bar{H}^{*v}_{q,\tau} H^{v}_{q,\tau}(r) \sum_2 C^v_q\,(z) \tag{term 3}$$

$$\frac{\Delta r}{4}\left(e^{i\bar{m}\varphi}+e^{-i\bar{m}\varphi}\right)\left(e^{i\bar{k}_z z}+e^{-i\bar{k}_z z}\right)\bar{H}^{*v}_{q,\tau}H^{s}_{q,\tau}(r)cosm_s\varphi\sum_{n_s}B_{n_s}(z)e^{in_s\bar{k}_z z}$$

(term 4)

Considering these individual terms, it is observed that 1 and 3 describe the situation where the volume field is coupled into itself, whilst 2 and 4 demonstrate scattering and potential coupling between the volume and surface fields. This section deals with the fundamental volume field harmonic $(n_v = 0)$ and assumes that for the surface field $(n_s \neq 0)$. On closer inspection it is therefore noted that terms 2 and 3 will integrate to zero and can be ignored. This is based on the fact that the $e^{in_s\bar{k}_z z}$ fast oscillation component of term 2, cannot be discarded simply by setting $n_s = 0$. Also, the $\frac{\Delta r}{4}$ parameter depends on the corrugation depth (Δr) thus requiring a surface field to give a non-trivial result. Term 3, which contains only volume field terms, is neglected to give:

$$\bar{J}_m\bar{H}^{*}_{q} = N'_v\int_0^{2\pi} r\left(r_0H^{*v}_{q,\tau}H^{v}_{q,\tau}(r)\sum_{2}C^{v}_{q}(z)\right.$$
$$+\frac{\Delta r}{4}\left(e^{i\bar{m}\varphi}+e^{-i\bar{m}\varphi}\right)\left(e^{i\bar{k}_z z}\right.$$
$$\left.\left.+e^{-i\bar{k}_z z}\right)H^{*v}_{q,\tau}H^{s}_{q,\tau}(r)cosm_s\varphi\sum_{n_s}B_{n_s}(z)e^{in_s\bar{k}_z z}\right)\Big|_{r=r_0}d\varphi$$

(2.3.39)

We can now rewrite $cosm_s\varphi$ as $^1/_2\left(e^{im_s\varphi}+e^{-im_s\varphi}\right)$ and take out the common factor, r_0 to obtain:

$$\bar{J}_m \bar{H}_q^* = N'_v {r_0}^2 \int_0^{2\pi} \Bigg(H_{q,\tau}^{*v}(r_0) H_{q,\tau}^{v}(r_0) \sum_2 C_q^v(z) + \frac{\Delta r}{8 r_0} H_{q,\tau}^{*v}(r_0) H_{q,\tau}^{s}(r_0) \left(e^{i\bar{k}_z z} + e^{-i\bar{k}_z z}\right)\left(e^{i\bar{m}\varphi} + e^{-i\bar{m}\varphi}\right)\left(e^{im_s\varphi} + e^{-im_s\varphi}\right) \sum_{n_s} B_{n_s}(z) e^{in_s \bar{k}_z z} \Bigg)\Bigg|_{r=r_0} d\varphi$$

(2.3.40)

In order to have a non-zero expression describing the coupling between volume and surface fields, the fast oscillations $\left(e^{i\bar{m}\varphi} + e^{-i\bar{m}\varphi}\right)$ and $\left(e^{im_s\varphi} + e^{-im_s\varphi}\right)$ must vanish. Multiplying out the brackets, we find that a non-zero result is achieved by setting $m_s = \bar{m}$.

Expanding the brackets

$$\left(e^{i\bar{m}\varphi} + e^{-i\bar{m}\varphi}\right)\left(e^{im_s\varphi} + e^{-im_s\varphi}\right) = e^{i\bar{m}\varphi + im_s\varphi} + e^{i\bar{m}\varphi - im_s\varphi} + e^{-i\bar{m}\varphi + im_s\varphi} + e^{-i\bar{m}\varphi - im_s\varphi}$$

and setting $m_s = \bar{m}$ gives the result:

$$\left(e^{i\bar{m}\varphi} + e^{-i\bar{m}\varphi}\right)\left(e^{im_s\varphi} + e^{-im_s\varphi}\right) = e^{-2i\bar{m}\varphi} + 2$$

The remaining exponential term $e^{-2i\bar{m}\varphi}$ will then integrate to zero, giving a final result of 2. It has been mathematically proven that the fundamental volume field harmonic can participate in coupling only on the condition that $m_s = \bar{m}$. Otherwise, the coupled eigenfield cannot be defined. Consequently, from the Bragg resonance condition ($\bar{m} = m_v + m_s$) we find that $m_v = 0$. This is one of the necessary criteria which must be satisifed to ensure coupling between the volume and surface fields, and supports the reasoning behind launching an azimuthally symmetric volume field into the structure.

Another important aspect of Eq. (2.3.40) is the presence of the geometric parameter $\frac{\Delta r}{r_0}$ which is closely linked to the coupling coefficient. For coupling to take place, both volume and surface field components must exist giving a non-zero expression when

multiplied by this term. In other words, "self-scattering" of either field cannot be defined by $\frac{\Delta r}{r_0}$. Taking this into account, when $m_s = \bar{m}$, Eq.(2.3.40) is shortened to:

$$\bar{J}_m \bar{H}_q^* = N_v' {r_0}^2 \int_0^{2\pi} \left(H_{q,\tau}^{*v}(r_0) H_{q,\tau}^{v}(r_0) \sum_2 C_q^v(z) + \frac{\Delta r}{4r_0} H_{q,\tau}^{*v}(r_0) H_{q,\tau}^{s}(r_0) \left(e^{i\bar{k}_z z} + e^{-i\bar{k}_z z} \right) \sum_{n_s} n_s(z) e^{i n_s \bar{k}_z z} \right) \Bigg|_{r=r_0} d\varphi \tag{2.3.41}$$

The remaining fast oscillations in the longitudinal direction are eliminated by multiplying the $e^{\pm i\bar{k}_z z}$ and $e^{i n_s \bar{k}_z z}$ components together and setting $n_s \pm 1$.

$$\int e^{in\bar{k}_z z} \left(e^{i\bar{k}_z z} + e^{-i\bar{k}_z z} \right) d\varphi = \int \left(e^{i\bar{k}_z z(1+n_s)} + e^{i\bar{k}_z z(n_s-1)} \right) d\varphi$$

$$= \int \left(1 + e^{\pm 2i\bar{k}_z z} \right) d\varphi = 1$$

The expression defining $\bar{J}_m \bar{H}_q^*$ in the case of coupling involving the fundamental volume field harmonic is now further reduced to give:

$$N'_v {r_0}^2 \int_0^{2\pi} \left(H_{q,\tau}^{*v}(r_0) H_{q,\tau}^{v}(r_0) \sum_2 C_q^v(z) + \frac{\Delta r}{4r_0} H_{q,\tau}^{*v}(r_0) H_{q,\tau}^{s}(r_0) \sum_{\substack{n_s=-1 \\ n_s \neq 0}}^{1} B_{n_s}(z) \Bigg|_{r=r_0} \right) d\varphi \tag{2.3.42}$$

Finally, we take $H_{q,\tau}^{*v}(r_0)$, $H_{q,\tau}^{v}(r_0)$, $H_{q,\tau}^{s}(r_0)$, $C_q^v(z)$ and $B_n(z)$ terms outside the integral since all these terms are functions of r_0 (or z in the case of $C_q^v(z)$) and $B_n(z)$) and have no φ dependence.

$$N'_v {r_0}^2 \left(H^{*v}_{q,\tau}(r_0) H^{v}_{q,\tau}(r_0) \sum_{2} C^{v}_{q}(z) \int_0^{2\pi} d\varphi + \frac{\Delta r}{4r_0} H^{*v}_{q,\tau}(r_0) H^{s}_{q,\tau}(r_0) \sum_{\substack{n=-1 \\ n\neq 0}}^{1} B_n(z) \int_0^{2\pi} d\varphi \right) \tag{2.3.43}$$

In Eq. (2.3.44) $C^{v}_{q}(z)$ is replaced with amplitude $\tilde{A}_q(z)$ to remain consistent with the rest of this analytical study where A is used to denote the amplitude of the volume field. The accent indicates that $\tilde{A}_q$ is different from the amplitudes A_n and $A_{\pm}$ introduced earlier in this work.

$$\bar{J}_m \bar{H}^*_q = 2\pi N'_v {r_0}^2 \left(H^{*v}_{q,\tau}(r_0) H^{v}_{q,\tau}(r_0) \sum_{q=1}^{2} \tilde{A}_q(z) + \frac{\Delta r}{4r_0} \bar{H}^{*v}_{q,\tau}(r_0) H^{s}_{q,\tau}(r_0) \sum_{\substack{n=-1 \\ n\neq 0}}^{1} B_{n_s}(z) \right) \tag{2.3.44}$$

In this final expression, the first term describes the situation where the volume field scatters into itself, while the second defines inductive coupling between the volume and surface fields when the appropriate conditions are met. This section relates to the specific case where only the fundamental harmonic of the volume field (defined by a forwards and backwards scattered wave) is taken into consideration. In §2.4.7, we take a more general approach to include some of the higher order volume field harmonics, and mathematically explore the possible scattering mechanisms in the cases where either $n_v = 0$ or $n_s = 0$, using a similar method as presented in this section. First, however, we repeat the analysis for the fundamental harmonic ($n_s = 0$) of the surface field, whilst limiting the volume field harmonics such that $n_v = \pm 1$.

2.3.6.2 Fundamental Harmonic of Surface Field

In this section, we consider the case where $n_s = 0$ (with $n_v = \pm 1$).The general integral expression defining the right-hand side of the wave equation was given in Eq. (2.3.3.7) of §2.3.5. Expressing this equation in terms of the surface field we can write:

$$\bar{J}_m \bar{H}_q^* = N'_s \int_0^{2\pi} r \left[r_0 + \frac{\Delta r}{4} \left(e^{i\bar{m}\varphi} + e^{-i\bar{m}\varphi} \right) \left(e^{i\bar{k}_z z} + e^{-i\bar{k}_z z} \right) \right] \bar{H}_{q,\tau}^{*,S}(r,\varphi) \left(H_{q,\tau}^{v}(r) \sum_2 C_q^v(z) + H_{q,\tau}^{s}(r) cos m_s \varphi \sum_{n_s} B_{n_s}(z) e^{i n_s \bar{k}_z z} \right) \Bigg|_{r=r_0} d\varphi \tag{2.3.45}$$

Recalling that $H_{q,\tau}^{*,S}(r,\varphi) = \bar{H}_{q,\tau}^{*,S}(r) cos\bar{m}\varphi$ and expanding yields:

$$\begin{aligned} \bar{J}_m \bar{H}_q^* = N'_s {r_0}^2 \int_0^{2\pi} & H_{q,\tau}^{*,S}(r_0) cos\bar{m}\varphi \; H_{q,\tau}^{v}(r_0) \sum_2 C_q^v(z) \\ & + H_{q,\tau}^{*,S}(r_0) cos\bar{m}\varphi \; H_{q,\tau}^{s}(r_0) cos\bar{m}\varphi \sum_{n_s} B_{n_s}(z) e^{in\bar{k}_z z} + \frac{\Delta r}{4 r_0} \left(e^{i\bar{m}\varphi} \right. \\ & \left. + e^{-i\bar{m}\varphi} \right) \left(e^{i\bar{k}_z z} + e^{-i\bar{k}_z z} \right) H_{q,\tau}^{*,S}(r_0) cos\bar{m}\varphi \; H_{q,\tau}^{v}(r_0) \sum_2 C_q^v(z) \\ & + \frac{\Delta r}{4 r_0} \left(e^{i\bar{m}\varphi} + e^{-i\bar{m}\varphi} \right) \left(e^{i\bar{k}_z z} \right. \\ & \left. + e^{-i\bar{k}_z z} \right) H_{q,\tau}^{*,S}(r_0) cos\bar{m}\varphi \; H_{q,\tau}^{s}(r_0) cos m_s \varphi \sum_{n_s} B_{n_s}(z) e^{i n_s \bar{k}_z z} \Bigg|_{r=r_0} d\varphi \end{aligned} \tag{2.3.46}$$

The terms inside the brackets of Eq.(2.3.46) are listed below:

$$H_{q,\tau}^{*,S}(r_0) cos\bar{m}\varphi \; H_{q,\tau}^{v}(r_0) \sum_2 C_q^v(z)$$

[term 1]

$$H_{q,\tau}^{*,s}(r_0)cos\bar{m}\varphi\ H_{q,\tau}^{s}(r_0)cos\bar{m}\varphi\sum_{n_s}B_{n_s}(z)e^{in_s\bar{k}_z z}$$

[term 2]

$$\frac{\Delta r}{4r_0}\left(e^{i\bar{m}\varphi}+e^{-i\bar{m}\varphi}\right)\left(e^{i\bar{k}_z z}+e^{-i\bar{k}_z z}\right)H_{q,\tau}^{*,s}(r_0)cos\bar{m}\varphi\ H_{q,\tau}^{v}(r_0)\sum_{2}C_q^v\,(z)$$

[term 3]

$$\frac{\Delta r}{4r_0}\left(e^{i\bar{m}\varphi}+e^{-i\bar{m}\varphi}\right)\left(e^{i\bar{k}_z z}+e^{-i\bar{k}_z z}\right)H_{q,\tau}^{*,s}(r_0)cos\bar{m}\varphi\ H_{q,\tau}^{s}(r_0)cosm_s\varphi\sum_{n_s}B_{n_s}(z)e^{in_s\bar{k}_z z}$$

[term 4]

It is evident from Eq.(2.3.46) that term 4 must be discarded since only expressions with both surface and volume field components may include the $\frac{\Delta r}{4r_0}$ geometric coupling parameter. Term 4 is also excluded on the basis that, for $n_s = 0$, the exponential term $e^{in_s\bar{k}_z z} = 1$ and thus multiplication with $\left(e^{i\bar{k}_z z}+e^{-i\bar{k}_z z}\right)$ cannot eliminate the remaining fast oscillation terms. Equation (2.3.4.6) is further reduced by neglecting term 1 since no apparent means of cancelling out the cosine component describing the field structure around the azimuth exists. Eq.(2.2.46) is therefore simplified to give:

$$N'_s{r_0}^2\int_0^{2\pi}H_{q,\tau}^{*,s}(r_0)cos\bar{m}\varphi\ H_{q,\tau}^{s}(r_0)cos\bar{m}\varphi\sum_{n}B_n(z)e^{in\bar{k}_z z}+\frac{\Delta r}{4r_0}\left(e^{i\bar{m}\varphi}+e^{-i\bar{m}\varphi}\right)\left(e^{i\bar{k}_z z}+e^{-i\bar{k}_z z}\right)H_{q,\tau}^{*,s}(r_0)cos\bar{m}\varphi\ H_{q,\tau}^{v}(r_0)\sum_{2}C_q^v\,(z)\Big|_{r=r_0}d\varphi$$

(2.3.47)

Substituting the Fourier expansion of the volume field harmonics in place of $C_q^v(z)$ allows for the $e^{\pm i\bar{k}_z z}$ terms associated with scattering in the longitudinal direction to

be eliminated. This result is further reduced and re-written by employing the identity $\left(e^{i\bar{m}\varphi}+e^{-i\bar{m}\varphi}\right)=2cos\bar{m}\varphi$.

$$N'_s{r_0}^2\left(H^{*,S}_{q,\tau}(r_0)H^{S}_{q,\tau}(r_0)B_0(z)\int_0^{2\pi}\left(\frac{1}{2}+\frac{1}{2}cos\bar{m}\varphi\right)d\varphi\right.$$
$$+\int_0^{2\pi}\left(\frac{\Delta r}{2r_0}\left(e^{i\bar{k}_z z}\right.\right.$$
$$\left.\left.\left.+e^{-i\bar{k}_z z}\right)cos\bar{m}\varphi H^{*,S}_{q,\tau}(r_0)cos\bar{m}\varphi\, H^{v}_{q,\tau}(r_0)\sum_{n_v}A_{n_v}(z)e^{in_v\bar{k}_z z}\right)d\varphi\right)$$

(2.3.48)

The remaining stage involves eliminating the leftover fast oscillation terms. This is achieved simply by setting $n_v=\pm1$ and substituting $A_{\pm n_v}\left(e^{i\bar{k}_z z(\pm n_v+1)}+e^{i\bar{k}_z z(\pm n_v-1)}\right)$. It is shown in section §6.3.7.2 that this is a valid coupling mechanism. However, the main focus of this work is the interaction between the $n_v=0$ and $n_s=\pm1$ harmonics. The final expression, describing scattering from the fundamental $n_s=0$ surface field into the $n_v=\pm1$ volume field harmonics is presented below.

$$\pi N'_s{r_0}^2\left(H^{*,S}_{q,\tau}(r_0)H^{S}_{q,\tau}(r_0)B_0(z)+\frac{\Delta r}{2r_0}H^{*,S}_{q,\tau}(r_0)\,H^{v}_{q,\tau}(r_0)\sum_{\substack{n_v=-1\\ n_v\neq0}}^{n_v=1}A_{n_v}(z)\right)$$

(2.3.49)

This expression is comprised of 2 parts describing the accumulation of a localised surface field (which has no contribution to the coupling between the volume and surface fields) and the scattering of the surface field into the volume field.

2.3.7- Coupled Wave Equations

Thus far, we have considered only the fundamental harmonics of the two fields. For completeness, and to provide a more thorough mathematical description of the possible scattering processes, the Fourier expansion of both fields is included, allowing different values of n_v and n_s to be explored. We follow the same procedure

as outlined above except in this case, multiplying $\bar{J}_m \overline{H}_q^*$ by $e^{-i\bar{k}_z z n_v}$ or $e^{-i\bar{k}_z z n_s}$, depending on whether the volume or surface field is studied. For a full solution to this problem, rather than the approximation presented in this work, it is necessary to carry out a Bloch expansion over the full set of modes (McIver 2007, Tymis and Thompson 2014). This is ongoing research and a potential subject of future work. The present study gives an insight into possible coupling between the $n_{v,s} = 0$ and $n_{v,s} = \pm 1,2$ volume and surface fields' spatial harmonics and is separated into two parts. The first (§2.3.7.1) describes scattering of the $n_v = 0$ volume field into the surface field while the second part (§2.3.7.1) is dedicated to the scattering of the $n_s = 0$ surface field into the volume field.

2.3.7.1 Scattering of the Fundamental Volume Field into the Surface Field

Through substitution of the identity $\left(e^{i\bar{m}\varphi} + e^{-i\bar{m}\varphi}\right) = 2cos\bar{m}\varphi$ into Eq.(2.3.37) and by multiplying the right-hand-side of the volume field expression Eq.(2.3.26) by $e^{-i\bar{k}_z z n_v}$ we can write

$$N_v' \int_0^{2\pi} r \left[r_0 + \frac{\Delta r}{2} cos\bar{m}\varphi \left(e^{i\bar{k}_z z} + e^{-i\bar{k}_z z} \right) \right] H_{q,\tau}^{*,v}(r) e^{-i\bar{k}_z z n_v} \left(H_{q,\tau}^{v}(r) \sum_{n_v} A_{n_v}(z) e^{i\bar{k}_z z n_v} + H_{q,\tau}^{s}(r) cos\bar{m}\varphi \sum_{n_s} B_{n_s}(z) e^{i n_s \bar{k}_z z} \right) \Bigg|_{r=r_0} d\varphi \tag{2.3.50}$$

By multiplying the radial exponential terms associated with the volume field, Eq.(2.3.50) is brought to the form:

$$N'_v {r_0}^2 \int_0^{2\pi} \Big[H_{q,\tau}^{*,v}(r_0) e^{-i\bar{k}_z z n_v} + \frac{\Delta r}{2r_0} \big(e^{i\bar{k}_z z - i\bar{k}_z z n_v} + e^{-i\bar{k}_z z - i\bar{k}_z z n_v} \big) H_{q,\tau}^{*,v}(r_0) cos\bar{m}\varphi \Big] \Bigg(H_{q,\tau}^{v}(r_0) \sum_{n_v} A_{n_v}(z) e^{i\bar{k}_z z n_v} + H_{q,\tau}^{s}(r_0) cos\bar{m}\varphi \sum_{n_s} B_{n_s}(z) e^{i n_s \bar{k}_z z} \Bigg) \Bigg|_{r=r_0} d\varphi$$

(2.3.51)

and neglecting the same terms as before yields the following result

$$N'_v {r_0}^2 \int_0^{2\pi} \Bigg(H_{q,\tau}^{*,v}(r_0) e^{-i\bar{k}_z z n_v} H_{q,\tau}^{v}(r_0) \sum_{n_v} A_{n_v}(z) e^{i\bar{k}_z z n_v} + \frac{\Delta r}{2r_0} \big(e^{i\bar{k}_z z (1-n_v)} + e^{-i\bar{k}_z z (1+n_v)} \big) H_{q,\tau}^{*,v}(r_0) cos\bar{m}\varphi H_{q,\tau}^{s}(r_0) cos\bar{m}\varphi \sum_{n_s} B_{n_s}(z) e^{i n_s \bar{k}_z z} \Bigg) \Bigg|_{r=r_0} d\varphi$$

(2.3.52)

Employing the trigonometric identity $cos^2(\bar{m}\varphi) = \frac{1}{2} + \frac{1}{2} cos\bar{m}\varphi$ and integrating:

$$2\pi {r_0}^2 N'_v \Bigg(H_{q,\tau}^{*,v}(r_0) H_{q,\tau}^{v}(r_0) \sum_{n_v} A_{n_v}(z) e^{i\bar{k}_z z n_v - i\bar{k}_z z n_v} + \frac{\Delta r}{4r_0} H_{q,\tau}^{*,v}(r_0) H_{q,\tau}^{s} \sum_{n_s} B_{n_s}(z) \big(e^{i\bar{k}_z z (1-n_v+n_s)} + e^{i\bar{k}_z z (-1-n_v+n_s)} \big) \Bigg)$$

(2.3.53)

where the fast oscillation term associated with the volume field disappears to give the final result below.

$$2\pi {r_0}^2 N_v' \Bigg(H_{q,\tau}^{*,v}(r_0) H_{q,\tau}^{v}(r_0) \sum_{n_v} A_{n_v}(z) + \frac{\Delta r}{4r_0} H_{q,\tau}^{*,v}(r_0) H_{q,\tau}^{s} \sum_{n_s} B_{n_s}(z) \left(e^{i\bar{k}_z z(1-n_v+n_s)} + e^{i\bar{k}_z z(-1-n_v+n_s)} \right) \Bigg)$$

(2.3.54)

For a non-zero result after integrating, we must have $1 - n_v + n_s = 0$ and $-1 - n_v + n_s = 0$. We split n_s into its 2 harmonic components, $n_s^1 = n_v - 1$ and $n_s^2 = n_v + 1$. Setting $n_v = 0$ and $n_v = \pm 1$ we find:

- If $n_v = 0, n_s^1 = -1;\ n_s^2 = 1;\ n_s^{1,2} = \pm 1$
- If $n_v = 1, n_s^1 = 0;\ n_s^2 = 2;$
- If $n_v = -1, n_s^1 = -2;\ n_s^2 = 0;$

This serves as mathematical validation that the fundamental volume field harmonic $n_v = 0$ couples with the $n_s \pm 1$ harmonics as anticipated. It has also been established that the $n_v = 1$ harmonic can potentially couple with the $n_s = 0, 2$ surface field harmonics, and likewise, scattering is expected to occur between the $n_v = -1$ and $n_s = 0, -2$ harmonics.

Referring back to the volume field description (Eq.2.3.18) we can write:

$$\bar{\nabla}_z^2 \left(\sum A_n(z) e^{in\bar{k}_z z} \right) + \frac{\omega \hat{\delta}}{c} \left(\sum A_n(z) e^{in\bar{k}_z z} \right) + \frac{\bar{\omega}_0 \Delta}{c^2} \left(\sum A_n(z) e^{in\bar{k}_z z} \right) = N_v' \oint \bar{J}_m \bar{H}_q^* \, d\sigma$$

Following from this, coupled wave equations are obtained by introducing a coefficient $\alpha_{v,s}$ defining the coupling from the volume field to the surface field. Expressions for the specific cases where $n_v = 0$ and $n_v = \pm 1$ are provided below.

For $n_v = 0$,

$$\left(\frac{\partial^2 A_0}{\partial z^2}\right) + \frac{\omega\hat{\delta}}{c}(A_0(z)) + \frac{\bar{\omega}_0\Delta}{c^2}\big(A_0(z)\big) = \alpha_{v,s}\big(B_{+1}(z) + B_{-1}(z)\big)$$

For $n_v = 1$,

$$\left(\frac{\partial^2 A_+(z)}{\partial z^2} - 2i\bar{k}_z\frac{\partial A_+(z)}{\partial z} - \bar{k}_z A_+(z)\right) + \frac{\omega\hat{\delta}}{c}(A_+(z)) + \frac{\bar{\omega}_0\Delta}{c^2}\big(A_+(z)\big) = \alpha_{v,s}\big(B_0(z) + B_{-2}(z)\big)$$

For $n_v = -1$,

$$\left(\frac{\partial^2 A_-(z)}{\partial z^2} + 2i\bar{k}_z\frac{\partial A_-(z)}{\partial z} - \bar{k}_z A_-(z)\right) + \frac{\omega\hat{\delta}}{c}(A_+(z)) + \frac{\bar{\omega}_0\Delta}{c^2}\big(A_+(z)\big) = \alpha_{v,s}\big(B_0(z) + B_{+2}(z)\big)$$

The coupling coefficient $\alpha_{v,s}$ is expressed:

$$\alpha_{v,s} = \pi r_0 N_v' \frac{\Delta r}{2} H_{q,\tau}^{*,v}(r_0) H_{q,\tau}^{s}$$

2.3.7.2. Scattering of the Fundamental Surface Field into the Volume Field

The scattering of the surface field into the volume field is investigated in a similar manner, in order to define the coupling coefficient $\alpha_{s,v}$ by multiplying the surface field component of Eq.(2.3.37) by $e^{-i\bar{k}_z z n_s}$.

$$r_0{}^2 N_s' \int_0^{2\pi} \left[1 + \frac{\Delta r}{2r_0}\left(e^{i\bar{k}_z z} + e^{-i\bar{k}_z z}\right)cos\bar{m}\varphi\right] e^{-in_s\bar{k}_z z}\, \bar{H}_{q,\tau}^{*,s}(r)cos\bar{m}\varphi$$

$$\left(H_{q,\tau}^{v}(r)\sum_{n_v=-\infty}^{\infty} A_{n_v}(z)e^{in_v\bar{k}_z z} + H_{q,\tau}^{s}(r)cos\bar{m}\varphi\sum_{n} B_n(z)e^{in\bar{k}_z z}\right)\Bigg|_{r=r_0} d\varphi \tag{2.3.55}$$

Rearranging the first term

$$r_0{}^2 N_s' \int_0^{2\pi} \bar{H}_{q,\tau}^{*,s}(r_0)cos\bar{m}\varphi\left[e^{-in_s\bar{k}_z z} + \frac{\Delta r}{2r_0}cos\bar{m}\varphi\left(e^{i\bar{k}_z z} + e^{-i\bar{k}_z z}\right)e^{-in_s\bar{k}_z z}\right]$$

$$\left(H_{q,\tau}^{v}(r_0)\sum_{n_v=-\infty}^{\infty} A_{n_v}(z)e^{in_v\bar{k}_z z} + H_{q,\tau}^{s}(r_0)cos\bar{m}\varphi\sum_{n} B_n(z)e^{in\bar{k}_z z}\right)d\varphi \tag{2.3.56}$$

and multiplying the exponentials by $e^{-in_s\bar{k}_z z}$ gives:

$$r_0{}^2 N_s' \int_0^{2\pi} \bar{H}_{q,\tau}^{*,s}(r_0)cos\bar{m}\varphi\left[e^{-in_s\bar{k}_z z} + \frac{\Delta r}{2r_0}cos\bar{m}\varphi\left(e^{i\bar{k}_z z(1-n_s)} + e^{-i\bar{k}_z z(1+n_s)}\right)\right]$$

$$\left(H_{q,\tau}^{v}(r_0)\sum_{n_v=-\infty}^{\infty} A_{n_v}(z)e^{in_v\bar{k}_z z} + H_{q,\tau}^{s}(r_0)cos\bar{m}\varphi\sum_{n_s} B_{n_s}(z)e^{in_s\bar{k}_z z}\right)d\varphi \tag{2.3.57}$$

Expanding and neglecting the same terms as before for the surface field leads to the expression

$$r_0{}^2 N_s' \int_0^{2\pi} \left(\frac{\Delta r}{2r_0} cos\bar{m}\varphi \left(e^{i\bar{k}_z z(1-n_s)} + e^{-i\bar{k}_z z(1+n_s)} \right) \bar{H}_{q,\tau}^{*,s}(r_0) cos\bar{m}\varphi H_{q,\tau}^{v}(r_0) \sum_{n_v=-\infty}^{\infty} A_{n_v}(z) e^{in_v\bar{k}_z z} + \bar{H}_{q,\tau}^{*,s}(r_0) cos\bar{m}\varphi e^{-in_s\bar{k}_z z} H_{q,\tau}^{s}(r_0) cos\bar{m}\varphi \sum_{n_s} B_{n_s}(z) e^{in_s\bar{k}_z z} \right) d\varphi$$

(2.3.58)

And since $e^{-in_s\bar{k}_z z} e^{in_s\bar{k}_z z} = 1$, the previous result is shortened to

$$r_0{}^2 N_s' \int_0^{2\pi} \left(\frac{\Delta r}{2r_0} cos\bar{m}\varphi \left(e^{i\bar{k}_z z(1-n_s)} + e^{-i\bar{k}_z z(1+n_s)} \right) e^{in_v\bar{k}_z z} H_{q,\tau}^{*,s}(r_0) cos\bar{m}\varphi H_{q,\tau}^{v}(r_0) \sum_{n_v=-\infty}^{\infty} A_{n_v}(z) + \bar{H}_{q,\tau}^{*,s}(r_0) cos\bar{m}\varphi H_{q,\tau}^{s}(r_0) cos\bar{m}\varphi \sum_{n_s} B_{n_s}(z) \right) d\varphi$$

(2.3.59)

$$r_0{}^2 N_s' \int_0^{2\pi} \left(\frac{\Delta r}{2r_0} cos\bar{m}\varphi \left(e^{i\bar{k}_z z(1-n_s+n_v)} + e^{-i\bar{k}_z z(1+n_s-n_v)} \right) H_{q,\tau}^{*,s}(r_0) cos\bar{m}\varphi H_{q,\tau}^{v}(r_0) \sum_{n_v=-\infty}^{\infty} A_{n_v}(z) + \bar{H}_{q,\tau}^{*,s}(r_0) cos\bar{m}\varphi H_{q,\tau}^{s}(r_0) cos\bar{m}\varphi \sum_{n_s} B_{n_s}(z) \right) d\varphi$$

(2.3.60)

Bearing in mind that $cos^2(\bar{m}\varphi) = \frac{1}{2} + \frac{1}{2}cos\bar{m}\varphi$ we obtain an equivalent expression for Eq.(2.3.60)

$$r_0{}^2 N_s' \int_0^{2\pi} \left(\frac{\Delta r}{2r_0} \left(\frac{1}{2} + \frac{1}{2} cos\bar{m}\varphi \right) \left(e^{i\bar{k}_z z(1-n_s+n_v)} + e^{-i\bar{k}_z z(1+n_s-n_v)} \right) H_{q,\tau}^{*,S}(r_0) H_{q,\tau}^{v}(r_0) \sum_{n_v=-\infty}^{\infty} A_{n_v}(z) + \bar{H}_{q,\tau}^{*,S}(r_0) \left(\frac{1}{2} + \frac{1}{2} cos\bar{m}\varphi \right) H_{q,\tau}^{S}(r_0) \sum_{n_s} B_{n_s}(z) \right) d\varphi \tag{2.3.61}$$

which, after integration, is brought to the form:

$$2\pi r_0{}^2 N_s' \left(\frac{\Delta r}{4r_0} \left(e^{i\bar{k}_z z(1-n_s+n_v)} + e^{-i\bar{k}_z z(1+n_s-n_v)} \right) H_{q,\tau}^{*,S}(r_0) H_{q,\tau}^{v}(r_0) \sum_{n_v=-\infty}^{\infty} A_{n_v}(z) + \frac{1}{2} \bar{H}_{q,\tau}^{*,S}(r_0) H_{q,\tau}^{S}(r_0) \sum_{n_s} B_{n_s}(z) \right) \tag{2.3.62}$$

Once again, to get rid of exponential terms and obtain a non-zero result after integration, the following conditions must hold true: $1 - n_s + n_v = 0$ and $1 + n_s - n_v = 0$ such that $n^{1,2}{}_v = n_s \mp 1$.

- If $n_s = 0, n_v^1 = -1;\ n_v^2 = 1;\ n_v^{1,2} = \mp 1$
- If $n_s = 1, n_v^1 = 0;\ n_v^2 = 2;$
- If $n_s = -1, n_v^1 = -2;\ n_v^2 = 0;$

We observe that if we couple the fundamental harmonic $n_s = 0$ it scatters into itself and the ∓ 1 harmonics of the volume field. Introducing the coupling coefficient $\alpha_{s,v}$, describing scattering from the surface field into the volume field, leads to the following set of coupled equations from Eq. (2.3.19)

$$\frac{\partial^2 B_0(z)}{\partial z^2} - \frac{\omega\hat{\delta}}{c} B_0(z) + \frac{\bar{\omega}_0 \Delta}{c^2} B_0(z) = \alpha_{s,v}\big(A_{+1}(z) + A_{-1}(z)\big)$$

$$\frac{\partial^2 B_+(z)}{\partial z^2} + 2i\bar{k}_z \frac{\partial B_+(z)}{\partial z} - \bar{k}_z{}^2 B_+(z) - \frac{\omega\hat{\delta}}{c} B_+(z) + + \frac{\bar{\omega}_0 \Delta}{c^2} B_+(z) = \alpha_{s,v}\big(A_0(z) + A_{-2}(z)\big)$$

$$\frac{\partial^2 B_+(z)}{\partial z^2} + 2i\bar{k}_z \frac{\partial B_+(z)}{\partial z} - \bar{k}_z{}^2 B_+(z) - \frac{\omega\hat{\delta}}{c} B_+(z) + \frac{\bar{\omega}_0 \Delta}{c^2} B_+(z) = \alpha_{s,v}\big(A_0(z) + A_{-2}(z)\big)$$

where:

$$\alpha_{s,v} = \pi r_0{}^2 N_s' \frac{\Delta r}{2r_0} H_{q,\tau}^{*,s}(r_0) H_{q,\tau}^{v}(r_0)$$

More generally, we can define the coupling coefficients $\alpha_{s,v}$ and $\alpha_{v,s}$ in the following way:

$$\bar{\nabla}_z^2 C_q^s(z) - \frac{\omega\hat{\delta}}{c} C_q^s(z) + \frac{\bar{\omega}_0 \Delta}{c^2} C_q^s(z) = N_s \oint \bar{j}_m \bar{H}_{q'}^* \, d\sigma$$

$$\frac{\partial^2 A_{n_v}(z)}{\partial z^2} - 2i(n_v)\bar{k}_z \frac{\partial A_{n_v}(z)}{\partial z} - \bar{k}_z (n_v)^2 A_{n_v}(z) + \left(\frac{\omega\hat{\delta}}{c} + \frac{\bar{\omega}_0 \Delta}{c^2}\right) A_{n_v}(z) = \alpha_{v,s}\left(B_{n_v-1}(z) + B_{n_v+1}(z)\right)$$

(2.3.63a)

$$\frac{\partial^2 B_{n_s}(z)}{\partial z^2} + 2i\bar{k}_z \frac{\partial B_{n_s}(z)}{\partial z} - \bar{k}_z{}^2 B_{n_s}(z) + \left(\frac{\bar{\omega}_0 \Delta}{c^2} - \frac{\omega\hat{\delta}}{c}\right) B_{n_s}(z) = \alpha_{s,v}\left(A_{n_s-1}(z) + A_{n_s+1}(z)\right)$$

(2.3.63b)

2.3.8. Coupling Coefficient of the PSL's Cavity Eigemode

To combine these coefficients into a single coupling parameter let us define α:

$$\alpha = \sqrt{\alpha_{v,s}\alpha_{s,v}}$$

To express $\alpha_{s,v}$ and $\alpha_{v,s}$ in terms of α

$$\alpha = \frac{\alpha_{v,s}}{\sqrt{\alpha_{v,s}}}\sqrt{\alpha_{s,v}}$$

$$\alpha = \frac{\alpha_{s,v}}{\sqrt{\alpha_{s,v}}}\sqrt{\alpha_{v,s}}$$

And hence we multiply Eq.(2.3.63a) by $\sqrt{\alpha_{s,v}/\alpha_{v,s}}$ and Eq.(2.3.63b) by $\sqrt{\alpha_{v,s}/\alpha_{s,v}}$ to renormalise :

$$\frac{\partial^2\left(\sqrt{\alpha_{s,v}}/\sqrt{\alpha_{v,s}}\,A_{n_v}(z)\right)}{\partial z^2} - 2i(n_v)\bar{k}_z\frac{\partial\left(\sqrt{\alpha_{s,v}}/\sqrt{\alpha_{v,s}}\,A_{n_v}(z)\right)}{\partial z} - \bar{k}_z(n_v)^2\left(\sqrt{\alpha_{s,v}}/\sqrt{\alpha_{v,s}}\right)A_{n_v}(z) + \left(\frac{\omega\hat{\delta}}{c} + \frac{\bar{\omega}_0\Delta}{c^2}\right)\left(\sqrt{\alpha_{s,v}}/\sqrt{\alpha_{v,s}}\right)A_{n_v}(z) = \alpha\left(B_{n_v-1}(z) + B_{n_v+1}(z)\right)$$

(2.3.64a)

$$\frac{\partial^2\left(\sqrt{\alpha_{v,s}}/\sqrt{\alpha_{s,v}}\right)B_{n_s}(z)}{\partial z^2} + 2i\bar{k}_z\frac{\partial\left(\sqrt{\alpha_{v,s}}/\sqrt{\alpha_{s,v}}\right)B_{n_s}(z)}{\partial z} - \bar{k}_z{}^2\left(\sqrt{\alpha_{v,s}}/\sqrt{\alpha_{s,v}}\right)B_{n_s}(z) + \left(\frac{\bar{\omega}_0\Delta}{c^2} - \frac{\omega\hat{\delta}}{c}\right)\left(\sqrt{\alpha_{v,s}}/\sqrt{\alpha_{s,v}}\right)B_{n_s}(z) = \alpha\left(A_{n_s-1}(z) + A_{n_s+1}(z)\right)$$

(2.3.64b)

Introducing new amplitude constants $\tilde{A}_{n_v}(z) = A_{n_v}(z)\sqrt{\alpha_{s,v}}/\sqrt{\alpha_{v,s}}$ and $\tilde{B}_{n_s}(z) = B_{n_s}(z)\sqrt{\alpha_{v,s}}/\sqrt{\alpha_{s,v}}$ gives the final, normalised coupled wave equations:

$$\frac{\partial^2\tilde{A}_{n_v}(z)}{\partial z^2} - 2i(n_v)\bar{k}_z\frac{\partial\tilde{A}_{n_v}(z)}{\partial z} - \bar{k}_z(n_v)^2\tilde{A}_{n_v}(z) + \left(\frac{\omega\hat{\delta}}{c} + \frac{\bar{\omega}_0\Delta}{c^2}\right)\tilde{A}_{n_v}(z) = \alpha\left(B_{n_v-1}(z) + B_{n_v+1}(z)\right)$$

(2.3.65a)

$$\frac{\partial^2 \tilde{B}_{n_s}(z)}{\partial z^2} + 2i\bar{k}_z \frac{\partial \tilde{B}_{n_s}(z)}{\partial z} - \bar{k}_z{}^2 \tilde{B}_{n_s}(z) + \left(\frac{\overline{\omega}_0 \Delta}{c^2} - \frac{\omega \hat{\delta}}{c}\right) \tilde{B}_{n_s}(z) = \alpha \left(A_{n_s-1}(z) + A_{n_s+1}(z)\right)$$

(2.3.65b)

where the coupling coefficient is defined below:

$$\alpha = \frac{\pi r_0 N_v' N_s' \Delta r}{2} \sqrt{\left(H_{q,\tau}^{*,v}(r_0) H_{q,\tau}^{s}\right)\left(H_{q,\tau}^{*,s}(r_0) H_{q,\tau}^{v}(r_0)\right)}$$

(2.3.66)

The evaluation of this coupling coefficient involves performing an integral mode calculation around the cross section of the structure due to its dependence on the wave norms N_v' and N_s'.

2.4. Chapter Conclusions

The cavity eigenfield's dispersion for the 2D PSL of cylindrical topology has been derived by substituting the lattice corrugation for a thin effective metadielectric (or high impedance layer) and taking into account the continuity conditions at the dielectric interface. In this initial description, the approximation of an infinite structure was applied. The cavity eigenmode was shown to have a hybrid field structure, comprised of both E_z and H_z components. Far from the structure's resonant frequency (i.e. $\tilde{n}_B = 1$) the dispersion was found to split, describing either *TE* or *TM* waves as expected. On the other hand, in the vicinity of the resonant frequency, the refractive index of the metadielectric $\tilde{n}_B$ is defined in terms of the eigenfield's wavenumber k and the longitudinal lattice wavenumber $\bar{k}_z$. The PSL's dispersive behaviour, when increasing $\tilde{n}_B$ by tailoring the lattice parameters, is studied in the following chapter.

The dispersion relation, derived for the effective metadielectric based on the cylindrical waveguide, also showed that the cavity eigenmode is not formed in the case of an azimuthally symmetric surface field, proving that $m_s \neq 0$. It was later confirmed via the magnetic surface current method that $m_s = \bar{m}$, justifying the requirement that $m_v = 0$.

Coupled wave equations were derived by considering an effective magnetic surface current in place of the lattice corrugation. In this theoretical model, a finite structure with slowly varying amplitude terms was considered. Detuning from the resonant frequency, as well as the detuning between the volume and surface fields, was taken into account, while ohmic and diffractive losses were neglected to simplify the problem. The scattering of the volume field into the surface field and vice versa was mathematically described for the fundamental harmonic of each field, and the accumulation of volume and surface fields associated with "self-scattering" was also demonstrated.

Some of the possible scattering processes were presented and it was established that the fundamental volume field can couple with the ±1 surface field harmonics provided the necessary conditions are met. This theory was developed under the assumption that $r_0 \gg \lambda$ and therefore gives an approximate insight into coupling of volume and surface fields in the PSLs of planar topology. Finally, an analytical expression describing the coupling coefficient for the structure's cavity eigenmode was presented in this chapter. Evaluating this coupling coefficient by performing a contour integral calculation is a possible topic of future work.

Chapter 3 - Analytical Dispersion of Cylindrical PSLs

3.1 Introduction

An overview of waveguide behaviour, including the waveguide dispersions of uncoupled volume and surface fields, was given in Chapter 1. Schematic Brillouin diagrams, illustrating the coupling of neighbouring volume field space harmonics, and resultant band-gap formation, were previously shown. The possibility for interaction between a cavity mode and charged particle beam was also demonstrated schematically in Chapter 1. In this chapter, an analytical dispersion equation, derived from the coupled wave equations of Chapter 2, is presented and solved to obtain analytical dispersion diagrams illustrating the coupling of volume and surface fields. It is shown that the parameters of the structure can be tailored to observe different dispersive properties, and that under certain conditions, the structure can support a Cherenkov interaction when coupled with a suitable electron beam. This chapter begins by introducing the coupled dispersion equation in §3.2. Dispersion plots, provided in §3.3, illustrate the EM behaviour of the PSL when the structure's parameters are varied for the cases of strong and weak coupling. Finally, the dispersion diagram of a W-band PSL, with the same parameters as that chosen for the Cherenkov maser experiment at Strathclyde, is presented in §3.4. The main results of this chapter are summarised in §3.5.

3.2. Dispersion Equation for Cylindrical PSL

A dispersion equation Eq.(2.1.45) describing the hybrid field structure of the cavity eigenmode was defined in Chapter 2.1 using the effective metadielectric model. Studying the dispersion characteristics of the structure using Eq.(2.1.45) proves problematic since the transverse wavenumber of the coupled surface field is unknown. Instead, the coupled mode equations Eq.(2.3.65a) and Eq.(2.3.65b) have been used to obtain a normalised dispersion relation. All parameters are renormalised by $\overline{K}$, where $\overline{K} = \Omega/c$ and Ω is defined below:

$$\Omega = \sqrt{\frac{(\omega_0^v)^2 + (\omega_0^s)^2}{2}}$$

(3.2.1)

Renormalising the coupled mode equations by $\overline{K}$ and introducing the dimensionless detuning parameter Γ leads to the following dispersion equation (Konoplev, MacLachlan et al. 2012):

$$(\omega_e^2 - \Lambda^2)[\Lambda^4 - 2\Lambda^2(2 + \Gamma^2 + \omega_e^2) + (2 - \Gamma^2 + \omega_e^2)^2] = 2\alpha^4(2 - \Gamma^2 + \omega_e^2 - \Lambda^2)$$

(3.2.2)

In the present analytical dispersion study, the normalised coupling coefficient α is treated as a variable parameter. The normalised wave vector is denoted by Λ and ω_e is a variable angular frequency defined by

$$\omega_e = \sqrt{\delta^2 + 2\delta + \widetilde{\Delta}^2} \qquad (3.2.3)$$

where $\delta = (\omega - \Omega)/\Omega$ and $\widetilde{\Delta} = \Phi/\Omega$ are detuning parameters and Φ is defined below:

$$\Phi = \sqrt{\frac{(\omega_0^s)^2 - (\omega_0^v)^2}{2}}$$

(3.2.4)

The parameters δ and $\widetilde{\Delta}$ are renormalised versions of $\hat{\delta}$ and Δ (introduced in chapter 2.2) and describe the detuning between the angular cut-off frequencies of the volume and surface fields. Once again, it has been assumed that $\widetilde{\Delta} = 0$, i.e. $\omega_0^v = \omega_0^s$. The overall detuning is described by the dimensionless parameter Γ which is defined:

$$\Gamma = \bar{k}_z/\overline{K} = 2\bar{k}_z c/((\omega_0^v)^2 + (\omega_0^s)^2)$$

(3.2.5)

The value of Γ determines the period and radius of the structure, and when the approximation $\widetilde{\Delta} = 0$ is made, Γ is written in the simplified form:

$$\Gamma = \frac{\bar{k}_z c}{\omega_0} = \frac{\lambda_c}{d_z} \tag{3.2.6}$$

where λ_c is the cut-off wavelength of the volume field inside the cylindrical waveguide and d_z is the longitudinal lattice period.

Some similarities can be noted when comparing the dispersion equations Eq.(3.2.1) and Eq.(2.2.25). For instance, the terms ε and $\bar{m}$ of Eq.(2.2.25) fulfil a similar role to the coupling coefficient α of Eq.(3.2.2) ensuring that if no coupling takes place, the right-hand sides equal zero. This splits the otherwise coupled equations into their uncoupled volume and surface field components. In the case of weak coupling when $\alpha \longrightarrow 0$, the right hand side of Eq.(3.2.2) is neglected, and the dispersion separates into the following expressions.

$$(\omega_e^2 - \Lambda^2) = 0 \tag{3.2.7a}$$

$$[\Lambda^4 - 2\Lambda^2(2 + \Gamma^2 + \omega_e^2) + (2 - \Gamma^2 + \omega_e^2)^2] = 0 \tag{3.2.7b}$$

Eq.(3.2.7a) is the conventional dispersion of an uncoupled volume field propagating through a cylindrical waveguide and can be written in the form:

$$\chi_{1,2} = \pm\omega_e = \pm\sqrt{\delta^2 + 2\delta - \Delta^2} \tag{3.2.8}$$

where $\chi_{1,2}$ represents the angular eigen-frequencies of the forwards and backwards scattered volume waves. Eq. (3.2.7b) describes the dispersion of the ± 1 spatial harmonics of the surface field. This splits into two functions.

$$\omega_e^2 = (\Lambda - \Gamma)^2 - 2 \tag{3.2.9a}$$

$$\omega_e^2 = (\Lambda + \Gamma)^2 - 2 \tag{3.2.9b}$$

The points where these unperturbed volume and surface dispersions intersect are of interest when considering the eigenfield inside the structure.

The analytical dispersion study has been carried out by varying Γ (which controls the lattice parameters) and α (which determines the strength of the coupling) and solving Eq. (3.2.1) using the mathematical software package MAPLE. The equation was solved for $\widetilde{\Delta} = 0$ (as stated previously) with specified values of Γ and α. The unperturbed waveguide dimensions and Bessel roots were used to establish the cut-off frequency of the near cut-off azimuthally symmetric volume field. Provided with an initial value of δ, the code loops over the chosen number of data points, increasing δ in small increments $\delta = \delta + \Delta\delta$ and solving equations Eq.(3.2.7.b), Eq.(3.2.8) and Eq.(3.2.1) for Λ at each value of δ. For every iteration k_z and ω are evaluated from the relations $k_z = \Lambda\overline{K}$ and $\omega = \delta\Omega + \Omega$. Solutions are separated into their real and imaginary components, and used to plot the coupled and uncoupled field dispersions. It should be noted that all the dispersion diagrams presented in this chapter are valid only in the case of coupling between the fundamental harmonic ($n = 0$) of the near cut-off, azimuthally symmetric volume field and the ± 1 harmonics of the surface field, as described in the previous chapter. Later, in Chapter 6, numerical dispersion plots for the 2D PSLs of planar topology will take into account the ± 1 spatial harmonics of both the volume and surface fields.

3.3 Analytical Dispersion Plots for W-band Cylindrical PSLs

Dispersion plots presented in figures (3.3.1.1-3.3.3.2) illustrate how the EM properties of the PSL can be controlled by varying the structure's parameters. In this section, the initial parameters were chosen to match those of the original electroformed, copper W-band structure (r_0 =10mm, d_z =3.0mm, m=20) designed to operate with the near cut-off $TM_{0,7}$ volume mode (f_c =100.9 GHz). The corrugation height Δr of the PSL is varied implicitly by changing α, while r_0 and d_z are modified by Γ. The value of Γ is set to 1, $\sqrt{2}$ and 2.3 for values of α corresponding to weak and strong coupling. As Γ is increased from 1 the structure becomes oversized, demonstrating the principle of mode-selection in a structure with large D_{wg}/λ, where D_{wg} is the diameter of the cylindrical waveguide. Increasing Γ is also equivalent to increasing the refractive index of the effective metadielectric, as shown in figure 3.3.3.2. In the dispersion diagrams presented in this Chapter, the unperturbed volume and surface fields are represented by blue and green dashed lines respectively. The PSL's eigenmode, comprised of coupled $TM_{0,7}$ and $EH_{20,1}$ modes, is illustrated by the solid red dispersion plots. When α is sufficiently large, more than one coupled dispersion branch is observed, and the maxima and minima of these branches which occur when the group velocity is zero ($\partial f/\partial k_z = 0$) indicate the locations of possible coupled eigenmodes. It is expected that, when the structure is sufficiently synchronised, in this case by the near-cut-off volume field, coupling of volume and surface fields will take place at just one of these frequencies, leading to coherent eigenmode formation and demonstrating mode-selection in an over-sized structure.

3.3.1 Dispersion Plots for W-band Cylindrical PSL with $\Gamma = 1$

Figure 3.3.1.1 demonstrates the lattice dispersion when $\Gamma = 1$ for the case of weak ($\alpha = 0.1$) coupling. The coupled dispersion (solid red line) deviates from the uncoupled volume and surface field dispersions as it approaches the crossing points, where coupling is expected to occur.

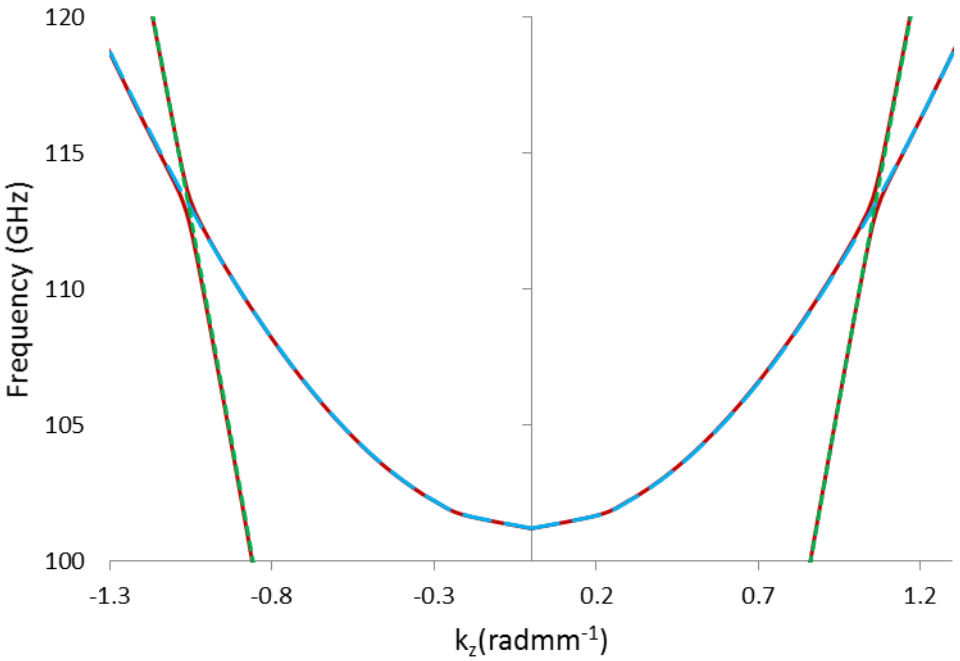

Figure 3.3.1.1. Eigenfield dispersion when $\Gamma = 1$ and $\alpha = 0.1$ (solid red lines). The dashed green lines are the ± 1 harmonics of the surface field when $\alpha = 0$ and the blue dashed lines are the unperturbed dispersion of the $TM_{0,7}$ volume field. Splitting of the eigenfield's dispersion is observed around the points where the unperturbed dispersions meet.

The modification at these points of intersection is illustrated more closely in figure 3.1.1.2 where it is observed that the gap between the branches is indicative of scattering and is not associated with the formation of a band-gap (which is often observed in periodic structures due to the scattering of waves off the perturbations, manifesting as a forbidden frequency zone). It can also be noted that the scattering takes place at frequencies around 113 GHz, significantly higher than the cut-off frequency of the volume field, $f_c \cong 101$ GHz. A dispersion diagram obtained using the same lattice parameters $(\Gamma = 1)$ for strong coupling $(\alpha = 1)$between the volume and surface fields is provided in figure 3.3.1.3. In this case, the coupling affects the entire dispersion of the coupled eigenfield, with the upper branch occuring around 48 GHz higher than the cut-off frequency of the uncoupled volume mode.

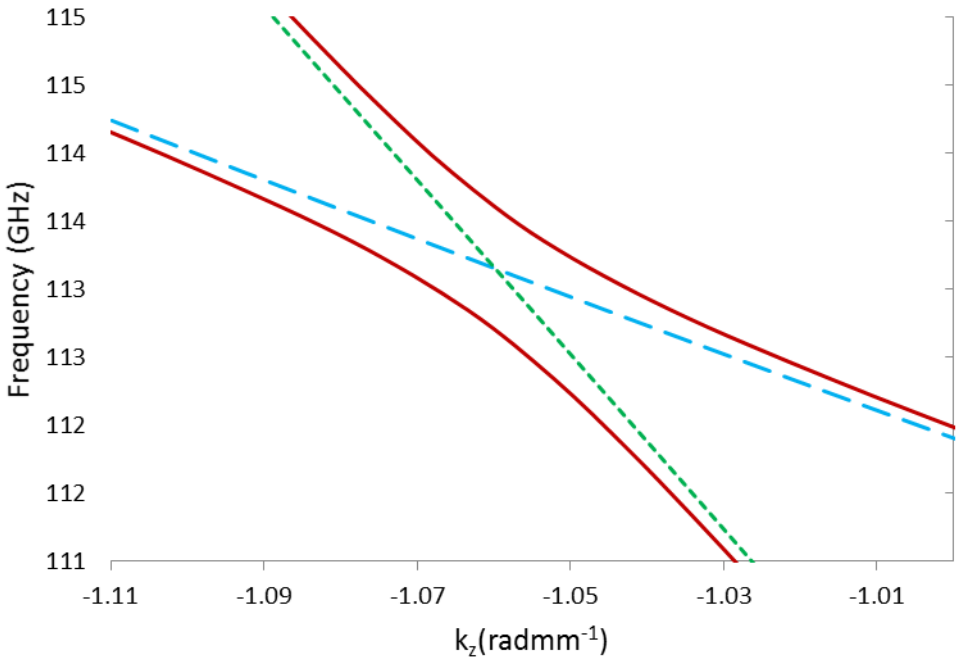

Figure 3.3.1.2. Close up view of eigenfield dispersion when $\Gamma = 1$ and $\alpha = 0.1$(solid red lines) showing splitting at the points where the unperturbed volume (blue dashed lines) and surface (green dashed lines) fields cross. This indicates scattering between the $TM_{0,7}$ and $EH_{20,1}$ fields and does not correspond to band gap formation.

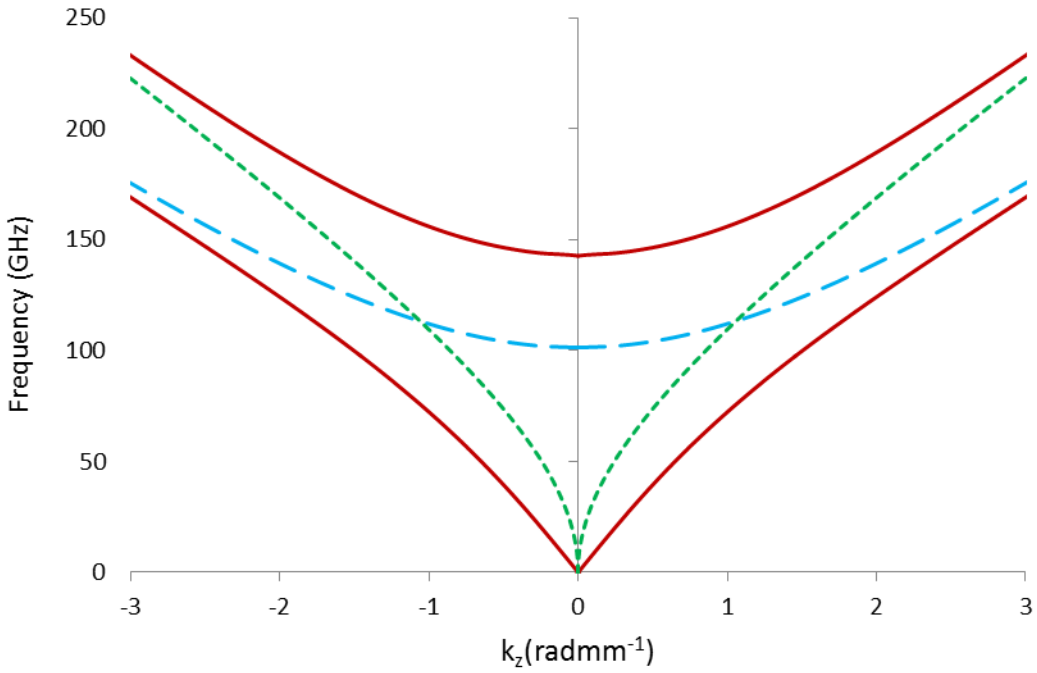

Figure 3.3.1.3. Eigenfield dispersion when $\Gamma = 1$ in the presence of strong coupling i.e. $\alpha = 1$ (solid red lines). The dashed green lines are the ± 1 harmonics of the surface field when $\alpha = 0$ and the blue dashed lines are the unperturbed dispersion of the $TM_{0,7}$ volume field.

3.3.2 Dispersion Plots for W-band Cylindrical PSL with $\Gamma = \sqrt{2}$

In this section it is shown that the uncoupled surface field harmonics intersect at the cut-off frequency of the volume field (when $k_z = 0$) when the lattice period is chosen to satisfy the condition $\bar{k}_z^2 = (k_\perp^v)^2 + (k_\perp^s)^2 \cong \sqrt{2} k_\perp^v$. This unique situation, demonstrated in figures 3.3.2.1-3.3.2.3, is observed when $\Gamma = \sqrt{2}$. In the previous example, where $\Gamma < \sqrt{2}$ the surface field harmonics intersect one another at a low frequency (~0 GHz). On the other hand, it will be shown in the next section, that the surface field harmonics shift further apart and cross at higher frequencies (> 200 GHz) when $\Gamma > \sqrt{2}$ (Konoplev, MacLachlan et al. 2011)

The frequency at which the surface field harmonics cross one another, along with the frequency at which they intersect the unperturbed volume field, determines the dispersive properties of the structure and predicts the locations of possible coupled eigenmodes. The dispersion plot for $\Gamma = \sqrt{2}$ in the presence of weak coupling (α =0.01) is shown in figure 3.3.2.1. As expected, the eigenmode dispersion

coincides closely with the unperturbed volume and surface field dispersions, only deviating slightly from the uncoupled surface field harmonics with increasing k_z. Increasing the strength of the coupling to $\alpha = 0.1$ imposes a change in the coupled dispersion surrounding $k_z = 0$ where the fields intersect. As a consequence of the stronger coupling, the dispersion splits into 3 distinct branches, as shown in figure 3.3.2.2. However, the middle branch still overlays the uncoupled volume field dispersion.

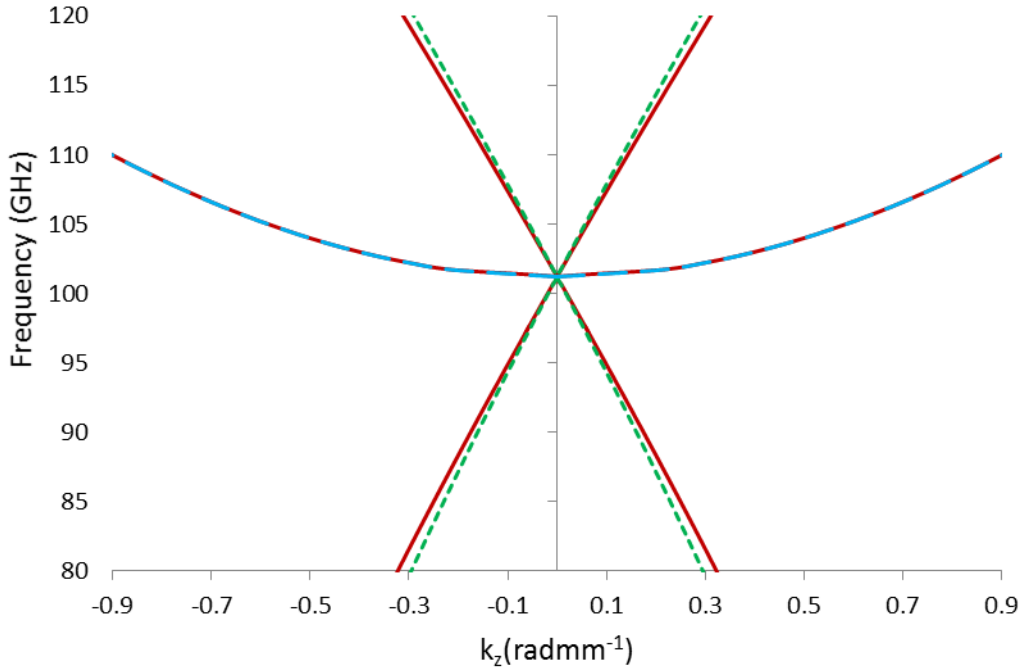

Figure 3.3.2.1 Eigenfield dispersion when $\Gamma = \sqrt{2}$ in the case of very weak coupling when $\alpha = 0.01$ (solid red lines). The dashed green lines are the ± 1 harmonics of the surface field when $\alpha = 0$ and the blue dashed lines are the unperturbed dispersion of the $TM_{0,7}$ volume field. In this case the unperturbed and coupled eigenfield dispersions meet at exactly the cut-off frequency of the $TM_{0,7}$ volume field. This is only observed in the case of weak coupling when $\Gamma = \sqrt{2}$.

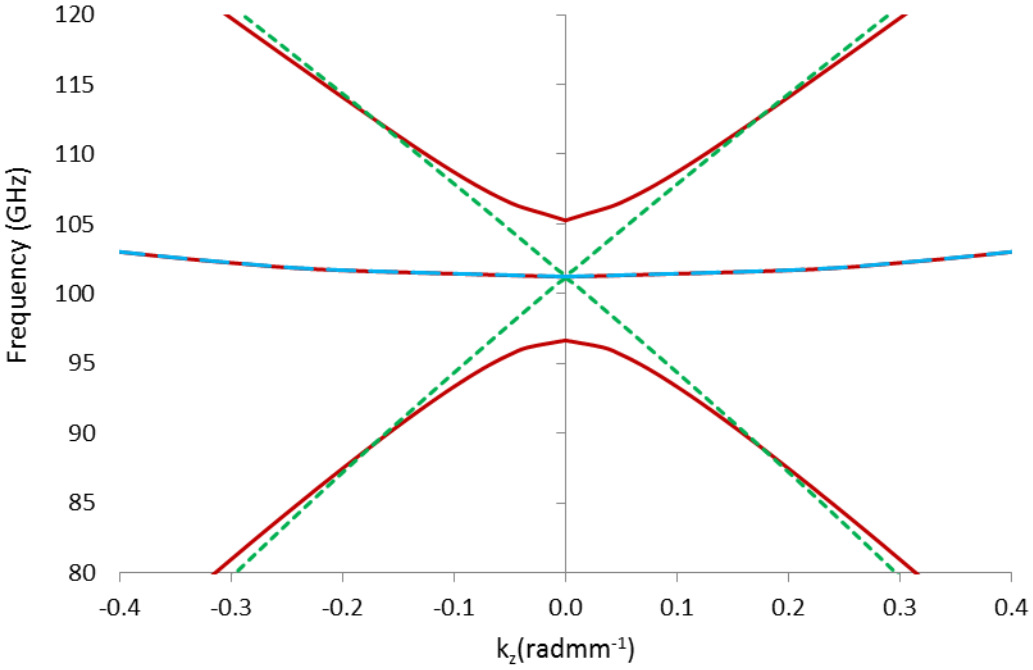

Figure 3.3.2.2. Eigenfield dispersion when $\Gamma = \sqrt{2}$ for the case of weak coupling when $\alpha = 0.1$(solid red lines). The dashed green lines are the ± 1 harmonics of the surface field when $\alpha = 0$ and the blue dashed lines are the unperturbed dispersion of the $TM_{0,7}$ volume field.

Again, as the coupling is further increased, the entire eigenfield's dispersion is affected leading to a greater frequency separation between the coupled branches. Only two coupled dispersion branches are evident in figure 3.3.2.3 for the cylindrical W-band PSL with $\Gamma = \sqrt{2}$ and $\alpha = 1$. The uppermost branch is shifted beyond 150 GHz, while the lowest branch has shifted below zero to give a non-real solution.

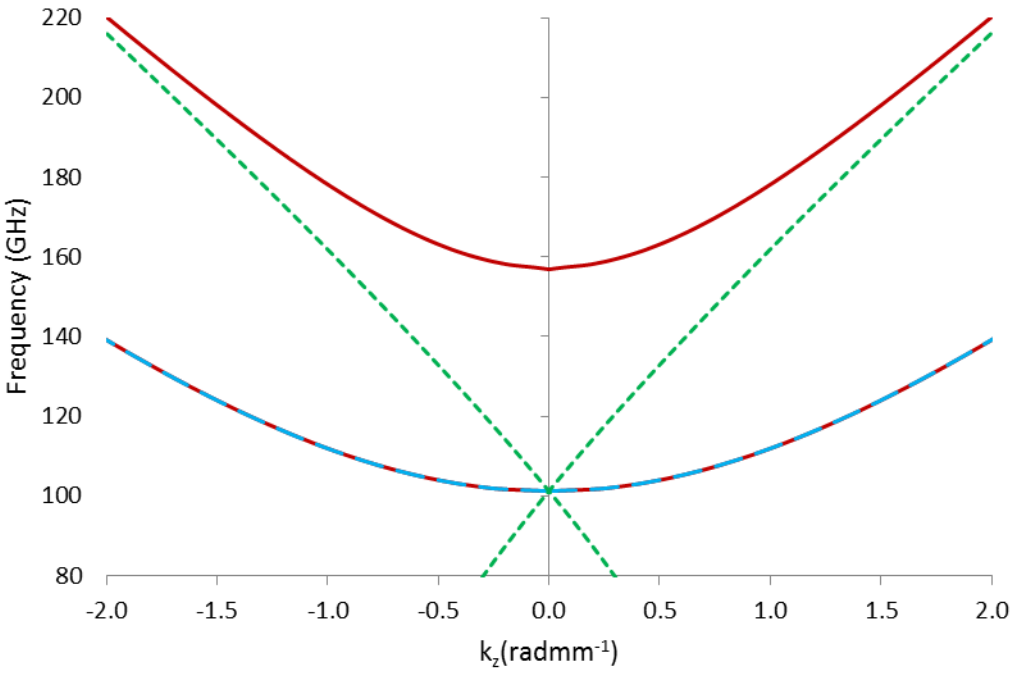

Figure 3.3.2.3. Eigenfield dispersion when $\Gamma = \sqrt{2}$ for the case of strong coupling when $\alpha = 1$ (solid red lines). The dashed green lines are the ± 1 harmonics of the surface field when $\alpha = 0$ and the blue dashed line is the fundamental harmonic of the unperturbed dispersion of the $TM_{0,7}$ volume field.

3.3.3 Dispersion Plots for W-band Cylindrical PSL with $\Gamma = 2.3$

Further changes to the coupled eigenfield occur as Γ is increased beyond $\sqrt{2}$ and interesting behaviour is observed for the cylindrical PSLs with $\Gamma = 2.3$ as illustrated in figures 3.3.3.1 and 3.3.3.2. Once again, when the volume and surface fields are weakly coupled (figure 3.3.3.1) the lower coupled dispersion branch overlays the dispersion curve of the unperturbed volume field. The uncoupled surface field harmonics intersect this branch at $k_z \cong 1.5$ corresponding to a frequency of around 125 GHz. Though the surface field harmonics cross one another around 210 GHz, the weak coupling $(\alpha = 0.1)$ is not sufficient for the formation of an additional branch close to this frequency. As the coupling is increased to $\alpha = 1$, however, the dispersion splits into three separate branches at the points of intersection, allowing for a potential interaction between the eigenfield and an electron beam at relatively low beam velocities. The lower coupled branch is shifted down by around 32 GHz

from the unperturbed volume field, confirming that increasing Γ is equivalent to increasing the refractive index, $\tilde{n}$ of the effective metadielectric.

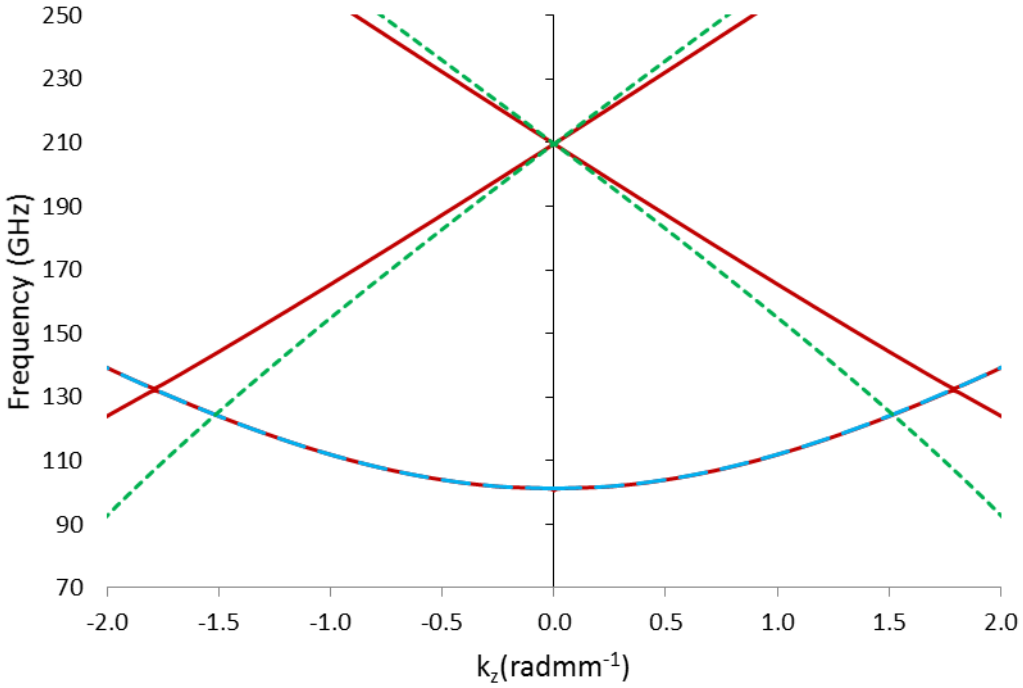

Figure 3.3.3.1. Eigenmode dispersion when $\Gamma = 2.3$ and $\alpha = 0.1$ (solid red lines). The dashed green lines are the ± 1 harmonics of the surface field when $\alpha = 0$ and the blue dashed line is the fundamental harmonic of the unperturbed $TM_{0,7}$ volume field.

Figure 3.3.3.2 illustrates the potential to observe slow waves, since the requirement that $f/k_z < c$ is satisfied. In addition to the eigenfield's phase velocity being less than c, the variation in the group velocity indicates the possibility of generating either forwards or backwards slow waves, thus demonstrating that the lattice can facilitate a forwards or backwards interaction with an appropriate electron beam. An example of a W-band cylindrical PSL dispersion plot with a suitable beam line is presented in the following section.

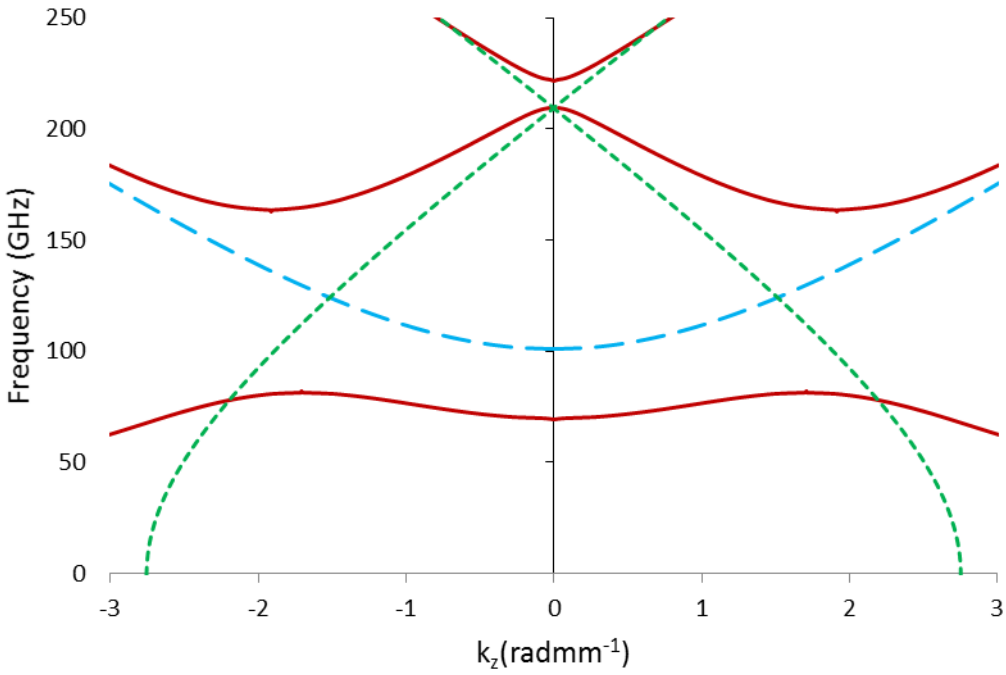

Figure 3.3.3.2. Eigenmode dispersion when $\Gamma = 2.3$ and $\alpha = 1$ (solid red lines). The dashed green lines are the ± 1 harmonics of the surface field when $\alpha = 0$ and the blue dashed line is the fundamental harmonic of the unperturbed $TM_{0,7}$ volume field.

3.4 Analytical Dispersion and Beam Interaction of Cylindrical PSL used in Experiment

The dispersion study of §3.3 was carried out for a W-band structure originally designed for the Cherenkov Maser experiment at Strathclyde and cold-tested using the Anritsu VNA. Due to experimental constraints, the W-band PSL used as the interaction region was modified, with both its radius and period reduced. The corrugation height of the updated structure was also increased to enhance the coupling. The updated parameters of the W-band PSL (obtained via 3D printing) and incorporated in the Cherenkov maser experiment (r_0 =4mm, d_z =1.6mm, $m = 7$ and $\Delta r =$ 0.8mm) approximately correlate to $\Gamma \cong 1.81$. Figure 3.4.1 shows the dispersion for the cylindrical W-band PSL with $\Gamma = 1.81$ and $\alpha = 1$. However, in practice, some detuning will exist i.e. $\tilde{\Delta} \neq 0$ and thus the dispersion with $\Gamma \cong 1.81$ provides only an approximate description of the structure's behaviour.

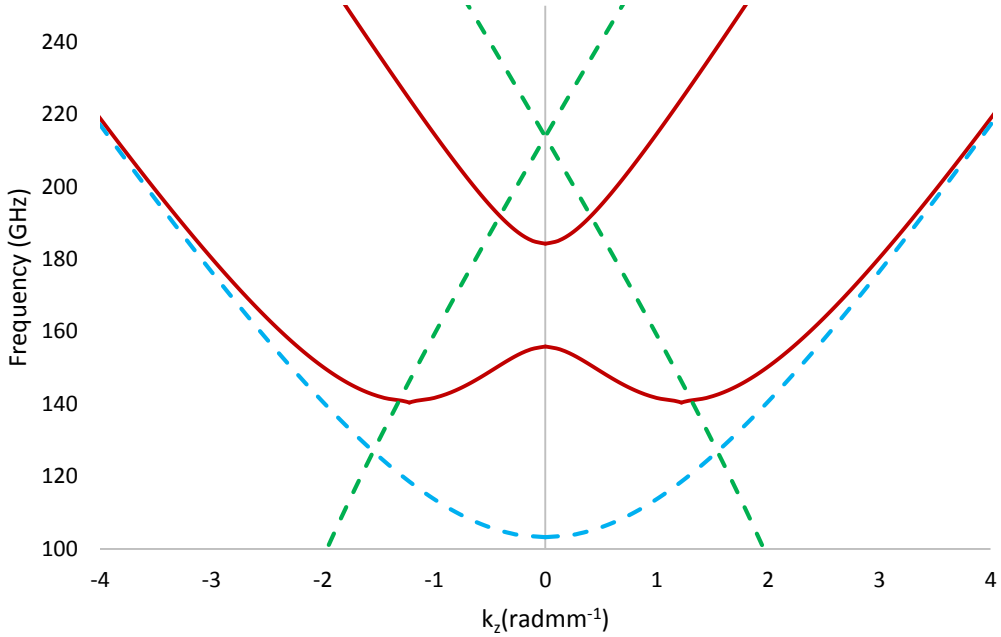

Figure 3.4.1. Eigenmode dispersion for W-band structure with $\Gamma = 1.81$ and $\alpha = 1$ (solid red lines). The dashed green lines are the ± 1 harmonics of the surface field when $\alpha = 0$ and the blue dashed line is the fundamental harmonic of the unperturbed volume field.

3.5 Chapter Conclusions

A coupled dispersion equation derived from the theory developed in Chapter 2 has been solved for different parameter values in order to carry out an analytical dispersion study of the coupled eigenfield inside a 2D cylindrical PSL. The dispersion plots in this chapter, obtained for a W-band structure, are identical in appearance yet shifted up in frequency compared to earlier work carried out for a Ka-band structure (Konoplev, MacLachlan et al. 2011) and thus verify the scalability of this work. It has been established that the dispersive properties of the structure's eigenfield are determined by the strength of the coupling α and Γ. When $\Gamma = \sqrt{2}$ the harmonics of the uncoupled surface field were shown to intersect precisely at the cut-off frequency of the volume field. In the case of strong coupling, the dispersions were found to split, forming separate branches at the points where the uncoupled fields intersect. The coupled dispersions' maxima and minima indicate the positions of the cavity eigenmodes and are different from the unperturbed

waveguide cut-off frequencies when the coupling is strong. When appropriate parameter values are chosen, the structure's ability to support either forwards or backwards slow waves was demonstrated thus confirming that the PSL structures have the potential to provide effective interaction regions for novel, coherent sources or radiation when coupled with a suitable electron beam.

Chapter 4 - Experimental Method and Preliminary Measurements

4.1 Introduction

This chapter describes the experimental methods and preliminary measurements leading to the results presented in chapter 5. Descriptions of the different planar PSL structures and their fabrication processes are discussed in §4.2-4.4 and §4.6, while detailed images of some of these structures, obtained using a Hirox microscope, are provided in §4.5. The experimental set-up involving the Vector Network Analyser and accompanying high frequency modules is detailed in §4.7 and §4.8. Preliminary measurements conducted to compare different waveguide horns and obtain output beam profiles for the chosen launching /receiving horns are presented in §4.9 and §4.10 respectively. §4.11 is dedicated to finding the refractive indices of the different FR-4 substrates. Two separate methods were considered. The first method sought to define the Brewster angle in the different dielectrics, while in the second technique, experiments measuring the phase in the dielectric were performed. The refractive indices of all three substrates was established and used in subsequent analysis throughout this work.

4.2 Planar PSLs without Substrates

The simplest structures studied in this work, consisting of planar copper PSLs with no substrates, designed to study the surface field exclusively, were manufactured using a process of laser etching. Four copper PSLs, each with a different periodicity, were fabricated by an external laser etching facility. The structures, which all share the same thickness (0.3mm) have the following periodicities: 1.50mm, 1.62mm, 1.74mm and 1.94mm and are designed to operate at the 140-200 GHz frequency band. As shown in the following chapter, these PSLs with no substrates share some similarities to inductive mesh structures (Ulrich, 1976) which have been well-documented for use as high band-pass filters.

4.3 Fabrication of Planar PSLs using Chemical Etching

The planar PSL structures discussed in this thesis are based on printed circuit boards (PCBs) consisting of a 35μm copper coating on either side of a fibreglass- epoxy composite (FR-4) substrate with an outer photoresist layer. The etching process used to fabricate the planar PSLs is outlined as follows. First, the lattice template, defining the period and intended operating wavelength of the structure, was designed and printed directly onto an acetate transparency sheet to form an etching mask. The resulting mask was positioned on top of the PCB, covering its outer photo-resistive layer. Prior to immersing the PCB in etching fluid, both the mask and PCB were irradiated by a UV source. The photoresist and copper in the regions unshielded by the mask were dissolved by the etching fluid to expose the FR-4 forming the unit cells of the PSL. Finally, the remaining photoresist was removed by submerging the etched PSLs into the fluid one last time. In half the samples, the copper backing of the PCB was left intact, whilst in the others, the copper was entirely dissolved. It was hoped that the copper backing may improve the synchronisation of the lattice and facilitate the coupling of volume and surface fields.

The etching process was carried out using four different masks corresponding to the same periodicities (1.50mm, 1.62mm, 1.74mm and 1.94mm) as the copper PSLs discussed in the proceeding section, each with a transverse size of 40 periods. To further vary the structures' properties, PCB samples of three different thicknesses were used. For each substrate and period, two structures (with and without the copper backing intact) were fabricated, resulting in a combination of 24 PSL structures, each with a unique set of parameters. The mean thicknesses of the stripped FR-4 samples were measured to be 0.41±0.005mm, 0.76±0.005mm and 1.43±0.005mm and were found to differ from the quoted values of 0.4mm, 0.8mm and 1.6mm. Examples of 1.62mm PSLs etched onto FR-4 substrates of different thicknesses are photographed in figure 4.3.1.

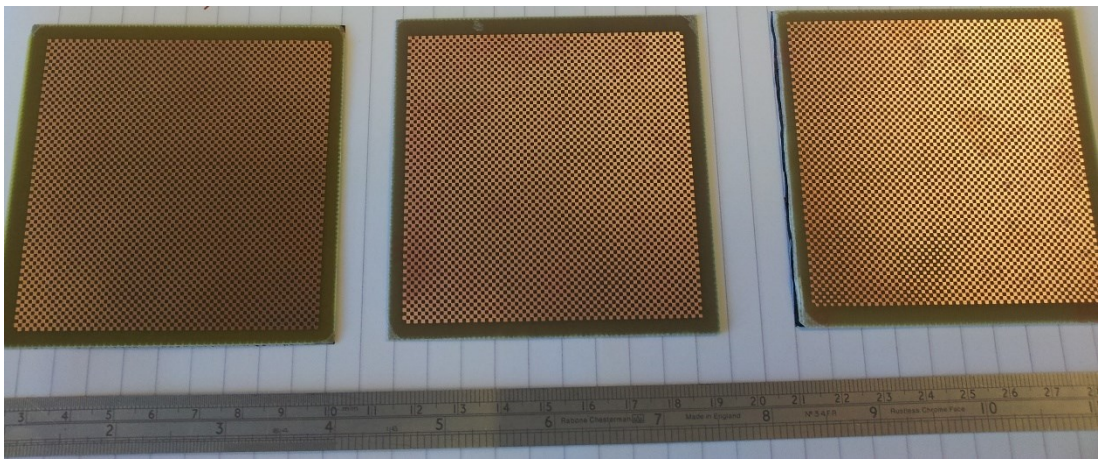

Figure 4.3.1. Photograph of PSLs with d_z= 1.62mm etched onto FR-4 substrates with thicknesses of 0.41mm, 0.76mm and 1.43mm (from left to right) manufactured using chemical etching facilities at Strathclyde.

Due to the nature of the etching process, it was difficult to ensure uniform etching across each sample, leading to some areas of the lattices becoming over or under-etched. The PSL template's susceptibility to being stretched in one direction when printed onto the acetate sheet, may also introduce some error in the structures' periodicity. To inspect the quality of the etching and measure the lattice cells, the PSLs were studied using a Hirox 3D Digital Microscope as discussed in §4.5.

4.4 High Frequency Planar PSL Structure

Since the theory presented in this work is scalable, a planar PSL structure composed of a 0.63mm PSL mounted on a 0.41mm copper-backed substrate was designed. The smaller dimensions of this structure are beyond the capabilities of the etching facilities available at Strathclyde and the structure was instead manufactured by a professional etching company. The purpose of this structure was twofold; firstly to extend the research to higher frequencies and confirm the scalability of this work, and also to measure the structure, which is intended to operate at the 325-500 GHz frequency band, at the lower 140-220 GHz frequency band, where it may behave more like a conventional metamaterial rather than a photonic structure. Detailed images of this high-frequency 0.63mm PSL are presented in the following section. At the middle of the 140-220 GHz frequency band, the PSL has λ/d_z =2.65, justifying its use as a metamaterial.

4.5 Hirox 3D Digital Microscope Images

The Hirox KH-7700 Digital Microscope consists of a 2 megapixel digital camera, light source, computer and software package that enable samples to be measured to a high precision and inspected for defects. When examining the structures under the high magnification lens, examples of under and over-etching, leading to shorted cells and defects were found. Evidence of over-etching is photographed in figure 4.5.1. The darker squares correspond to the unit cells of the PSL, while the lighter regions are the copper scatterers. As a consequence of over-etching, the copper regions are not joined, disrupting the synchronisation of the lattice. The pictured cells are isolated, preventing the surface current from flowing around the neighbouring cells. Although this could lead to unwanted capacitive effects, this localised defect is unlikely to influence the overall behaviour of the structure which is determined by the collective properties of all the lattice cells.

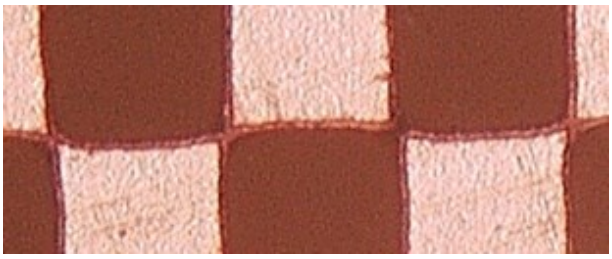

Figure 4.5.1. Localised over-etching observed in the 1.94mm PSL etched onto the 0.76mm substrate and photographed using the Hirox imager.

An example of under-etching is shown for the 1.50mm PSL mounted on the 0.41mm copper-backed substrate in figure 4.5.2. In this case, each cell has a slightly rounded appearance, with large joins between the copper scatterers, facilitating synchronisation of the surface field. Despite the under-etching, the mean lattice period was measured to be 1.503±0.034mm (table 4.5.1) in accordance with the intended 1.50mm period. Further defects are evident in the 1.62mm PSL mounted on the 1.43mm copper-backed substrate and figure 4.5.3 illustrates a shorted cell. Isolated defects such as this are unlikely to significantly affect the PSLs studied in this work, where the number of lattice periods is sufficiently large.

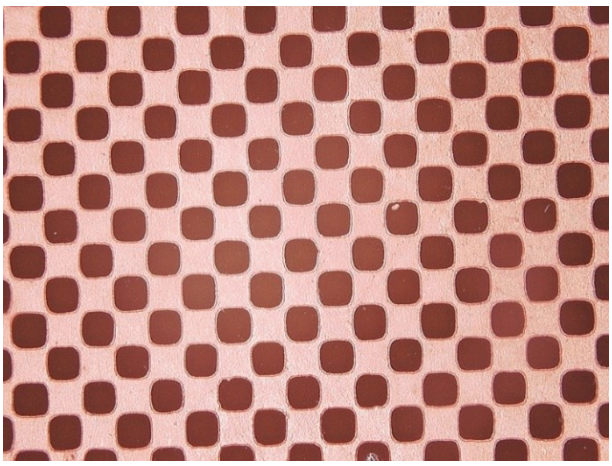

Figure 4.5.2. Image obtained with the Hirox microscope showing under-etching in the 1.50mm PSL mounted on the 0.41mm copper-backed substrate.

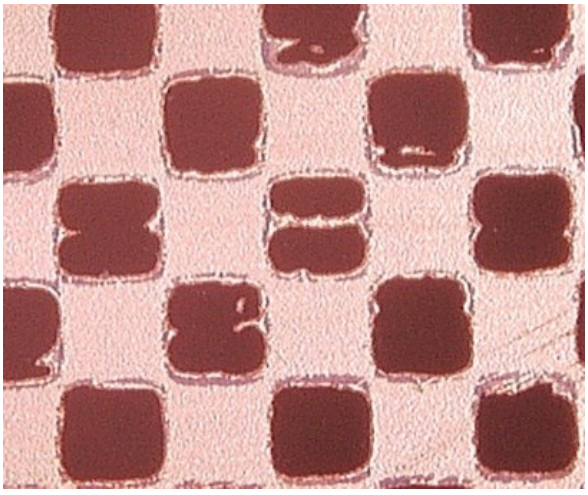

Figure 4.5.3. Image obtained with the Hirox microscope showing defects in the 1.62mm PSL mounted on the 1.43mm copper-backed substrate.

Photographs of the 1.50mm PSL mounted on the 0.76mm substrate and the 1.62mm PSL mounted on the 1.43mm substrate, annotated with measuring lines, show well-etched structures. In both cases, the period measured in both directions, is close to the desired periods of 1.50mm and 1.62mm, and lie well within the calculated error margins (table 4.5.1).

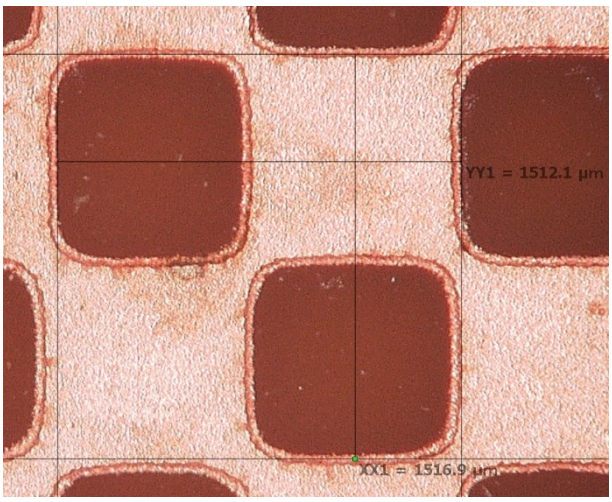

Figure 4.5.4. Photograph of 1.50mm PSL etched onto the 0.76mm substrate, obtained using the Hirox microscope and annotated with measuring lines. The measurements provided (1.5121mm in the horizontal direction and 1.5169mm in the vertical direction) show close agreement with each other and the expected lattice period (1.50mm).

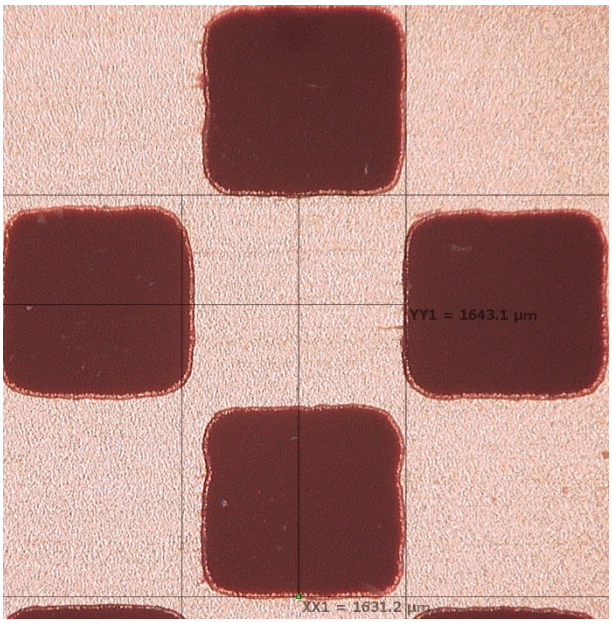

Figure 4.5.5. Photograph of the 1.62mm PSL etched onto the 1.43mm substrate. The measured dimensions (1.6431mm and 1.6312mm) are consistent in both directions and agree with the expected period (1.62mm).

The professionally etched high frequency structure, photographed using the Hirox microscope and annotated with measuring lines, is presented in figure 4.5.6. The measured period (0.638mm) is consistent in both directions and close to the anticipated value of 0.63mm. Figure 4.5.7 demonstrates the overall appearance of

the high-frequency structure which appears uniformly etched with no apparent defects. The 3D representation provided in figure 4.5.8 was obtained using the microscope's inbuilt software and high magnification lens to focus on the dielectric and copper surfaces, scanning between the two to build up a 3D profile of the structure. The scale on the right-hand side ranges from 0 to 35.805 μm confirming that the corrugation depth of the PSLs is close to 35 μm.

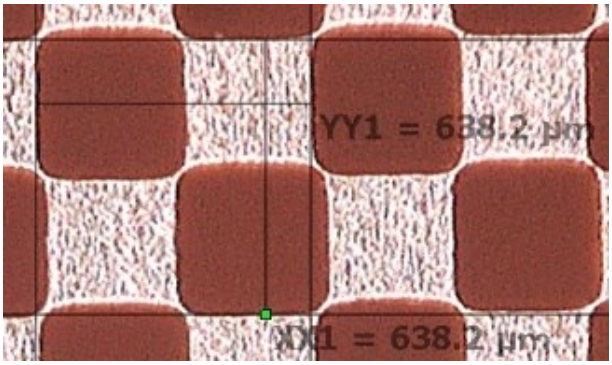

Figure 4.5.6. Close up view of professionally etched structure with lattice period 0.638mm, designed to operate in the 325-500 GHz frequency band. The measuring lines show a period of 0.638mm in both directions.

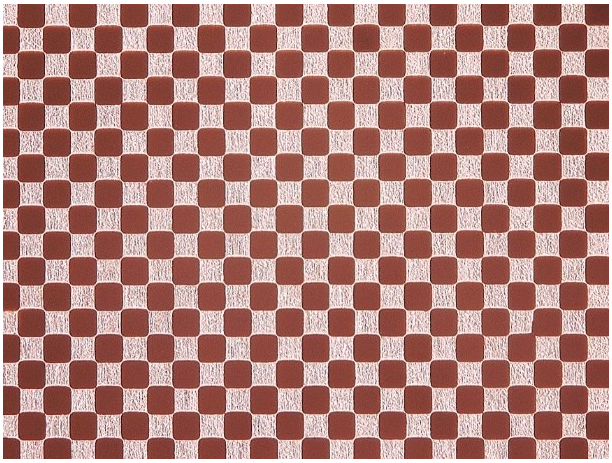

Figure 4.5.7. Hirox microscope photograph of the professionally etched structure with lattice period 0.638mm.

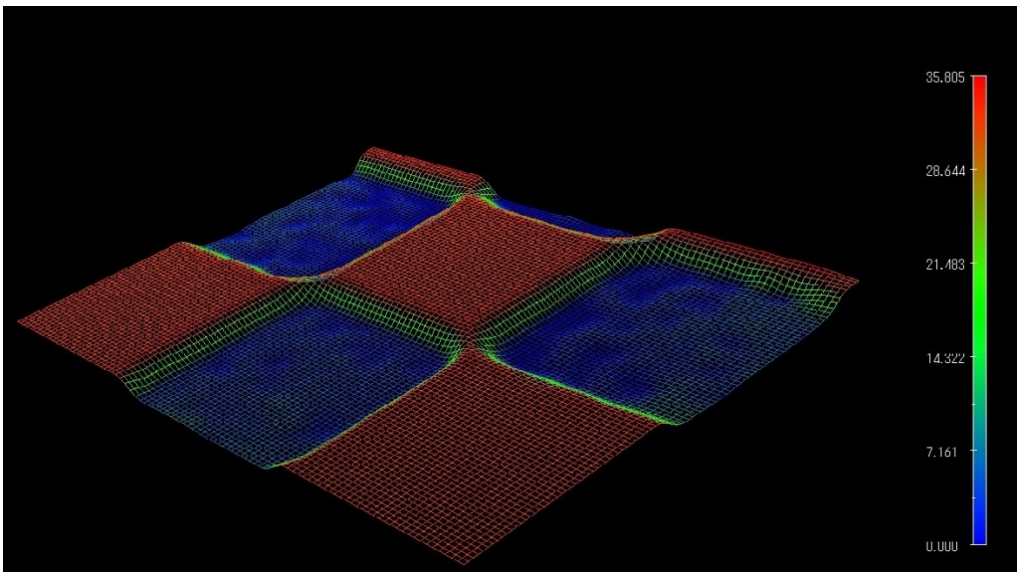

Figure 4.5.8. 3D representation of the professionally etched 0.638mm PSL obtained using the 3D profiling feature of the Hirox microscope. The blue areas represent the unit cells and the copper corrugation has a depth of 35.805µm.

The lattice dimensions of all the structures were measured in both directions at various points using the Hirox imager and a travelling microscope. The mean periods and error margins are presented in tables 4.5.1 and 4.5.2 below. Table 4.5.1 lists the measurements and uncertainties for the set of PSLs etched onto the copper-backed substrates, while data for the structures composed of PSLs and substrates (without copper backing) is provided in table 4.5.2. For the structures designed to operate at the 140-220 GHz band the mean measured period, when quoted to two decimal places, was found to match the expected lattice period. The higher frequency PSL, with an expected period of 0.63mm, had a mean measured period of 0.64mm (quoted to two decimal places) which was only slightly larger than expected, despite the manufacturing challenges associated with the PSL's small size.

FR-4 Thickness (mm)	Expected Lattice Period (mm)	Mean Lattice Period (mm)
0.410±0.005	1.50	1.503±0.034
0.410±0.005	1.62	1.623±0.023
0.410±0.005	1.74	1.741±0.028
0.410±0.005	1.94	1.940±0.013
0.410±0.005	0.63	0.638±0.012
0.762±0.005	1.50	1.500±0.038
0.762±0.005	1.62	1.621±0.033
0.762±0.005	1.74	1.742±0.025
0.762±0.005	1.94	1.941±0.015
1.433±0.005	1.50	1.500±0.030
1.433±0.005	1.62	1.620±0.025
1.433±0.005	1.74	1.742±0.028
1.433±0.005	1.94	1.944±0.035

Table 4.5.1. Table listing the mean lattice periods quoted with error margins for the PSL structures etched onto the copper-backed FR-4 substrates. The higher frequency 0.638mm PSL is included in this table.

FR-4 Thickness (mm)	Expected Lattice Period (mm)	Mean Lattice Period (mm)
0.410±0.005	1.50	1.499±0.033
0.410±0.005	1.62	1.621±0.020
0.410±0.005	1.74	1.740±0.030
0.410±0.005	1.94	1.939±0.008
0.762±0.005	1.50	1.503±0.058
0.762±0.005	1.62	1.623±0.021
0.762±0.005	1.74	1.742±0.030
0.762±0.005	1.94	1.943±0.025
1.433±0.005	1.50	1.501±0.020
1.433±0.005	1.62	1.623±0.022
1.433±0.005	1.74	1.741±0.035
1.433±0.005	1.94	1.942±0.015

Table 4.5.2. Table listing the mean lattice periods quoted with error margins for the PSL structures etched onto the FR-4 substrates (without copper backing).

4.6 Planar PSL with Air Gap

A tunable "air-gap" structure based on a 1.94mm PSL was constructed. The schematic diagram (figure 4.6.1) shows the copper PSL secured by Perspex holders, and held by four nylon screws at a variable distance from a copper back plate. The air separation was adjusted to specific values (1mm, 1.6mm and 3mm) with equivalent optical path lengths to the 0.41mm, 076mm and 1.43mm FR-4 substrates. This arrangement (photographed in figure 4.6.2) allowed the study of a low loss PSL structure which is of particular importance when scaling the PSLs up to even higher frequencies, where significant dielectric loss may inhibit the coherent synchronisation of the lattice. Further experimental measurements involved the insertion of dielectric and aluminium frames. It was hoped that these would provide well-defined boundaries, reducing the levels of radiation leaked from the edges, whilst maintaining the low-loss air separation.

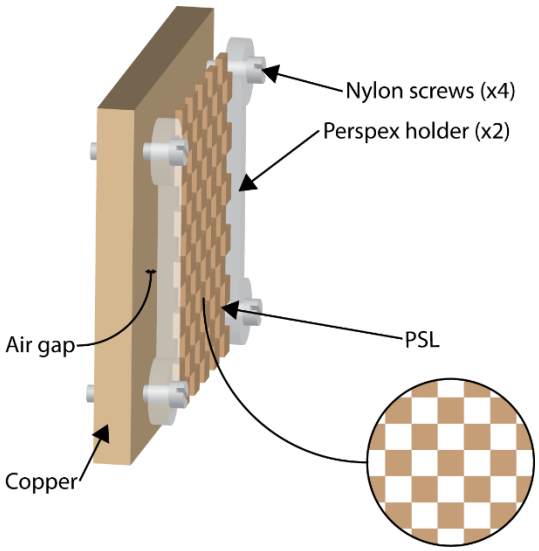

Figure 4.6.1. Schematic diagram showing tunable "air-gap" structure based on the 1.94mm PSL. The air separation is adjusted by the four nylon screws.

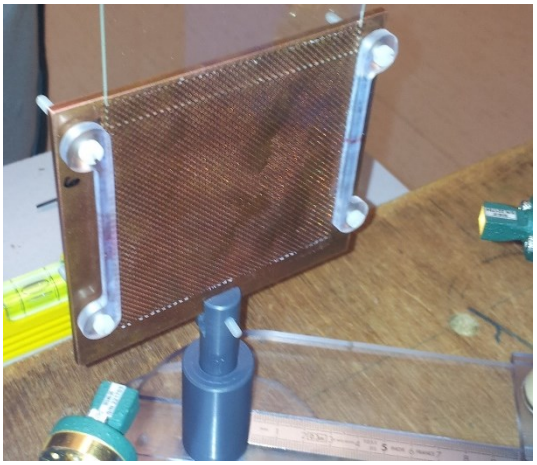

Figure 4.6.2.Photograph of "air-gap" structure based on a 1.94mm PSL held at a variable distance from a copper back plate. The gap spacing is adjusted by turning the nylon screws.

4.7 Vector Network Analyser

All experimental measurements were performed using a vector network analyser (VNA) to generate an incident plane wave which allowed transmission, reflection, and phase measurements to be carried out over a broad frequency range. The model used was an Anritsu Vector Star (MS4647A) with G-band (140-220 GHz) OML mm-wave modules (or 325-500 GHz OML modules when working at higher frequencies) calibrated to measure 3200 data points. The VNA and modules were used in conjunction with a 3739 Broadband Test Set. When operating at G-band, the mm-wave modules were connected directly to the Broadband Test Set via the local oscillator (LO) and radio frequency (RF) drives (figure 4.7.1), while at the 325-500 GHz frequency band, two signal generators (MG3692) were required, along with the Broadband Test Set, to supply the desired frequency output. The insertion of a -30dB attenuator between one of the signal generators and the 325-500 GHz OML module was essential to protect the equipment from damage. The VNA was calibrated using the standard Anritsu WR-05 and WR-2.2 waveguide calibration kits for the 140-220 GHz and 325-500 GHz frequency bands respectively. For both configurations, an offset short (SSLT) calibration method, in which the difference between the length of two shorts was used to help define the reflection measurements (Scalzi, Slobodnik et. al, 1988), was chosen.

Figure 4.7.1. shows the Anritsu Vector Star VNA connected to the Broadband Test Set and G-band (140-220 GHz) OML modules. The scanning platform, used to conduct measurements over a range of angles as detailed in the next section, and one of the PSL structures with no substrate, as described in §4.2, are also pictured.

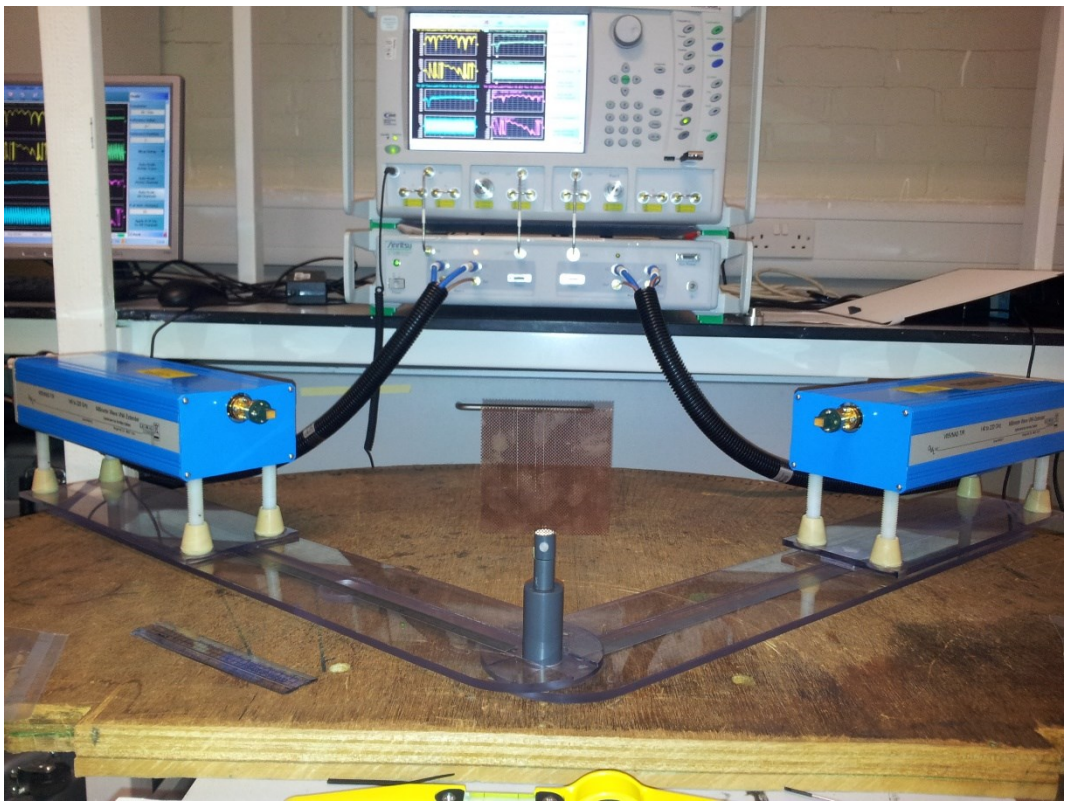

Figure 4.7.1. Photograph illustrating the experimental set-up. The VNA is connected to the 140-200 GHz OML mm-wave modules. The copper PSL (without substrate) is fixed at 0° and irradiated with a pair of G-band horns using the scanning platform.

4.8 Experimental Set-up

The experimental set-up allowing reflection measurements of the PSL structures to be made was photographed in figure 4.7.1. As the experiments progressed, the set-up evolved over time to allow faster, more reliable measurements. This involved the construction of an improved scanning platform, allowing more precise alignment between the waveguide horns and structure. When carrying out the reflection measurements, the high frequency OML modules were rotated on the scanning platform, with the PSL structure held in a fixed position, at the pivot point of the rotating arms ($\theta_i = 0°$). Grooves machined into the Perspex arms were designed to hold the OML modules in place, while the use of runners allow them to be moved forwards or backwards as necessary. The angles of incidence θ_i and reflection θ_r were marked on the wooden protractor in 1° increments, allowing the experimental set-up for the reflection measurements to be arranged such that $\theta_i = \theta_r$. Transmission measurements were also made for the set of PSLs without the

substrates. This experimental arrangement, with the launching/receiving horns directly aligned, is photographed in figure 4.8.1. In this case the PSL was rotated in gradual increments, using the plastic protractor for reference.

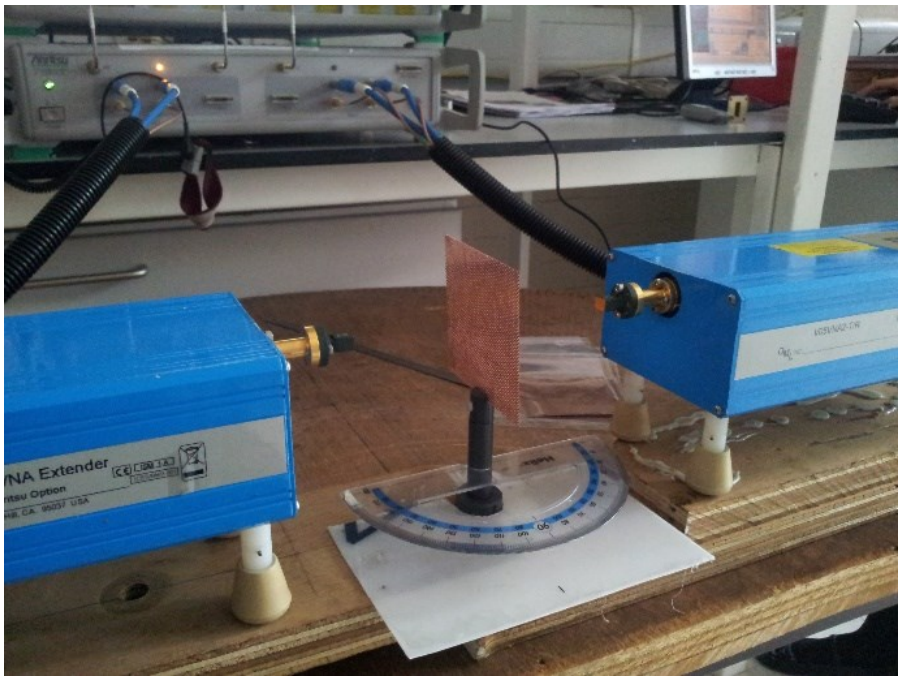

Figure 4.8.1. Experimental set-up for the transmission measurement of the PSL with no substrate. The G-band horns (attached to the 140-220 GHz OML modules) are aligned and kept stationary, while the PSL is rotated, using the protractor for reference.

All the measurements were carried out in the far field (Fraunhofer) region, where the criterion for the far field boundary is given by $d_{farfield} \geq \frac{{D_{horn}}^2}{\lambda}$ with $d_{farfield}$ defined as the distance between the launching/receiving horn and the PSL. D_{horn} denotes the largest dimension of the antenna, while λ is the wavelength of the radiation source. The distance d was set to 75mm for all the 140-220 GHz band measurements and 8mm for the 325-500 GHz band measurements.

A preliminary experiment was carried out to check for diffraction and establish whether or not the PSLs behave like diffractive surfaces at the measured frequency band. One of the launching/receiving horns was fixed at a particular incident angle θ_i, while the other was swept through the full angular range in 1° increments . The results of this preliminary measurement are presented in figure 4.8.2. No diffraction

pattern is observed, as verified by the diffraction condition discussed in the next chapter. Instead, it is confirmed that maximum power is achieved by setting $\theta_i = \theta_r$, which justifies the experimental set-up used to obtain the reflection measurements.

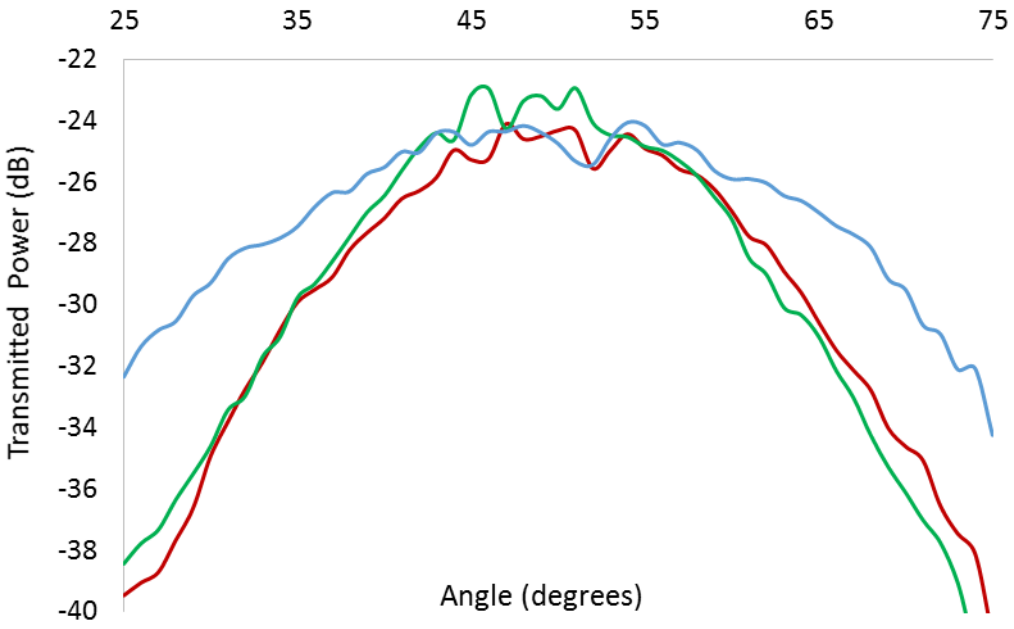

Figure 5.8.2. Diffraction Measurements made at an incident angle of 50° at frequencies of 140 GHz (blue) 180 GHz (red) and 220 GHz (green) for the 1.62mm PSL mounted on the 0.41mm substrate (without the copper backing).

4.9 Comparison of W-band and G-band Horns

Preliminary measurements were also conducted to establish the performance of the launching/receiving antennae. The quality of the results was improved across the frequency band by replacing the W-band launching/receiving horns, used in earlier experiments, with more compatible G-band (or WR2.2 when working at 325-500 GHz) launching/receiving antenna. Prior results (obtained using the W-band horns) were affected by mode conversion at high frequencies due to the waveguide step. In these early measurements, it was necessary to calibrate the raw data by subtracting the reflection measurements for a smooth metal plate. Measurements of an earlier, 1.79mm PSL etched onto a 0.76mm substrate, carried out using both W-band (blue plot) and G-band (red plot) horns are compared in figure 4.9.1.

Similarly, results for a 1.79mm PSL etched onto a 0.41mm substrate, measured with the W-band (blue plot) and G-band (red plot) horns, are plotted alongside each other in figure 4.9.2. Although two resonances are observed at lower frequencies in both cases, the performance of the W-band horns is poor above 170 GHz. Improving the experimental set-up by incorporating the G-band horns greatly enhanced the quality of the measurements. The reproducibility of the results obtained with this set-up is demonstrated in chapter 5.

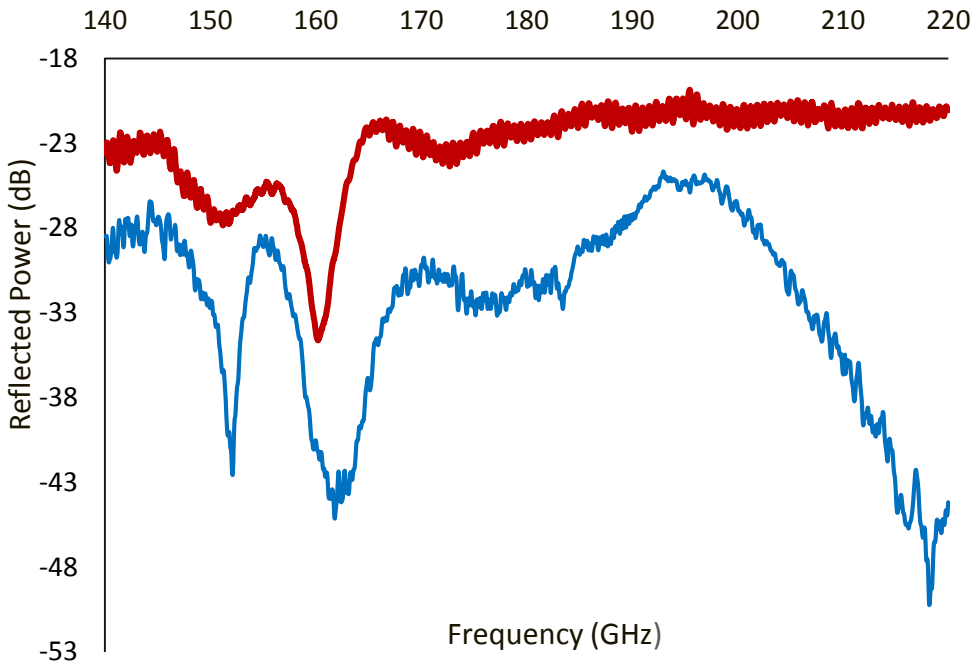

Figure 4.9.1. Reflected power measurements for 1.79mm PSL etched onto a 0.76mm substrate, made using W-band (blue) and G-band (red) waveguide horns.

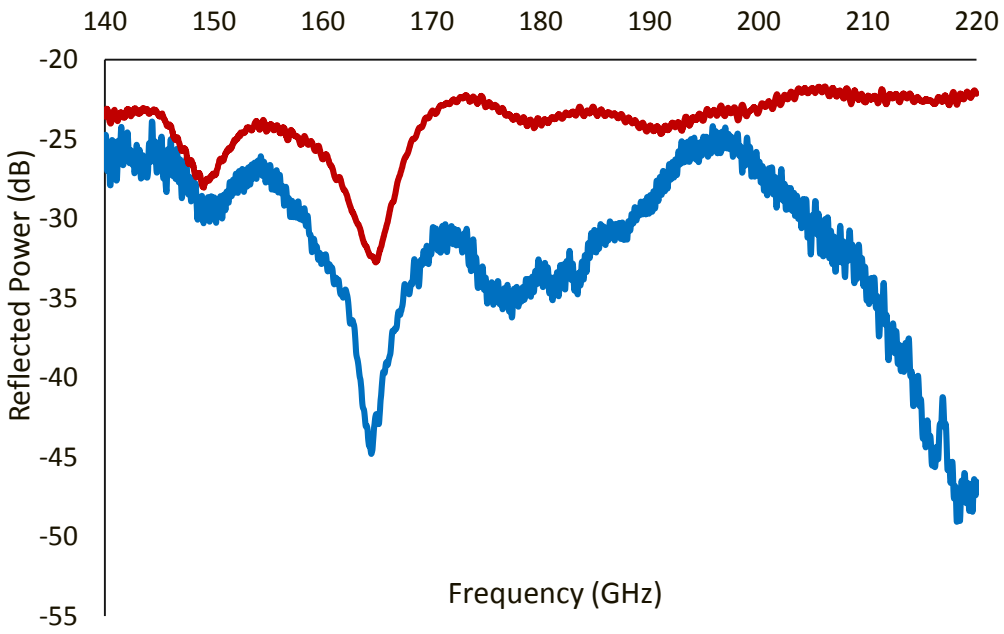

Figure 4.9.2. Reflected power measurements for 1.79mm PSL etched onto a 0.41mm substrate, made using W-band (blue) and G-band (red) waveguide horns.

4.10 Mode Scans of Launching/Receiving Antennae

When carrying out experimental measurements, it was important to ensure uniform illumination across the PSL. Factors such as inadequate irradiation of the PSL or potential edge effects, arising from side lobes in the output of the horns striking the edges of the structure, may lead to poor results. The objective was to illuminate an optimum number of scatterers in order to achieve a high cavity Q, whilst at the same time preventing the side lobes from impinging on the PSL boundaries as much as possible. One way of controlling the spot size was to choose an optimum distance, within the far-field, between the sample and the launching/ receiving horns.

The output beam profiles of the G-band (140-200 GHz) and WR2.2 (325-500 GHz) antennae were obtained by conducting mode scans. This involved keeping one horn stationary and scanning the second horn over a range of angles. The angular sweep was limited by the length of the cables attached to the OML modules, allowing for a range of -15° to 55° for the G-band horns and -30° to 60° for the WR2.2 horns. While waveguide twists (WR2.2) with a 90° rotation, thus converting the polarisation from

the H to E plane, were used to measure both polarisations for the WR2.2 horns, no such twists were available for use at G-band.

Due to their small aperture dimensions, the WR2.2 horns proved difficult to align. This problem was exacerbated by a slight offset in the waveguide attachment of the OML modules. To compensate, the horns were aligned by maximising the transmitted power. Since these measurements were deemed less reliable than those at G-band, mode scans for the WR2.2 horns were carried out on two separate occasions, with the set-up reassembled between measurements. The experimental findings were compared to theoretical values (Silver, 1949) describing the radiation output from a rectangular waveguide aperture. This approximation does not take into account the flared geometry of the horn and assumes plane wave radiation. The following equations were used to describe the E and H planes:

$$E_\theta = 2\left(\frac{\mu}{\varepsilon}\right)^{\frac{1}{2}} \frac{{a_{wg}}^2 b_{wg}}{\pi\lambda^2 R_{far}} \left[1 + \frac{k_z^{wg}}{k} cos\theta + \Gamma_{ref}\left(1 - \frac{k_z^{wg}}{k} cos\theta\right)\right] \frac{sin\left(\frac{\pi b_{wg}}{\lambda} sin\theta\right)}{\frac{\pi b_{wg}}{\lambda} sin\theta} e^{-jkR_{far}}$$

$$H_\theta = -\left(\frac{\mu}{\varepsilon}\right)^{\frac{1}{2}} \frac{\pi {a_{wg}}^2 b_{wg}}{2\lambda^2 R_{far}} \left[cos\theta + \frac{k_z^{wg}}{k} + \Gamma_{ref}\left(cos\theta - \frac{k_z^{wg}}{k}\right)\right] \frac{cos\left(\frac{\pi a_{wg}}{\lambda} sin\theta\right)}{\left(\frac{\pi a_{wg}}{\lambda} sin\theta\right)^2 - \frac{\pi^2}{4}} e^{-jkR_{far}}$$

The parameters a_{wg} and b_{wg} are the dimensions of the rectangular antennae, k_z^{wg} is the longitudinal wavenumber of the fundamental rectangular waveguide mode, R_{far} is the radius of the far field and Γ_{ref} is a reflection coefficient defined by the ratio of the transverse components of the reflected and incident electric field vectors. When the antennae aperture is large in comparison to the operating wavelength λ, $\Gamma_{ref} \approx 0$. (Silver, 1949) The aperture dimensions of the G-band ($a_{wg} = 12.548$, $b_{wg} = 9.55$)mm and WR2.2($a_{wg} = 1.89$, $b_{wg} = 2.58$)mm horns are sufficiently large, allowing the reflection coefficient terms to be neglected.

4.10.1 G-Band Mode Scans (H-Plane)

The normalised transmission measurements (green plots) demonstrating the output beam profiles for the H-plane of the G-band horns at frequencies of 140 GHz, 180 GHz and 220 GHz are presented in figures 4.10.1.1-4.10.1.3. These are plotted alongside the normalised theoretical profiles (red plots) predicted by Silver. The plots show good agreement between the theoretical and experimental results, despite a small dip in the transmitted power around 0° at 180 GHz (figure 4.10.1.2).

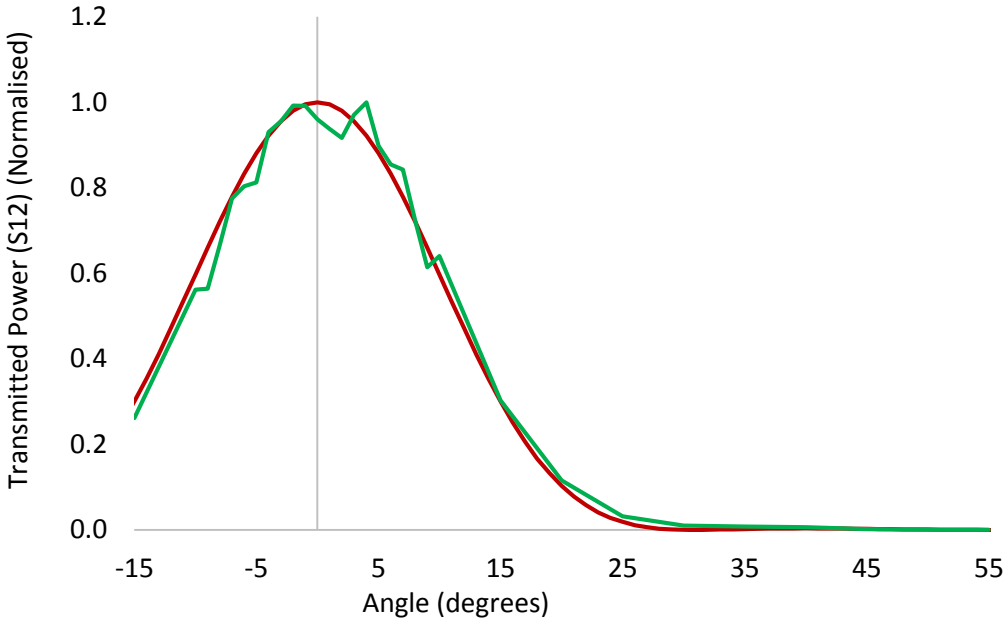

Figure 4.10.1.1. Beam-profile showing the normalised transmitted power of the G-band, standard gain horn at 140 GHz, polarised in the H-plane (green plot). The red plot shows the theoretical beam-profile predicted by Silver.

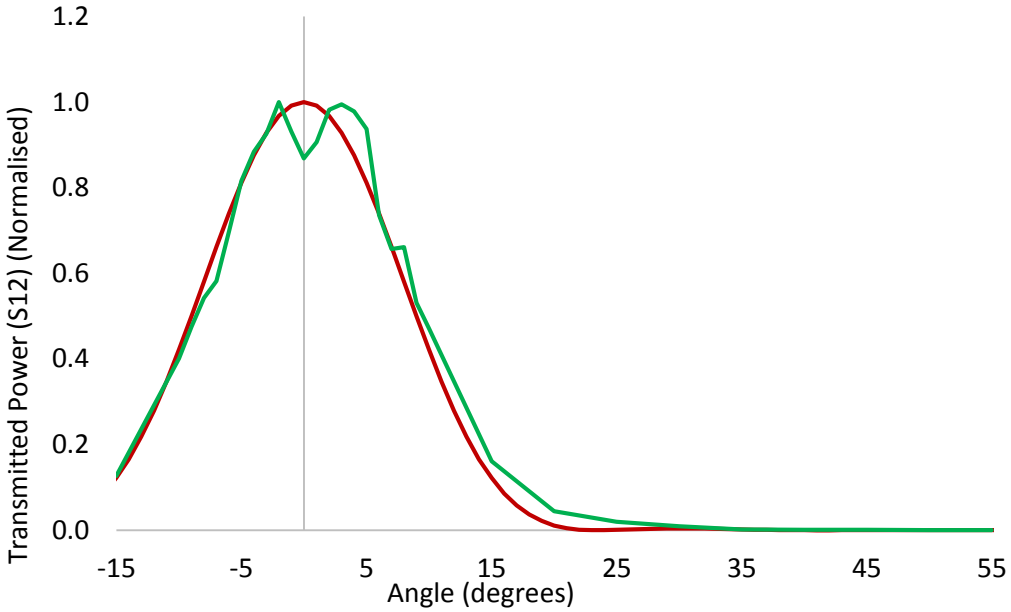

Figure 4.10.1.2. Beam-profile showing the normalised transmitted power of the G-band, standard gain horn at 180 GHz, polarised in the H-plane (green plot). The red plot shows the theoretical beam-profile predicted by Silver. A dip is observed at the centre of the main lobe, around 0º.

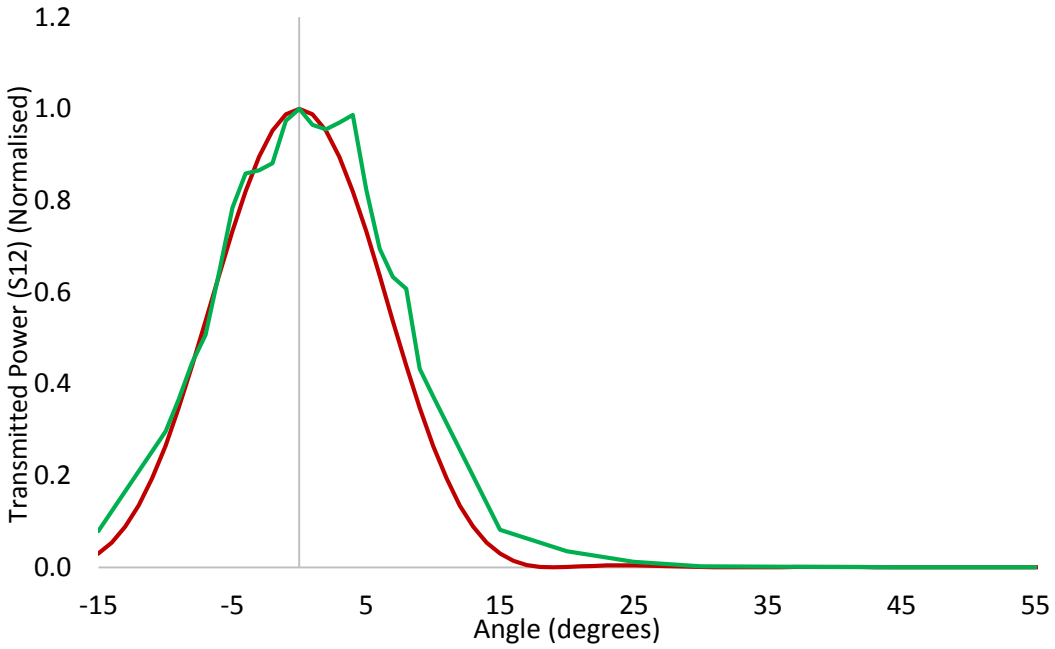

Figure 4.10.1.3. Beam-profile showing the normalised transmitted power of the G-band, standard gain horn at 220 GHz, polarised in the H-plane (green plot). The red plot shows the theoretical beam-profile predicted by Silver. As expected, the beam-width is narrowest at 220 GHz. The dip in the main lobe is least pronounced at this frequency.

4.10.2 WR2.2 Waveguide Horns – H-plane Results

Figures 4.10.2.1-4.10.2.3 show the normalised transmission measurements, made on two separate occasions (green, purple plots), for the H-plane of the WR2.2 horns at frequencies of 140GHz, 180 GHz and 220 GHz. Both sets of data are compared to the normalised, theoretical output beam profile (Silver, 1949) with the best performance observed at the centre of the frequency band (figure 4.10.2.2). To account for a systematic error, the green plot as been corrected for a 2° offset.

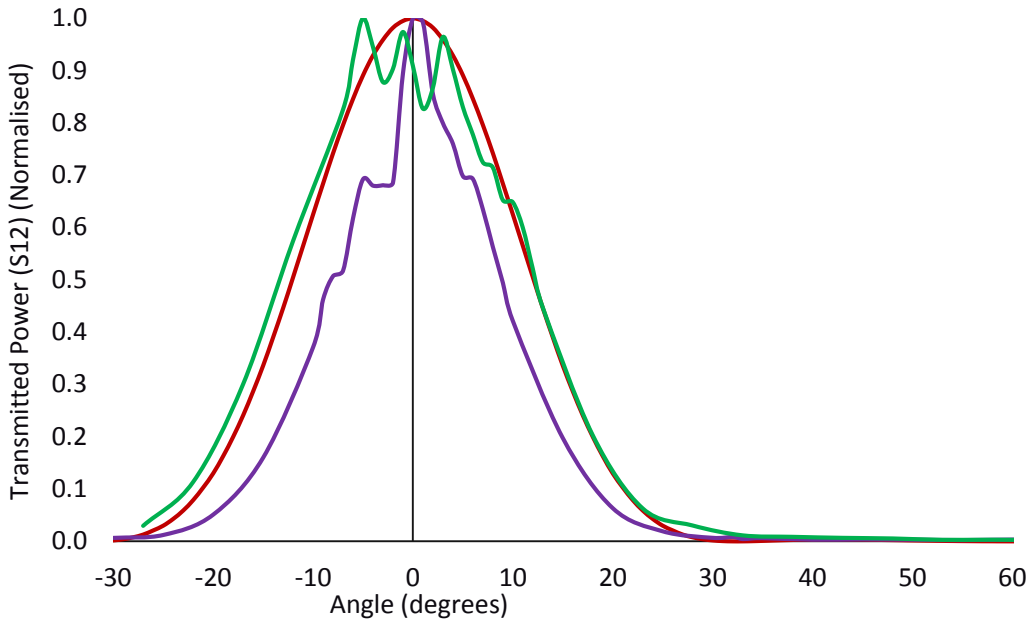

Figure 4.10.2.1. Beam-profile showing the normalised transmitted power of the WR2.2 waveguide standard gain horn at 325 GHz, polarised in the H-plane (green and purple plots). The red plot represents the theoretical values predicted by Silver for a rectangular waveguide aperture with WR2.2 dimensions at 325 GHz.

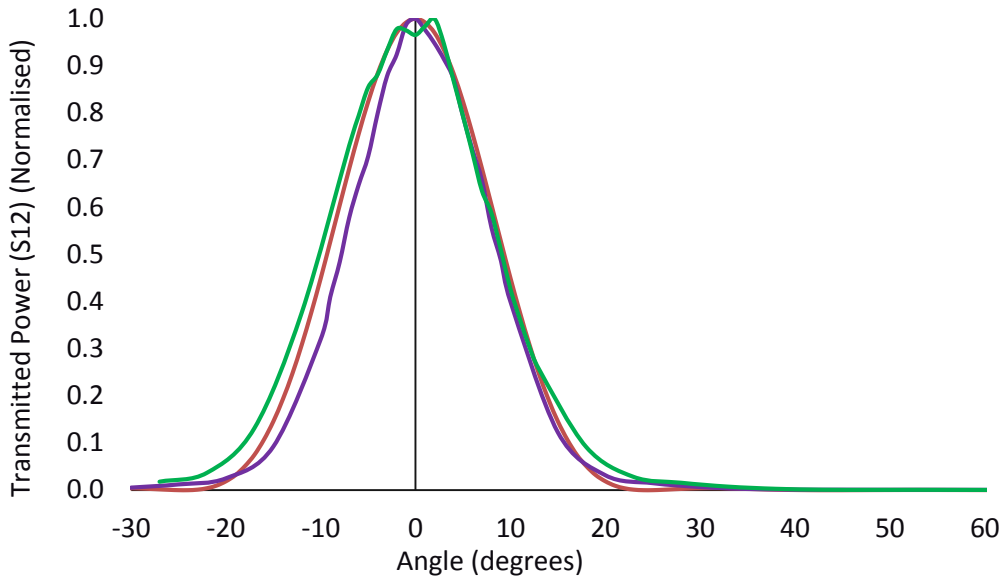

Figure 4.10.2.2. Beam-profile showing the normalised transmitted power of the WR2.2 waveguide standard gain horn at 412.5 GHz, polarised in the H-plane (green and purple plots). The red plot represents the theoretical values predicted by Silver for a rectangular waveguide aperture with WR2.2 dimensions at 412.5 GHz.

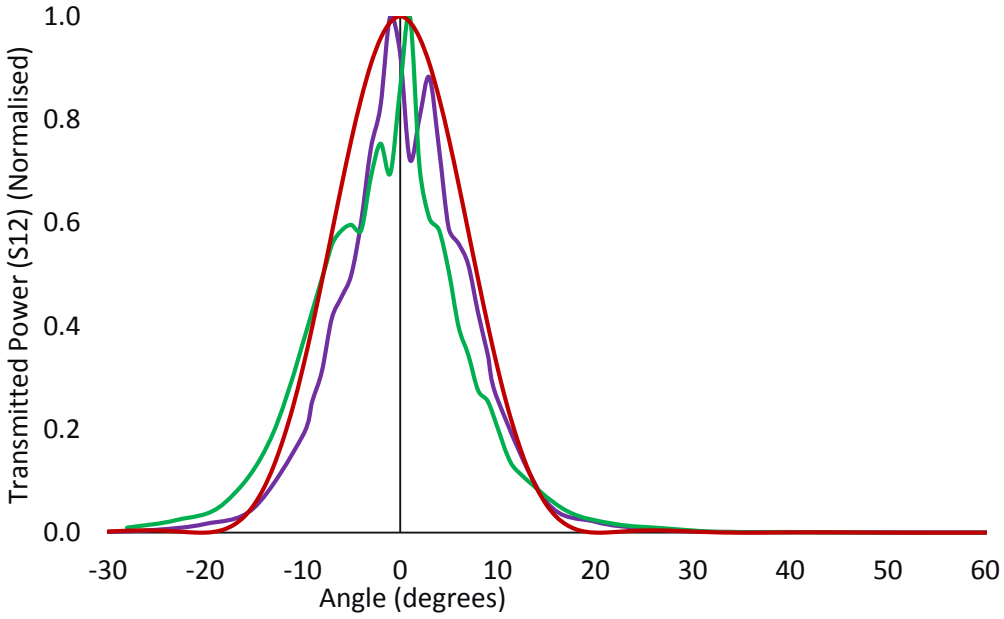

Figure 4.10.2.3. Beam-profile showing the normalised transmitted power of the WR2.2 waveguide standard gain horn at 500 GHz, polarised in the H-plane (green and purple plots). The red plot represents the theoretical values predicted by Silver for a rectangular waveguide aperture with WR2.2 dimensions at 500 GHz.

4.10.3 WR2.2 Waveguide Horns – E-plane

Finally, measurements were made for the WR2.2 horns, polarised in the E-plane using the pair of waveguide twists. The experimental transmission measurements (green, purple plots) are once more plotted alongside the theoretical beam profile (red plot) at frequencies of 140 GHz, 180 GHz and 220 GHz. Again, optimum performance was measured at the middle of the frequency band. Besides the main lobe, the first side lobe is visible at all frequencies due to the E-plane polarisation.

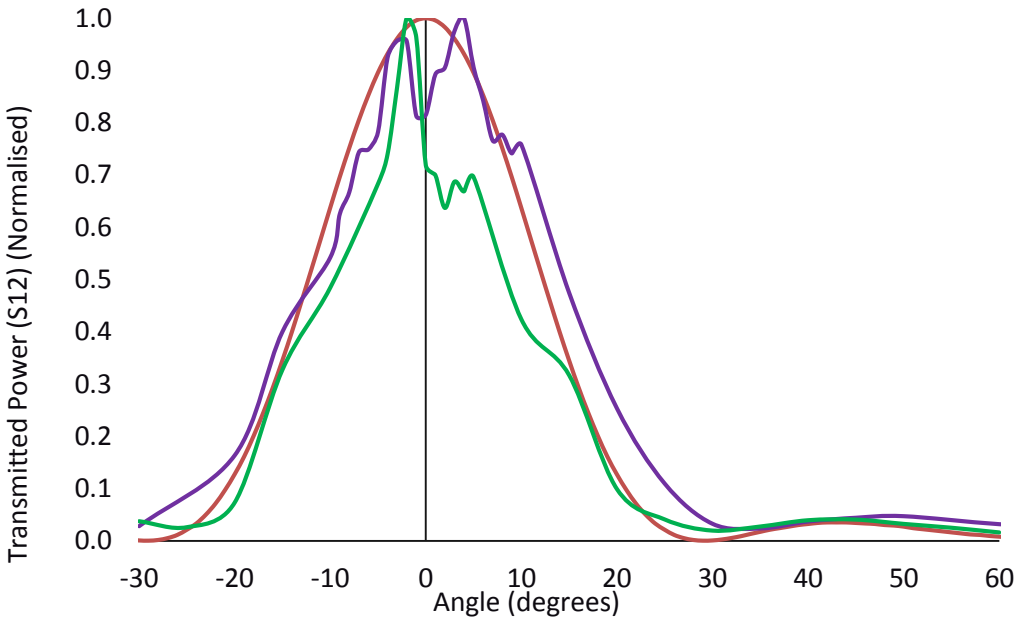

Figure 4.10.3.1. Beam-profile showing the normalised transmitted power of the WR2.2 waveguide standard gain horn at 325 GHz (green and purple plots). The horns are polarised in the E-plane using a pair of waveguide twists. The red plot represents the theoretical values predicted by Silver for a rectangular waveguide aperture with WR2.2 dimensions (A=1.89mm, B=2.58mm) at 325 GHz.

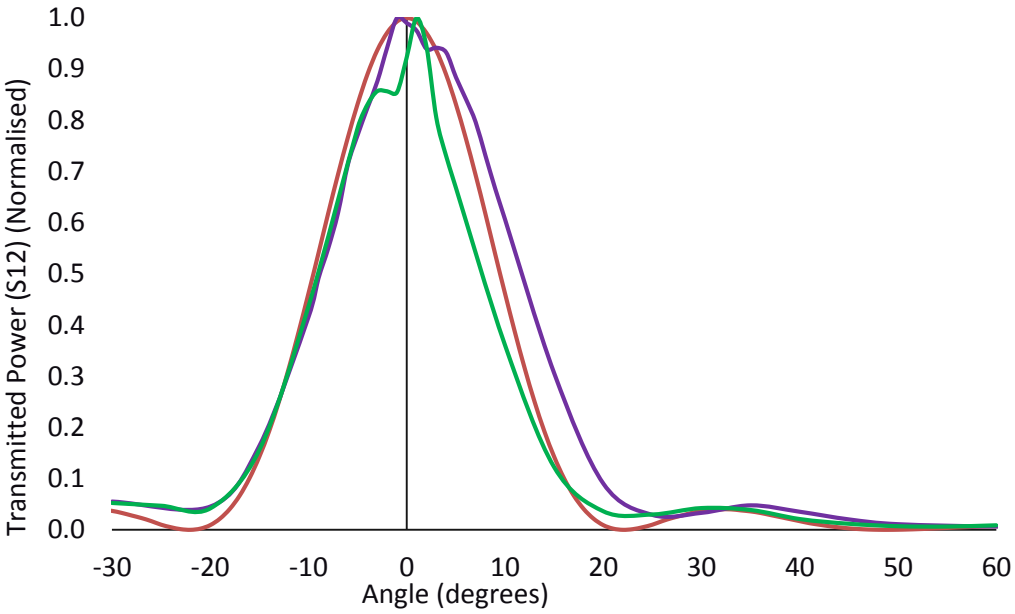

Figure 4.10.3.2. Beam-profile showing the normalised transmitted power of the WR2.2 waveguide standard gain horn at 412.5 GHz (green and purple plots). The horns are polarised in the E-plane using a pair of waveguide twists. The red plot represents the theoretical values predicted by Silver for a rectangular waveguide aperture with WR2.2 dimensions (A=1.89mm, B=2.58mm) at 412.5 GHz.

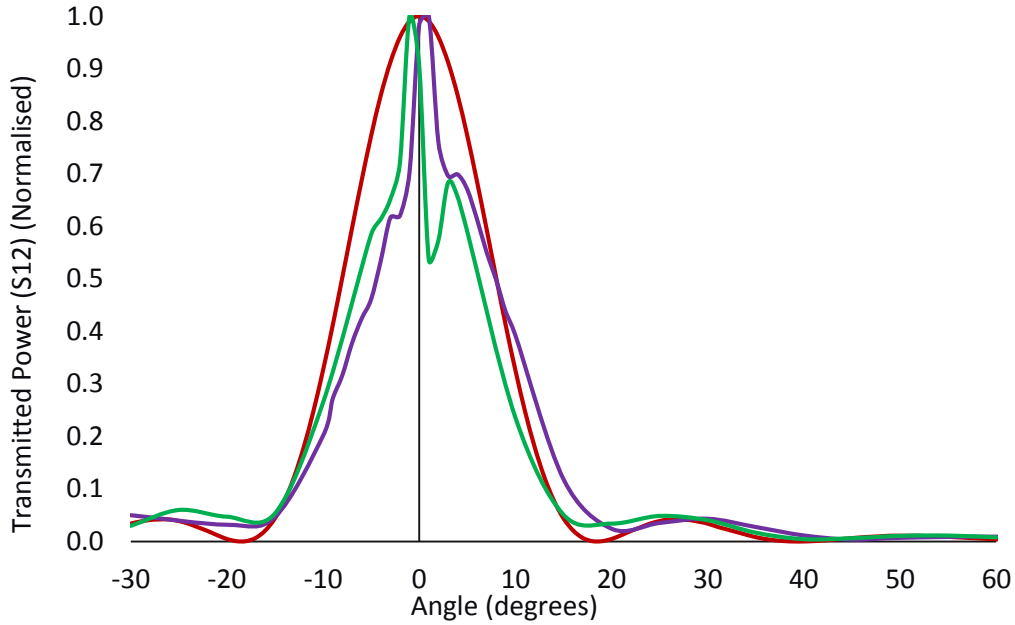

Figure 4.10.3.3.Beam-profile showing the normalised transmitted power of the WR2.2 waveguide standard gain horn at 500 GHz (green and purple plots). The horns are polarised in the E-plane using a pair of waveguide twists. The red plot represents the theoretical values predicted by Silver for a rectangular waveguide aperture with WR2.2 dimensions (A=1.89mm, B=2.58mm) at 500 GHz.

4.11 Permittivity of dielectric samples of different thickness

FR-4 is conventionally used in low frequency microwave components and little is known about its electromagnetic properties at 140 GHz and beyond. In addition to high frequency dielectric losses, the manufacturing of FR-4 is seldom regulated to tight specifications, meaning there can be a relatively large variation in its dielectric permittivity, especially for samples of different thickness. In fact, it is reported that thinner samples, such as the 0.41mm substrate used in some of the PSL structures, are typically produced using a slightly different chemical composition (Lee, 2014). Two methods were used in an attempt to define the dielectric permittivity at 140-220 GHz for the dielectric samples of different thickness.

4.11.1 Brewster Method

In this section the method of determining the dielectric refractive index n_d by measuring Brewster's angle at the 140-200 GHz frequency band is discussed. Typically, Brewster measurements are conducted at optical frequencies with the use of a laser beam (Ouseph, Driver et al. 2001). However, measurements of dielectric sheets at microwave frequencies by a similar approach have been documented (Afzalzadeh 1998).

The experiment described in this section has been carried out with the G band horns rotated to have the electric field polarised parallel to the plane of incidence (E-plane polaristaion). Reflection measurements were made for the different dielectric samples at 1° increments. The data obtained with the VNA was studied at frequencies of 140 GHz, 180 GHz and 220 GHz over the full angular range in order to identify a minimum in the reflected signal. The angle at which the minimum reflected power is observed is the Brewster angle θ_B. When θ_B is known, the refractive index of the dielectric can be evaluated from Brewster's Law: $n_d = n_i tan\theta_B = tan\theta_B$ (Brewster 1815) A more sophisticated method involves using $n_d = tan\theta_B$ to determine an initial value of the dielectric's refractive index (n_d) and gradually varying n_d, using the Least Squares method to achieve the closest fit to the Fresnel equation (Corson and Lorrain 1962, Hecht 1998) below.

$$R_{\parallel} = \left(\frac{-\cos\theta_i + (n_1/n_2)\cos\theta_t}{\cos\theta_i + (n_1/n_2)\cos\theta_t} \right)^2$$

θ_i is the angle of incidence and θ_t is the transmitted angle given by Snell's Law: $\sin\theta_i/\sin\theta_t = n_2/n_1 = n_d$. The reflection measurements at frequencies of 140 GHz (green plot), 180 GHz (blue plot) and 200 GHz (red plot) are presented in figure 4.11.1.1. At all three frequencies, the minimum (observed around 60°-70°) is distorted by oscillations. The reflected power at lower angles showed poor agreement with Fresnel's equation, and attempts to fit the data proved unsuccessful.

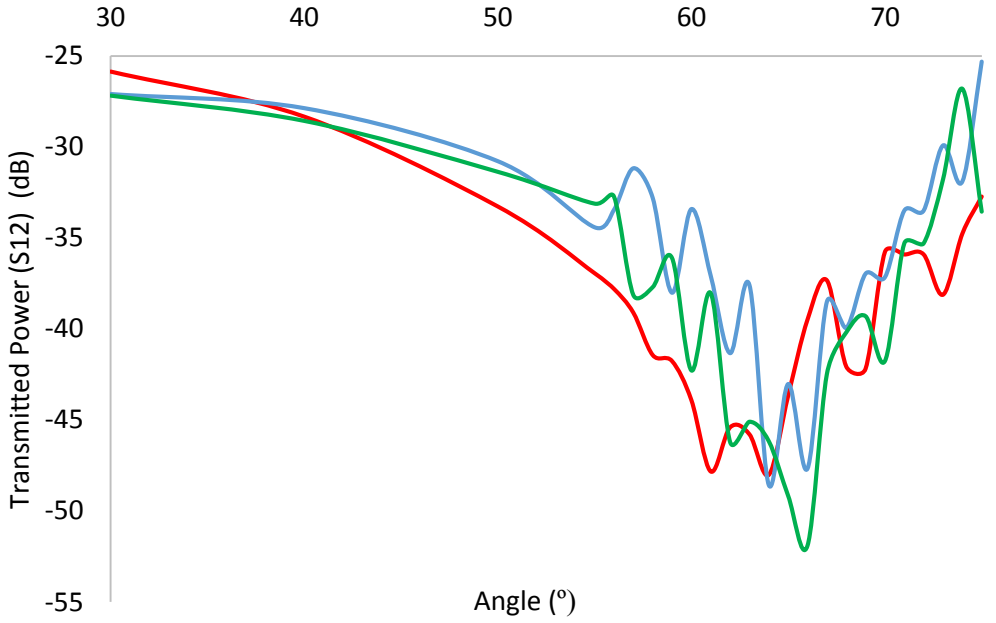

Figure 4.11.1.1. Brewster measurements in the E-plane polarisation for the 0.76mm FR-4 sample at frequencies of 140 GHz (green line) 180 GHz (blue line) and 220 GHz (orange line). Oscillations are observed in the region of the Brewster angle.

The oscillations of figure 4.11.1.1 suggest possible interference of the antennae side lobes. The schematic presented in figure 4.11.1.2 shows that the side lobes may couple directly into each other when $\theta_s = 90 - \theta_B$, where θ_s is equivalent to the complimentary angle, θ_c. If the Brewster angle ($\theta_i = \theta_B$) is assumed to lie between 64.6° and 67.3° depending on the thickness of the dielectric (as calculated from the phase measurements made in the next section, §4.11.2) then the corresponding

angle at which the two output beams directly feed into one another, without first striking the dielectric, occurs between θ_s =25.4° and θ_s =22.7°.

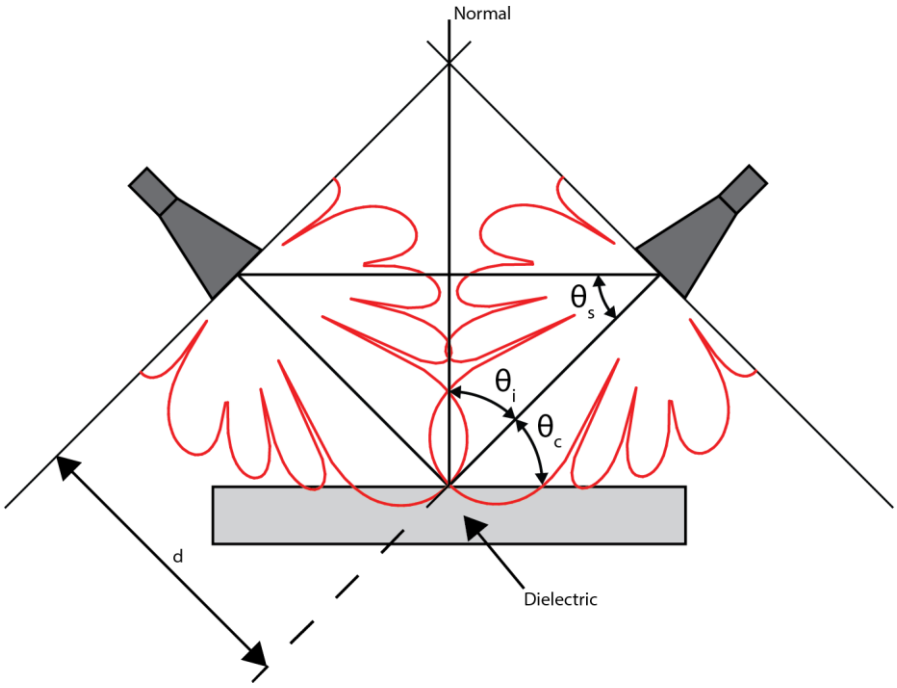

Figure 4.11.1.2 Schematic diagram demonstrating interference of the launching/receiving antennae. Direct coupling between the output beams, occurs at angle θ_s given by $\theta_s = 90 - \theta_B$.

Figure 4.11.1.3 shows the theoretical beam profile for the G-band horns at frequencies of 140 GHz (green plot), 180 GHz (blue plot) and 220 GHz (yellow plot), polarised in the E-plane. The pair of red dashed lines at 22.7°, and black dashed lines at 25.4° mark the angles at which the horn output beams can directly couple at the Brewster angle for the thinnest and thickest FR-4 substrates. When superimposed on the theoretical beam profile, it is evident that both the main lobe and first side lobe may couple into each other at the oblique incident angles required for the Brewster measurements, thus distorting the results. The refractive indices of the 0.41mm, 0.76mm and 1.43mm FR-4 dielectrics were therefore determined by an alternative method, detailed in the following section.

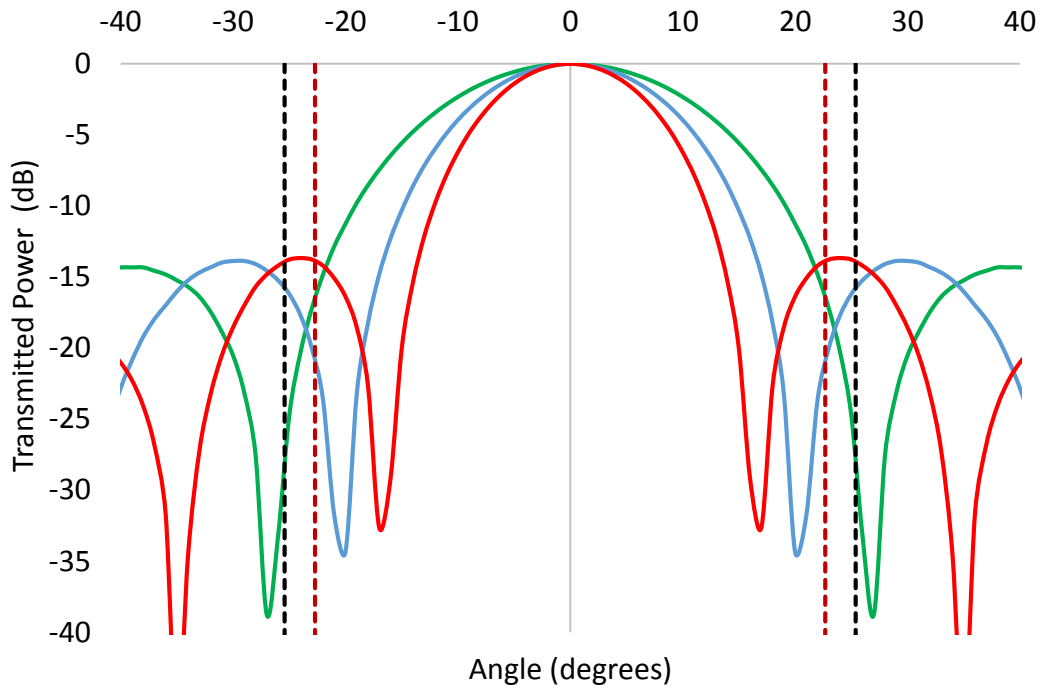

Figure 4.11.1.3. Theoretical beam profile for the G-band horns polarised in the E-plane at frequencies of 140 GHz (green plot), 180 GHz (blue plot) and 220 GHz (red plot). The dashed lines mark θ_S when the Brewster angle θ_B falls between 64.6° and 67.3. The plot indicates that part of the main and first side lobes feed directly into each other without first striking the dielectric, leading to interference.

4.11.2 Change in Phase Method

The dielectric permittivity of the different substrates was calculated by measuring the phase using the VNA and placing the dielectric samples between the 140-220 GHz launching/receiving horns as shown in figure 4.11.2.1.

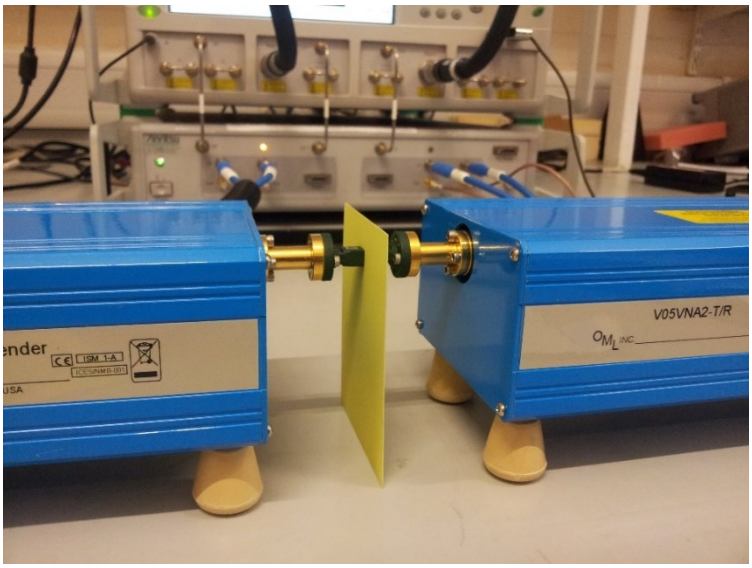

Figure 4.11.2.1. Photograph demonstrating the change in phase method used to establish the permittivity of the FR-4. The phase of the dielectric was measured by positioning the sample between the G-band horns as shown.

The phase change was established by removing the sample and recording the phase of the resultant air-gap. From optics, (Hecht, 1998) the phase in the air θ_{air} and dielectric θ_{diel} media of a given length, L is defined:

$$\theta_{air,diel} = Lk_{air,diel}$$

where k is the wavenumber which is written $k_{air} = 2\pi/\lambda_0$ and $k_{diel} = 2\pi n_d/\lambda_0$ for the air and dielectric regions respectively, and n_d is the refractive index of the dielectric sample. The phase change $\Delta\theta$ is then:

$$\Delta\theta = \theta_{diel} - \theta_{air} = \frac{2\pi}{\lambda_0} L(n_d - 1)$$

In measuring the phase, the VNA contributes its own unknown phase element, and the overall phase change θ_{VNA} is expressed

$$\theta_{VNA} = \Delta\theta + 2\pi w$$

where w is an arbitrary integer number. Taking this unknown phase element into account, the phase change between the two media can be expressed

$$\Delta\theta = \frac{2\pi f(n_d - 1)L}{c} - 2\pi w$$

Differentiating this phase change with respect to the frequency gives:

$$\frac{\partial\Delta\theta}{\partial \mathrm{f}} = \frac{2\pi L(n_d - 1)}{c}$$

and rearranging for the refractive index, n_d gives the equation below.

$$n_d = 1 + c\frac{\partial\Delta\theta/\partial \mathrm{f}}{2\pi L}$$

Plots illustrating the phase change over frequency, and demonstrating the lines of best fit used to obtain $\partial\Delta\theta/\partial \mathrm{f}$, are presented for all the FR-4 samples in figures 4.11.2.2.-4.11.2.4. Measurements were repeated several times, and the four overlaid plots of figure 4.11.2.5 show the reproducibility of the phase change results for the 1.43mm dielectric. The phase, both for the dielectric and equivalent air space, was measured four times and the error in the gradient of the line of best fit was found to be ±0.0002. The fractional uncertainties of the dielectric thickness (±0.005) and change in phase measurements (±0.0002) were combined to give the overall error in the refractive indices, listed in table 4.11.1.

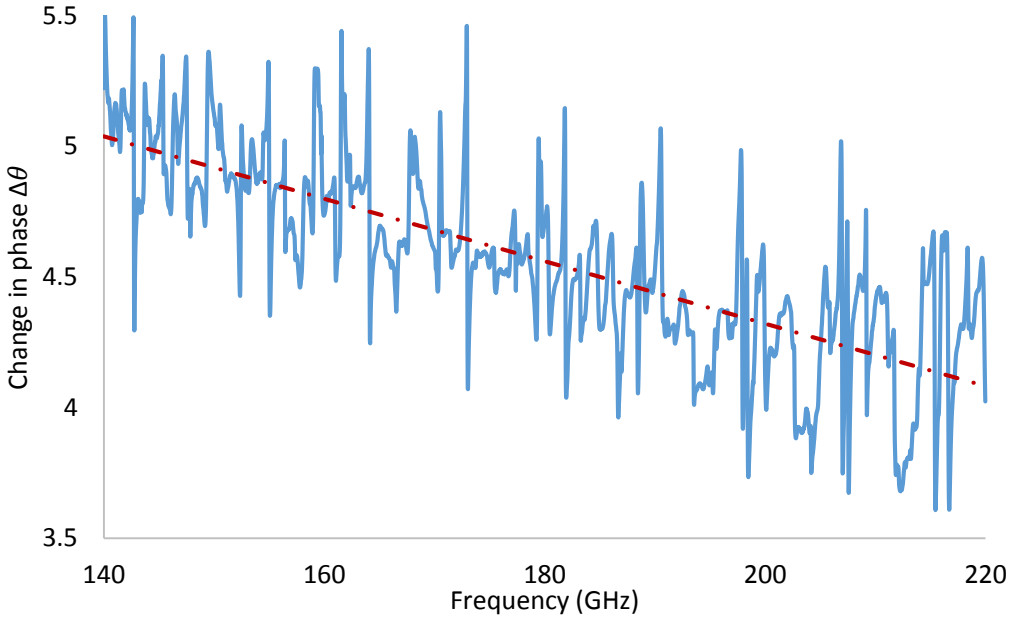

Figure 4.11.2.2. Change in phase for a signal travelling through the 0.41mm FR-4 dielectric compared to the phase measured for the same air distance. The line of best fit is marked by the red dashed line.

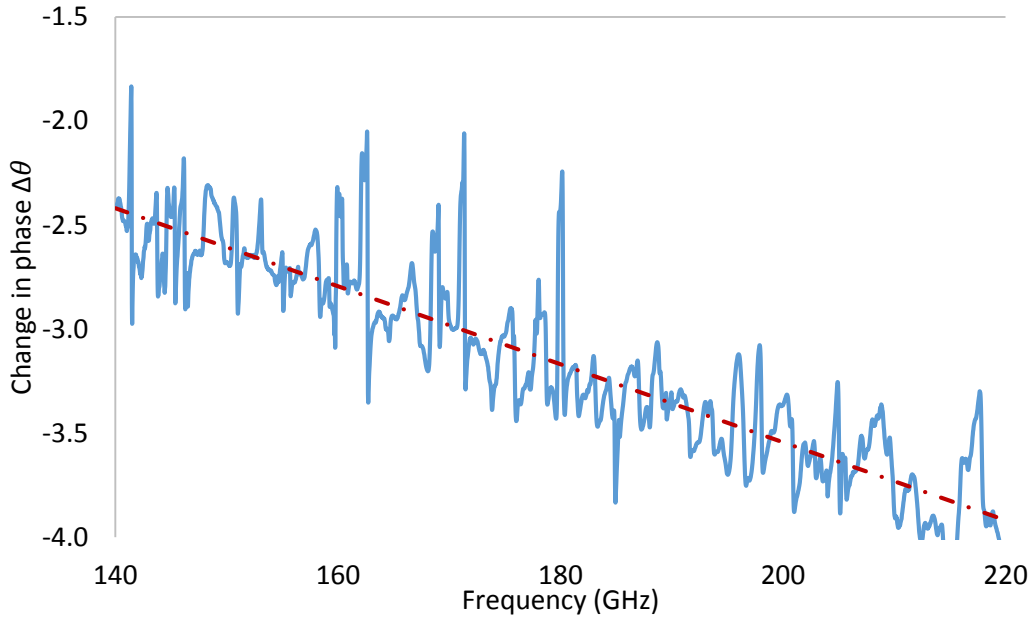

Figure 4.11.2.3. Change in phase for a signal travelling through the 0.76mm FR-4 dielectric compared to the phase measured for the same air distance. The line of best fit is marked by the red dashed line.

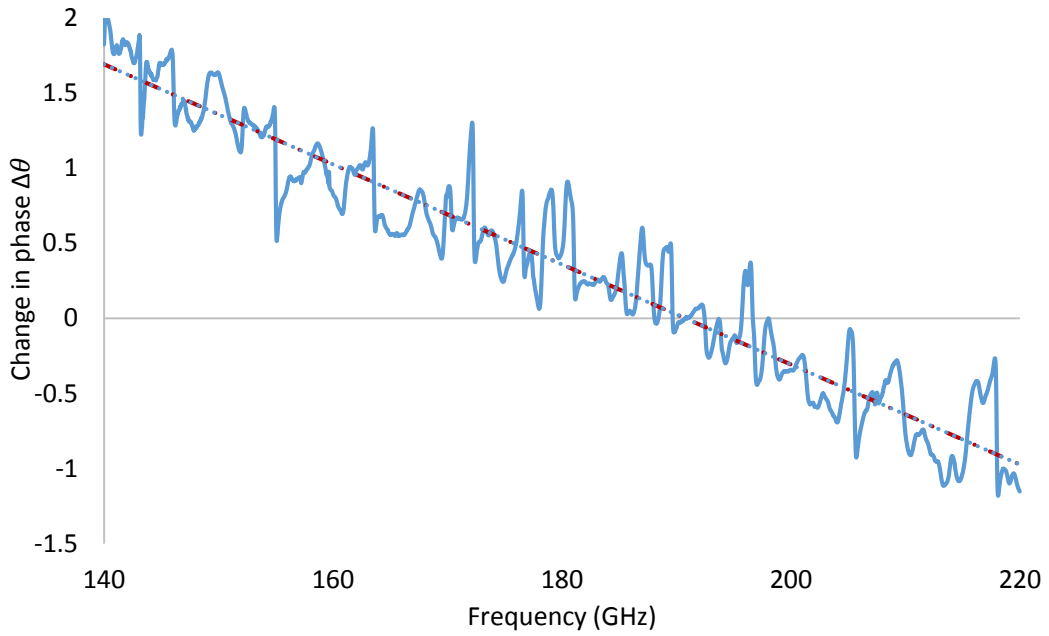

Figure 4.11.2.4. Change in phase for a signal travelling through the 1.43mm FR-4 dielectric compared to the phase measured for the same air distance. The line of best fit is marked by the red dashed line.

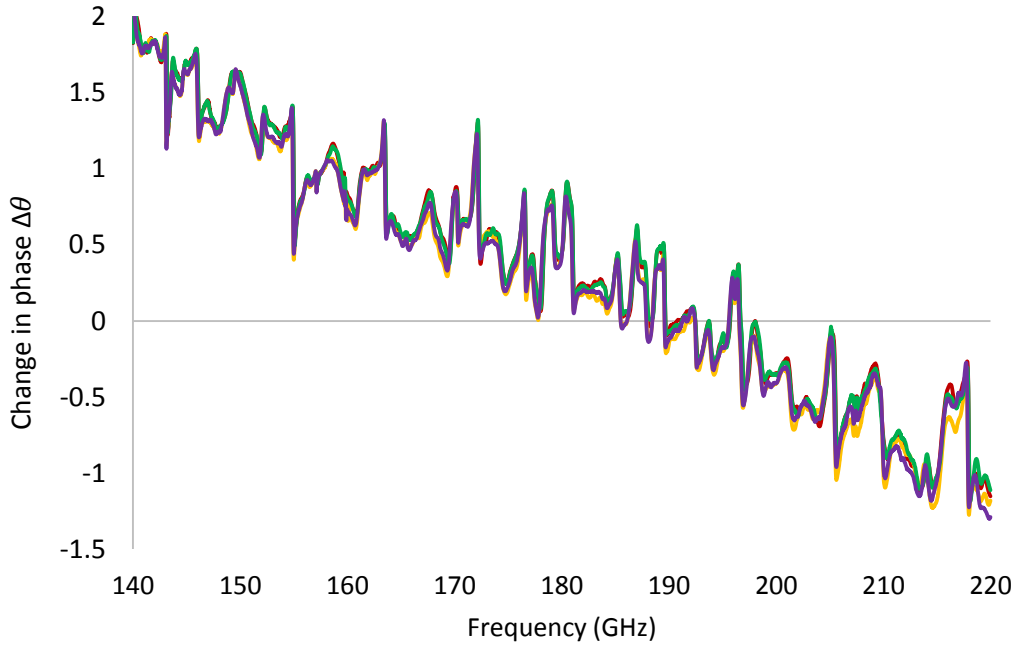

Figure 4.11.2.4. Change in phase for the 1.43mm FR-4 sample. The four overlaid plots demonstrate the reproducibility of the phase measurements. The error in the gradient of the line of best fit for the four measurements was found to be

Material	Dielectric Thickness (mm)	$\partial\Delta\theta/\partial$f	Refractive index n_d
FR-4	0.410±0.005	0.0119±0.0002	2.384±0.032
FR-4	0.762±0.005	0.0187±0.0002	2.252±0.019
FR-4	1.433±0.005	0.0333±0.0002	2.109±0.013

Table 4.11.1. Table of results listing the mean gradients and refractive indices with error margins for the measured dielectric samples.

4.12 Chapter Conclusions

Planar PSLs without substrates were manufactured using advanced laser etching techniques, with a view to studying the surface field exclusively. The chemical etching process used to fabricate the PSLs mounted on the FR-4 substrates (with and without the copper backing) was discussed. These structures are thought to be capable of supporting a volume mode, which under certain conditions, may couple with the PSL's surface field. A similar structure, scaled up to operate at the 325-500 GHz band, was presented and the construction of an "air-gap" structure based on one of the PSLs was described. Detailed images, including a 3D representation of the 325-500 GHz PSL, were obtained for the planar structures using a Hirox 3D imager. Some localised defects arising from non-uniform etching were observed. However, the structures' periodicity, measured using the Hirox imager and a travelling microscope, were found to coincide with the expected values with small uncertainty margins. Preliminary measurements demonstrated the importance of using compatible waveguide horns in order to avoid mode conversion. The measured output beam profiles of the G-band and WR2.2 horns used in the experiments, showed good agreement with the theoretical predictions, with optimum performance typically observed at the middle of the frequency band. Finally, two methods of measuring the refractive index of a dielectric sample were discussed. The Brewster angle method proved unsuccessful due to interference of the launching/receiving horn lobes. Measuring the phase in the dielectric, however, led to refractive indices of 2.38±0.03, 2.25±0.02 and 2.11±0.01 for the 0.41mm, 0.76mm and 1.43mm substrates respectively, demonstrating a significant variation between samples.

Chapter 5- Experimental Results for 2D Planar PSLs

5.1 Introduction

The experimental results for the 2D planar PSL structures are presented in this chapter. The results for the simplest structures, consisting of copper PSLs designed to study the surface field, are discussed in §5.2. Another layer of complexity is introduced in §5.3, where electromagnetic behaviour associated with the volume and surface fields is demonstrated for the set of PSLs mounted on the 0.76mm FR-4 substrates. When the copper backing is added, the PSLs etched onto the 0.76mm copper-backed substrates, studied in §5.4, are shown to facilitate coherent coupling between volume and surface fields. The reproducibility of these key results, which demonstrate coherent eigenmode formation, is established in §5.5.

Subsequent sections are devoted to the study of the PSLs etched onto the thinner 0.41mm (§5.6) and thicker 1.43mm (§5.7) substrates where further complex behaviour is observed. The effect of changing the dielectric boundaries is explored in §5.8. A reflection measurement of the higher frequency, 0.63mm structure (designed to operate at the 325-500 GHz frequency band) is presented (§5.9), confirming the scalability of this work. In §5.10 the 0.63mm PSL is measured at 140-220 GHz, where it better satisfies the metamaterial criterion, and exhibits unique EM properties. Finally, the role of the dielectric is investigated by measuring the “air-gap” structure, based on the 1.94mm PSL. Measurements made for different air separations are discussed in §5.11. To conclude, the main outcomes of this chapter are summarised in §5.12.

5.2 Planar PSLs without Substrates

Measurements were first made for simple PSLs with no dielectric or copper backing. These PSLs, with no well-defined waveguide boundaries to support volume waves, allowed exclusive study of the surface waves. For structures of this type, the ratio of the lattice period d_z to the wavelength λ determines whether or not the PSL will behave like a diffractive surface in the transverse direction. At normal incidence, the PSLs diffract radiation when $d_z/\lambda > 1$. However, when the PSLs are irradiated at θ_i >0°, the diffraction condition $\frac{2\lambda}{d_z}(1 + sin\theta_i) < 1$ applies. The PSLs with $d_z \approx \lambda$ therefore operate in the non-diffractive regime, where mesh structures such as the PSLs studied in this work, are known to behave like high-pass filters (Ulrich 1968,1976). This explains why no diffraction pattern was observed in the preliminary measurements conducted in §4.8.

Surface currents induced in the copper flow around each unit cell and are scattered by the lattice perturbations to produce a surface field which, in turn interferes with the reflected signal, resulting in a sharp resonance. Figure 5.2.1 demonstrates the reflection measurements for the set of PSLs without substrates at a fixed incident angle of 40°. The periodicity defines the resonant frequency of the PSL with larger periods corresponding to lower frequencies. The highest frequency resonance was observed for the 1.50mm PSL (red plot), while the lowest was measured for the 1.94mm PSL (purple plot).

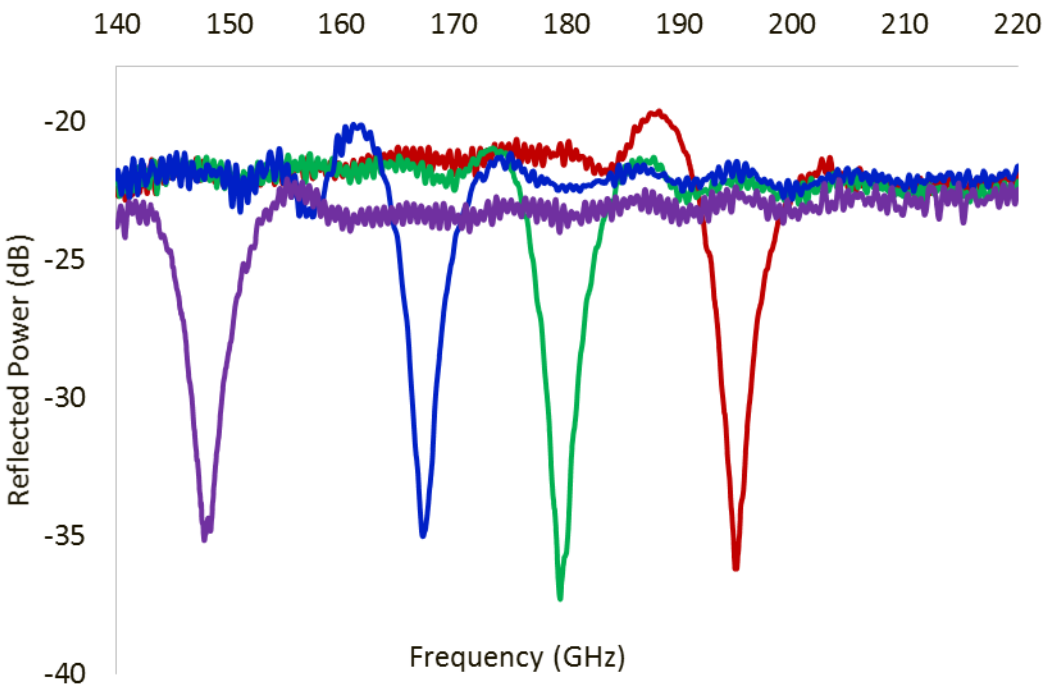

Figure 5.2.1 Reflection measurements at 40° for the set of copper PSLs (without substrates). The lattice periods are as follows: 1.50mm (red), 1.62mm (green), 1.74mm (blue) and 1.94mm (purple) at an incident angle of 40°. The resonant mode of the PSL shifts down the frequency band with increasing d_z.

Each lattice cell supports a surface field when $\lambda_s \cong d_z$. As an approximation, the PSL can be described as an array of rectangular waveguide apertures, where the reflected frequency lies close to the cut-off frequency of the fundamental $TE_{1,0}$ mode. Degenerate modes are neglected due to asymmetries associated with the fabrication of the PSLs. The periodicity of the lattice, however, is not the only factor in determining the operating frequency of the PSL which corresponds to the surface field's resonance. Figure 5.2.2 shows that the PSL resonances are also characterised by a strong angular dependence. For all four PSLs, the frequency of the resonance shifts down with increasing incident angle.

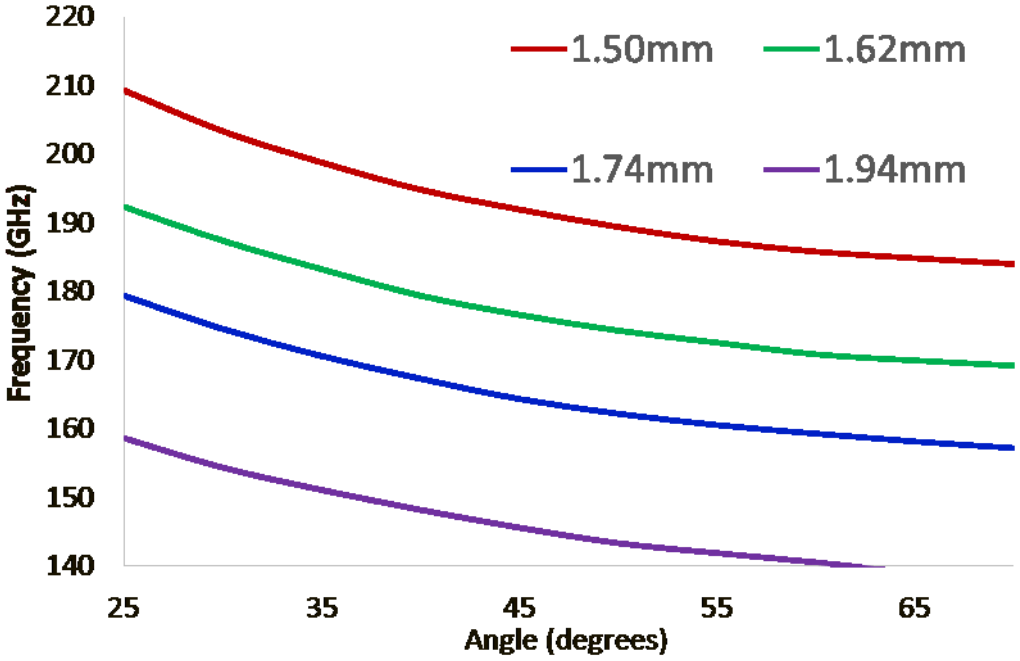

Figure 5.2.2. Reflection measurements made at different angles for the set of copper PSLs (without substrates). The lattice periods are as follows: 1.50mm (red), 1.62mm (green), 1.74mm (blue) and 1.94mm (purple).The resonant mode of the PSL shifts down the frequency band with increasing angle.

This may be attributed to a phase shift, introduced when θ_i >0°. The individual perturbations of the PSL oscillate slightly out of phase with one another. This phase shift is most pronounced when the signal strikes the structure at large angles. The reflection measurements for the set of PSLs, carried out over a range of incident angles from 25° to 65° are presented in figures 5.2.3-5.2.6. From these measurements it is observed that the resonances are typically sharper at large incident angles where they appear most constrained and shift to a lesser extent with increasing angle. For instance, figure 5.2.3 shows a frequency separation of 6.1 GHz between the resonances at 25° and 35° while a difference of just 0.85 GHz exists between those at 65° and 70°. The measured resonances are indicative of the PSL's surface field, and at lower incident angles (θ_i =30°- 35°) occur when $\lambda_s \cong d_z$.

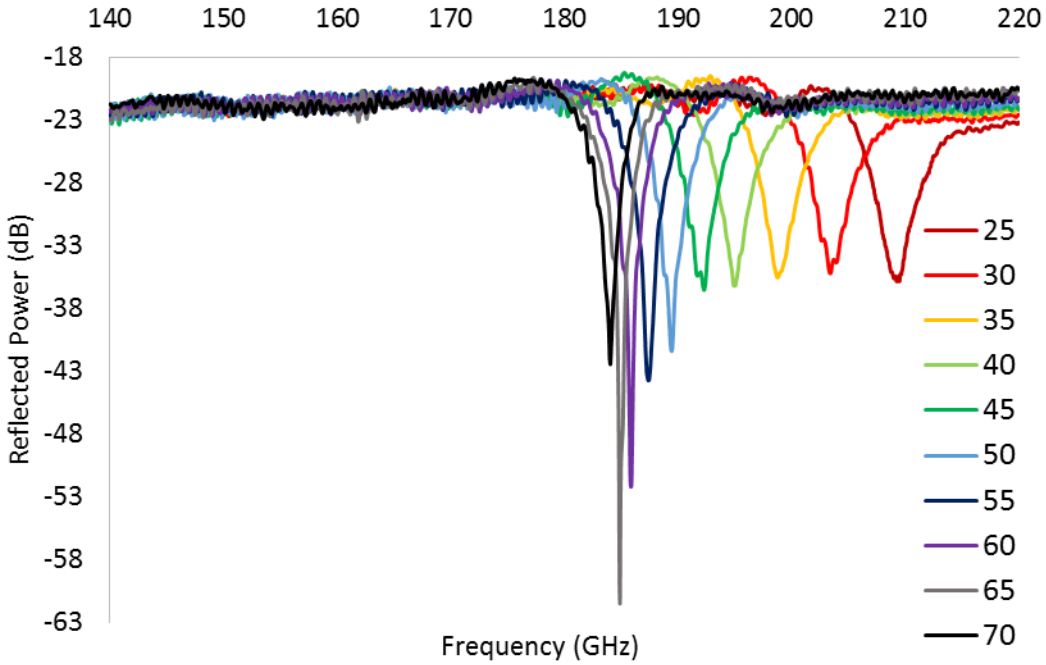

Figure 5.2.3. Reflected power for 1.50mm PSL without dielectric substrate for varying angle of incidence from 25° to 70°.

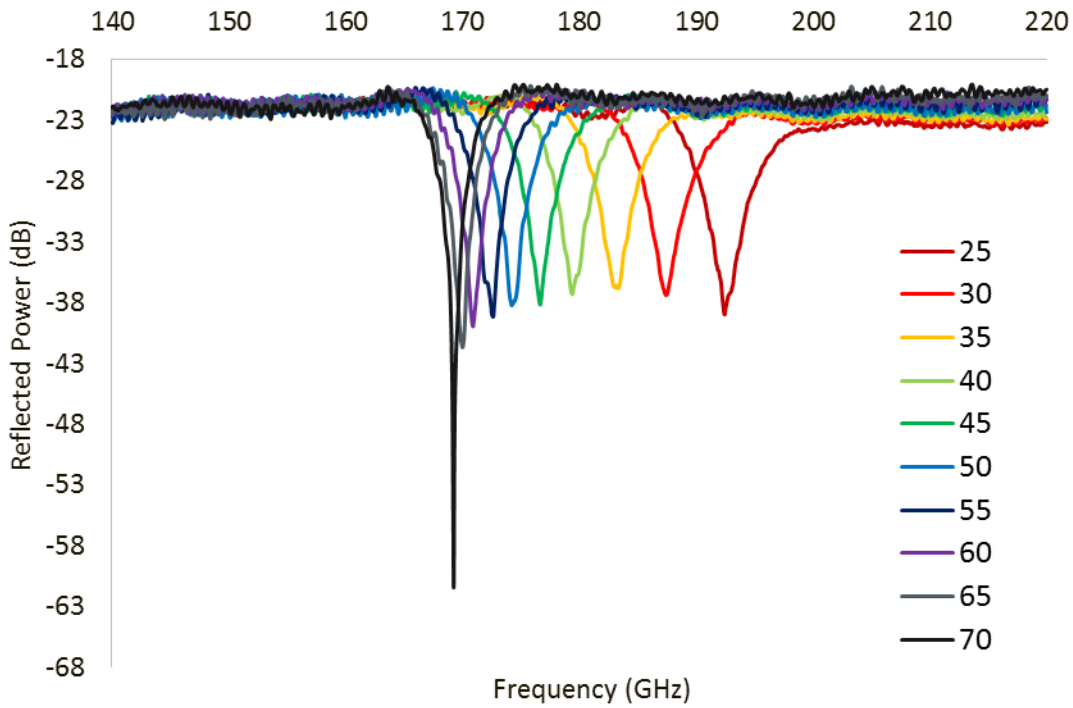

Figure 5.2.4. Reflected power for 1.62mm PSL without dielectric substrate for varying angle of incidence from 25° to 70°.

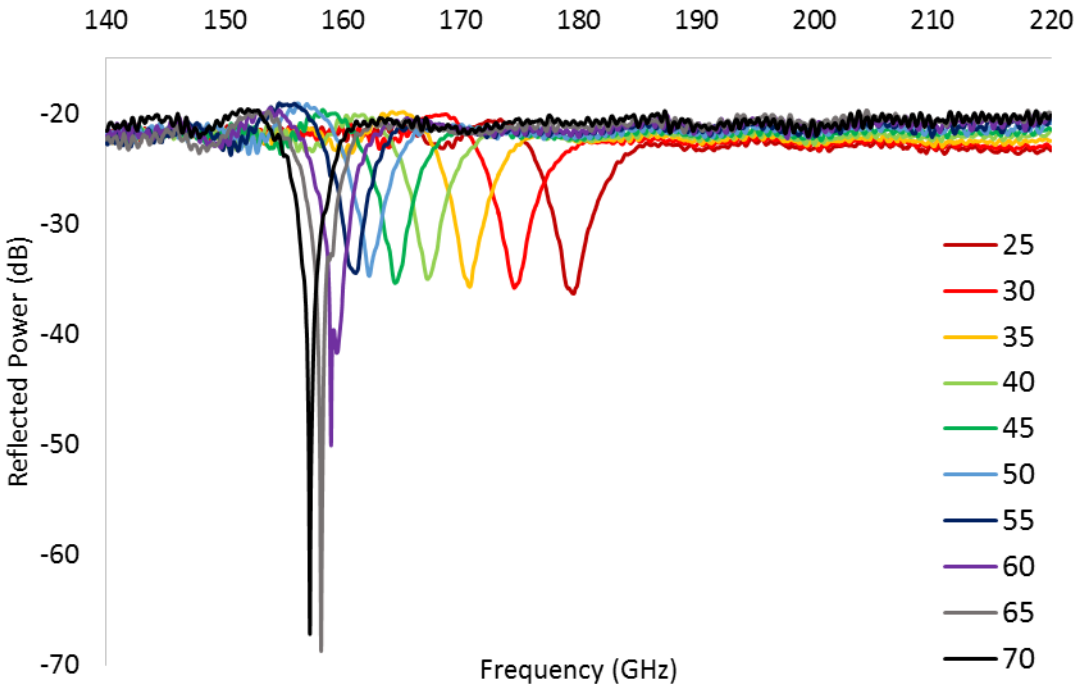

Figure 5.2.5. Reflected power for 1.74mm PSL without dielectric substrate for varying angle of incidence from 25° to 70°.

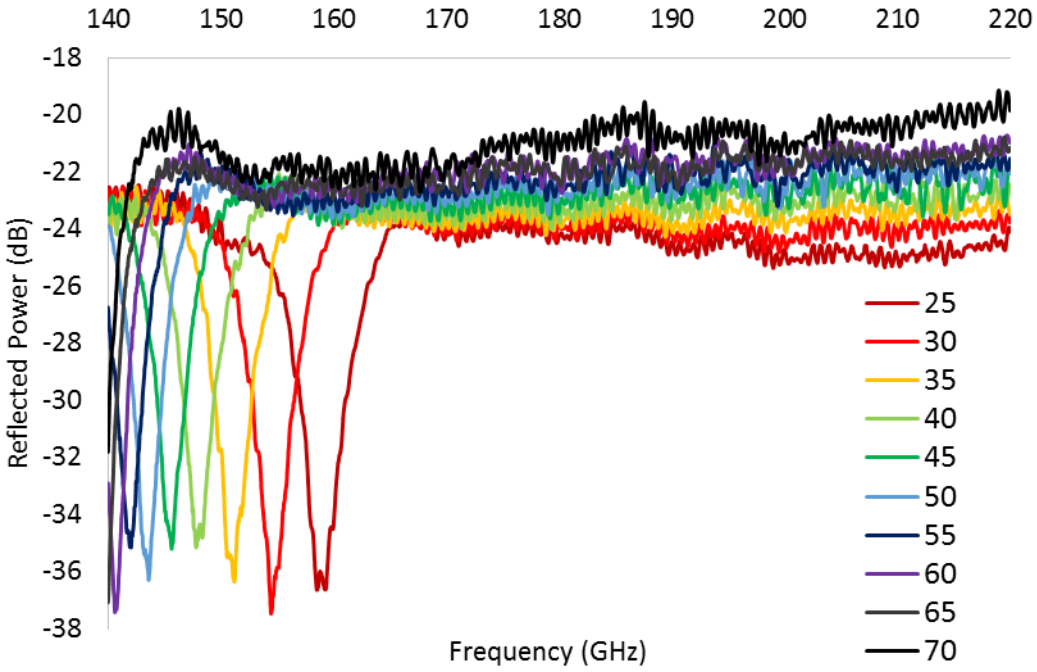

Figure 5.2.6. Reflected power for 1.94mm PSL without dielectric substrate for varying angle of incidence from 25° to 70°.

Transmission measurements were also made for the set of PSLs with no substrates. As expected, the transmitted frequencies of the structures were found to coincide with the reflected resonances demonstrated in figures 5.2.3-5.2.6. Figure 5.2.7 shows the transmitted power, over a range of incident angles from 10° to 80°, for the 1.94mm PSL. Close agreement is observed between the reflected and transmitted frequencies of figures 5.2.6 and 5.2.7.

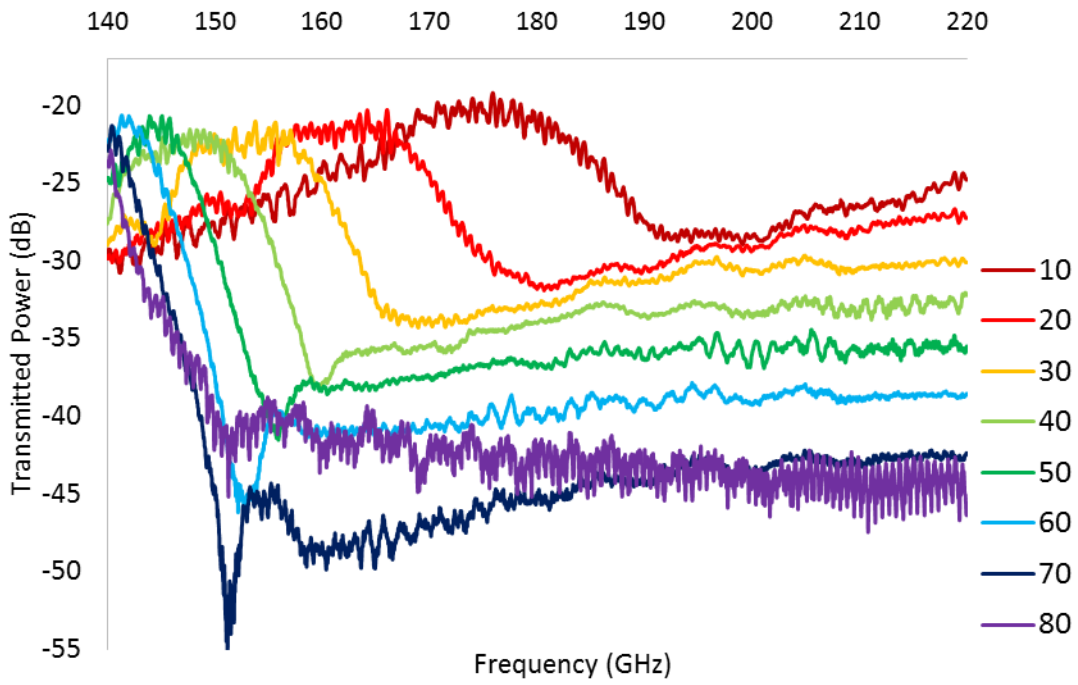

Figure 5.2.7. Transmitted power for the 1.94mm PSL without the dielectric substrate at varying angles of incidence (10° to 80°).

5.3 Planar PSLs with 0.76mm Substrates

Having investigated the EM response of the PSLs alone, measurements of the PSLs etched onto dielectric substrates (with no copper backing) were studied. Initially, the PSLs mounted on the 0.76mm FR-4 substrates (with $\varepsilon = 4.71$) were considered. Measurements of the PSLs etched onto the thinner (0.41mm) and thicker (1.43mm) substrates are presented later in this chapter (§5.6 and§5.7). Weak volume waves inside the dielectric are internally reflected when θ_i >26°. The inclusion of the lossy dielectric introduces experimental noise which significantly attenuates the field magnitude, particularly at larger incident angles.

Of the set of PSLs etched onto the 0.76mm substrates, the clearest results were obtained for the 1.62mm PSL, shown in figure 5.3.1. The surface field, most prominent at 25°, is comparable to that of the 1.62mm PSL alone (figure 5.2.4) with some deviation between the two results (~3GHz) at low incident angles. Further complex behaviour evident in figure 5.3.1 may be attributed to the presence of a volume field within the dielectric. This volume field is thought to be weakened by the lack of well-defined waveguide boundaries. Without the copper backing, the unbound volume field is less effective at synchronising the PSL, as required for coherent radiation. Weak reflection at the back surface of the dielectric, however, may still facilitate weak coupling between volume modes and the surface mode of the PSL.

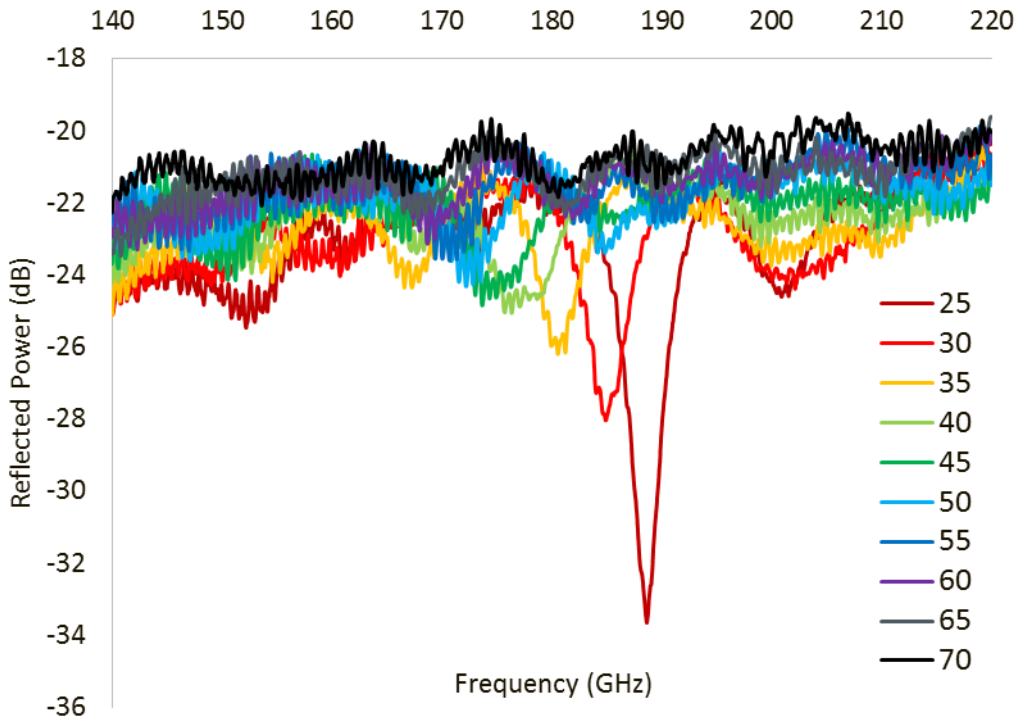

Figure 5.3.1 Reflected power for 1.62mm PSL with 0.76mm dielectric substrate (without copper backing) over a range of incident angles from 25° to 70°.

Throughout the duration of the experiment, measurements were repeated on separate occasions, with a period of several months between each measurement. The experimental set-up was completely dismantled and reassembled on each occasion, and the VNA was recalibrated for each set of measurements. The collective

reproducibility of the set of structures (excluding the PSLs mounted on the 0.76mm copper-backed substrates which are discussed in §5.4-§5.5) was found to be $\pm$ 0.8 GHz (frequency) and $\pm$ 2 dB (magnitude). These error margins were calculated by evaluating the standard deviation of the mean for each resonance, and choosing the largest values to give an overall error approximation. The uncertainty associated with the angular resolution of the scanning platform is covered by the frequency uncertainty. The quoted magnitude instability of the 140-200 GHz VNA modules is $\sim \pm 0.25$ dB, which is negligible in comparison to the magnitude uncertainty associated with the experimental alignment.

Figure 5.3.2 shows three overlaid plots (dotted, dashed and solid lines), measured on three separate occasions, for the 1.62mm PSL with the 0.76mm substrate at low incident angles ($\theta_i \leq 40°$) where the resonances are best defined. The results demonstrate good reproducibility between the measurements.

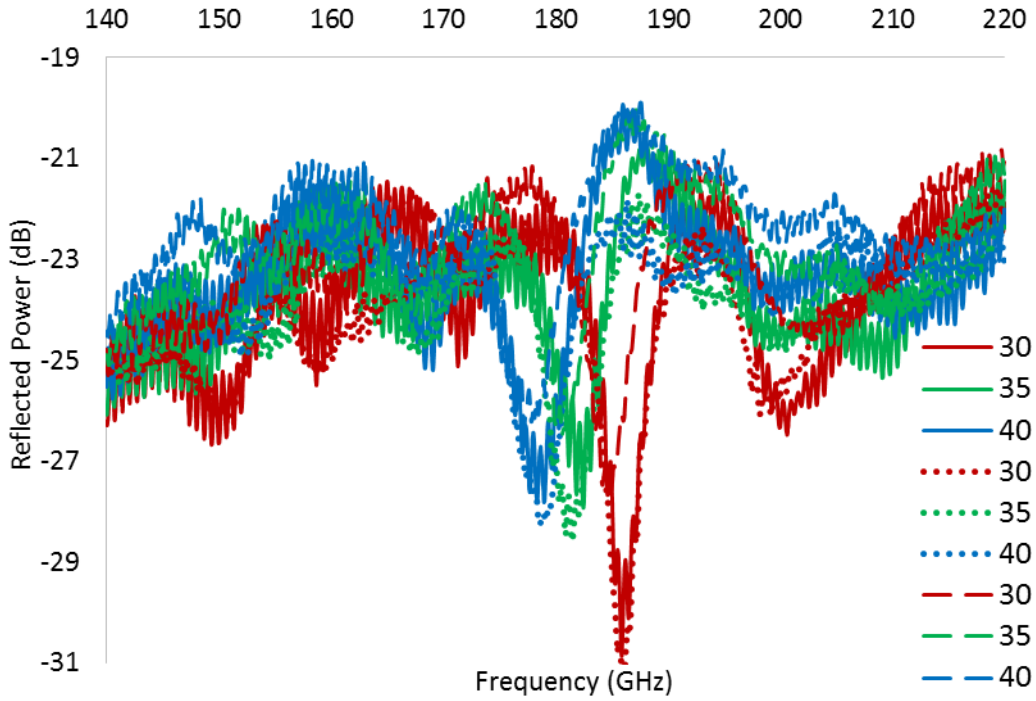

Figure 5.3.2. Reflection measurements for the 1.62mm PSL with 0.76mm substrate without copper backing. Results have been measured on three separate occasions (dotted, dashed and solid lines) to demonstrate the repeatability of the results.

Having established the reproducibility of the measurements, the results of figure 5.3.2 are studied at a fixed angle in order to interpret some of the structure's complex behaviour. Four distinct resonances are identified in figure 5.3.3a, which shows the reflected power for the 1.62mm PSL with the 0.76mm substrate at an incident angle of 35°. The trace provided in figure 5.3.3.b shows the surface field (resonance 3) annotated with error bars to illustrate the $\pm$ 0.8 GHz frequency uncertainty. A similar plot is shown in figure 5.3.3.c, where the shaded region demonstrates the $\pm$ 2dB magnitude uncertainty.

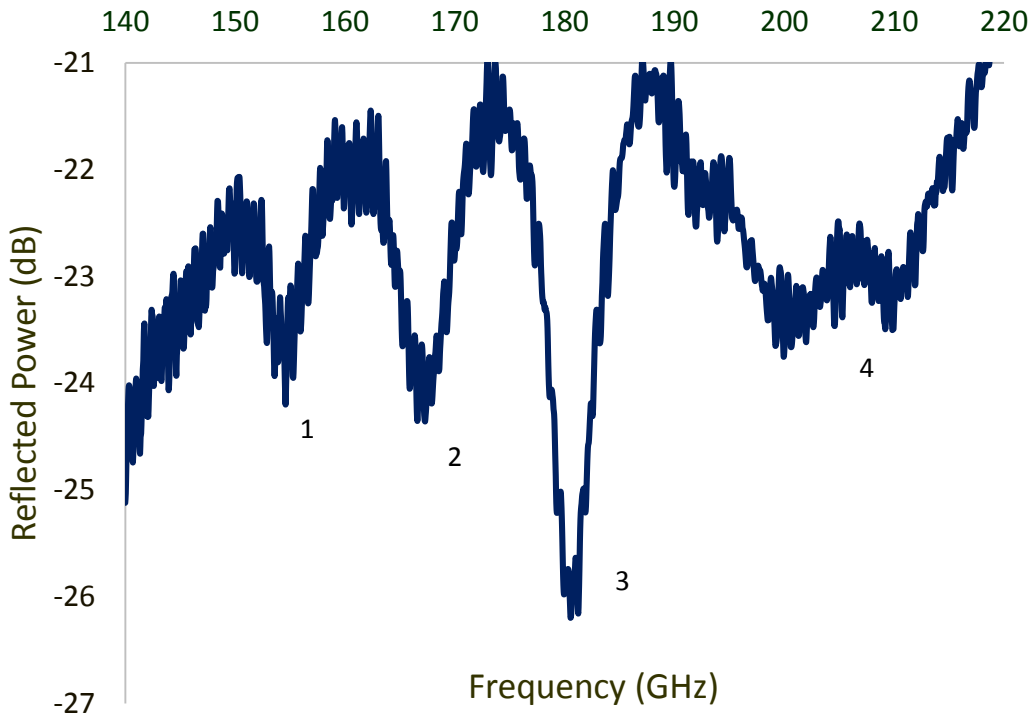

Figure 5.3.3a. Reflected power for 1.62mm PSL with 0.76mm dielectric substrate (without copper backing) at an incident angles of 35°.

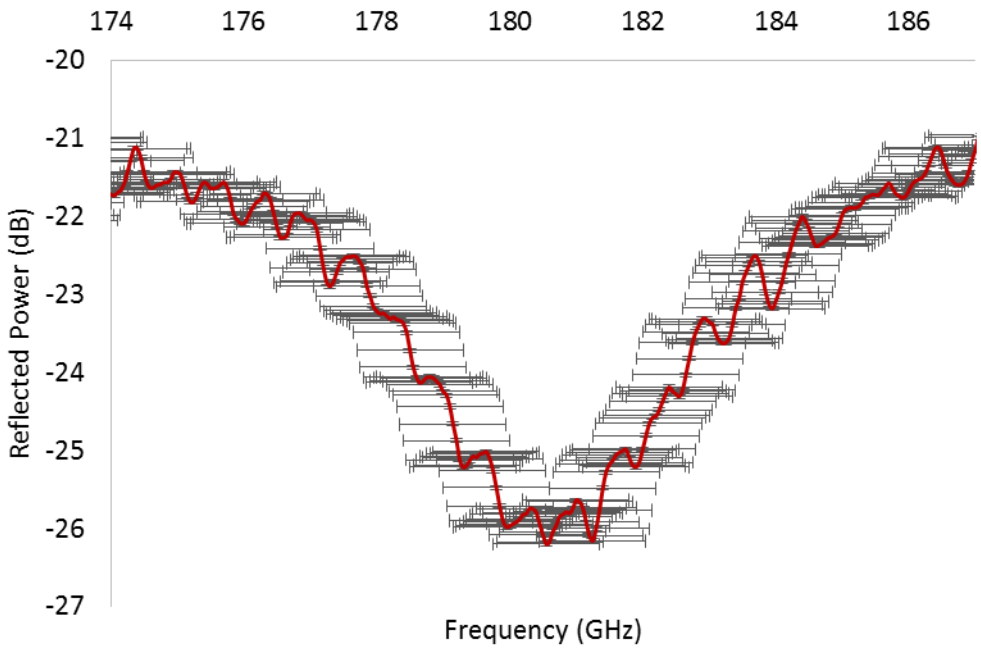

Figure 5.3.3.b. Plot showing ±0.8 GHz frequency uncertainty error bars for the surface field (resonance 3) of the 1.62mm PSL mounted on the 0.76mm dielectric substrate (without copper backing) at an incident angles of 35°.

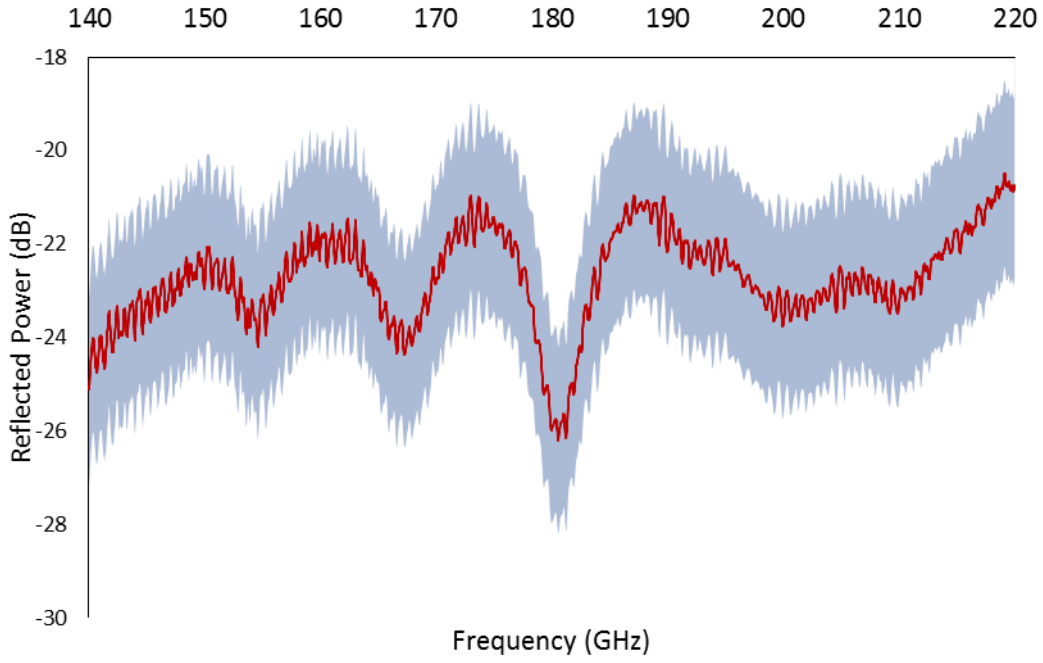

Figure 5.3.3.c. Plot showing ±2 dB magnitude uncertainty (shaded region) for the 1.62mm PSL mounted on the 0.76mm dielectric substrate (without copper backing) at an incident angles of 35°.

Resonance 1 may indicate a possible volume mode existing within the dielectric while resonance 2, which lies almost exactly between 1 and 3, may represent weak coupling between the volume and surface modes, facilitated by weak reflection at the dielectric boundary. Earlier in this section, figure 5.3.1 showed the uppermost resonance (4) shifting up with increasing angle, in the opposite direction to the others. This behaviour is most prominent in the PSLs with larger periodicities and is similar to that observed in a Fabry-Perot cavity. For example, measurements of the 1.74mm PSL (figure 5.3.4) show possible Fabry-Perot resonances that are comparable in magnitude to the PSL's surface field. Likewise, for the 1.94mm PSL (figure 5.3.5) the Fabry-Perot behaviour appears to dominate over the surface field of the PSL. Some similarities exist between the reflection measurements of the 1.94mm PSL etched onto the 0.76mm substrate (figure 5.3.5) and the 0.76mm FR-4 sample alone (figure 5.3.6). In both cases, the Fabry-Perot resonance manifests around 185 GHz at θ_i =30° and shifts up in frequency as the incident angle in increased.

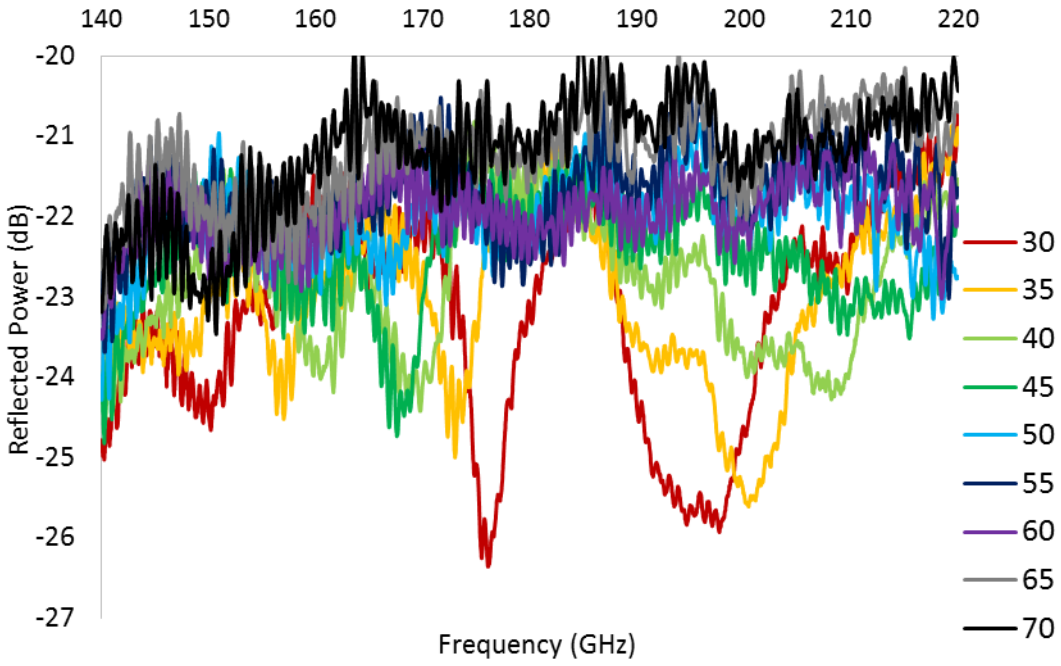

Figure 5.3.4. Reflection measurement for the 1.74mm PSL with the 0.76mm dielectric substrate (without copper backing) over a range of incident angles from 30° to 70°.

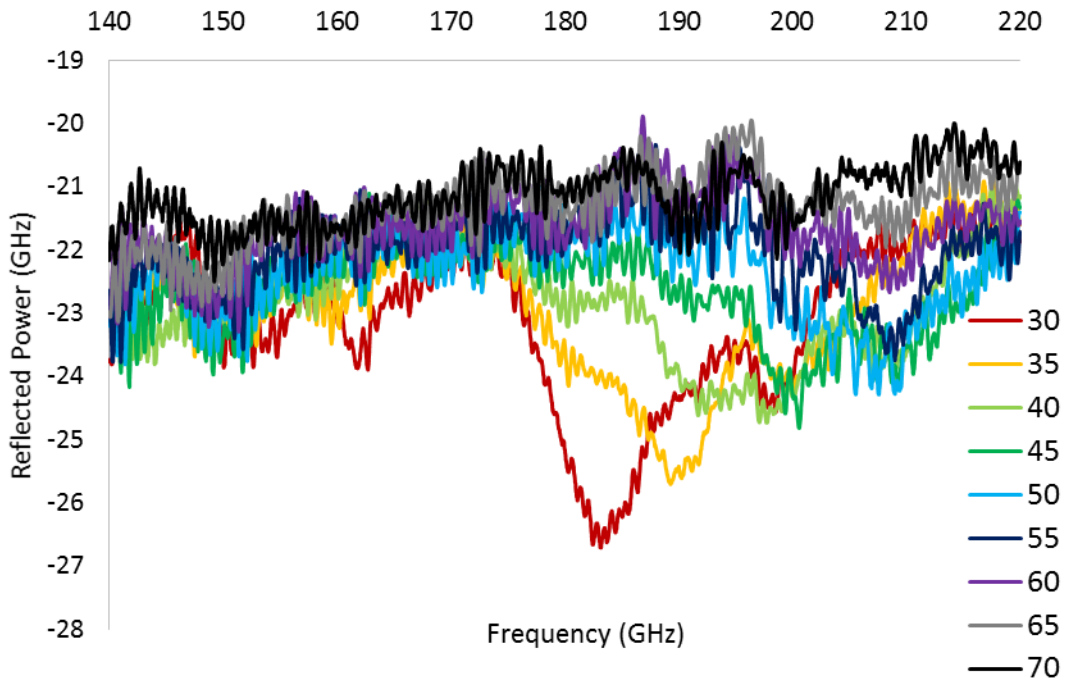

Figure 5.3.5. Reflection measurement for the 1.94mm PSL with the 0.76mm dielectric substrate (without copper backing) over a range of incident angles from 30° to 70°.

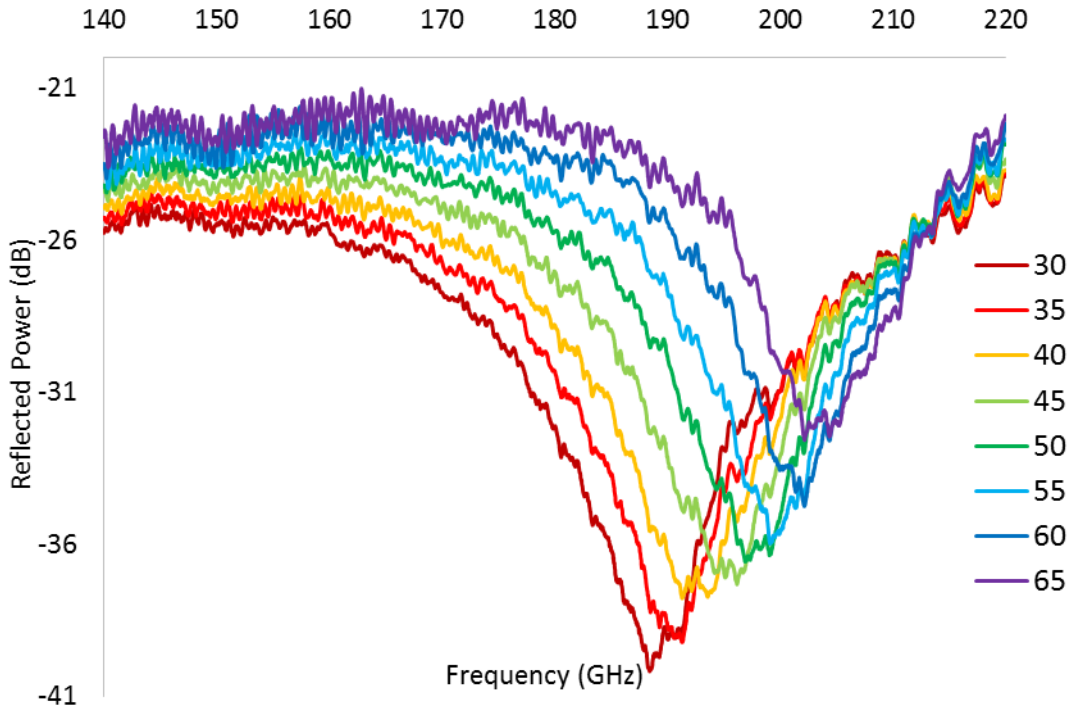

Figure 5.3.6 Reflection measurements for the 0.76mm dielectric (FR-4) sample. The results show possible Fabry-Perot resonances that shift up in frequency with increasing incident angle.

5.4 Eigenmode Formation in Planar PSLs with 0.76mm Copper-backed Substrates

Introducing the copper backing further changes the EM properties of the structure. Under certain conditions, and when the PSL is assembled like a Fabry-Perot cavity (with the PSL acting as one of the mirrors and the copper backing acting as the second) coupling between volume and surface modes can take place, leading to the formation of a cavity eigenmode. The copper backing facilitates coupling by increasing the quality of the cavity structure and better synchronising the modes. When the lattice is properly synchronised by the volume mode trapped inside the dielectric, the resulting resonance appears to be locked at a particular frequency, irrespective of the incident angle.

Reflection measurements showing coherent eigenmode formation for the set of PSLs mounted on copper-backed 0.76mm FR-4 substrates are presented in figures 5.4.1-5.4.4. Although the position of the eigenmode still varies with the PSL's periodicity, the measured resonances appear within a narrow frequency range (~145-165 GHz). Unlike previous measurements of the PSL and substrate, where multiple resonances were identified, a single well-defined resonance is observed, indicative of coherent cavity eigenmode formation. The coupling of volume and surface takes place at a specific frequency and dominates over other competing behaviour.

For all the PSLs, the 'mode-locking' associated with the formation of the coupled eigenmode is most effective at higher incident angles. For example, measurements of the 1.50mm PSL show an angular dependence at 30° and 35°. However, it is noted that the resonances are moving up with increasing angle, in the opposite direction to before, indicating that the strong coupling, facilitated by the copper backing, alters the behaviour of the structure at all incident angles. For the set of PSLs mounted on the 0.76mm copper backed structures, mode-locking is best observed at angles above 40°, possibly due to a decreased frequency separation between the uncoupled volume and surface fields at higher angles. The mode-locking illustrated in figures 5.4.1-5.4.4 demonstrates the principle of mode selection in an over-sized structure.

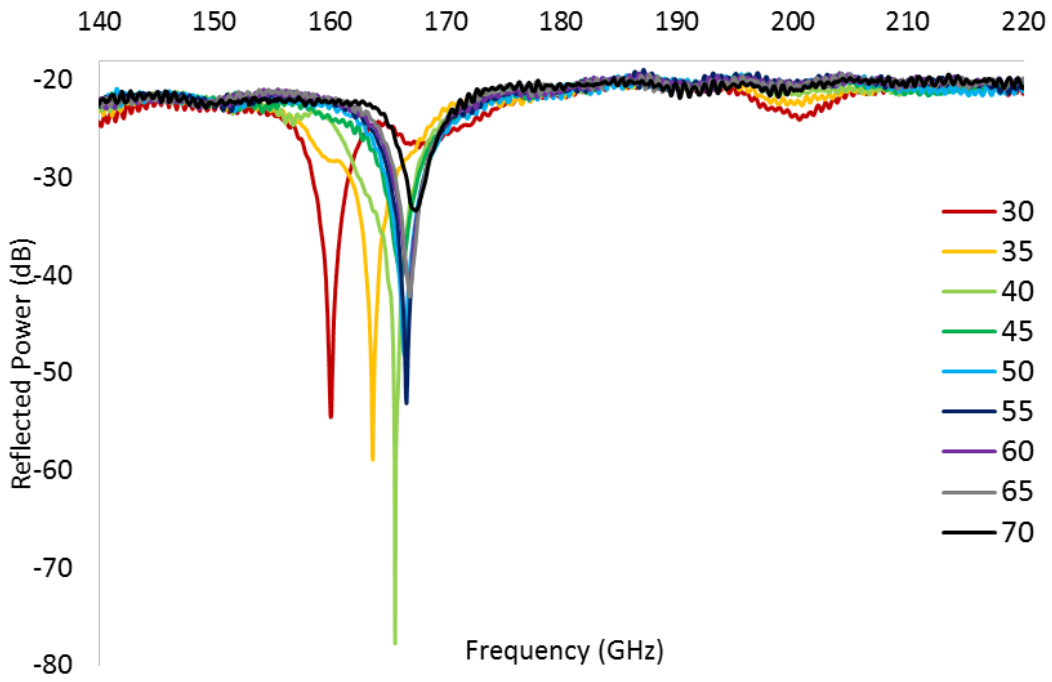

Figure 5.4.1. Coherent, coupled eigenmode formation observed for the 1.50mm PSL etched onto the 0.76mm copper backed substrate

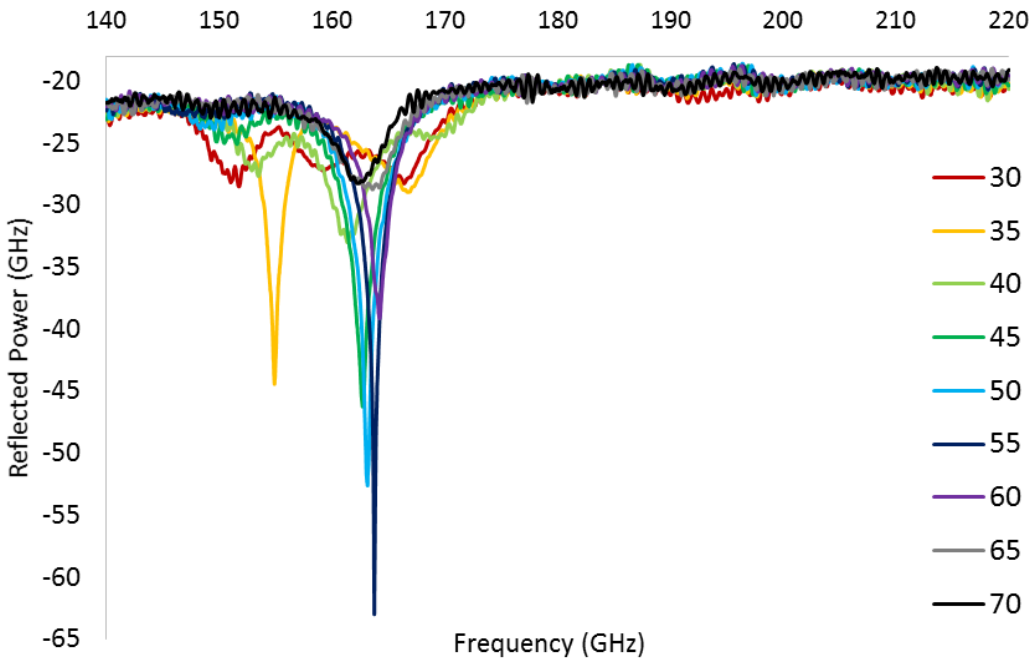

Figure 5.4.2. Coherent, coupled eigenmode formation observed for the 1.62mm PSL etched onto the 0.76mm copper backed substrate

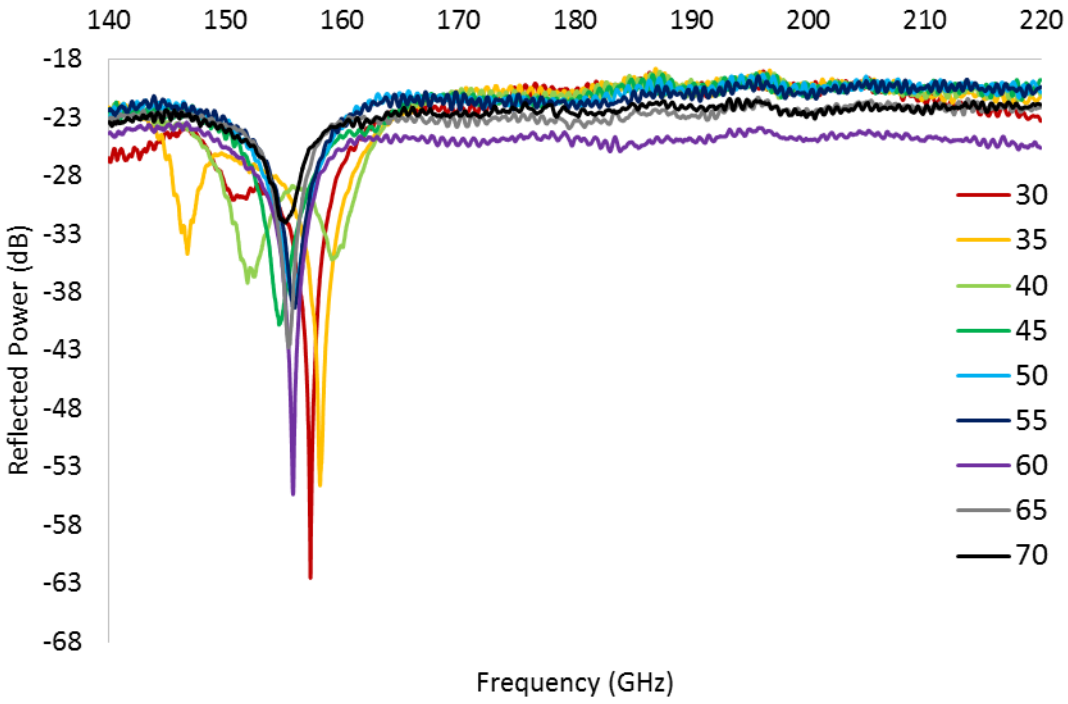

Figure 5.4.3. Coherent, coupled eigenmode formation observed for the 1.74mm PSL etched onto the 0.76mm copper backed substrate

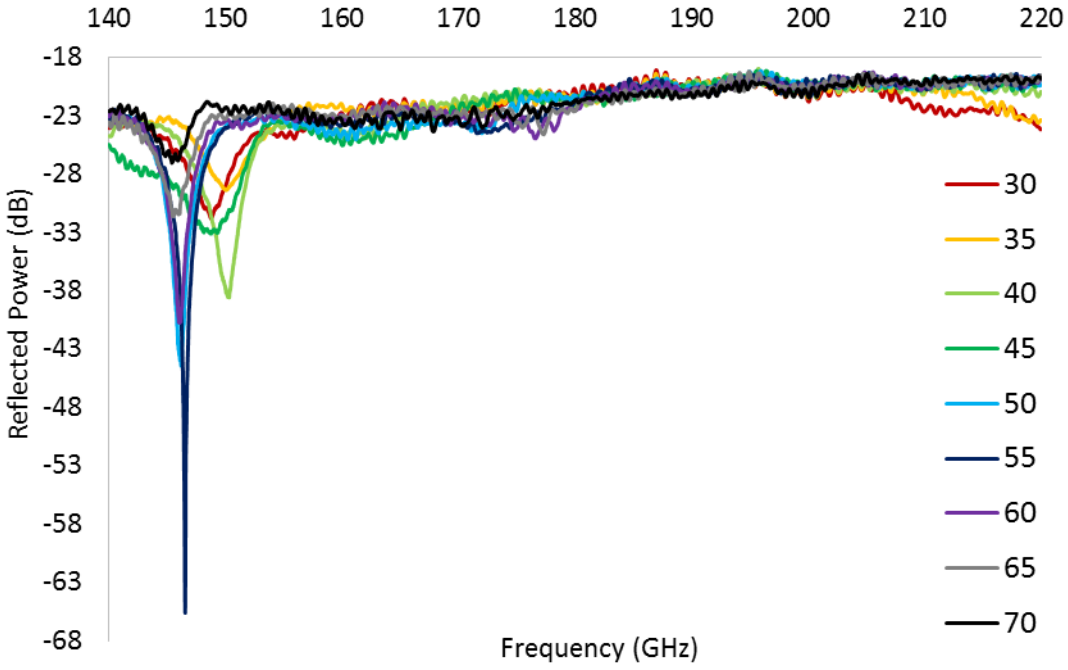

Figure 5.4.4. Coherent, coupled eigenmode formation observed for the 1.94mm PSL etched onto the 0.76mm copper backed substrate.

5.5 Reproducibility of Coherent Eigenmode Formation Measurements

The demonstration of coherent, high Q eigenmode formation in the planar PSLs is the main focus of this work, and it was therefore important to prove the reproducibility of these results. In doing so, the experimental set-up was completely re-assembled and the VNA measurements were repeated on three separate occasions spread over intervals of months. During this period, the experimental set-up evolved to allow faster and more reliable measurements. Replacing the original wooden scanning platform with an updated Perspex set-up led to improved alignment between the VNA heads and the PSL sample, increasing the precision of the angular measurements.

The three overlaid traces of figure 5.5.1, made on three separate occasions, illustrate the reproducibility of the 1.62mm PSL (mounted on the 0.76mm copper-backed substrate) when measured at an incident angle of 35°. The results, which exhibit a high degree of reproducibility ($\pm$0.3GHz) in frequency, confirm that mode-locking is less effective at lower incident angles, where two and in some cases three, resonances are observed. As stated previously, this may be due to a larger frequency separation between the volume and surface fields at lower incident angles. The $\pm$0.3GHz frequency uncertainty for the mode-locked structures (§5.4) is lower than the uncertainty quoted for the set of structures as a whole ($\pm$0.8GHz).

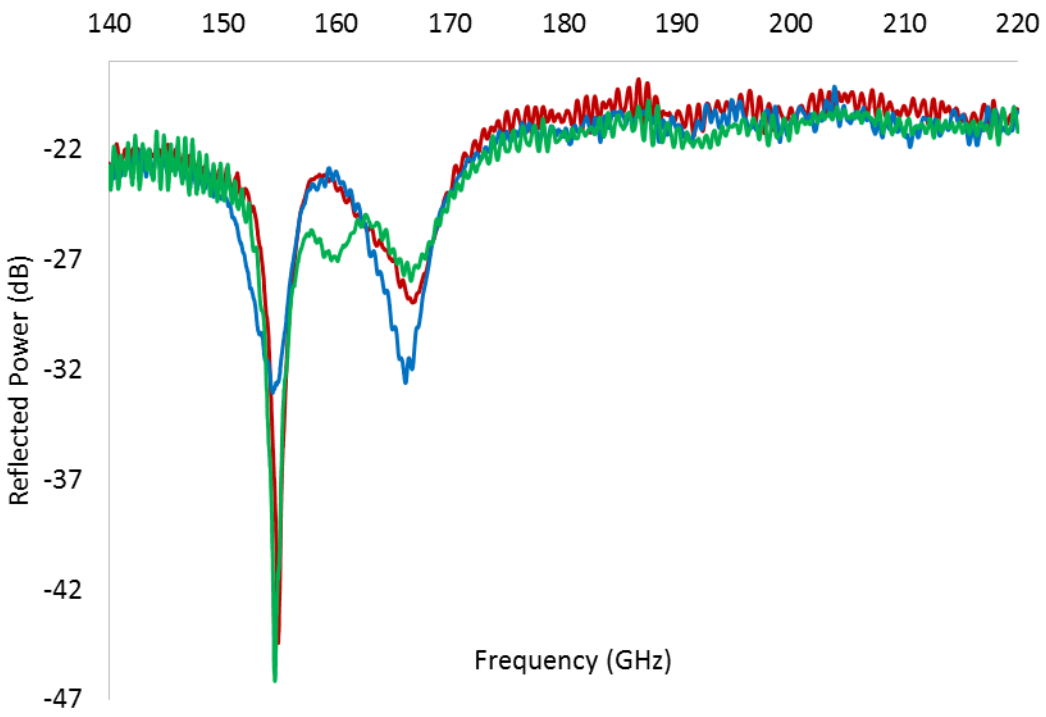

Figure 5.5.1. Reflected power for the 1.62mm PSL etched onto the 0.76mm copper backed substrate. The measurement was repeated on 3 separate occasions, with several months between measurements to establish the reproducibility of the results.

The reproducibility of the magnitude ($\pm$16dB) is poor in comparison, as shown by the large fluctuation in the reflected power measurements. Figure 5.5.2 shows the same, 1.62mm PSL structure measured at an incident angle of 45° on three separate occasions. The black plot demonstrates a high-Q cavity mode, with a reflected power of ~-75dB, while the blue plot illustrates a comparatively weak ~-37dB resonance. Precise alignment is essential to achieve optimum power response, and the construction of a higher precision set-up may improve the magnitude stability of the results.

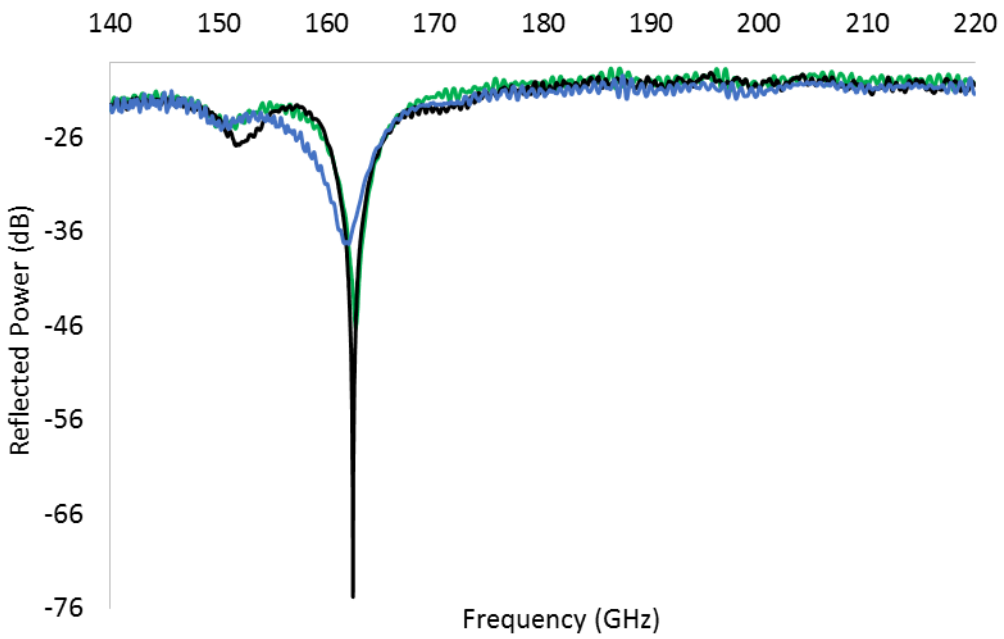

Figure 5.5.2. Comparison of 3 separate measurements for the 1.62mm PSL with the copper-backed 0.76mm FR-4 substrate at an incident angle of 45°

The error bars included in figure 5.5.3 demonstrate the frequency uncertainty in the coupled, mode-locked eigenmode of the 1.50mm PSL mounted on the 0.76mm copper backed substrate at 40°. The large ±16dB magnitude uncertainty is illustrated by the shaded region of figure 5.5.4.

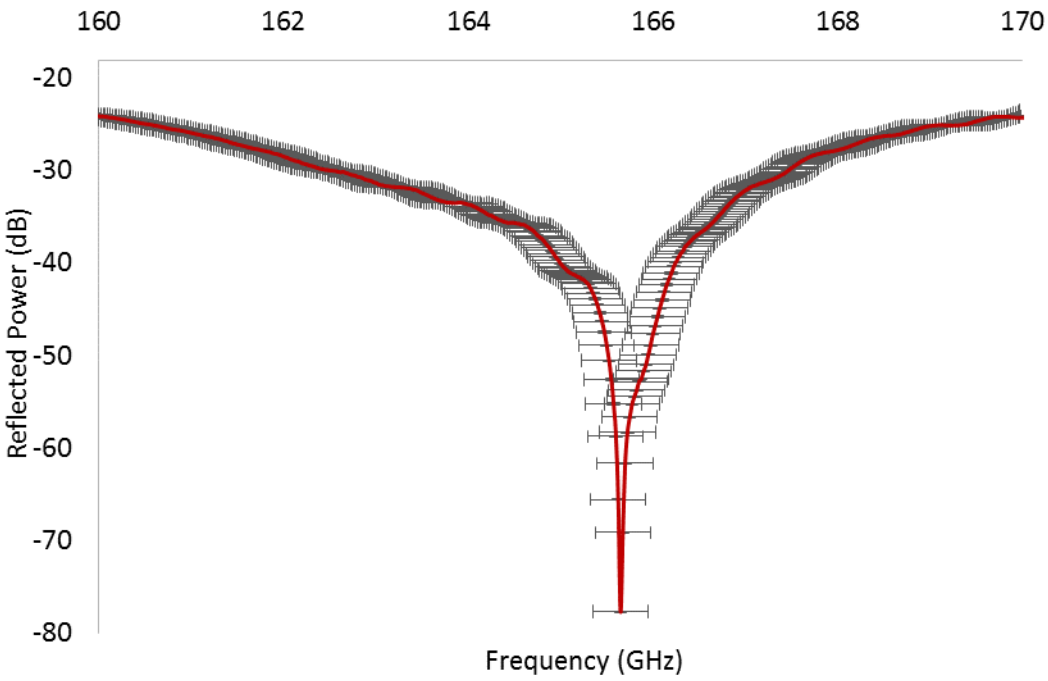

Figure 5.5.3. Plot demonstrating the ±0.3GHz frequency uncertainty for the coupled, mode-locked eigenmode of the 1.50mm PSL mounted on the 0.76mm copper backed substrate at 40°.

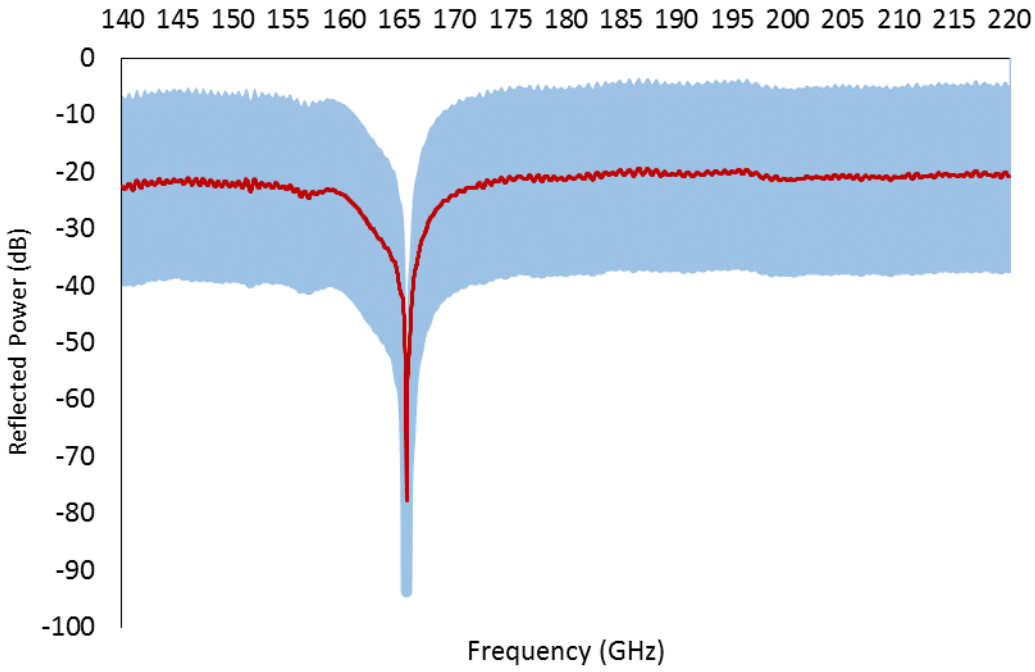

Figure 5.5.4. Plot demonstrating the ±16dB magnitude uncertainty (shaded region) for the coupled, mode-locked eigenmode of the 1.50mm PSL mounted on the 0.76mm copper backed substrate at 40°.

5.6 Planar PSLs with 0.41mm Substrates

The effect of decreasing the dielectric thickness, thereby reducing the number of half wavelengths inside the substrate, was studied for the set of PSLs etched onto 0.41mm substrates, with and without the copper foil backing. The reflection measurements for each case are presented in §5.6.1 and §5.6.2.

5.6.1 Planar PSLs with 0.41mm Substrates (no copper backing)

The set of PSLs mounted on the 0.41mm substrates without the copper backing are considered in this section. For the structures of this type with ε=5.69, total internal reflection is expected to occur at the air/ dielectric interface when θ_i >25° and may facilitate weak coupling by confining some of the field within the dielectric. Reflection measurements for the 1.50mm PSL etched onto the 0.41mm substrate are provided in figure 5.6.1.1.

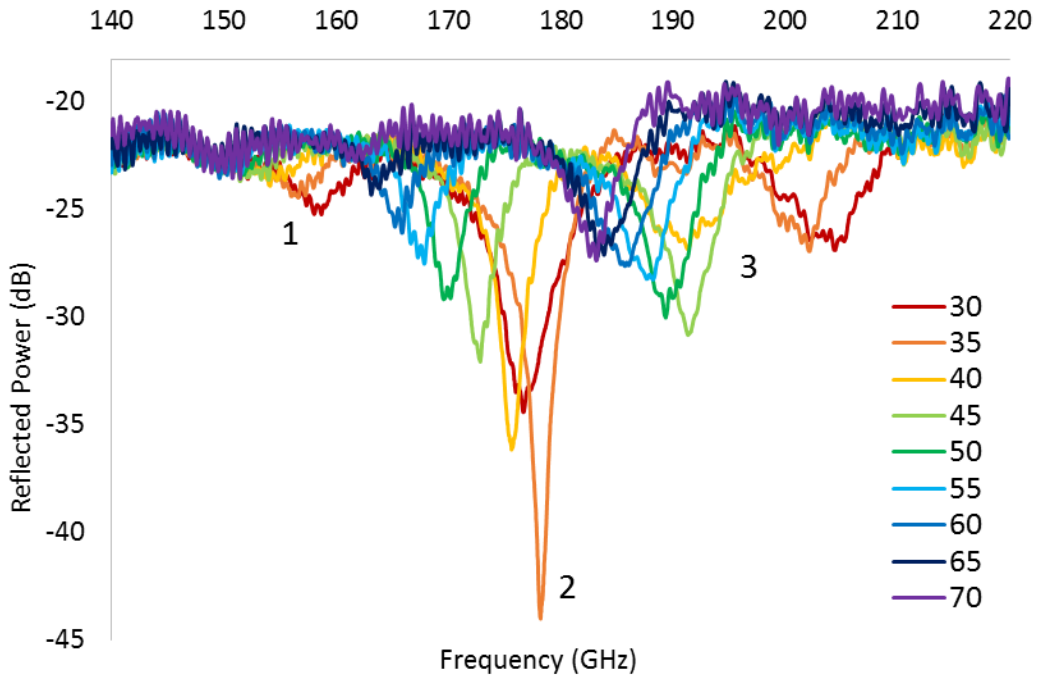

Figure 5.6.1.1. Reflection measurements for the 1.50mm PSL etched onto the 0.41mm dielectric substrate (without copper backing) at incident angles of 30° to 70°.

Three distinct resonances are identified. Resonance 1 represents a mode inside the dielectric with a clear angular dependence. The frequency position of the second resonance (2) (which matches the coupled eigenmode of figure 5.4.1 when θ_i ≥55°)

is suggestive of weak scattering between the volume and surface fields. Unlike the coherent eigenmode observed in §5.4, this resonance is not mode locked, and therefore varies with angle. Phenomena, such as weak reflection at the dielectric boundary and total internal reflection, may confine some of the field within the dielectric, contributing to the formation of a weakly coupled eigenmode.

The highest frequency resonance (3) represents the surface field of the PSL. Figure 5.6.1.2 compares the surface field of the present structure (solid lines) to that of the 1.50mm PSL with no substrate shown in figure 5.2.3 (dashed lines), when $\theta_i \geq 45°$. Despite the large disparity in magnitude, the two sets of results demonstrate good frequency agreement as anticipated.

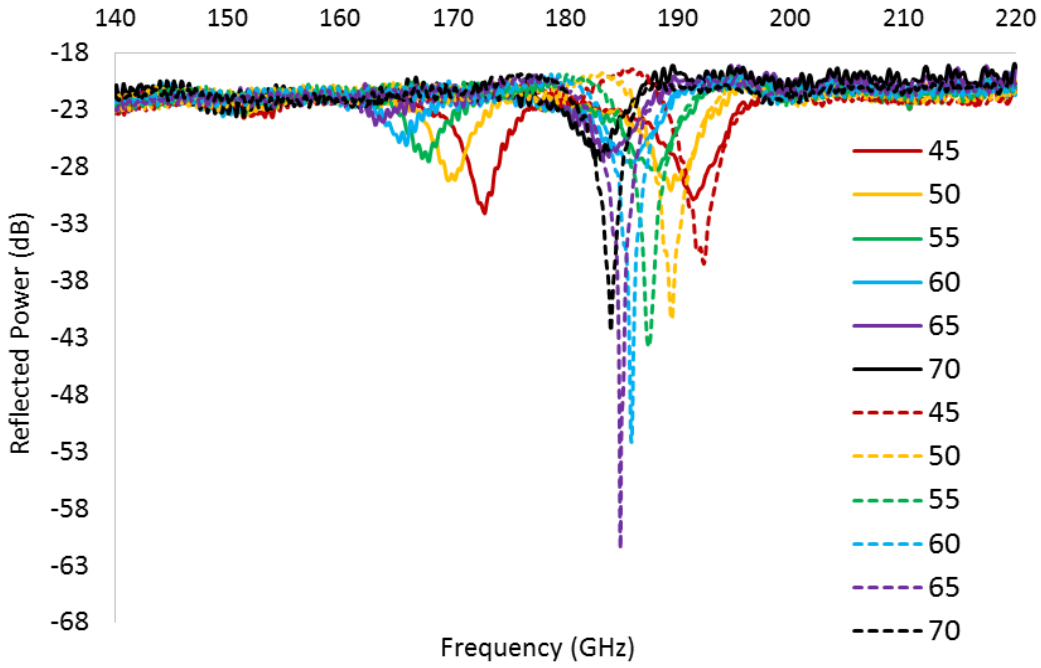

Figure 5.6.1.2. Comparison of reflection measurements of the 1.50mm PSL etched onto the 0.41mm substrate (solid lines) and the 1.50mm PSL without the substrate (broken lines) at incident angles of 45° to 70°.

Similar behaviour is observed for the 1.62mm PSL (mounted on the 0.41mm substrate) where three resonances exist within the measured frequency band (figure 5.6.1.3 -5.6.1.4). All three resonances are best-defined at higher incident angles and, for clarity, the results are studied at $\theta_i \geq 40°$ as plotted in figure 5.6.1.4. The weakest resonance (1), may represent a weakly defined volume mode within the dielectric. It

is worth noting that this may contribute to the sharp, low frequency resonance observed in the following section (figure 5.6.2.2). Once again, resonance 2, which is formed around 160-170 GHz, may correspond to a weakly coupled eigenmode that lies between the mode inside the dielectric (1) and the surface field (3) of the 1.62mm PSL.

As the lattice period is increased to 1.94mm (figure 5.6.1.5), all three resonances are further shifted down the frequency band, suggesting that the lattice period influences the volume field as well as the surface field. The 1.94mm PSL exhibits significant experimental noise. In this case it is difficult to distinguish possible eigenmode formation from the PSL's surface field, as the two phenomena, which manifest at similar frequencies, may coincide with one another. The resonance at ~150 GHz, however, appears fixed at its lower edge, suggesting possible mode locking and incoherent eigenmode formation at this frequency.

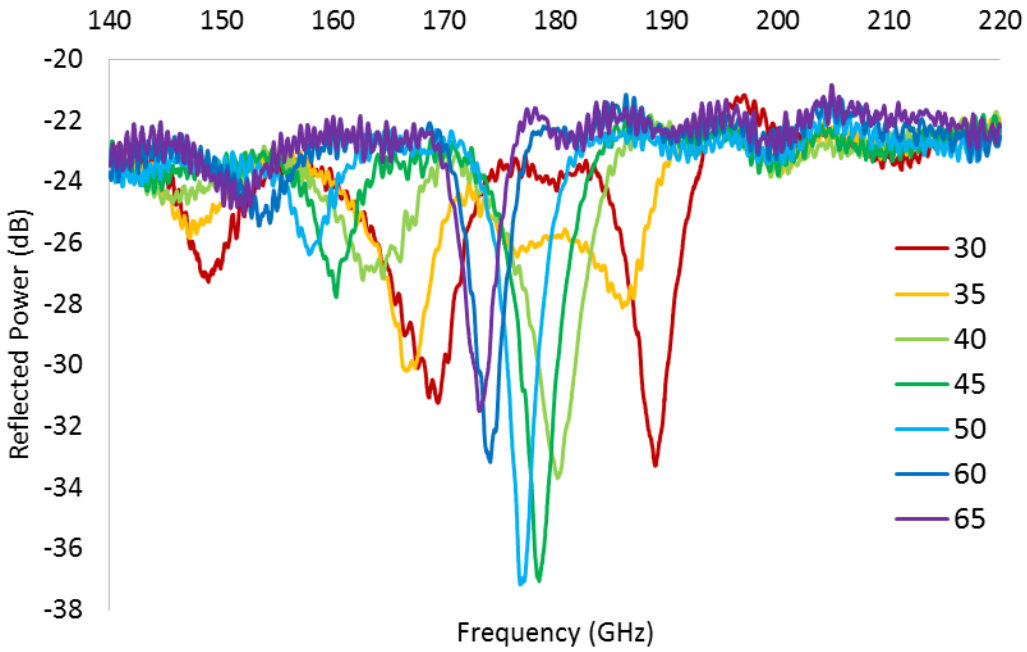

Figure 5.6.1.3. Reflection measurement for the 1.62mm PSL etched onto the 0.41mm, dielectric substrate (without copper backing) at incident angles of 30° to 65°.

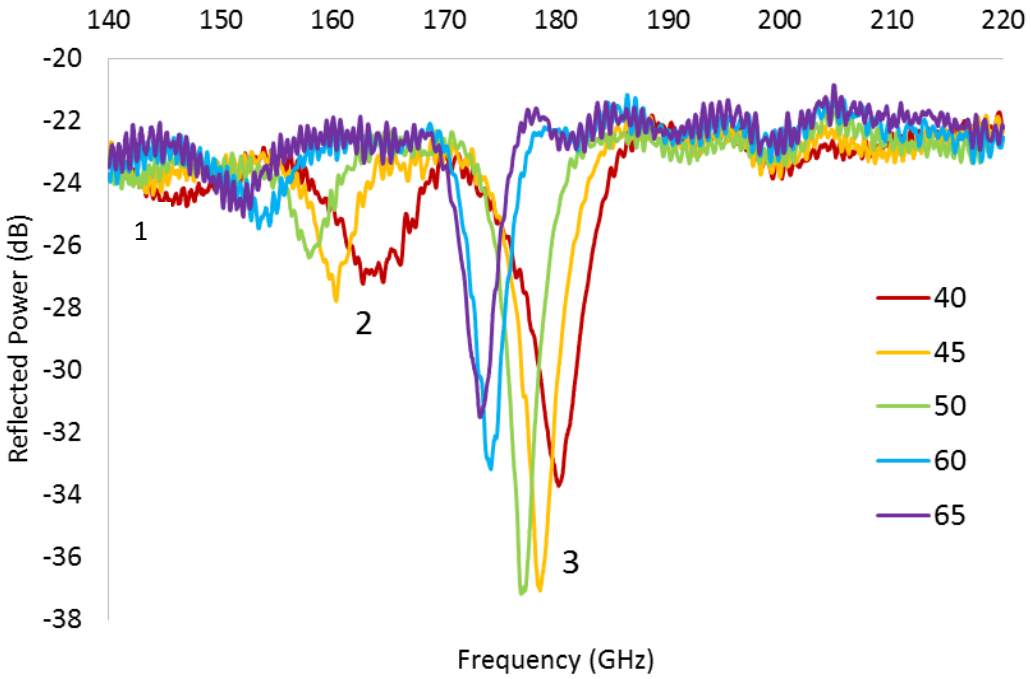

Figure 5.6.1.4. Reflection measurement for the 1.62mm PSL etched onto the 0.41mm, dielectric substrate (without copper backing) at incident angles $\theta_i \geq 40°$.

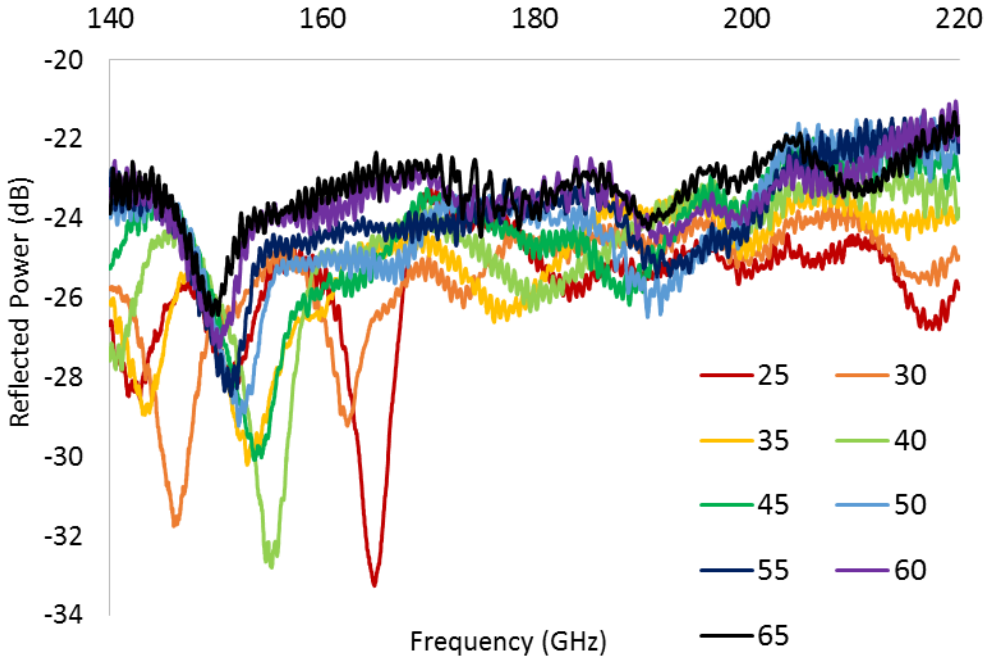

Figure 5.6.1.5. Reflection measurement for the 1.94mm PSL etched onto the 0.41mm, dielectric substrate (without copper backing) at incident angles. 25° to 65°.

5.6.2 Planar PSLs with 0.41mm Copper-backed Substrates

While the PSLs etched onto 0.41mm substrates with no copper backing exhibit clear resonances at frequencies determined by the lattice period and incident angle, the structures composed of PSLs mounted on 0.41mm copper-backed substrates appear to behave like reflective surfaces across most of the frequency band. It is possible that the 0.41mm dielectric may be too thin to support a suitable volume mode. Sharp resonances, however, are present at the lower edge of the frequency band for the 1.50mm and 1.62mm PSLs presented in figures 5.6.2.1 and 5.6.2.2. Similarities can be drawn between these two resonances and the mode-locked eigenmode resonances of §5.4. The resonance measured for the 1.62mm PSL (figure 5.6.2.2), for instance, exhibits no obvious angular dependence and appears locked at 140 GHz, while the 1.50mm PSL's resonance (figure 5.6.2.1) varies slightly with angle and shifts up in frequency with increasing θ_i, rather than down. This is similar to the behaviour observed in the 1.50mm PSL mounted on the 0.76mm copper-backed substrate (figure 5.4.1) for which mode-locking is most effective at higher incident angles. Both structures demonstrate the potential for high-Q cavity modes, with optimum reflected powers of ∼-50dB and ∼-40dB. The presence of just one resonance, as oppose to the multiple resonances measured in the structures without the copper backing, provides further evidence of strong coupling .

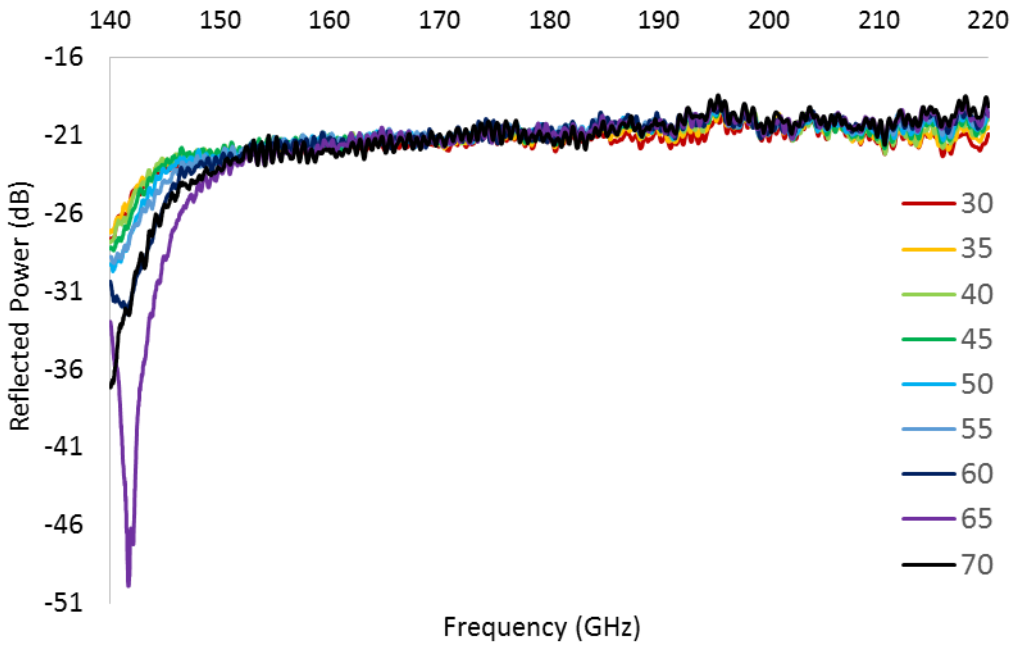

Figure 5.6.2.1. Reflection measurement for 1.50mm PSL etched onto 0.41mm copper-backed substrate. A well-defined (~-50dB) *resonance is observed at ~141.7GHz.*

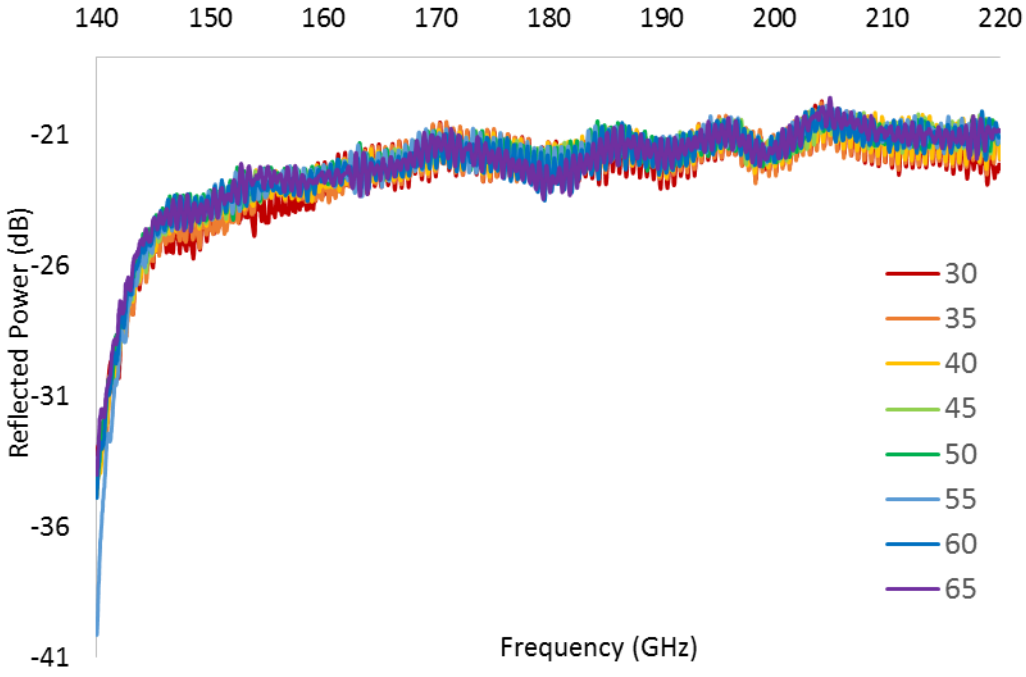

Figure 5.6.2.2. Reflection measurement for the 1.62mm PSL with 0.41mm copper-backed substrate. A well-defined (~-40dB) *resonance is observed at ~140GHz.*

Boundary constraints, imposed by the thinner, 0.41mm copper-backed substrates, allow only higher frequency volume waves to exist within the dielectric. This is

slightly mitigated by the higher (ε =5.69) dielectric permittivity. One possible reason for the resonances of figures 5.6.2.1 and 5.6.2.2 being lower than anticipated, is the potential involvement of a TEM mode inside the copper-backed PSLs, which resemble parallel plate waveguides in the regions between the two conductors. Since the entire field is not contained within the dielectric region, due to the perforated boundary of the PSL, the structure is unlikely to support a pure TEM mode. Instead, a quasi TEM mode may exist when $d \ll \lambda$ (Pozar 1998) This condition is satisfied at very low frequencies in the PSLs with the thin, 0.41mm copper-backed substrates and may lead to coupling between the quasi-TEM mode and surface field of the PSL. TEM modes within these structures are studied in Chapter 6.

Resonances are observed at both ends of the frequency band in the case of the 1.74mm PSL (figure 5.6.2.3). These results, which shift up with increasing incident angle, resemble Fabry-Perot resonances. The lower resonance, which manifests at small incident angles (25°-35°), may otherwise represent a possible coupled eigenmode, similar to that shown in the previous examples (figures 5.6.2.1 and 5.6.2.2).

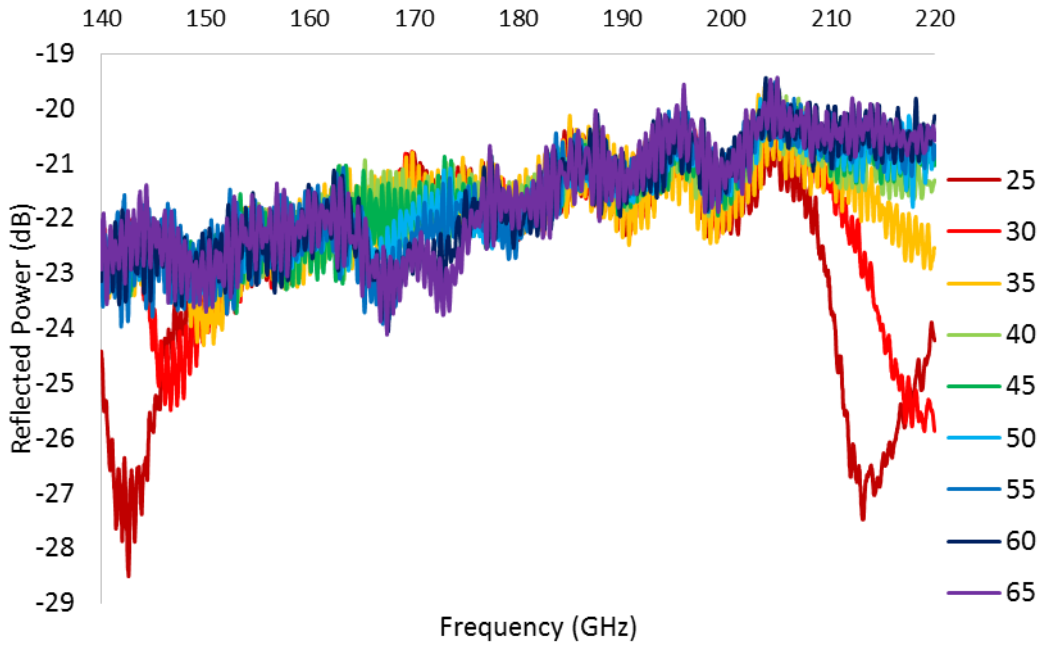

Figure 5.6.2.3. Reflection measurement for the 1.74mm PSL etched onto the 0.41mm copper-backed substrate at incident angles of 30° to 65°.

Fabry-Perot resonances are also evident at high frequencies in the measuements of the 1.94mm PSL, presented in figure 5.6.2.4. Even though these results are affected by experimental noise, a weak resonance (~ 3db) is visible at ~158 GHz. The fixed frequency position of this resonance again suggests possible coupling. However, further study is required to understand the complex nature of these resonances.

In addition to a TEM mode, it may be possible for these structures to support a parallel plate waveguide mode. Taking into account the thickness and permittivity of the dielectric, the cut-off frequency for the first parallel plate waveguide mode is ~ 154GHz. Although this may account for the weak resonance at 158 GHz in figure 5.6.2.4, no similar resonances are present for the other lattice periodicities. The reflection measurement of the 0.41mm FR-4 sample is provided in figure 5.6.2.5. Two resonances, which move further apart with increasing incident angle, are observed.

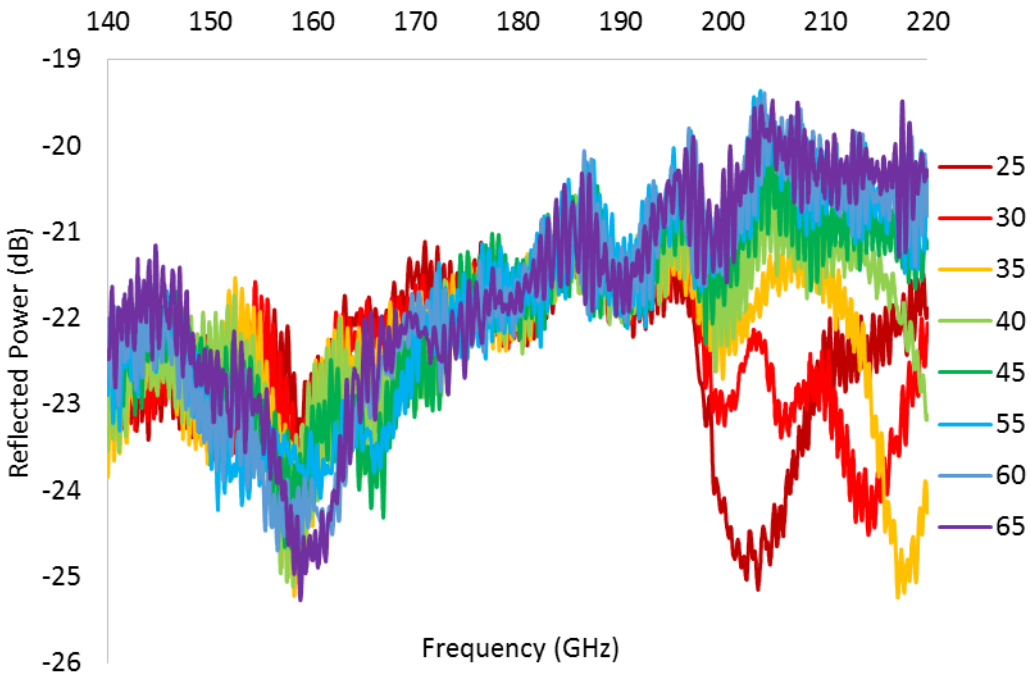

Figure 5.6.2.4. Reflection measurement for the 1.94mm PSL etched onto the 0.41mm copper-backed substrate at incident angles of 25° to 65°.

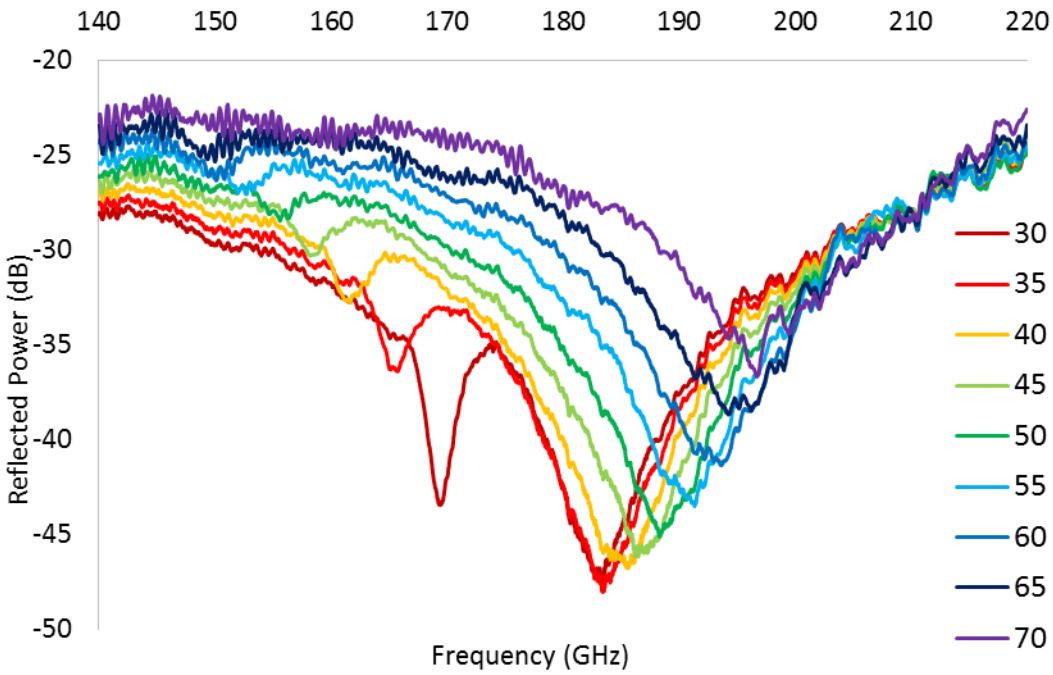

Figure 5.6.2.5. Reflection measurement for the 0.41mm FR-4 sample at incident angles of 30° to 70°.

5.7 Planar PSLs with 1.43mm Substrates

The experimental measurements for the set of structures consisting of PSLs etched onto 1.43mm FR-4 substrates, with and without the copper backing, are presented in this section. For the thicker, 1.43mm substrates with ε =4.45, total internal reflection occurs when θ_i >28°.

5.7.1 Planar PSLs with 1.43mm Substrates (no copper backing)

Figure 5.7.1 illustrates the reflected power for the 1.50mm PSL mounted on the 1.43mm substrate (with no copper backing). The surface field of the PSL (resonance 4) is evident between ~190 GHz and ~200GHz. The lowest, and best defined resonance (1), appears locked at its lower edge and may represent a weakly coupled eigenmode. Similarly, the weak (~3dB) neighbouring resonance (2), which does not vary with angle and exists at the same frequency as the coupled eigenmode of the 1.50mm PSL mounted on the thinner, 0.76mm copper-backed substrate, may occur due to weak coupling of volume and surface fields. The presence of an additional

resonance (3) at ~180GHz, not observed in the PSLs with the thinner dielectrics, suggests that the 1.43mm substrate is over-moded.

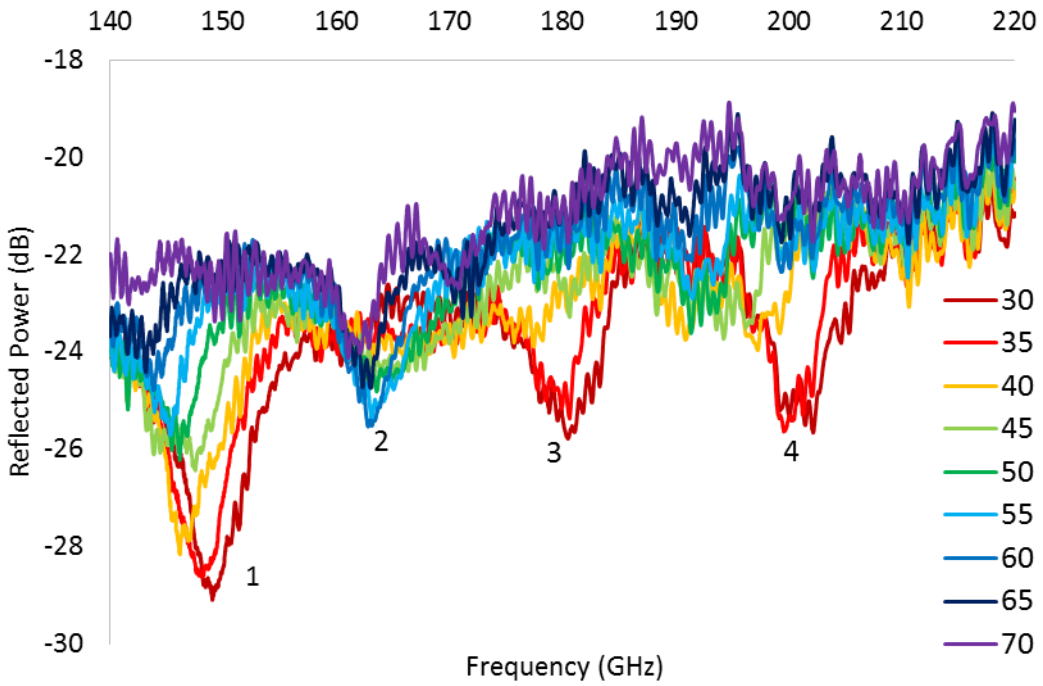

Figure 5.7.1.1. Reflection measurement for the 1.50mm PSL etched onto the 1.43mm substrate (without copper backing) at incident angles of 30° to 70°.

The reflection measurements for the 1.62mm PSL with the 1.43mm substrate are presented in figure 5.7.1.2. Once again, the uppermost resonance (4) describes the surface field of the PSL, while the lowest resonance (1), which varies slightly with angle, represents a mode within the dielectric. The middle resonance (2), which appears mode-locked at higher incident angles ($\theta_i \geq 40°$), lies between the mode inside the dielectric (1) and the surface field of the PSL (4), and is characteristic of a coupled eigenmode. In this case, the lattice is not sufficiently synchronised, partly due to the absence of the copper backing, and consequently, the eigenmode is weakly defined (~5dB). Finally, resonance 3, which is observed at lower incident angles, provides further evidence that the 1.43mm dielectric may be over-moded.

A distinct resonance, centred around 150 GHz and similar to that shown in figure 5.4.4, is observed for the 1.94mm PSL, presented in figure 5.7.1.3. This is another

example of incoherent eigenmode formation, associated with the weak coupling of volume and surface fields.

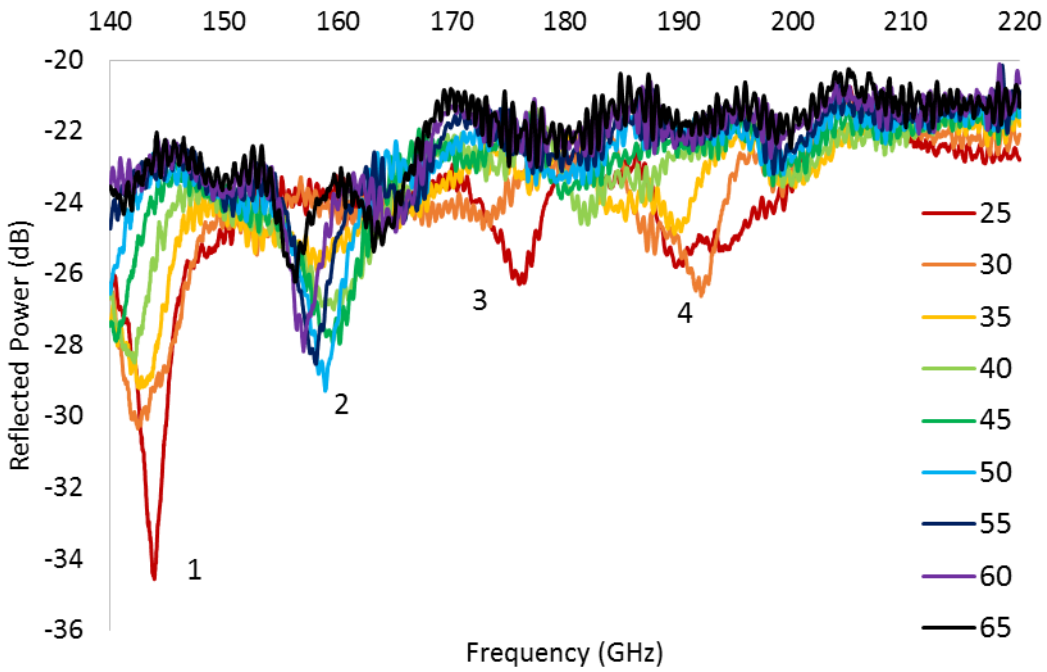

Figure 5.7.1.2. Reflection measurement for the 1.62mm PSL etched onto the 1.43mm substrate (without copper backing) at incident angles of 25° to 65°.

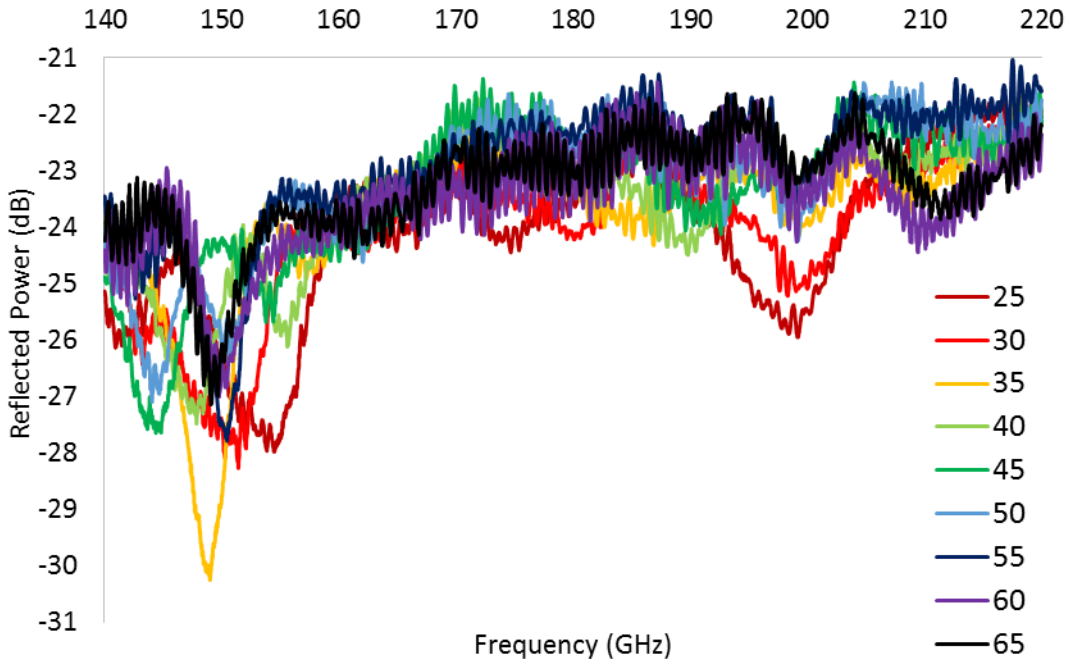

Figure 5.7.1.3. Reflection measurement for the 1.94mm PSL etched onto the 1.43mm substrate (without copper backing) at incident angles of 25° to 65°.

5.7.2 Planar PSLs with 1.43mm Copper-backed Substrates

In this section, the results for the set of PSLs mounted on the 1.43mm copper-backed substrates are presented and compared to those for the PSLs with the 1.43mm substrates and no copper backing (§5.7.1). Figure 5.7.2.1 shows four resonances measured for the 1.50mm PSL with the 1.43mm copper-backed substrate. All four resonances exist at frequencies close to those of figure 5.7.1.1. The magnitude of resonance 2, however, is significantly greater (∼-39dB) when the copper-backing is included (figure 5.7.2.1) and demonstrates a high Q-factor at lower angles in particular. This resonance, which shows no clear angular dependence, may represent a coupled cavity eigenmode that is more coherently formed in the presence of the copper backing. This eigenmode is weaker than that of the 1.50mm PSL mounted on the thinner, 0.76mm copper-backed substrate, possibly due to the greater absorptive losses associated with the thicker 1.43mm dielectric. The 1.43mm dielectric's capacity to become over-moded may also inhibit the coherent synchronisation of the PSL, leading to the observation of multiple resonances. Typically, the resonances

appear equally distributed across the frequency band, suggesting a possible cavity effect due to reflection off the copper surface.

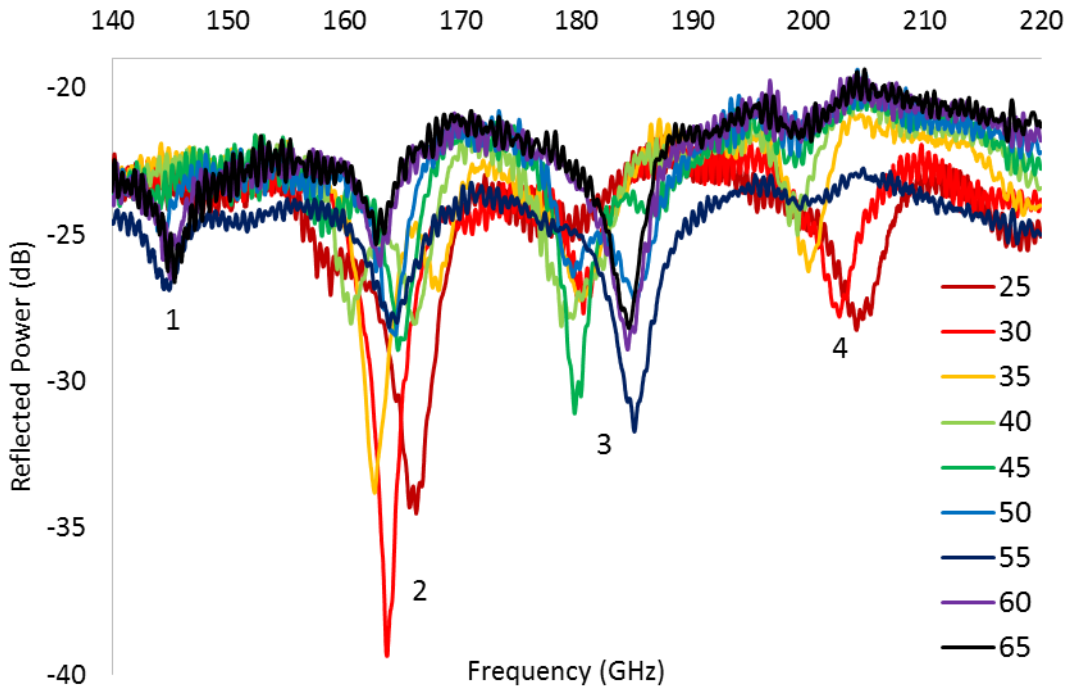

Figure 5.7.2.1. Reflection measurements for the 1.50mm PSL etched onto the 1.43mm copper-backed substrate at incident angles of 25° to 65°.

With the inclusion of the copper backing, the structure has the potential to behave partially like a parallel plate waveguide. In this event, the structure may support waveguide modes of a TE or TM nature. Taking into account the thickness and permittivity of the dielectric, the second and third parallel plate waveguide modes (with cut-off frequencies of 143GHz and 199GHz) may propagate within the measured frequency range. Although a corresponding resonance exists around 145GHz, this is also present in the structure without the copper backing (figure 5.7.1.1) and is therefore unlikely to represent a parallel plate waveguide mode.

For the 1.62mm PSL shown in figure 5.7.2.2, the lowest resonance (1) has slightly shifted down in frequency, compared to the equivalent structure without the copper backing (figure 5.7.1.2). Resonance 1 now resembles the low frequency, mode-locked resonance observed in the 1.62mm PSL with the thin, 0.41mm copper-backed

substrate (figure 5.6.2.2). The middle resonances (2 and 3) are better-defined (~-30dB) due to the enhanced coupling associated with the copper backing.

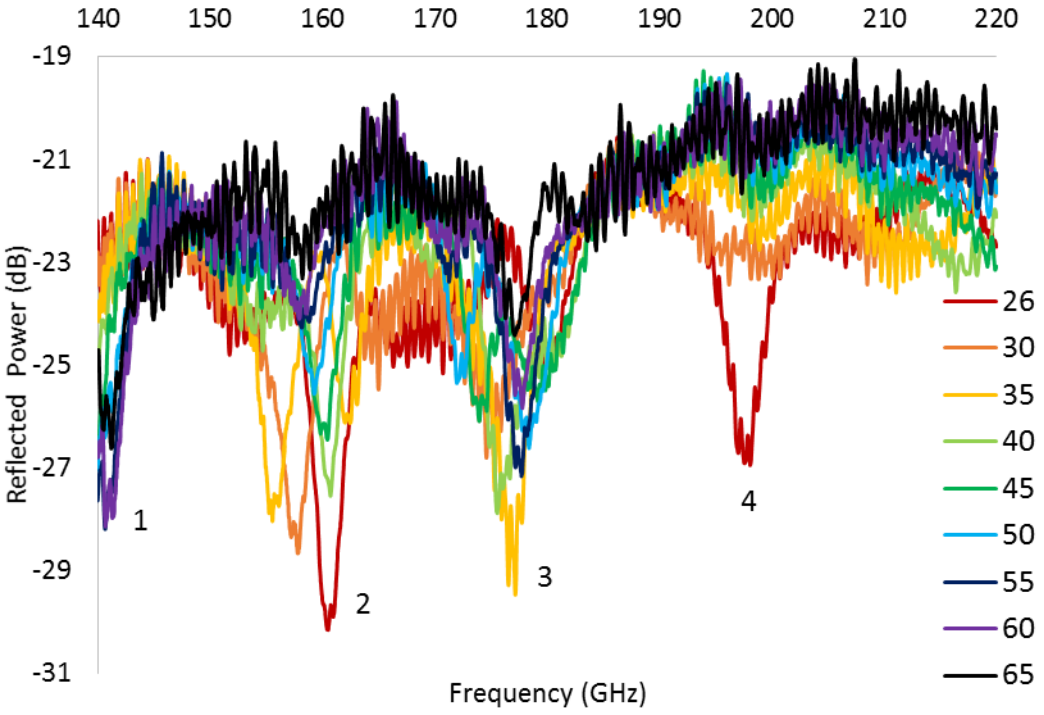

Figure 5.7.2.2.Reflection measurements for the 1.62mm PSL etched onto the 1.43mm copper-backed substrate at incident angles of 25° to 65°.

Reflection measurements for the 1.94mm PSL etched onto the 1.43mm copper-backed substrate are provided in figure 5.7.2.3. The sharp resonance at ~150 GHz (similar to that of figure 5.4.4) is indicative of the PSL's coupled eigenmode. Although there is a slight frequency shift with angle, indicating that the resonances are not fully mode-locked, they appear constrained at the lower frequency edge. Since the PSL is not entirely synchronised, owing to the larger dielectric losses associated with the thick substrate, further behaviour, manifesting in the form of weak resonances (~160-180 GHz), is evident. This complex behaviour again suggests that the 1.43mm dielectric is over-moded. Figure 5.7.2.4 shows the reflection measurement of the 1.43mm FR-4 sample alone. The lower resonance (~150-175 GHz) which is well-defined at θ_i =30°, may account for some of the behaviour observed in the 1.94mm

PSL mounted on the 1.43mm copper-backed substrate (figure 5.7.2.3). The upper resonance is attributed to a Fabry-Perot cavity effect.

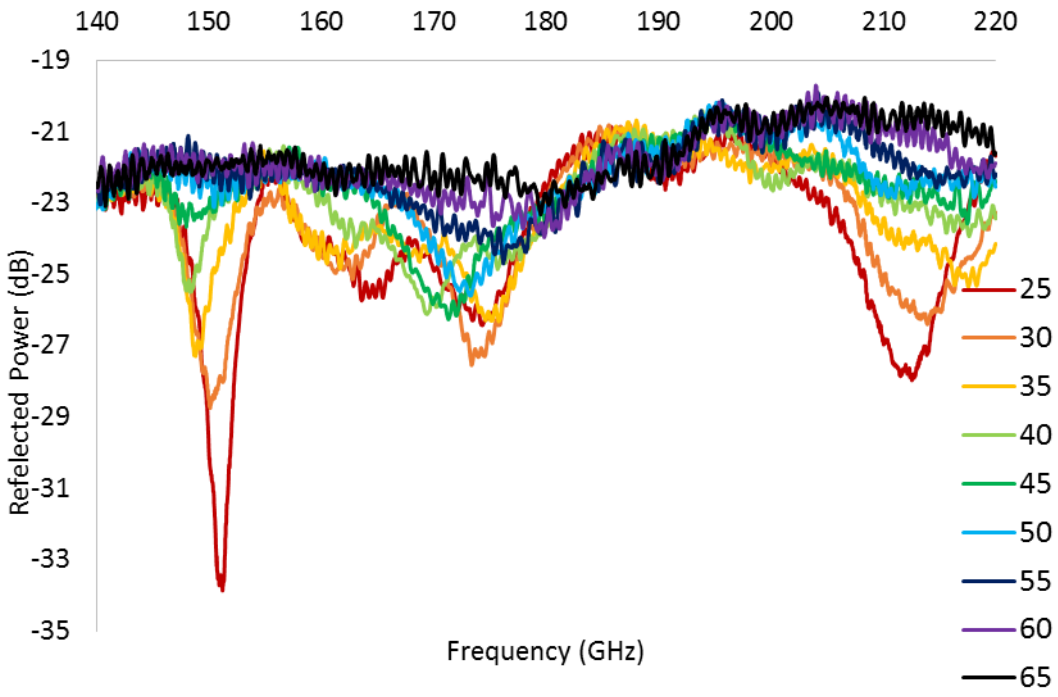

Figure 5.7.2.3. Reflection measurements for the 1.94mm PSL etched onto the 1.43mm copper-backed substrate at incident angles of 25° to 65°.

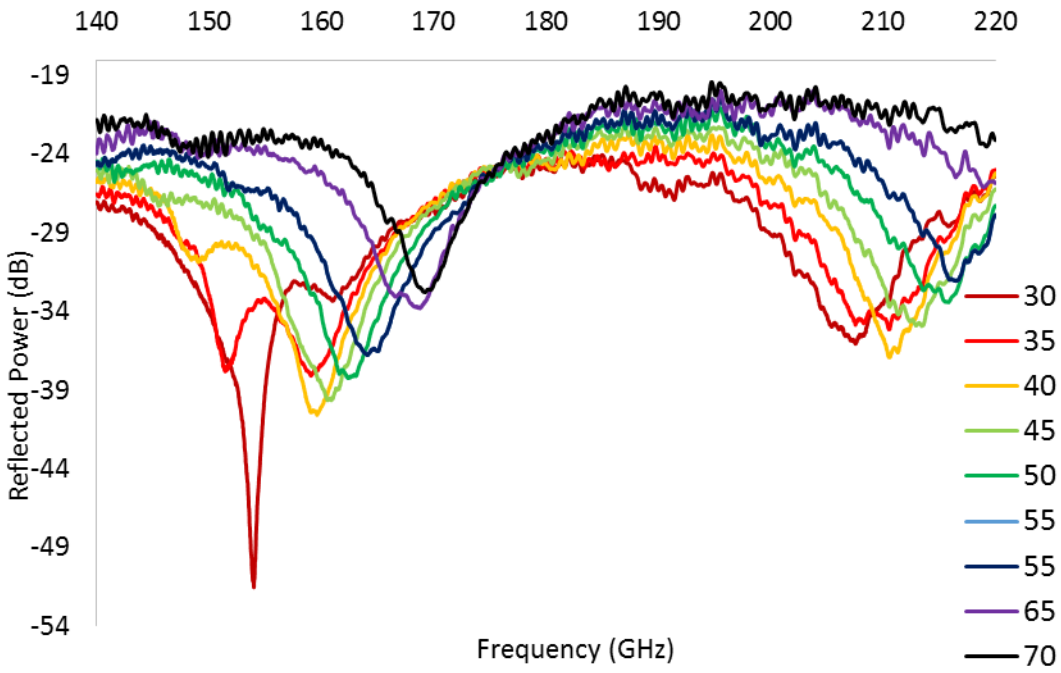

Figure 5.7.2.4. Reflection measurements for the 1.43mm FR-4 sample at incident angles of 25° to 65°.

Overall, for the set of PSLs mounted on the 1.43mm copper-backed substrates, the coupled eigenmodes are less well-defined, and not as constrained, possibly due to absorptive losses within the dielectric and also the capability of the thicker dielectric to become over-moded.

5.8 PSL Structures with Reduced Dielectric Borders

It has so far been demonstrated that the dielectric thickness affects the properties of the PSL structures. In order to investigate the effect of changing the dielectric width, which may influence the volume field, structures consisting of planar PSLs with a reduced, 3mm dielectric border were obtained by trimming the excess substrate. Structures composed of 1.62mm PSLs etched onto 1.43mm thick substrates, with and without the copper backing, were trimmed accordingly. The results presented in figure 5.8.1 (for the 1.62mm PSL with the reduced, 1.43mm substrate) almost exactly match those of figure 5.7.1.2, suggesting that the width of the dielectric has little effect on the electromagnetic characteristics of the structure. Likewise, the

reflection measurements for the 1.62mm PSL mounted on the 1.43mm copper-backed substrate with a reduced, 3mm dielectric border (figure 5.8.2) replicate those obtained for the original 1.62mm PSL mounted on the 1.43mm copper-backed structure.

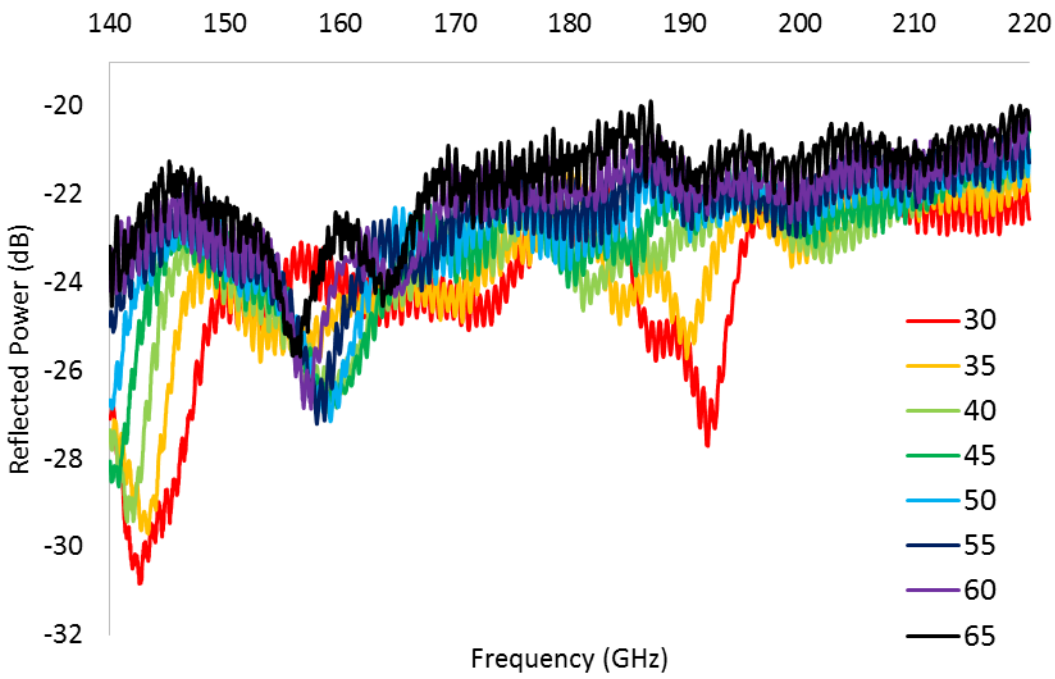

Figure 5.8.1. Reflection measurements for the 1.62mm PSL etched onto the 1.43mm substrate (without copper backing). The boundaries of the substrate have been trimmed to leave a thin, 3mm dielectric border at the edges of the PSL.

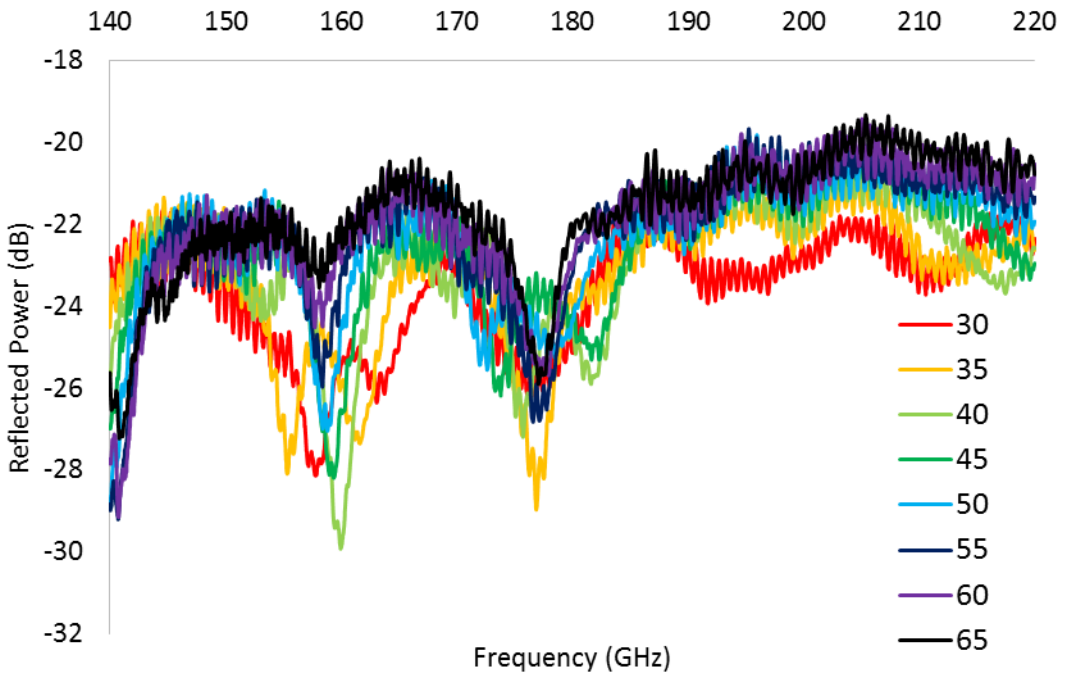

Figure 5.8.2. Reflection measurements for the 1.62mm PSL etched onto the 1.43mm copper-backed substrate. The boundaries of the substrate have been trimmed to leave a thin, 3mm dielectric border at the edges of the PSL.

5.9 High-Frequency Planar PSL Structure

Measurements were made for the professionally etched 0.63mm PSL at the 325-500GHz frequency band using a pair of 325-500GHz band horns to prevent mode conversion. The structure (composed of a 0.41mm copper-backed FR-4 substrate) has similar properties to those previously shown to support coherent eigenmode formation at the 140-200GHz band. In this case, a coupled eigenmode is observed around 371 GHz and, like the results presented in §5.4, the resonances appear to be mode-locked at one specific frequency.

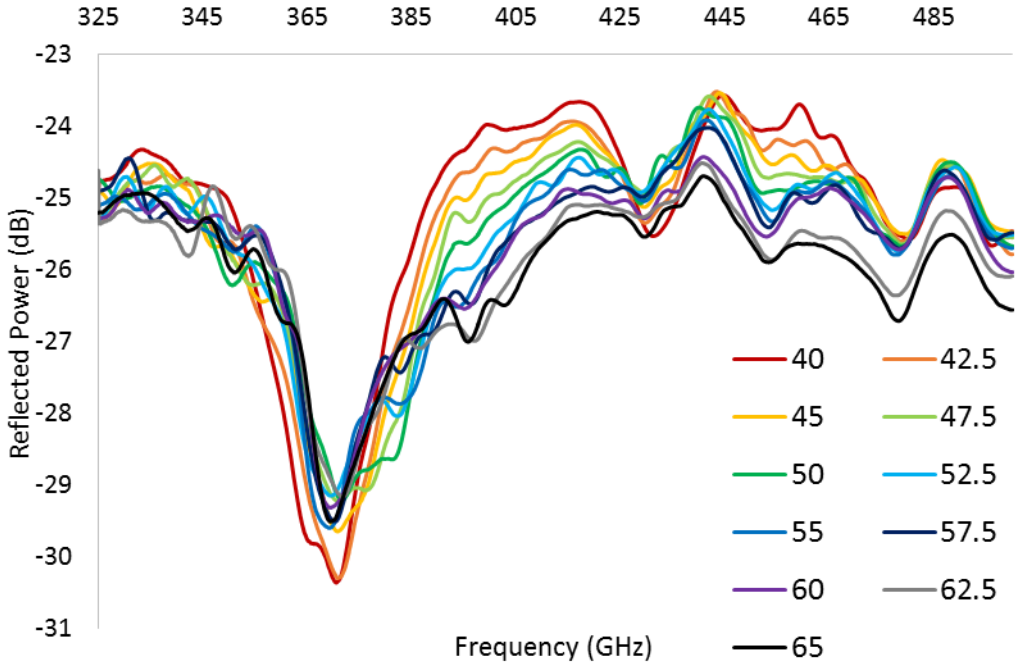

Figure 5.9.1. Reflected power of the 0.63mm PSL etched onto the 0.41mm copper-backed substrate, measured at the 325-500 GHz frequency band. Coherent, coupled eigenmode formation is observed around 371 GHz.

Measurements were made over a restricted range of angles due to the shorter cables required to connect the high frequency modules to the VNA. To compensate for this, the angle was varied in smaller increments to obtain the same amount of data presented in previous sets of results. Precise alignment of the pair of high-frequency (325-500 GHz) horns required to make these measurements proved difficult and, consequently, the reflected power (~5dB) and therefore quality of the coupled cavity mode, is poor in comparison to the mode-locked structures designed to operate at the 140-220 GHz band. Nevertheless, the results demonstrate the fundamental "proof of principle" coupling between volume and surface waves at a single frequency and verify the scalability of the PSLs. This lays the foundation for future work which may involve further scaling up of the PSL structures to operate at the THz regime.

5.10 Metamaterial PSL Structure

Thus far, the structures have been considered to behave like metadielectrics in the plane of incidence, due to the corrugation depth (35μm) being much smaller than the operating wavelength. However, since the lattice period is comparable with the wavelength, the structures do not strictly satisfy the metamaterial criteria. In order to investigate the electromagnetic properties when the structure moves closer to the true definition of a metamaterial, the 0.63mm PSL is measured at the 140-200GHz frequency band, as shown in figure 5.10.1. The PSL is now characterised by an effective permittivity and permeability, derived from its subwavelength structure. The structure displays unique behaviour when measured at the lower, 140-220 GHz frequency band, and despite the copper backing and thin substrate, no longer exhibits mode-locked eigenmode formation. It is noted that the frequency of the measured resonance (~175-188 GHz) now shifts up with increasing incident angle. Further work and analysis is required to understand this complex behaviour.

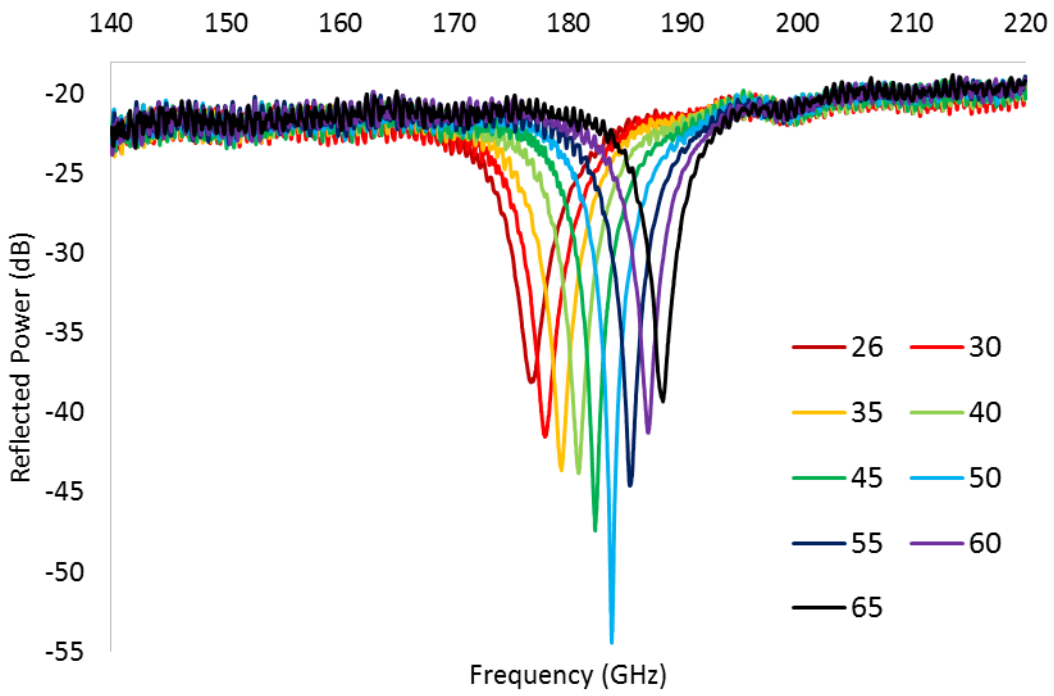

Figure 5.10.1. Reflected power of the 0.63mm PSL structure measured at the 140-220 GHz frequency band where the PSL is expected to behave more like a metamaterial. The resonances shift up with angle, in the opposite direction to the PSLs with $d_z \approx \lambda$.

5.11 Measurements of PSL Structures with Air Gaps

Reflection measurements for a 1.94mm PSL structure, with a tunable air gap between the PSL and copper backing, are presented in this section. The spacing between the 1.94mm PSL and copper backing was adjusted to have an optical path difference equivalent to that of the FR-4 substrates. The purpose of carrying out these measurements was two-fold; first to establish whether or not the dielectric is essential for the coupling of volume and surface fields, and also to investigate the possibility of coupling in low loss structures, which may lead to enhanced, high Q cavity modes. Measurements made for air separations of 1mm, 1.6mm and 3mm, comparable to the 1.94mm PSLs etched onto the 0.41mm, 0.76mm and 1.43mm copper-backed substrates, are shown in figures 5.11.1-5.11.3. For each gap width, a distinct resonance with a reflected power of up to -40 dB is observed at ~150-155 GHz, only at certain incident angles. Significant experimental noise is present, especially around 165-170 GHz and 185-190 GHz where further resonances, attributed to reflection off the copper backing, exist.

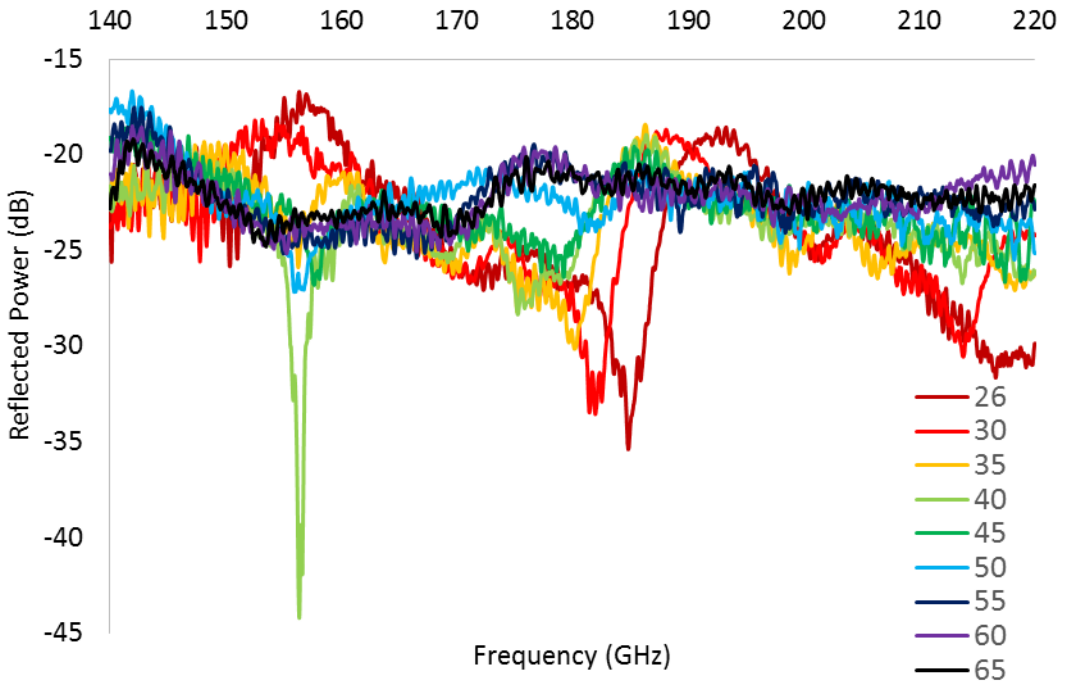

Figure 5.11.1 Reflection measurement for the 1.94mm PSL structure with an air separation of 1mm, and an optical path difference equivalent to the 0.41mm FR-4 substrate.

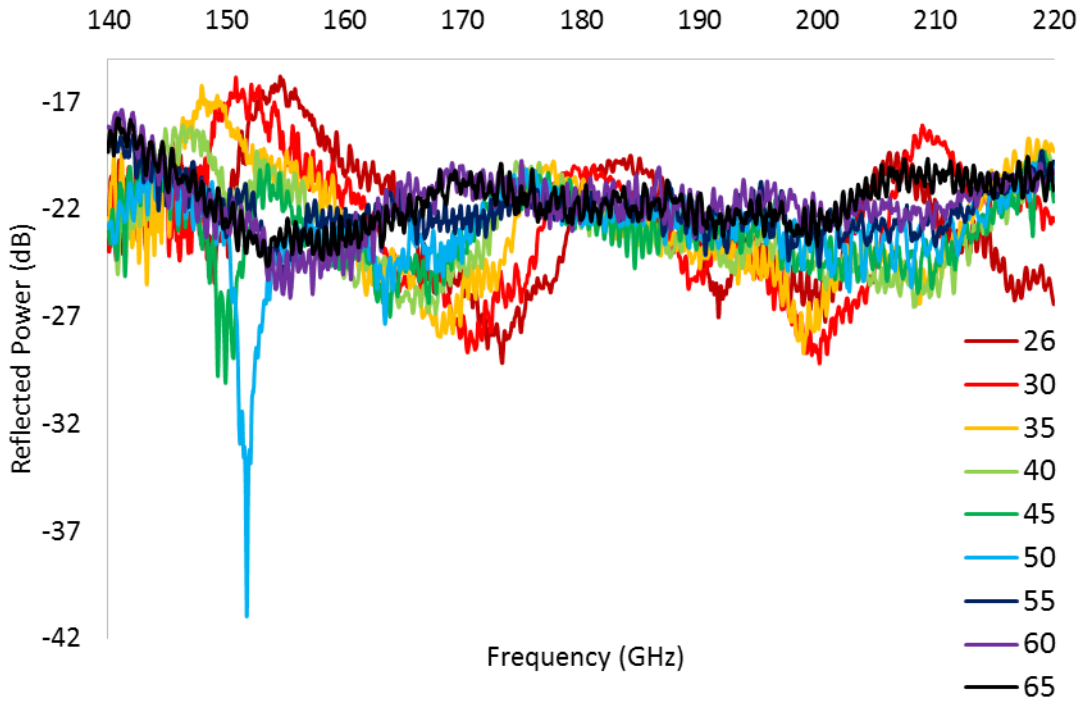

Figure 5.11.2. Reflection measurement for the 1.94mm PSL structure with an air separation of 1.6mm and an optical path difference equivalent to the 0.76mm FR-4 substrate.

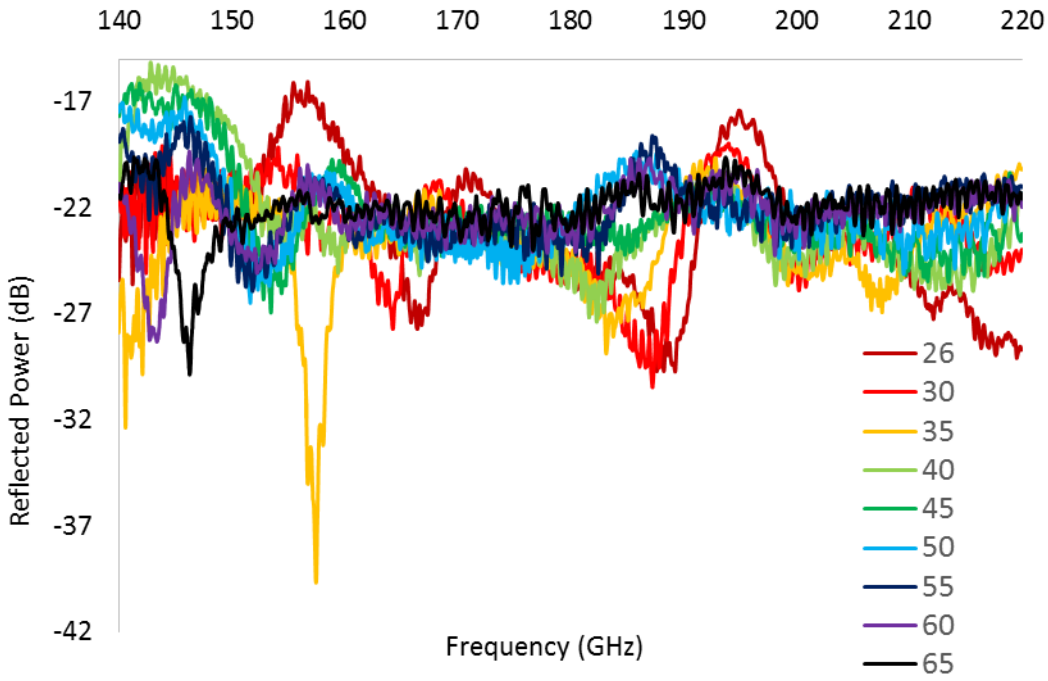

Figure 5.11.3. Reflection measurement for the 1.94mm PSL structure with an air separation of 3mm, and an optical path difference equivalent to the 1.43mm FR-4 substrate.

Figure 5.11.4 compares the results for the 1.94mm PSL with the 1.6mm air separation (green trace) to the mode-locked, 1.94mm PSL etched onto the 0.76mm copper-backed substrate (red trace), at a fixed angle of 45°. Both measurements demonstrate resonances at 150 GHz and 163 GHz, showing that the gap structure has the potential to support weak eigenmode formation at some angles. Despite the reduced dielectric loss, coherent eigenmode formation is not observed at all angles due to energy escaping from the unbound edges. Previously, with the dielectric, the field was internally reflected and confined within the structure.

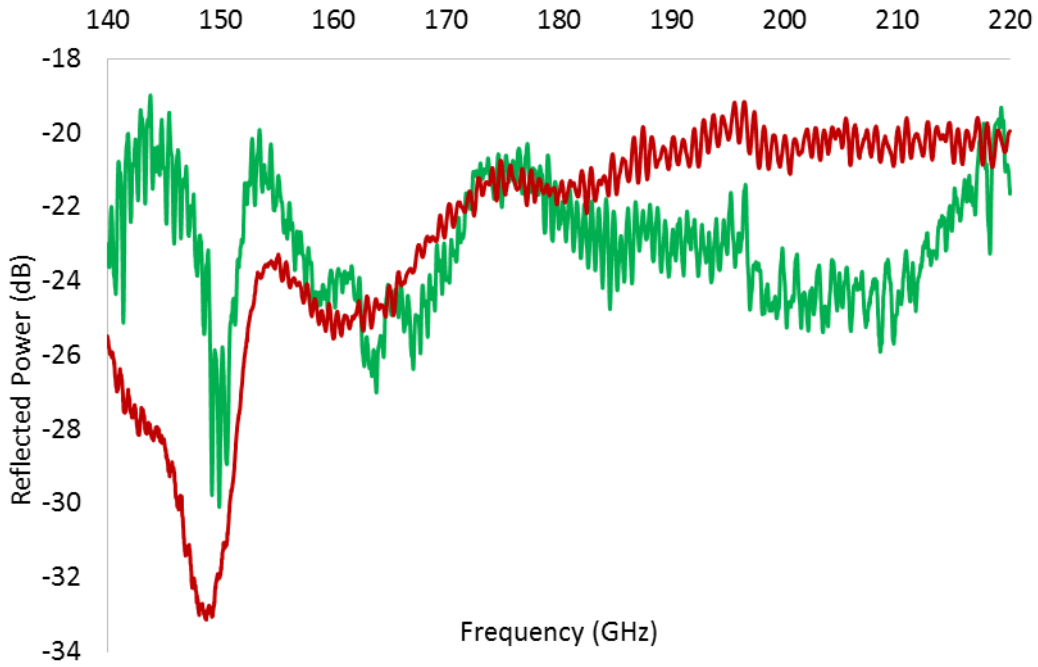

Figure 5.11.4. Reflection measurements for the 1.94mm PSL structure with an air separation of 1.6mm (green trace) and the 1.94mm PSL mounted on the 0.76mm copper-backed substrate.

Finally, in an attempt to confine a volume field inside the structure whilst maintaining the low loss air gap, dielectric and metal frames were inserted between the 1.94mm PSL and the copper backing. Measurements made for the air-gap structure with FR-4 (figure 5.11.5) and aluminium (figure 5.11.6) borders, designed to provide dielectric and metal boundaries, are presented below.

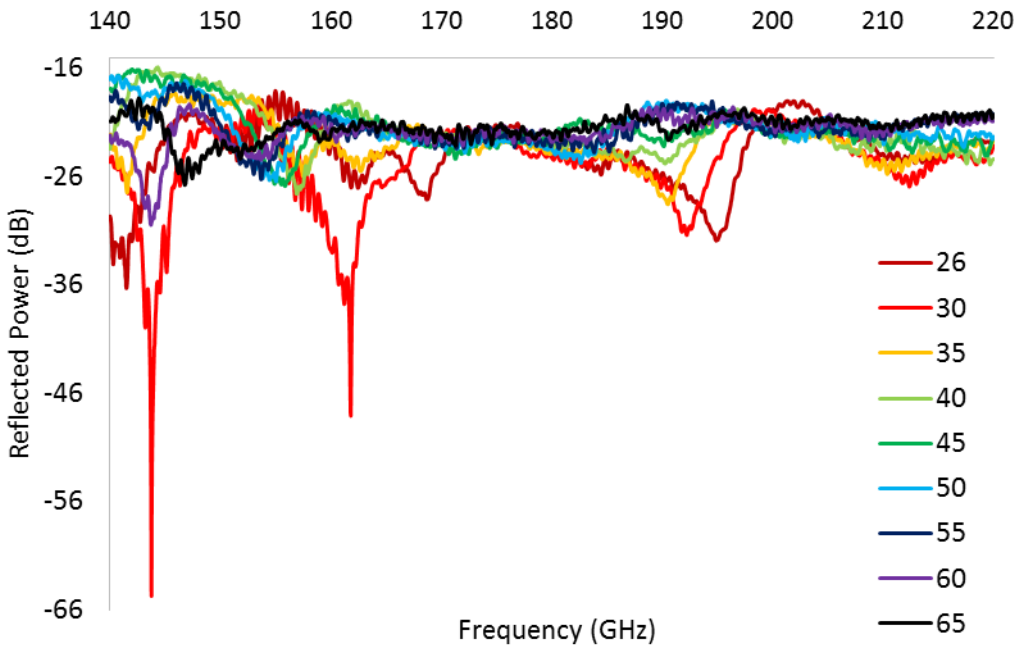

Figure 5.11.5. Reflection measurements for the air-gap structure based on the 1.94mm PSL with a dielectric boundary provided by a FR-4 frame.

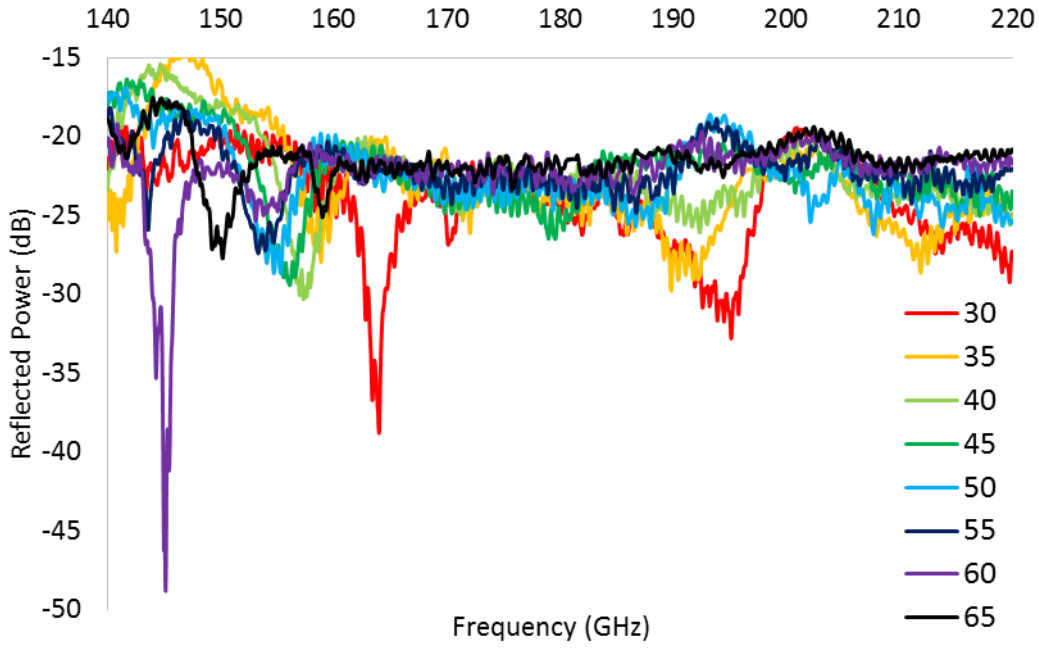

Figure 5.11.6. Reflection measurements for the air-gap structure based on the 1.94mm PSL with an aluminium boundary to confine the field inside the structure.

Both the structures with the dielectric and aluminium frames have the capability to support high Q cavity modes. The structure with the FR-4 frame (figure 5.11.5) has a reflected power of -65dB at 144 GHz when measured at an incident angle of 30°. This resonance resembles the coupled eigenmode of the 1.94mm PSL, although the presence of additional resonances (around 160 GHz and 190 GHz) indicate that, while the frame improves the quality of the cavity, it is not sufficient for coherent synchronisation of the lattice, which requires a dielectric substrate with carefully chosen parameters. Though the aluminium frame would be expected to further increase the quality of the cavity, a reduction in power is evident in figure 5.11.6, where the strongest reflection (-49 dB) occurs at 145 GHz. A large magnitude uncertainty ($\pm$ 16dB) was previously demonstrated for the coupled resonances in §5.4 and may account for this apparent reduction in power.

5.12 Chapter Conclusions

Reflection measurements for the simple PSLs (with no dielectric or copper backing) showed a sharp resonance corresponding to the PSL's surface field at a specific frequency, dependent upon the period of the PSL. Larger periodicities led to lower frequency resonances as expected, demonstrating that the EM properties of the structure are tailored by varying the lattice parameters. It was also shown that the frequency of the PSL's surface field can be shifted by changing the angle of incidence, with the frequency shifting down with increasing angle. Transmission measurements confirmed that the PSLs transmit and reflect at the same frequencies.

More complex behaviour was observed in the PSLs with dielectric substrates which support weakly defined volume waves. Above the critical angle, internally reflected volume waves can facilitate weak coupling with the surface field. Varying the dielectric thickness changed the EM properties of the PSL structures. Typically, three resonances, corresponding to the PSL's surface field as well as modes within the dielectric, including weakly coupled eigenmodes, were observed. Additional resonances, measured for the 1.43mm substrates, imply that the thicker dielectric has the capacity to become over-moded, while Fabry-Perot resonances, which shift up in frequency with increasing angle, were identified in several of the structures.

Coherent eigenmode formation was observed in the PSLs etched onto the 0.76mm copper-backed substrates. The results showed sharp, mode-locked resonances at a specific frequency, dependent on the periodicity of the PSL. The presence of a single, mode-locked resonance indicated that the PSLs were coherently synchronised by the field confined within the dielectric, allowing all the individual scatters to oscillate in phase. This illustrated the fundamental "proof of principle" coupling between volume and surface fields in the planar PSLs, and established their potential for use as the interaction region of a high, power coherent radiation source. Good frequency reproducibility (±0.3 GHz) was established for these important results.

Possible coherent eigenmode formation was also observed at the lower edge of the frequency band for the 1.50mm and 1.62mm PSLs mounted on the 0.41mm copper backed substrates. The sharp resonances measured in these structures may, however, represent complex behaviour such as coupling between a TEM type mode and the surface field of the PSL. The nature of these resonances is further investigated in Chapter 6. As a consequence of the large dielectric losses in the 1.43mm dielectric, which disrupts the coherent synchronisation of the lattice, coherent eigenmode formation was not seen in the PSLs mounted on the 1.43mm copper-backed substrates.

While the dielectric thickness was found to influence the properties of the structure, with suitable dimensions required for coherent eigenmode formation, changing the boundaries by reducing the dielectric bordering the PSL showed no significant effect. Experiments involving the tunable "air-gap" structure based on the 1.94mm PSL confirmed that the dielectric substrate plays a crucial role in coupled eigenmode formation, synchronising the PSL and reducing the radiation leaked from the edges.

Finally, measurements of the 0.63mm PSL at the 325-500 GHz frequency band verified the scalability of this work, while unique EM behaviour was observed for the same structure measured at 140-220 GHz where it was assumed to behave more like a metamaterial.

Chapter 6: Numerical Dispersions of Planar PSLs

6.1. Introduction

Further analysis of the experimental results presented in chapter 5 requires studying and comparing the dispersion plots of the planar PSLs. An analytical approach was used to obtain dispersion diagrams for the cylindrical PSLs in chapter 3. This technique proves difficult when considering the planar PSLs, for which the volume field inside the substrate is not clearly defined, and the individual volume and surface modes that constitute the cavity eigenmode are unknown. Instead, dispersion diagrams are obtained by modelling the planar PSLs using the EM software package CST Microwave Studio (CST MWS). This method calculates the possible modes inside the structure and does not take into account the source of radiation or incident angle as discussed in §6.2. If approximate values for the cut-off frequency of the uncoupled volume field and detuning parameter Γ are observed through numerical modelling, the MAPLE code (based on the analytical study of the cylindrical PSLs with very large radii) can be adapted and compared to the CST MWS dispersion plots for the planar PSLs. The layout of this chapter is as follows:

A description of the CST MWS model and appropriate boundary conditions is provided in §6.2. The CST MWS dispersions are then compared with the analytical dispersion plots of Chapter 3 (§6.3) and the experimental results presented in Chapter 5 (§6.4). In §6.4 the set of PSLs mounted on the 0.41mm and 0.76mm copper-backed substrates and 1.94mm PSL with the thicker, 1.43mm copper-backed substrate are investigated. Subsections 6.4.4 and 6.4.5 are devoted to the study of the 0.63mm PSL modelled at the 325-500 GHz and 140-200 GHz frequency bands. The main conclusions of this chapter are summarised in §6.5.

6.2. CST Microwave Studio Model

Dispersion diagrams for the planar PSLs were obtained using the Eigenmode Solver of CST Microwave Studio (CST MWS). Out of the two available eigenmode solvers,

the Advanced Krylov Subspace method (AKS) - which calculates a specified number of modes with the lowest resonant frequencies in a lossfree structure - was chosen for its fast computation time. The AKS Eigenmode solver was used in conjunction with a parameter sweep, calculating a specified number of eigenmodes as the phase was varied from -360° to 360°. An important feature of the eigenmode solver is its use of periodic boundaries. Figure 6.2.1 shows a unit cell of the PSL structure with periodic boundaries in the direction of the lattice corrugation (*x* and *z* axes). The boundary conditions along the y-axis force the tangential magnetic field to zero (H_t=0) at the corrugated surface and the transverse electric field to zero (E_t=0) at the metal wall. For the structures without the copper backing, the boundary conditions were defined by setting H_t=0 at the corrugated surface and back wall of the dielectric.

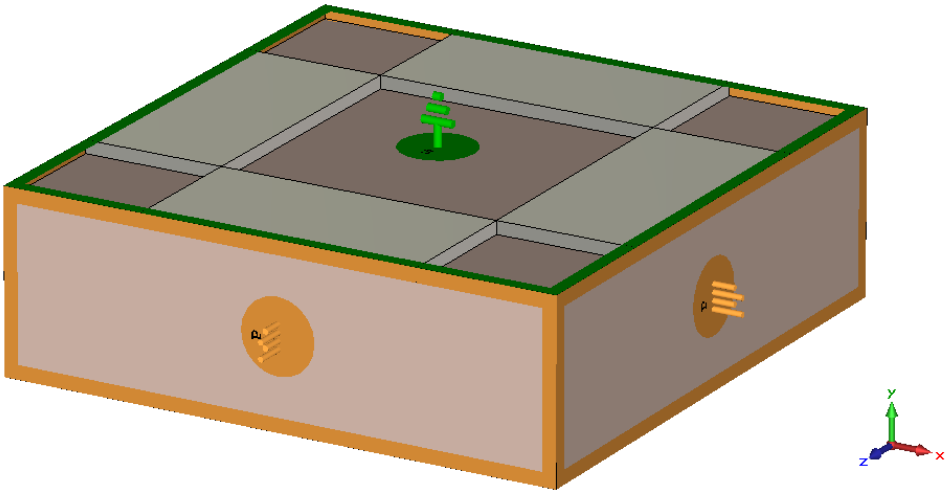

Figure 6.2.1. Unit cell of the planar 2D PSL with periodic boundaries along x and z, used to obtain a dispersion relation with the Eigenmode solver of CST Microwave Studio. H_t*=0 at the corrugated surface and* E_t*=0 at the metal wall.*

One of the limitations of this model is that the CST MWS Eigenmode solver considers only modes that can exist inside the structure and does not calculate for a given incident angle. This accounts for small differences between the frequencies at which the experimental resonances are observed and the location of the eigenmodes predicted by the numerical dispersions. The dispersions are therefore best compared to the equivalent experimental results at the lowest incident angle.

Diffractive edge effects, as well as the possibility of non-uniform irradiation by the excitation source, and potential side lobe involvement are not taken into consideration in these simulations. Another physical aspect neglected by the CST MWS Eigenmode Solver is the Ohmic and dielectric losses associated with the copper lattice and dielectric substrate. Although viable coupling mechanisms may be observed in the dispersions, in practice the losses may impact on the structure's ability to support a coupled eigenmode. In addition to the above, although the E_t=0 boundary appropriately describes the copper backed substrates, the H_t=0 magnetic boundary for the structures without the copper backing provides a less accurate representation.

6.3. Comparison of Numerical and Theoretical Models

The CST MWS model of the planar PSL structure was compared to the analytical dispersion study of the oversized cylindrical PSLs solved using MAPLE. The planar and cylindrical geometries for which the two models were developed are related by the assumption that the mean radius of the cylindrical waveguide is very large. Differences between the numerical and theoretical methods adopted in this work, including the geometry of the PSL structures, were taken into account. The approximations $\omega_0^v \cong \omega_0^s$ and $\tilde{\Delta} = 0$ were used to simplify the analytical dispersion study while in the CST MWS model, the specific cut-off frequencies of the individual modes were calculated. Furthermore, just one known volume mode (near cut-off mode of the cylindrical waveguide) was considered in the analytical model, while the CST MWS Eigenmode Solver computes a number of possible modes. The inclusion of these extra modes may lead to the observation of several possible coupling mechanisms, resulting from the surface field coupling with different volume fields. In addition to this, the analytical dispersions only take into account the fundamental space harmonic of the volume field, whereas the simulations performed using CST MWS include the ± 1 spatial harmonics of the volume field and allow for possible eigenmodes formed by the coupling of neighbouring volume field harmonics. The

coupled spatial harmonics alter the gradient and overall appearance of the dispersion curves introducing further disparity between the two approaches. Despite these differences, some similarities can be drawn between the numerical and analytical dispersion plots when appropriate parameter values are chosen.

One of the thinner, and therefore less over-moded, structures consisting of the 1.94mm PSL mounted on a 0.41mm dielectric was modelled and compared to the analytical dispersion. A corrugation depth of 35 μm was chosen to match the planar PSL structures measured in the experiment. For simplicity, and to allow a better comparison between the two methods, only the fundamental harmonic of the volume mode (dashed blue lines) is considered in this section. The spatial harmonics of the surface field occur at intervals of $n\bar{k}_z$ allowing the ± 1 harmonics to exist within the calculated k_z range. Figure 6.3.1 shows the CST MWS dispersion plot for the 1.94mm PSL mounted on the 0.41mm dielectric. Three coupled dispersion branches (red plots) and a volume mode (dashed blue lines) are observed. It is assumed that the volume mode with f_c ≅125 GHz couples with the surface field to form dispersion branches 1-3.

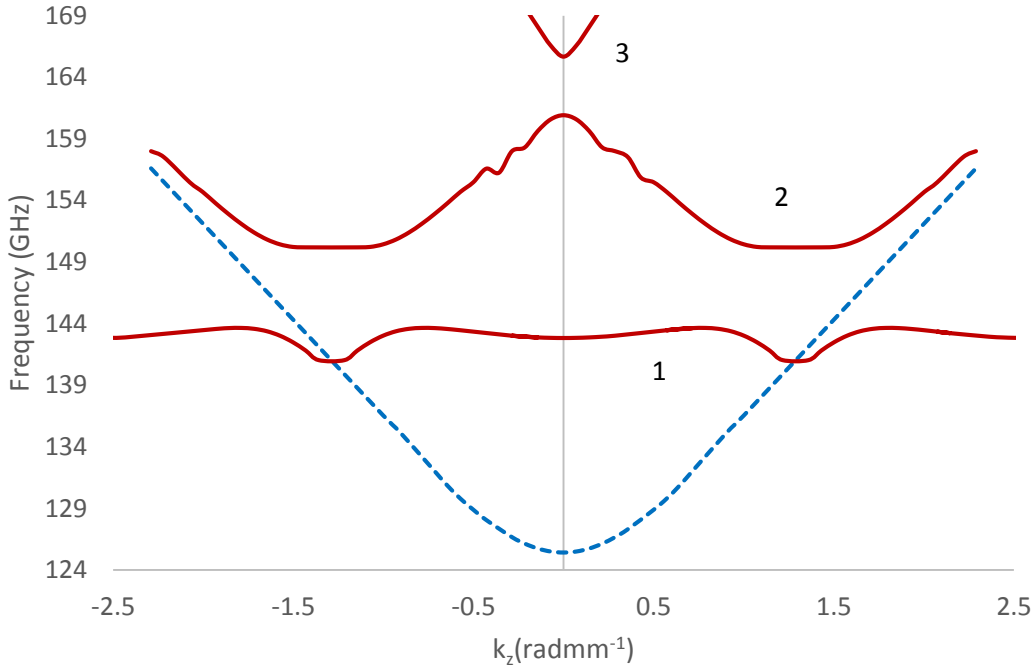

Figure 6.3.1. Dispersion plot for the 1.94mm PSL with Δr =35 μm mounted on a 0.41mm dielectric substrate with $\varepsilon = 4.3$ and obtained using the Eigenmode solver of CST Microwave Studio. The dashed blue line represents a volume mode within the dielectric while branches 1-3 (red lines) indicate possible coupled dispersions.

It was demonstrated in Chapter 3 that the structure of the dispersion plots is determined by the strength of the coupling between the volume and surface fields, α, and also by the detuning parameter Γ which is related to the frequency separation of the individual volume and surface modes. The frequency of the surface mode supported by the 1.94mm PSL at low incident angles is given by the experimental results of figure 5.2.6 (Chapter 5), while the cut-off frequency of the volume field is estimated from the CST MWS dispersion of figure 6.3.1. Approximate values of 125 GHz and 160 GHz (for the volume and surface fields respectively) were obtained from the numerical and experimental results allowing Γ to be evaluated using equation 3.2.2 (Chapter 3), stated below.

$$\Gamma = \frac{2\bar{k}_z c}{\sqrt{((\omega_0^v)^2 + (\omega_0^s)^2)}}$$

An approximate value of $\Gamma \cong 1.52$ was calculated from Eq.3.2.2 and used to obtain an analytical dispersion plot (figure 6.3.2) which was then compared to the CST MWS results of figure 6.3.1. The analytical dispersion was solved using the following parameters: $\Gamma \cong 1.52$, $\tilde{\Delta}=0.76$, $\alpha = 0.5$. Similarities can be drawn between the numerical and analytical dispersions. In particular, the upper coupled dispersion branches (2,3) and volume mode (blue dashed lines) of figure 6.3.1 resemble the coupled (red solid lines) and uncoupled volume field (dashed blue line) dispersions of figure 6.3.2.

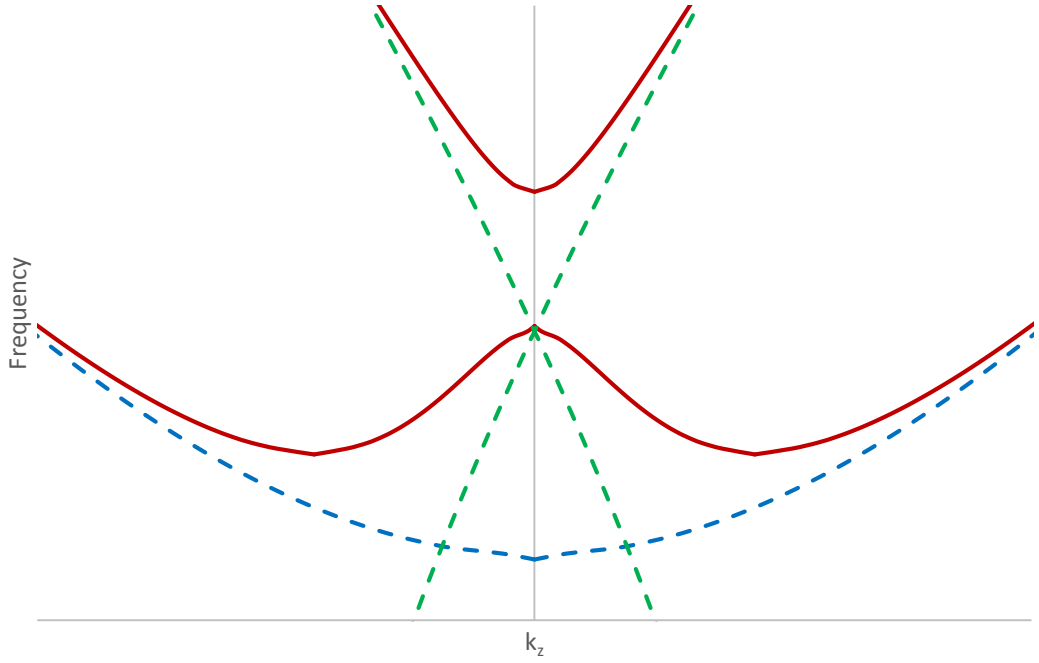

Figure 6.3.2. Analytical dispersion plot obtained from Eq.3.2.2 and solved for $\Gamma \cong 1.52$ using the mathematical software package MAPLE. The red plots indicate coupled dispersion branches, while the dashed blue and green lines represent the uncoupled volume and surface fields respectively.

Chapter 3 showed that, given sufficient coupling, and on the condition that $\Gamma \geq \sqrt{2}$, the surface field (which has an imaginary transverse wavenumber and therefore no cut-off frequency) is incorporated into the coupled dispersion of the structure, and cannot be separated from the contribution of the volume field. Although the surface field is not observed exclusively, the location at which the uncoupled surface field harmonics intersect one another governs the maximum and minimum frequencies of the coupled dispersion. For example, in the analytical dispersion of figure 6.3.2,

the maximum frequency of the lower dispersion branch (red line) coincides with the intersection of the uncoupled surface field harmonics (green dashed lines). This is also evident in the CST MWS dispersion of figure 6.3.1 where the maximum of branch 2 (161 GHz) matches the frequency of the surface field measured in the experimental study of the 1.94mm PSL with no substrate (figure 5.2.6).

On the other hand, when k_z is large, the coupled dispersion tends towards that of the uncoupled volume field and in certain cases, as demonstrated in Chapter 3, the coupled dispersion's lower branch overlays the dispersion of the uncoupled volume field i.e. when α is small as in figures 3.3.1.1 and 3.3.3.1 or when $\Gamma \approx \sqrt{2}$ (figure 3.3.2.3)). Consequently, even when the volume and surface fields are coupled, experimental resonances may exist close to the frequencies of the uncoupled volume and surface fields. The extent of the coupling α influences the frequency at which possible eigenmodes are located.

It was discussed in Chapter 2 that the coupling coefficient α of the cylindrical PSL varies directly with $\Delta r/r_0$ and therefore, increasing the corrugation depth of the planar PSL whilst maintaining the same dielectric thickness, effectively increases α. The CST MWS dispersion plot for the 1.94mm PSL with an increased corrugation depth of 0.1mm, mounted on the 0.41mm substrate with no copper backing, is presented in figure 6.3.3. The general appearance of the dispersion is similar to the previous example for the 1.94mm PSL with Δr =35 μm (figure 6.3.1). However, as expected, the dispersion branches have shifted slightly further apart due to the enhanced coupling. Branch 1 has shifted down from 143 GHz to 141GHz, while the upper branch (2) has moved up from 150 GHz to 151 GHz, increasing the separation of the branches by 3 GHz. The oscillations present in branch 2 can be reduced by

increasing the mesh refinement of the CST MWS model from ten cells per wavelength. However, this significantly increases the computation time.

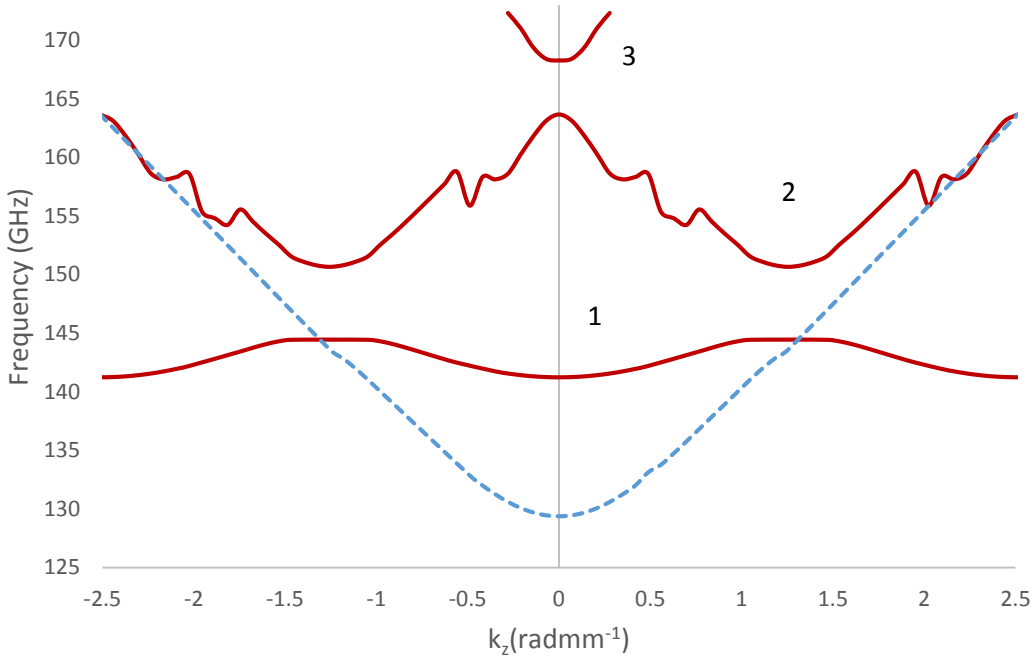

Figure 6.3.3. Dispersion plot for the 1.94mm PSL with Δr =0.1mm mounted on a 0.41mm dielectric substrate with $\varepsilon = 4.3$ and obtained using the Eigenmode solver of CST Microwave Studio. The dashed blue line represents a volume mode within the dielectric while branches 1-3 (red lines) indicate possible coupled dispersions.

The detuning parameter Γ, which influences the overall appearance of the dispersion, is controlled by the period of the PSL and the thickness and permittivity of the dielectric substrate. The effect of increasing ε, without changing the thickness of the substrate and implicitly increasing Γ, is investigated. Figure 6.3.4 shows the CST MWS dispersions for the 1.94mm PSL mounted on a 0.41mm dielectric substrate with ε =5.69 and $\Gamma \cong$1.63.

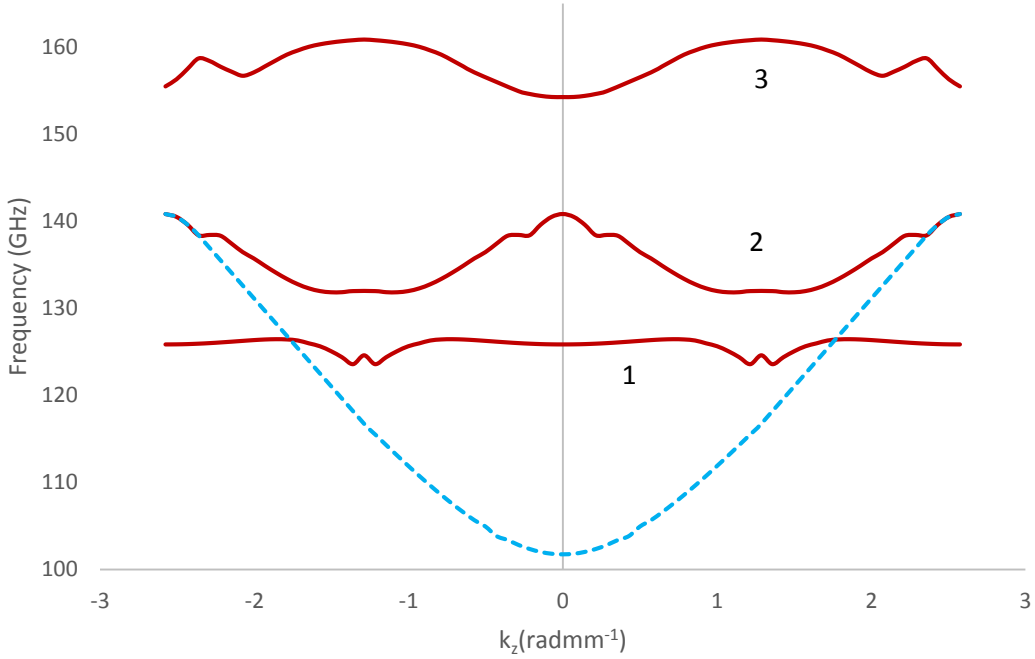

Figure 6.3.4. Dispersion plot for the 1.94mm PSL with Δr =35 μm mounted on a 0.41mm dielectric substrate with $\varepsilon = 5.69$ and obtained using the Eigenmode solver of CST Microwave Studio. The dashed blue line represents a volume mode within the dielectric while branches 1-3 (red lines) indicate possible coupled dispersions.

Although dispersion branches 1 and 2 resemble those of figures 6.3.1 and 6.3.2, the increase in ε from 4.3 to 5.69 reduces the cut-off frequency of the volume mode, causing both branches to shift down in frequency by approximately 18 GHz. As before, branch 3, characterised by maxima and minima at 161 GHz and 154 GHz, may describe coupling of volume and surface fields taking place close to the measured surface field. The altered appearance of branch 3 is due to the change in Γ (from 1.52 to 1.63) associated with the increased dielectric permittivity.

As expected, the dielectric permittivity ε has a significant effect on the location of the coupled eigenmodes, and in the following sections, the value of ε is chosen to match the dielectric samples used in the fabrication of the planar PSL structures. It is worth noting, however, that due to possible variations in the composition of FR-4, even between samples of the same thickness, as well as experimental uncertainties in the measurement of ε, a small deviation in ε may exist between the CST MWS model and the structures measured in the experiment. This is taken into account,

along with the differences discussed in §6.2, when comparing the numerical and experimental results.

Overall, the CST MWS dispersions show some correlation to the analytical dispersions obtained using MAPLE if the correct parameter values are chosen. It has been demonstrated that the coupled eigenmode should lie between the uncoupled volume and surface modes, although resonances associated with the individual surface and volume fields may also be observed. This may explain the additional resonances present in the 1.43mm substrates (when the dielectric losses affect the lattice synchronisation) and in all the substrates without the copper backing which is required to confine the volume field. Other behaviour, including coupling between volume field harmonics and Fabry Perot resonances, is also present to some extent.

6.4. Comparison of Experimental and Numerical Results

The CST MWS dispersion plots describing the planar PSL structures were compared to the experimental results by noting the frequencies of the coupled dispersions' maxima and minima points which indicate the positions of possible cavity eigenmodes. The frequencies of the experimental resonances were compared to the CST MWS dispersions for the PSLs mounted on the different substrates, including the high frequency 0.63mm PSL and the metadielectric structure. The differences between the numerical and experimental models, discussed in §6.2, were taken into account, allowing for small discrepancies between the two sets of results.

6.4.1. Planar PSLs with 0.41mm substrates

The CST MWS dispersion of the 1.50mm PSL mounted on the 0.41mm substrate (without the copper backing) is presented in figure 6.4.1.1 and compared to the experimental results of figure 5.6.1.1 Potential eigenmodes located at 155 GHz and 162 GHz, formed by coupled volume field space harmonics (blue dashed lines) may account for the experimental resonance at 159 GHz when θ_i =25. Two coupled dispersion branches (red lines) thought to arise from coupled volume and surface

modes, are observed between 180 GHz and 220 GHz. In particular, (1) which has a suitably flat profile with the potential to facilitate mode-locking in a well synchronised PSL, corresponds to the sharpest experimental resonance (~44dB) measured at 178 GHz and is indicative of coupled eigenmode formation. The upper branch (2) is formed close to the PSL's surface field, and has a minimum frequency at 209 GHz which may be linked to the experimental resonance at 205 GHz.

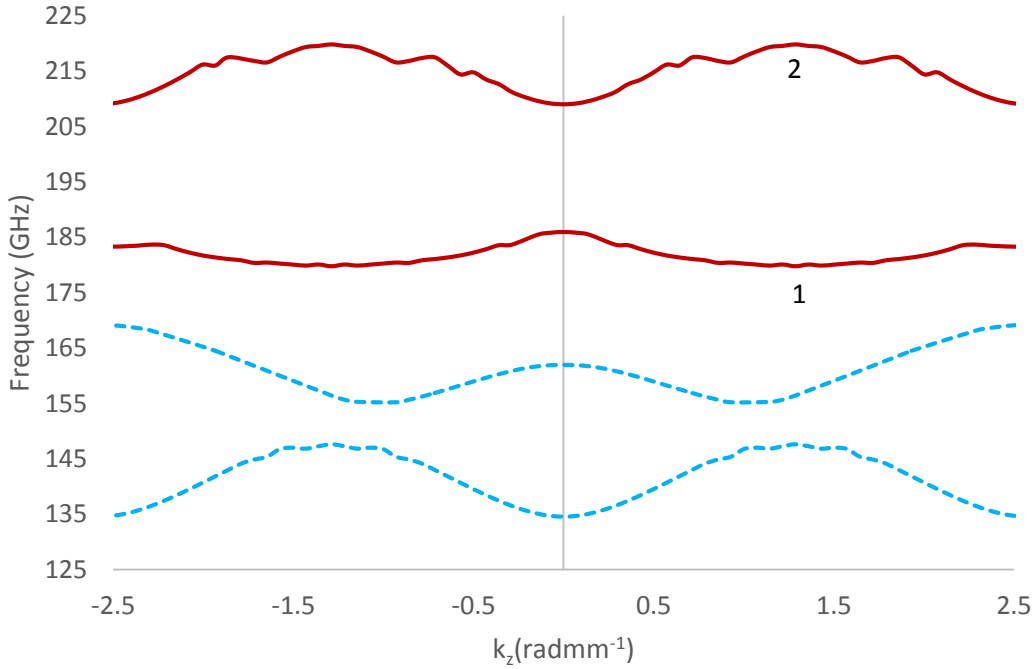

Figure 6.4.1.1. Dispersion plot for the 1.50mm PSL with Δr =35 μm mounted on the 0.41mm dielectric substrate with $\varepsilon = 5.69$ and obtained using the Eigenmode solver of CST Microwave Studio. The dashed blue lines represent volume modes coupled to neighbouring space harmonics while branches 1 and 2 (red lines) indicate possible coupled dispersions.

6.4.1.1. 1.50mm PSL with 0.41mm Copper-backed Substrate

Introducing the copper backing changes the EM properties of the structure. In chapter 5, the possible involvement of a TEM mode, coupling with the volume or surface modes of the structure and contributing to the sharp, and possibly mode-locked, resonances measured for the 1.50mm and 1.62mm PSLs (with the copper-backed 0.41mm substrates) was discussed. Figure 6.4.1.1.1 shows the numerical dispersion of the 1.50mm structure, plotted at low frequencies. As expected, a TEM

mode (black lines) is supported between the two conductors. The ± 1 spatial harmonics of the TEM mode, which cease to exist beyond 93 GHz, intersect one another and interact with a volume mode around 74 GHz. Although this may lead to coupling of the two modes, the resulting eigenmode lies below the measured frequency band (140-220 GHz). The CST MWS results show that, for the set of PSLs with $d_z \cong \lambda_{op}$, the TEM mode always exists below the measured frequency range, and is therefore neglected.

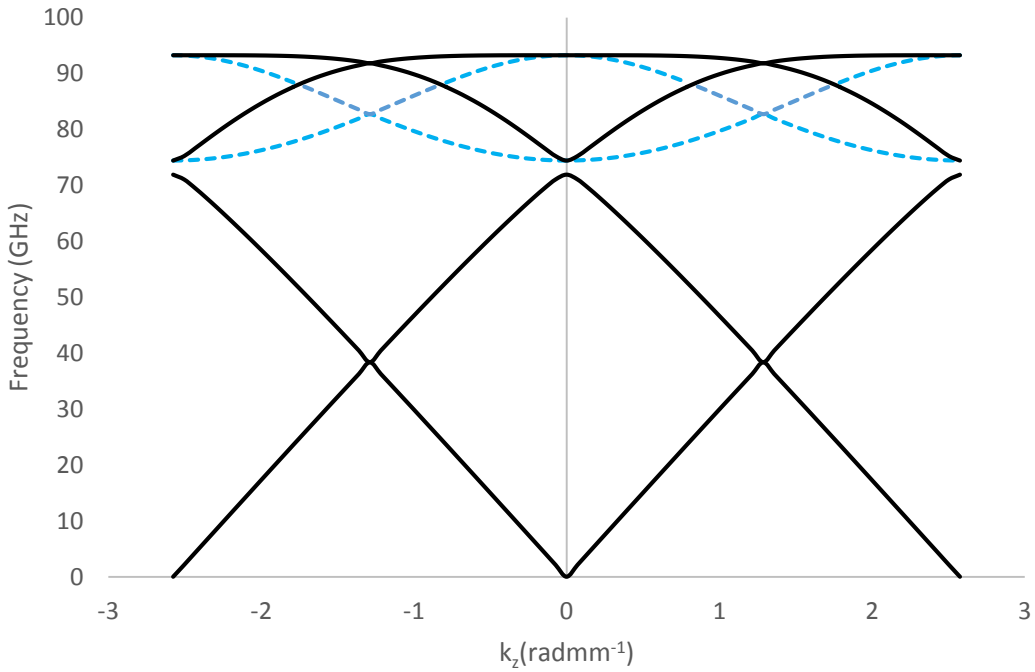

Figure 6.4.1.1.1. *Dispersion plot obtained using the Eigenmode Solver of CST MWS showing the space harmonics of the TEM mode (black lines) interacting with a coupled volume mode (dashed blue lines) at 74 GHz and 94 GHz, for the 1.50mm PSL with Δr =35 μm mounted on the 0.41mm copper-backed dielectric substrate with $\varepsilon = 5.69$.*

The dispersion plot for the 1.50mm PSL with the 0.41mm copper backed substrate at higher frequencies (figure 6.4.1.1.2) shows two possible coupled dispersions. Both dispersion branches are relatively flat across the frequency band, again demonstrating the potential for mode-locking. Branch 1, evident around 151 GHz, may correspond to the experimental resonance measured at 140 GHz. The relatively large deviation (~11 GHz) between the two results can be attributed to the various

differences between the numerical model and experiment, and may also be explained by a slight variation in ε, which may fluctuate throughout the set of 0.41mm samples. Branch 1 is intersected by the spatial harmonics of the volume field (dashed blue lines). Despite the common substrate, volume modes are observed at different frequencies in the 1.62mm, 1.74mm and 1.94mm PSLs (figures 6.4.1.2.1, 6.4.1.3.1 and 6.4.1.3.1, indicating that the volume modes are influenced not only by the dielectric thickness and permittivity, but by the periodicity of the structure as well. These volume modes, along with the surface field, contribute to the formation of the coupled dispersion branches.

It is interesting to note that the upper dispersion branch (2), formed around 170 GHz, lies close in frequency to the mode-locked resonance (~167 GHz) observed in the 1.50mm PSL with the thicker, 0.76mm copper-backed structure. The position of this upper branch may be largely determined by the surface field. Branch 2 is similar in appearance, though shifted down by 10 GHz, to branch 1 of the structure without the copper backing (figure 6.4.1.1). The increased coupling facilitated by the copper backing may shift the coupled branches, which would otherwise be formed close to the surface field, further towards the volume mode.

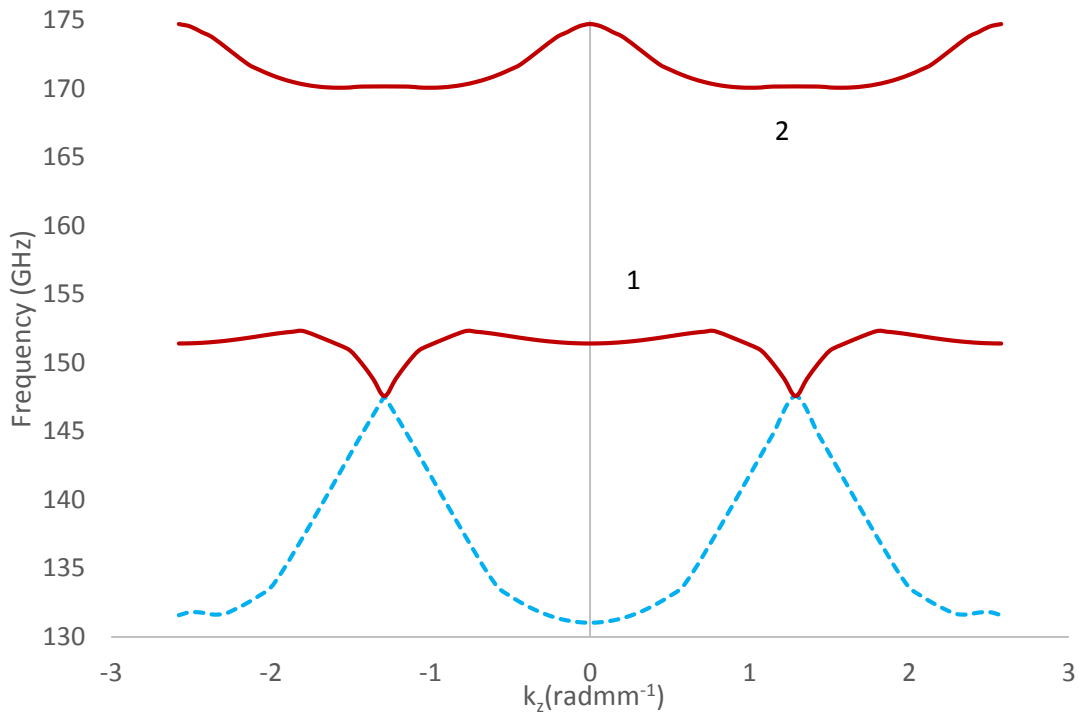

Figure 6.4.1.1.2. *Dispersion plot for the 1.50mm PSL with Δr =35 μm mounted on the 0.41mm copper-backed dielectric substrate with $\varepsilon = 5.69$ and obtained using the Eigenmode solver of CST Microwave Studio. The dashed blue lines represent volume modes coupled to neighbouring space harmonics while branches 1 and 2 (red lines) indicate possible coupled dispersions.*

6.4.1.2. 1.62mm PSL with 0.41mm Copper-backed Substrate

The CST MWS dispersion of the 1.62mm PSL mounted on the 0.41mm copper-backed substrate is presented in figure 6.4.1.2.1. The dashed blue lines represent volume modes contained within the dielectric, while the red plots indicate possible coupled dispersions. As with the dispersion of the 1.50mm PSL (figure 6.4.1.1.2), the spatial harmonics of the volume field intersect and contribute to the formation of branch 1, which manifests around 145 GHz and may relate to the experimental resonance at 140 GHz. Compared with the previous example, the cut-off frequency of the volume field is shifted down by around 6 GHz. Again, the upper dispersion branch (with maxima and minima at 164mm and 160mm respectively) coincides with the mode-locked resonance (~164 GHz) of the 1.62mm PSL with the 0.76mm copper-backed substrate.

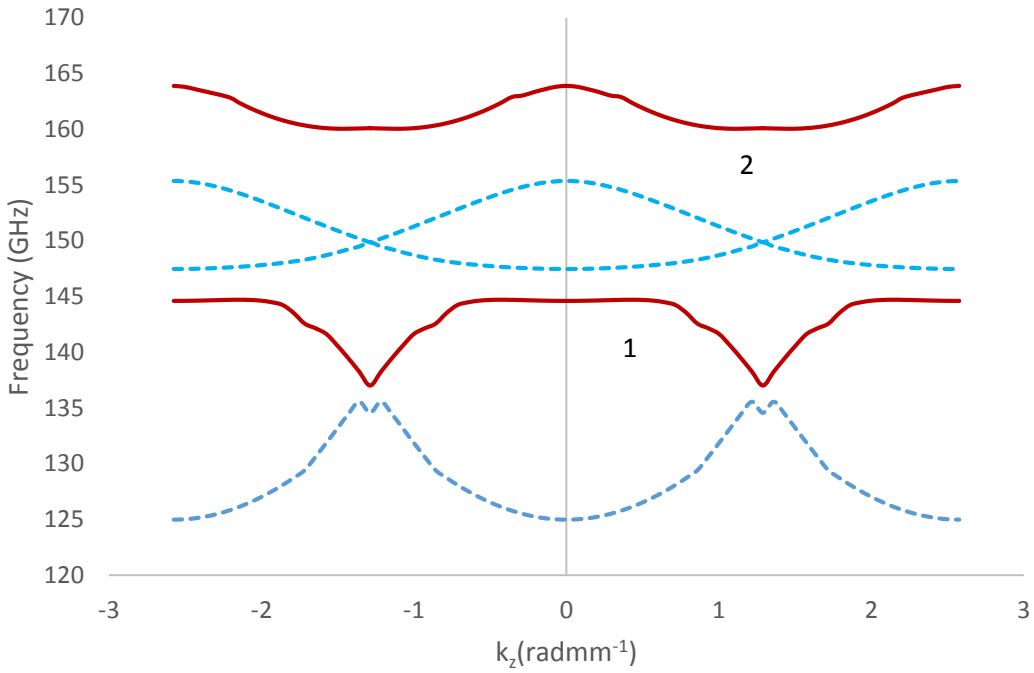

Figure 6.4.1.2.1. Dispersion plot for the 1.62mm PSL with Δr =35 μm mounted on the 0.41mm copper-backed dielectric substrate with $\varepsilon = 5.69$ and obtained using the Eigenmode solver of CST Microwave Studio. The dashed blue lines represent volume modes coupled to neighbouring space harmonics while branches 1 and 2 (red lines) indicate possible coupled dispersions.

6.4.1.3. 1.74mm PSL with 0.41mm Copper-backed Substrate

CST MWS dispersions for the 1.74mm PSL with the 0.41mm copper-backed substrate are provided in figure 6.4.1.3.1. The cut-off frequency of the lower volume field has shifted down by approximately 5 GHz compared to that of figure 6.4.1.2.1 confirming that the periodicity of the PSL influences the volume mode, with larger periods corresponding to lower cut-off frequencies. Although the upper volume field has shifted down by the same amount, the appearance of the dispersion has also changed. The flattened appearance of 1 is uncharacteristic of a simple volume mode and may indicate that the surface field is participating in coupling at this frequency, affecting the dispersive behaviour. The experimental resonance at 142.5 GHz was previously attributed to Fabry-Perot behaviour since the frequency was seen to shift up with angle. While this may be the case, it is also possible that the resonance corresponds to branch 1 of figure 6.4.1.3.1, which at 142 GHz, demonstrates close agreement with the experiment, and may represent coupled volume and surface

modes. Once again, dispersion branch 2 (with maxima and minima at 151 GHz and 154.5 GHz) is observed close to the frequency of the mode-locked resonance (~155 GHz) of the 1.74mm PSL etched onto the 0.76mm copper-backed substrate.

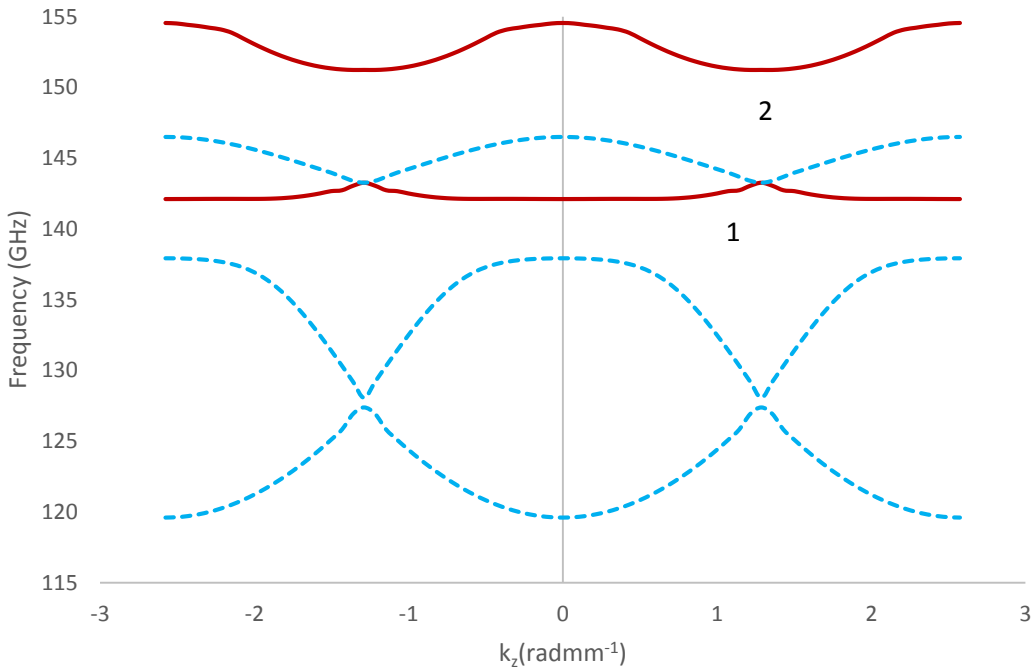

Figure 6.4.1.3.1. Dispersion plot for the 1.74mm PSL with Δr =35 µm mounted on the 0.41mm copper-backed dielectric substrate with $\varepsilon = 5.69$ and obtained using the Eigenmode solver of CST Microwave Studio. The dashed blue lines represent volume modes coupled to neighbouring space harmonics while branches 1 and 2 (red lines) indicate possible coupled dispersions.

6.4.1.4. 1.94mm PSL with 0.41mm Copper-backed Substrate

Finally, CST MWS results for the 1.94mm PSL etched onto the 0.41mm copper-backed substrate are provided in figure 6.4.1.4.1. The lower coupled dispersion branch has shifted below the measured frequency range as anticipated. The experimental results for this structure show a very weak resonance fixed at around 159 GHz for all angles of incidence. This may correspond to the maxima of the upper coupled dispersion branch at approximately 157 GHz.

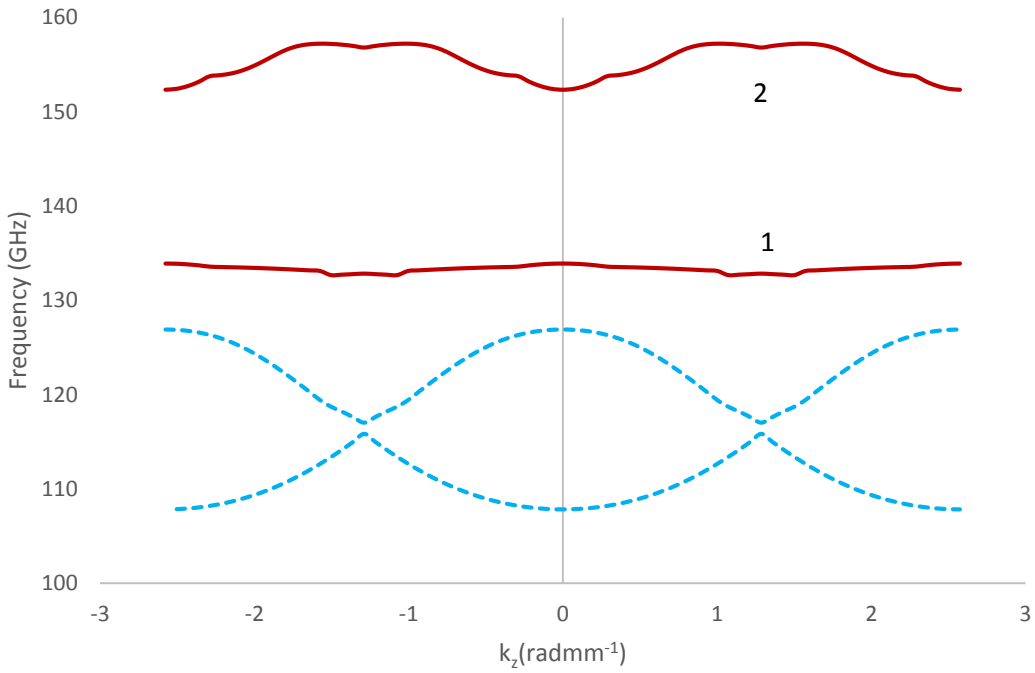

Figure 6.4.1.4.1 Dispersion plot for the 1.94mm PSL with Δr =35 μm mounted on the 0.41mm copper-backed dielectric substrate with $\varepsilon = 5.69$ and obtained using the Eigenmode solver of CST Microwave Studio. The dashed blue lines represent volume modes coupled to neighbouring space harmonics while branches 1 and 2 (red lines) indicate possible coupled dispersions.

It has been shown for the copper-backed structures that the TEM mode is not implicated in coupling at the frequency range of interest (140-220 GHz). It was also confirmed that the frequency of the volume field is influenced by the lattice periodicity with larger periods corresponding to lower cut-off frequencies. The simulations performed with CST MWS demonstrated two possible coupled dispersion branches indicating coupling of volume and surface fields at different frequencies. Taking into account known differences between the simulations and experiment, some correlation was found between the lower dispersion branches and the experimental resonances of the 1.50mm and 1.62mm PSLs. Since the experimental resonances, which do not exhibit a clear angular dependence, appear to be mode locked, only one eigenmode is formed and hence coupling associated with the higher dispersion branch is not observed.

The thin dielectric of the planar PSL is equivalent to a small radius r_0 when considering the PSL of cylindrical geometry, and from the theory developed in Chapter 2, it is known that $\alpha \propto \Delta r/r_0$. This, in addition to the reduced dielectric losses of the thinner FR-4, may lead to stronger coupling in the 0.41mm copper-backed structures, in comparison to the PSLs with the thicker substrates, and may explain the observation of mode-locked resonances at frequencies much lower than the surface field. For the 1.94mm PSL, the lower branch lies below the measured frequency range (140-220 GHz) and the weak experimental resonance at 159 GHz suggests possible eigenmode formation and mode-locking associated with the upper dispersion branch.

6.4.2. Planar PSLs with copper-backed 0.76mm substrates

6.4.2.1. 1.50mm PSL with 0.76mm Copper-backed Substrate

The CST MWS dispersion of the 1.50mm PSL with the copper-backed 0.76mm substrate presented in figure 6.4.2.1.1, shows two possible coupled dispersion branches. Both branches exist at frequencies close to the experimental resonance of figure 5.4.1, which appears 'mode-locked' at 168 GHz when measured at oblique incident angles. The eigenmode located at the minimum of dispersion branch 2 best matches this experimental result. However, closer to normal incidence, for instance at 30°, mode-locking is less effective and the eigenmode, now formed at 160 GHz, exhibits better agreement with branch 1. The maximum of branch 1, which exists at 164 GHz, appears to be formed by the coupled spatial harmonics of the volume field (dashed blue lines) and thus the surface field harmonics are expected to intersect further up the frequency band.

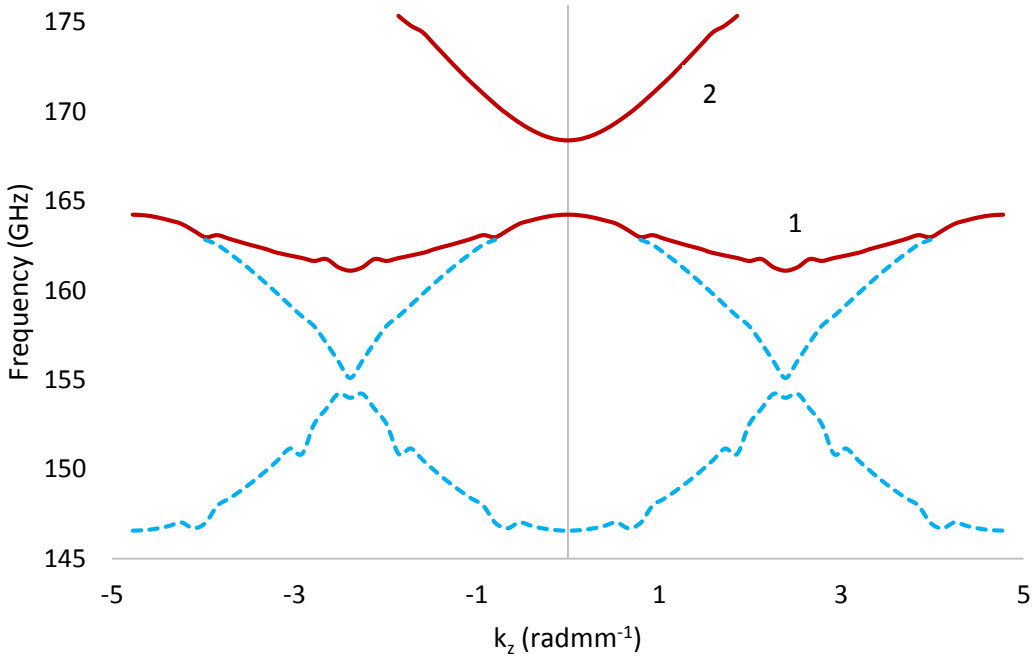

Figure 6.4.2.1.1. Dispersion plot for the 1.50mm PSL with Δr =35 µm mounted on the 0.76mm copper-backed dielectric substrate with $\varepsilon = 4.71$ and obtained using the Eigenmode solver of CST Microwave Studio. The dashed blue lines represent volume modes coupled to neighbouring space harmonics while branches 1 and 2 (red lines) indicate possible coupled dispersions.

6.4.2.2. 1.62mm PSL with 0.76mm Copper-backed Substrate

Two possible coupled dispersion branches (1 , 2) describing the 1.62mm PSL mounted on the 0.76mm copper-backed substrate are shown in figure 6.4.2.2.1. The volume mode at 142 GHz (blue dashed lines) is coupled to its neighbouring spatial harmonics and, as with the previous example, forms the maximum of branch 1. Together, the coupled dispersion branches predict the existence of potential eigenmodes at 154 GHz, 160 GHz, 163 GHz and 170 GHz. At the lowest incident angle (25°) the

experimental resonances evident at 152 GHz, 159 GHz and 167 GHz, all lie within $\pm$4GHz of one of the possible eigenmodes shown in figure 6.4.2.2.1.

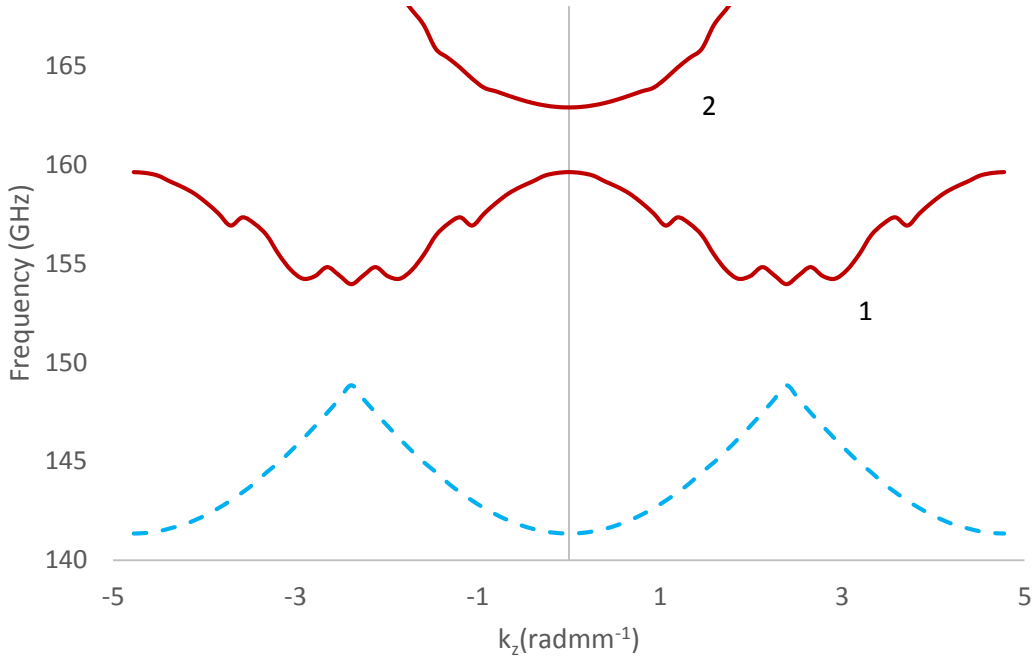

Figure 6.4.2.2.1. Dispersion plot for the 1.62mm PSL with Δr =35 µm mounted on the 0.76mm copper-backed dielectric substrate with $\varepsilon = 4.71$ and obtained using the Eigenmode solver of CST Microwave Studio. The dashed blue lines represent volume modes coupled to neighbouring space harmonics while branches 1 and 2 (red lines) indicate possible coupled dispersions.

6.4.2.3 1.74mm PSL with 0.76mm Copper-backed Substrate

Two dispersion branches, describing the possible eigenmodes associated with the 1.74mm PSL with the 0.76mm copper-backed substrate, are illustrated in figure 6.4.2.3.1. As before, the maxima and minima points of these branches (144 GHz, 149 GHz and 156 GHz) indicate the frequency position of potential eigenmodes. When θ_i =25°, the experimental findings of figure 5.4.3 demonstrate resonances at 142 GHz, 151 GHz and 157 GHz, all of which appear within $\pm$2 GHz of the eigenmodes predicted by CST MWS. Mode locking is most effective at $\theta_i \geq$50 when the experimental resonance is fixed at 156 GHz, corresponding to the maximum frequency of branch 2.

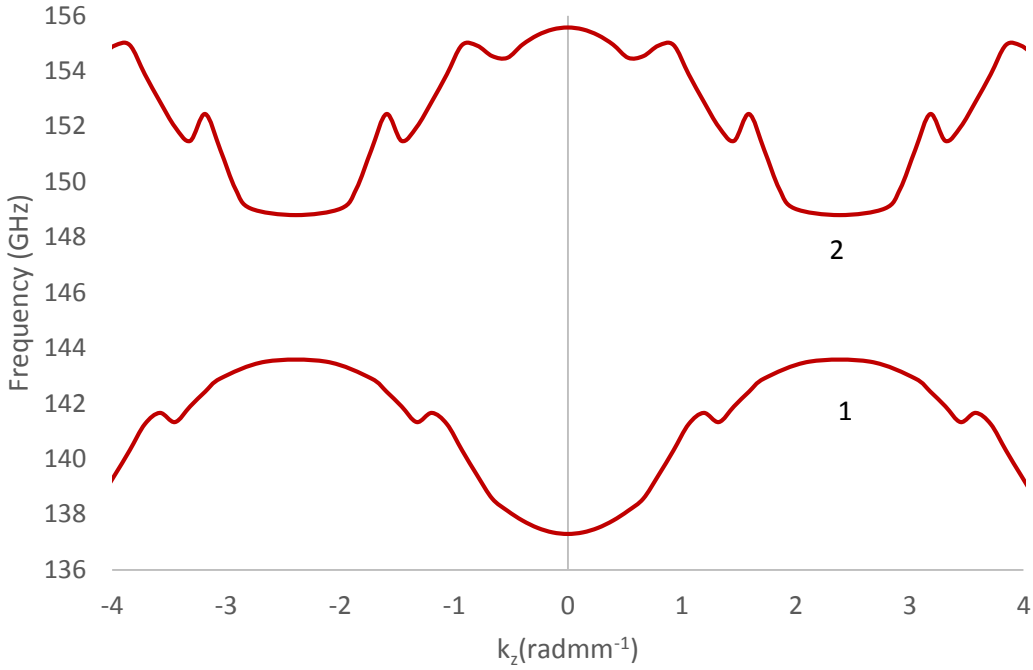

Figure 6.4.2.3.1. Dispersion plot for the 1.74mm PSL with Δr =35 µm mounted on the 0.76mm copper-backed dielectric substrate with $\varepsilon = 4.71$ and obtained using the Eigenmode solver of CST Microwave Studio. The red plots (1,2) indicate coupled dispersion branches and the maxima and minima represent possible eigenmodes.

In chapter 5 (figures 5.2.2-5.2.6) it was established that, at higher incident angles, the surface mode is shifted down in frequency, possibly increasing its ability to couple with the volume mode by reducing the frequency separation between the two modes. This may explain why mode locking is typically observed at higher angles of incidence. As the surface mode shifts down in frequency, the parameter value of Γ increases, modifying the overall appearance of the coupled dispersion at higher incident angles.

6.4.2.4. 1.94mm PSL with 0.76mm Copper-backed Substrate

The CST MWS dispersion diagram for the 1.94mm PSL mounted on the 0.76mm copper-backed substrate is presented in figure 6.4.2.4.1. Three possible coupled dispersion branches are observed in the frequency range of interest. The lowest branch (1) lies outside the measured frequency range, while the maxima and minima of the middle branch (2) correspond to ~152 GHz and ~147 GHz respectively. Both demonstrate good agreement with the experimental results where mode locking is

observed around 146.5 GHz at higher incident angles and ~150 GHz at angles below 50°. The potential eigenmodes located at the maximum and minima of branch 2 are close in frequency, and the experimental results suggest that mode selection between the two is determined by the incident angle.

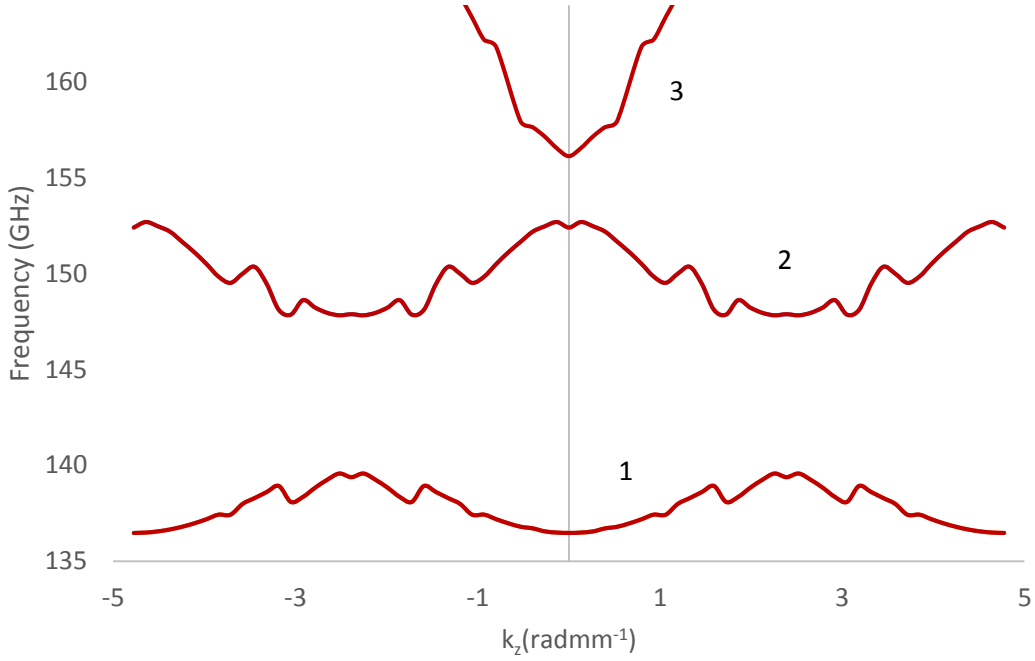

Figure 6.4.2.4.1. Dispersion plot for the 1.94mm PSL with Δr =35 µm mounted on the 0.76mm copper-backed dielectric substrate with $\varepsilon = 4.71$ and obtained using the Eigenmode solver of CST Microwave Studio. The red plots (1-3) indicate coupled dispersion branches and the maxima and minima represent possible eigenmodes.

6.4.3. 1.94mm PSL with 1.43mm Copper-backed Substrate

The EM behaviour when the dielectric thickness is further increased is explored by modelling the 1.94mm PSL with the 1.43mm copper-backed substrate. The experimental resonance of figure 5.7.2.3 appears mode-locked at its lower edge (~149 GHz) and is centred around 151 GHz at 25°, correlating to the minimum frequency of dispersion branch 1 in figure 6.4.3.1. A weaker resonance, evident around 165 GHz at 25°, may correspond to the maxima of dispersion branch 2. The

uppermost resonance, manifesting around 172 GHz, is seen from figure 5.7.2.3 to shift up with increasing incident angle, and is most likely associated with Fabry-Perot behaviour. It is important to note that lower order volume modes, as well as the TEM mode supported between the two conductors, exist below the plotted frequency range. When modelling these structures, a large number of modes (∼50) were considered and for clarity only those in the frequency ranges of interest, as determined by the experimental results, are presented. As expected, this structure with the largest cavity dimensions supports lower frequency volume modes than the PSLs mounted on the 0.41mm and 0.76mm substrates. These lower order modes are neglected in the present study.

As stated previously, the CST MWS model neglects the dielectric loss. The increased losses, associated with the thicker 1.43mm dielectric, may lead to extra experimental resonances (compared to the same PSL with the 0.41mm or 0.76mm copper-backed substrate) occurring due to poor lattice synchronisation. In the ideal case of a loss-free dielectric, it is expected that the PSL will be more effectively synchronised, facilitating coupling at just one of the possible frequencies indicated in figure 6.4.3.1.

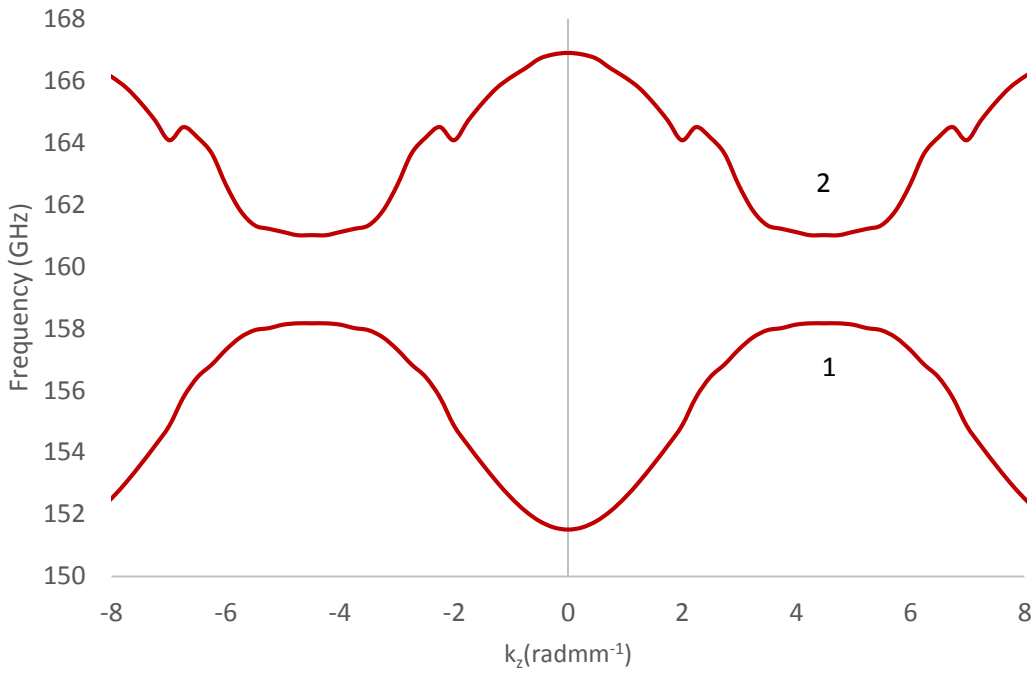

Figure 6.4.3.1. Dispersion plot for the 1.94mm PSL with Δr =35 μm mounted on the 1.43mm copper-backed dielectric substrate with $\varepsilon = 4.71$ and obtained using the Eigenmode solver of CST Microwave Studio. The red plots (1-3) indicate coupled dispersion branches and the maxima and minima represent possible eigenmodes.

6.4.4. 0.63mm Planar PSL Modelled at 325-500 GHz

The 0.63mm PSL with the 0.76mm copper-backed substrate was modelled at 325-500 GHz to investigate the coupling of volume and surface modes at higher frequencies. The experimental results demonstrate mode-locking around 370 GHz for all incident angles. This corresponds to the maxima of the uppermost coupled dispersion branch (figure 6.4.4.1). Both the CST MWS dispersion and experimental results exhibit similar behaviour to that observed for the set of 140-220 GHz PSLs, verifying the scalability of the structures.

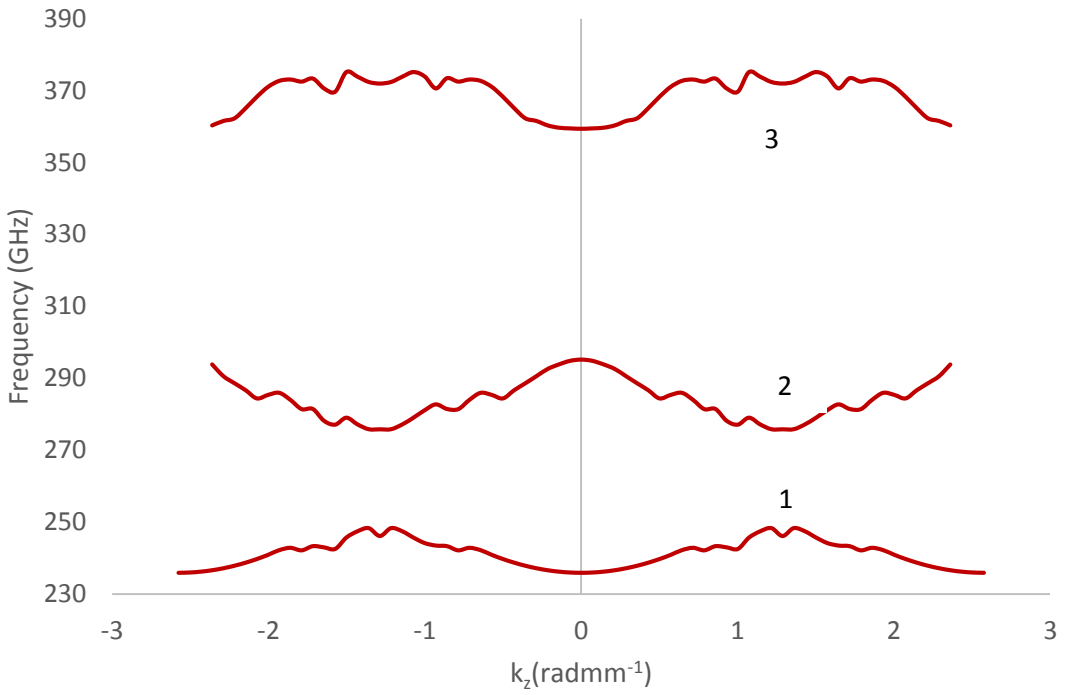

Figure 6.4.4.1. Dispersion plot obtained using the Eigenmode Solver of CST MWS showing coupled dispersion branches for the 0.63mm PSL with Δr =35 µm mounted on the 0.76mm copper-backed dielectric substrate with $\varepsilon = 4.71$ and modelled at 325-500 GHz.

6.4.5. 0.63mm Planar PSL Modelled at 140-220 GHz (Metamaterial)

When the 0.63mm PSL is measured at 140-220 GHz, thus behaving more like a conventional metamaterial, a distinct resonance ranging from 178 GHz to 187 GHz depending on the incident angle, is observed. Despite these experimental observations, no obvious coupling between volume and surface fields is evident in the dispersion plots obtained from the CST MWS model. However, according to figure 6.4.5.1, the TEM mode exists up to frequencies of around 220 GHz, allowing for possible coupling with volume fields in the 140-220 GHz range. While the lowest volume field (occurring at 89 GHz) lies outside the measured frequency region, the volume field at 176 GHz, which is intersected by the TEM mode at 183 GHz, may account for the sharp resonance of figure 5.10.1. This may explain the behaviour of the measured resonance which, unlike the resonances associated with the coupled volume and surface modes observed in the set of 140-220 GHz PSLs, shifts up in

frequency with increasing incident angle. Other resonances exhibiting this characteristic are possibly attributed to Fabry-Perot behaviour

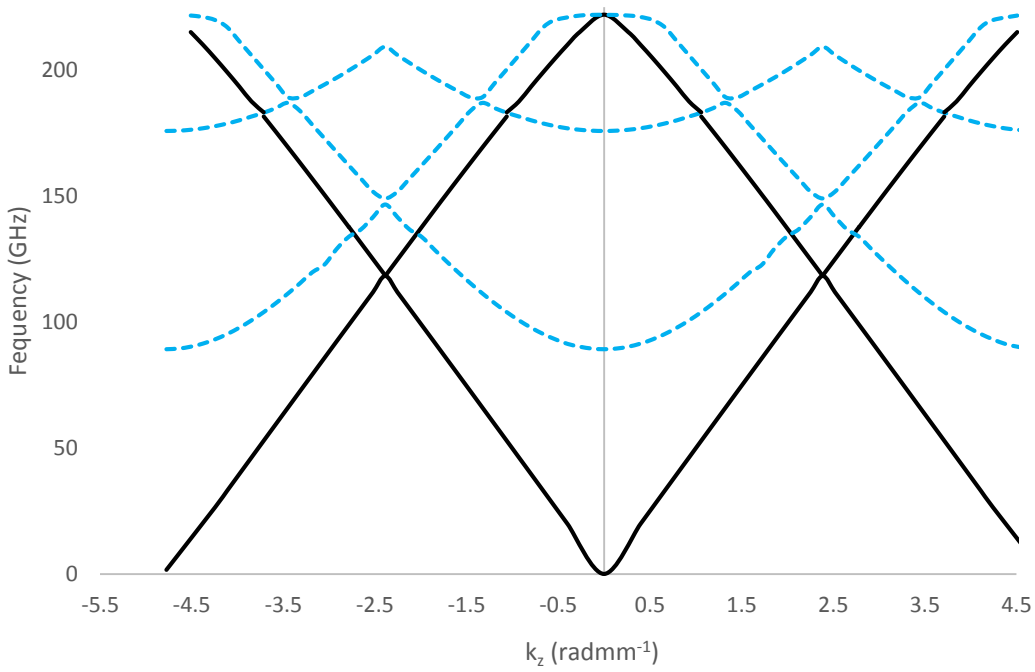

Figure 6.4.5.1 Dispersion plot obtained using the Eigenmode Solver of CST MWS for the 0.63mm PSL modelled at 140-220 GHz. The 0.63mm PSL is thought to behave like a metadielectric at this frequency range. The TEM mode (black lines) intersects the two volume modes (blue dashed lines) around 133 GHz and 183 GHz.

6.5. Chapter Conclusions

In conclusion, the numerical dispersions of eigenmodes formed by the coupling of volume and surface modes have been studied and compared to the experimental results, allowing some of the complex EM behaviour to be interpreted. Generally, close agreement between the CST MWS dispersion plots and the experimental results was demonstrated. Furthermore, strong similarities were observed between the 1.94mm PSL (with the 0.41mm substrate) and the analytical dispersion with equivalent parameters, thus linking the CST MWS dispersions with the theory developed in chapter 2 for the cylindrical PSL with large radius.

The experimental results were compared to the maxima and minima of the CST MWS dispersion branches which indicate the location of potential eigenmodes. When

coherent lattice synchronisation is achieved, leading to the observation of a single mode-locked resonance, coupling occurs at just one of these possible frequencies. This behaviour, observed in the PSLs with the 0.76mm copper-backed substrates, as well as the 1.50mm and 1.62mm PSLs with the 0.41mm copper-backed substrates, increases the structures' suitability for use as the interaction region of a high-power source.

Multiple resonances can arise for various reasons including the formation of additional eigenmodes associated with the individual volume and surface modes, especially in the case of weak coupling. Also, the surface mode of the PSL may interact with different volume modes inside the substrate, resulting in several possible coupling zones. In some cases, additional resonances may be attributed to coupling between neighbouring volume field harmonics.

The manifestation of more than one resonance suggests that the lattice is not ideally synchronised and occurs when the metal backing is not in place to confine the volume field, or when the dielectric losses impede the synchronisation. The PSLs with the 1.43mm substrates do not exhibit mode-locking, despite the copper backing, due to large dielectric losses (associated with the increased thickness) inhibiting the synchronisation of the lattice and resulting in weak coupling at various frequencies. The scalability of the PSLs has been demonstrated by modelling the 0.63mm PSL with the copper-backed 0.76mm substrate at 325-500 GHz and comparing the dispersion to the experimental findings. Once again, the structure is mode-locked and behaves much like the set of 140-220 GHz PSLs.

Finally, it has been shown that the 0.63mm PSL displays unique EM characteristics when modelled at the 140-220 GHz frequency band, where it becomes more like a conventional metamaterial. The potential for TEM involvement at this frequency range was established as a possible explanation for the structure's distinctive behaviour.

7 - Conclusions and Future Work

7.1 Conclusions

The focus of the theoretical, numerical and experimental work described in this thesis was the observation and understanding of the role of PSLs in the coupling of volume and surface fields, resulting in the formation of a cavity eigenmode. The theory presented in this thesis was developed for a PSL with cylindrical geometry under the assumption that $r_0 \gg \lambda$. Planar geometry rather than a cylindrical geometry was adopted in the numerical modelling and experimental measurements in order to investigate and demonstrate the fundamental "proof of principle" coupling between the volume and surface fields. Planar PSLs were fabricated by etching copper-coated dielectric substrates and under certain circumstances, coherent eigenmode formation was observed. In this work the planar PSLs were not intended for use within electron-beam-driven, high power coherent sources. However, conformal mapping allows PSLs in planar geometry to be mapped into PSLs in cylindrical geometry that are compatible with the construction of high power electron-beam-driven sources. The conclusions of the theoretical, experimental and numerical work presented in this thesis are summarised in §7.1.2 -7.1.4 while potential future work is discussed in §7.2.

7.1.1. Theoretical Study of PSLs

A theoretical description of a PSL based on an oversized cylindrical waveguide with a very large mean radius ($r_0 \gg \lambda$) was presented. Due to the assumption that $r_0 \gg \lambda$, the theoretical studies provide an approximate description of the PSLs in planar geometry as well as the cylindrical PSLs for which the theory was developed. As stated previously, conformal mapping allows PSLs in planar geometry to be mapped into PSLs in cylindrical geometry. The theoretical description of the PSL was divided into two main parts. Initially, the corrugated inner wall of the structure with $\Delta r \ll \lambda_{op}$ was described as an effective metadielectric, or high-impedance layer, by defining the field structure in the two distinct (air and dielectric) regions and applying known boundary conditions at the lattice-air interface as laid out in (Konoplev, MacLachlan et. al 2011). Using this approach led to a dispersion equation describing the hybrid surface field and an expression for the refractive index of the metadielectric close to the structure's resonant frequency. In the second (part

of the theoretical study, possible scattering mechanisms were explored and coupled wave equations were derived using the method of fictitious magnetic sources, where the structure was described as a cylindrical waveguide with a magnetic surface current in place of the corrugation at the inner wall. An analytical expression for the coupling coefficient, describing the strength of the coupling between the volume and surface fields, was derived using this method.

A coupled dispersion equation was obtained by renormalising the coupled wave equations derived using the method of fictitious magnetic sources for the oversized cylindrical PSL as published in (Konoplev, MacLachlan et al. 2012). An analytical study was carried out by varying the lattice parameters and coupling coefficient using the mathematical software package MAPLE (Konoplev, MacLachlan et al. 2012, MacLachlan, Konoplev et al. 2013). It was shown that, under certain conditions, when driven by a suitable electron beam, the structure is capable of supporting a Cherenkov instability, demonstrating the potential of PSLs for use in electron-beam-driven high power, coherent sources

7.1.2. Experimental Set-up and Results

A description of the chemical etching procedure used to fabricate the set of PSL structures mounted on dielectric substrates, with and without the copper backing, was provided. Photographs of the planar PSLs taken using a Hirox KH-770 Digital Microscope were presented. The tendency for structures to become over or under-etched due to non-uniform etching was discussed, and the presence of defects in some of the samples was demonstrated. The importance of using an appropriate set of waveguide horns to avoid mode conversion at higher frequencies was established. Refractive indices of 2.38±0.03, 2.25±0.02 and 2.11±0.01, as reported in (MacLachlan, Phipps et.al 2014), were determined for the 0.41mm, 0.76mm and 1.43mm dielectric samples respectively, using an Anritsu Vector Network Analyser (VNA) to measure the samples' phase. Further preliminary measurements showed that, at the measured frequencies, the structures do not behave like diffractive surfaces, and maximum reflected power was achieved by setting the angle of the receiving horn equal to the incident angle, as stated in (MacLachlan, Phipps et al. 2014).

Experiments were first performed for the simplest structures, consisting of copper PSLs without substrates. These structures, with no well-defined waveguide boundaries to support volume waves, allowed exclusive study of the surface field. Surface currents

induced in the copper flow around each unit cell and are scattered by the lattice perturbations to form a surface field, which in turn interferes with the reflected signal of the PSL, leading to a sharp resonance. This resonance was seen to shift down the frequency band with increasing lattice period allowing the PSLs to be tailored to operate at a specific frequency. Transmission measurements of the PSLs showed similar behaviour, with the transmitted frequencies corresponding to the frequency of surface field resonances.

Measurements were made over a range of angles, where it was discovered that increasing the incident angle also caused the resonance to shift down in frequency. This was attributed to a phase shift introduced by the angle of the radiation striking the PSL in a non-uniform manner. Though neighbouring cells are effectively synchronised by the surface current, without the substrate in place to support a volume field (which acts as the "global oscillator", driving possible collective phenomena) the individual scatterers oscillate out of phase with one another. This concept, shown schematically in (MacLachlan, Phipps et al. 2013), may explain why mode-locking was observed only in the case of coherent lattice synchronisation.

Coherent cavity eigenmode formation was demonstrated for the set of PSLs mounted on the 0.76mm copper-backed substrates (MacLachlan, Phipps et al. 2014, 2015), including the shorter wavelength 0.63mm PSL, establishing the potential for achieving single mode operation through the coupling of volume and surface fields and verifying the scalability of the structures. When the required conditions for cavity eigenmode formation were satisfied, the resulting resonance was locked to a particular frequency which did not vary with incident angle. This 'mode-locked' behaviour was typically observed at higher incident angles, possibly due to the reduced frequency separation between the volume and surface fields facilitating coupling between the two fields. The reproducibility of these important results was demonstrated by re-assembling the experimental set-up and repeating measurements on separate occasions over the course of several months (MacLachlan, Phipps et al. 2014, 2015).

The sharp resonances measured in the 0.41mm copper-backed structures were also characteristic of a coupled eigenmode, especially in the structures with smaller lattice periods. Numerical modelling (discussed in §7.1.4) ruled out the possibility of coupling between the surface field and a TEM type mode. Coherent eigenmode formation was not

observed in the samples without the copper backing (required to confine the volume field) or when the dielectric losses were large, disrupting the coherent synchronisation of the lattice. Weak coupling, however, induced by internally reflected volume waves within the dielectric, led to the observation of incoherent coupled modes in the PSLs mounted on the dielectric substrates (without the copper backing) reported in (MacLachlan, Phipps et al. 2014, 2015). In this case, multiple resonances were measured, all of which varied with angle, due to inadequate synchronisation of the PSL. This was also true of the PSLs mounted on the 1.43mm copper-backed substrates as a consequence of their large dielectric losses and capacity to become overmoded.

The shorter wavelength 0.63mm PSL, when measured at the 140-220 GHz frequency band where it is expected to behave more like a conventional metamaterial, displayed unique EM characteristics. A sharp resonance, shifting up in frequency with increasing incident angle (in the opposite direction to the larger wavelength PSLs which behave more like photonic structures) was observed. Finally, the importance of the dielectric was established through the study of the "air-gap" structures, which showed that without the dielectric substrate to support the volume mode, the cavity eigenmode was not coherently formed. Although a resonance corresponding to possible eigenmode formation was observed in certain cases, this was not consistent at all angles, and the observed resonances were not mode-locked.

7.1.3. Numerical Modelling of Planar PSLs

Dispersion diagrams for the planar PSLs were obtained using the Eigenmode Solver of the modelling software 'CST Microwave Studio' (CST MWS) and compared to the analytical dispersion diagrams and experimental results. When appropriate parameter values were chosen, strong similarities between the analytical dispersion (plotted using MAPLE) and the CST MWS dispersion were reported, showing a correlation between the theory developed for the cylindrical PSL with $r_0 \gg \lambda$ and the numerical model of the planar PSLs. Taking into account the notable differences between the CST MWS model and the experimental measurements, good agreement was demonstrated between the frequency of the experimental resonances and the location of the coupled eigenmodes predicted by the maxima and minima points of the CST MWS dispersions. The results of the CST MWS modelling, combined with the analytical MAPLE dispersions, suggested that the occurrence of multiple resonances in the weakly coupled structures, may correspond to the separate

branches of the coupled dispersion. It was evident, for the case of weak coupling, that eigenmodes exist close to the frequencies of the individual volume and surface fields. Typically, the best-defined coupled eigenmode was found to lie between the two. It was demonstrated in both theory (Konoplev, MacLachlan et al. 2012) and modelling that the coupled dispersion's branches move further apart in the case of strong coupling. This may provide further explanation as to why only one sharp resonance is observed in the measured frequency range for the well synchronised, mode-locked structures, where strong coupling is present. The potential for the surface field to couple with different volume modes within the dielectric, as well as the possibility of coupling between the volume field's spatial harmonics, was established through numerical modelling.

7.2. Future Work

Future work may involve the construction of PSLs mounted on low-loss substrates, using dielectric material intended for use at microwave frequencies and beyond. This may lead to the observation of cavity eigenmodes with a higher Q-factor than shown in this work. Mode selection in highly over-moded planar structures can then be studied by increasing the thickness of the low-loss dielectric, thereby increasing the cavity dimensions and enhancing the structure's capacity for a high output power when mapped into cylindrical coordinates and coupled with a suitable electron beam. Further experimental measurements may determine the extent to which the low-loss substrate can be increased before the coherent lattice synchronisation starts to break down and mode-selection can no longer be achieved. In doing so, ways of improving the experimental alignment by arranging the PSL and waveguide horns with greater precision, and considering the use of an automated system configured to measure results over the full angular range, could be explored.

Continuation of the research presented in this thesis may also include converting a planar PSL, of the type studied in this work, into cylindrical geometry using conformal mapping with a view to eventually coupling energy into the structure. Further studies into the structure's behaviour when the PSL is pushed further into the metamaterial regime is another interesting topic of future research. All the PSLs considered are scalable and therefore the concepts discussed in this work are applicable to a broad range of frequencies throughout the microwave and mm-wave range and stretching into the THz and far-infrared regions of the spectrum. Manufacturing ever smaller scale PSL structures for even shorter

wavelengths becomes more difficult. Extension of this work to study higher frequency structures may therefore involve some investigation into alternative manufacturing techniques.

Another possible avenue of research, related to the realisation of high frequency structures, is the excitation of surface polaritons, which can be generated on thin, film metal surfaces in place of the lattice corrugation, and form the basis of novel structures such as polaritonic crystals (Zayats, Smolyaninov et al.2004) designed to act as two-dimensional photonic crystals for surface polaritons. The innovation of using a nanometal film with dielectric-medium loading, and then exciting surface polaritons by a uniformly moving electron bunch has been shown to be able to create a novel tunable surface polariton Cherenkov light radiation source for the visible light and ultraviolet frequency regimes (Shenggang Liu, Zhang et al. 2012) and may be applied to this work in the future.

References

Abraham, E., A. Younus, A. El Fatimy, J. C. Delagnes, E. Nguéma and P. Mounaix (2009). "Broadband terahertz imaging of documents written with lead pencils." Optics Communications **282**(15) 3104-3107

Afzalzadeh, R (1998) "Dielectric constant measurements of finite-size sheet at microwave frequencies by pseudo-Brewster's angle method," *IEEE Transactions on Microwave Theory and Techniques* **46**(9) 1307-1309

Barnes, W., T. Priest, S. Kitson and J. Sambles (1996) “Photonic Surfaces for Surface-Plasmon Polaritons”, Physical Review B **14**(7) 1654-1659

Barnes, W. L., A. Dereux and T. W. Ebbesen (2003). "Surface plasmon subwavelength optics." Nature **424**(6950) 824-830

Benabid, F., J. C. Knight, G. Antonopoulos and P. S. J. Russell (2002). "Stimulated Raman Scattering in Hydrogen-Filled Hollow-Core Photonic Crystal Fiber." Science **298**(5592) 399-402

Bergman, D. J. and M. I. Stockman (2003). "Surface plasmon amplification by stimulated emission of radiation: Quantum generation of coherent surface plasmons in nanosystems." Physical Review Letters **90**(2) 027402

Bratman, V., G. G. Denisov, N. Ginzburg and M. Petelin (1983). "FEL's with Bragg reflection resonators: Cyclotron autoresonance masers versus ubitrons." Quantum Electronics, IEEE Journal of **19**(3) 282-296

Bratman, V. L., B. S. Dumesh, A. E. Fedotov, P. B. Makhalov, B. Z. Movshevich and F. S. Rusin (2010). "Terahertz orotrons and oromultipliers." IEEE Transactions on Plasma Science **38**(6) 1466-1471

Brewster, D(1815) "On the laws which regulate the polarisation of light by reflection from transparent bodies," Philosophical Transactions of the Royal Society of London, **105** 125-159

Burt, G., S. V. Samsonov, K. Ronald, G. G. Denisov, A. R. Young, V. L. Bratman, A. D. R. Phelps, A. W. Cross, I. V. Konoplev, W. He, J. Thomson and C. G. Whyte (2004). "Dispersion of helically corrugated waveguides: Analytical, numerical, and experimental study." Physical Review E **70**(4) 046402

Carr, G. L., M. C. Martin, W. R. McKinney, K. Jordan, G. R. Neil and G. P. Williams (2002). "High-power terahertz radiation from relativistic electrons." Nature **420**(6912) 153-156

Clarricoats, P. J. B., Oliver, A. D. (1984) “Corrugated Horns for Microwave Antennas”, Peter Peregrinus Ltd, London

Cook, A. M., R. Tikhoplav, S. Y. Tochitsky, G. Travish, O. B. Williams and J. B. Rosenzweig (2009). "Observation of narrow-band terahertz coherent cherenkov radiation from a cylindrical dielectric-lined waveguide." Physical Review Letters **103**(9) 095003

Cooke, S. J. and G. G. Denisov (1998). "Linear theory of a wide-band gyro-TWT amplifier using spiral waveguide." IEEE Transactions on Plasma Science **26**(3) 519-530

Corson, D. R. and P. Lorrain (1962). Introduction to electromagnetic fields and waves, W. H. Freeman, San Francisco

Cross, A. W., I. V. Konoplev, A. D. R. Phelps and K. Ronald (2003). "Studies of surface two-dimensional photonic band-gap structures." Journal of Applied Physics **93**(4) 2208-2218

Cross, A. W., I. V. Konoplev, K. Ronald, A. D. R. Phelps, W. He, C. G. Whyte, N. S. Ginzburg, N. Y. Peskov and A. S. Sergeev (2002). "Experimental studies of two-dimensional coaxial Bragg structures for a high-power free-electron maser." Applied Physics Letters **80**(9) 1517-1519

Dolling, G., C. Enkrich, M. Wegener, C. M. Soukoulis and S. Linden (2006). "Simultaneous Negative Phase and Group Velocity of Light in a Metamaterial." Science **312**(5775) 892-894

Doucas, G., V. Blackmore, B. Ottewell, C. Perry, P. G. Huggard, E. Castro-Camus, M. B. Johnston, J. L. Hughes, M. F. Kimmitt, B. Redlich and A. van der Meer (2006). "Longitudinal electron bunch profile diagnostics at ~45MeV using coherent Smith-Purcell radiation." Physical Review Special Topics - Accelerators and Beams **9**(9) 092801

Fedotov, V. A., M. Rose, S. L. Prosvirnin, N. Papasimakis and N. I. Zheludev (2007). "Sharp trapped-mode resonances in planar metamaterials with a broken structural symmetry." Physical Review Letters **99**(14) 147401

Ginzburg, N. S., I. V. Konoplev and A. S. Sergeev (1996). "Application of 2-dimensional distributed feedback for emission synchronization in FEL with large-diameter piped REB." Tech. Phys. **66**(5) 108-117

Ginzburg, N. S., N. Y. Peskov, A. S. Sergeev, A. D. R. Phelps, I. V. Konoplev, G. R. M. Robb, A. W. Cross, A. V. Arzhannikov and S. L. Sinitsky (1999). "Theory and design of a free-electron maser with two-dimensional feedback driven by a sheet electron beam." Physical Review E **60**(1) 935-945

Ginzburg, N. S., A. M. Malkin, N. Y. Peskov, A. S. Sergeev, V. Y. Zaslavsky, K. Kamada and R. Ando (2009). "Free electron laser with terahertz band Bragg reflectors." Physical Review Special Topics - Accelerators and Beams **12**(6) 060702

Ginzburg N. S., V. Yu. Zaslavskii, E. V. Ilyakov, I. S. Kulagin, A. M. Malkin, N. Yu. Peskov and A. S. Sergeev (2011) “Powerful Cherenkov Oscillators with 2D Distributed Feedback” **56** (12) 1791-1801

Ginzburg N. S., V. Yu. Zaslavskii, A. M. Malkin and A. S. Sergeev (2012) “Relativistic Surface Wave Oscillators with 1D and 2D Periodic Structures”. Technical Physics **57**(12) 1692-1705

Ginzburg, N. S., A. M. Malkin, A. S. Sergeev and V. Zaslavsky (2013). "Oversized co-axial and cylindrical surface-wave oscillators with two-dimensional periodical grating (quasi-optical model)." Journal of Applied Physics **113**(10) 104504

Ginzburg, N. S., A. M. Malkin, I. V. Zheleznov, V. Y. Zaslavskii and E. R. Kocharovskaya (2014). "Wave propagation in oversized planar waveguides with weakly corrugated surface." Journal of Communications Technology & Electronics **59**(12) 1426-1433

Glass, N. E. (1987). "Enhanced Smith-Purcell radiation from a bigrating surface through multiplasmon excitation." Physical Review A **36**(11) 5235-5250

A. N. Grigorenko, A. N, A. K. Geim, H. F. Gleeson, Y. Zhang, A. A. Firsov, I. Y. Krushchev and J. Petrovic (2005) "Nanofabricated media with negative permeability at visible frequencies", Nature, **438**, 335-338

Grishin, Y. A., M. R. Fuchs, A. Schnegg, A. A. Dubinskii, B. S. Dumesh, F. S. Rusin, V. L. Bratman and K. Möbius (2004). "Pulsed Orotron - A new microwave source for submillimeter pulse high-field electron paramagnetic resonance spectroscopy." Review of Scientific Instruments **75**(9): 2926-2936.

Hecht, E. (1998) “Optics”, 3rd Edition, Addision-Wesley, New York

Ishizaki, K. and S. Noda (2009). "Manipulation of photons at the surface of three-dimensional photonic crystals." Nature **460**(7253): 367-370

Jackson, J. D. (1999). Classical electrodynamics, Wiley, New York

Katsenelenbaum, B. Z. (1998). Theory of nonuniform waveguides : the cross-section method, Institution of Electrical Engineers, London, UK

Kitson. S, W. Barnes and J. Sambles (1996) "Full Photonic Band Gap for Surface Modes in the Visible", Physical Review Letters **77** (2670) 101103

Kogelnik, H. and C. V. Shank (1972). "Coupled-wave theory of distributed feedback lasers." Journal of Applied Physics **43**(5): 2327-2335.

Konoplev, I. V. (2001) "Free-Electron Maser with Two Dimensional Distributed Feedback", PhD Thesis, University of Strathclyde.

Konoplev, I. V., A. W. Cross, W. He, A. D. R. Phelps, K. Ronald, G. R. M. Robb, C. G. Whyte, N. S. Ginzburg, N. Y. Peskov and A. S. Sergeev (2000). "Progress of the Strathclyde Free Electron Maser experiment using a 2D Bragg structure." Nuclear Instruments and Methods in Physics Research, Section A: Accelerators, Spectrometers, Detectors and Associated Equipment **445**(13): 236-240.

Konoplev, I. V., A. W. Cross, P. MacInnes, W. He, A. D. R. Phelps, C. G. Whyte, K. Ronald and C. W. Robertson (2008) "Free-electron maser based on a cavity with two- and one- dimensional distributed feedback". Applied Physics Letters **92** (21) 211501

Konoplev, I. V., L. Fisher, A. W. Cross, A. D. R. Phelps, K. Ronald and C. W. Robertson (2010). "Surface wave Cherenkov maser based on a periodic lattice." Applied Physics Letters **96**(26) 261101

Konoplev, I. V., L. Fisher, A. W. Cross, A. D. R. Phelps, K. Ronald and M. Thumm (2010). "Excitation of surface field cavity and coherence of electromagnetic field scattering on two-dimensional cylindrical lattice." Applied Physics Letters **97**(26) 261102

Konoplev, I. V., L. Fisher, K. Ronald, A. W. Cross, A. D. R. Phelps, C. W. Robertson and M. Thumm (2010). "Surface-field cavity based on a two-dimensional cylindrical lattice." Applied Physics Letters **96**(23) 231111

Konoplev, I. V., A. J. MacLachlan, C. W. Robertson, A. W. Cross and A. D. R. Phelps (2011). "Cylindrical periodic surface lattice as a metadielectric: Concept of a surface-field Cherenkov source of coherent radiation." Physical Review A - Atomic, Molecular, and Optical Physics **84**(1) 013826

Konoplev, I. V., A. J. MacLachlan, C. W. Robertson, A. W. Cross and A. D. R. Phelps (2012). "Cylindrical, periodic surface lattice-theory, dispersion analysis, and experiment." Applied Physics Letters **101**(12) 121111

Korbly, S. E., A. S. Kesar, J. R. Sirigiri and R. J. Temkin (2005). "Observation of Frequency-Locked Coherent Terahertz Smith-Purcell Radiation." Physical Review Letters **94**(5) 054803

Kovalev, N. F., I. M. Orlova and M. I. Petelin (1972). "Wave transformation in a multimode waveguide with corrugated walls." Radiophysics and Quantum Electronics **11**(5): 449-450

Lee, T. H. "Planar Microwave Engineering: A Practical Guide to Theory, Measurement, and Circuits" Cambridge University Press (2004)

Lier, E., D. H. Werner, C. P. Scarborough, Q. Wu and J. A. Bossard (2011). "An octave-bandwidth negligible-loss radiofrequency metamaterial." Nat Mater **10**(3) 216-222

Liu, S., P. Zhang, W. Liu, S. Gong, R. Zhong, Y. Zhang and M. Hu (2012). "Surface Polariton Cherenkov Light Radiation Source." Physical Review Letters **109**(15): 153902

Luo, C., M. Ibanescu, S. G. Johnson and J. D. Joannopoulos (2003). "Cerenkov Radiation in Photonic Crystals." Science **299**(5605) 368-371.

MacLachlan A. J, A. R. Phipps, C. W. Robertson, I. V. Konoplev, , A. W. Cross and A. D. R. Phelps (2013) "MM-wave Cylindrical, Periodic-Surface Lattice Cavities for Cherenkov Sources**",** IRMMW-THz 2013 38th International Conference on Infrared, Millimeter and Terahertz Waves, Congress Center Mainz, Mainz, Germany

MacLachlan A. J, A. R. Phipps, C. W. Robertson, I. V. Konoplev, , A. W. Cross and A. D. R. Phelps (2013) "Periodic-Surface-Lattice Cavities for Millimetre-wave Cherenkov Sources**",** UCMMT 2013, 6th UK, Europe, China Millimeter Waves and THz Technology Workshop, National Roman Museum, Rome, Italy

MacLachlan A. J, A. R. Phipps, C. W. Robertson, I. V. Konoplev, , A. W. Cross and A. D. R. Phelps (2014) "Planar Periodic Surface Lattices for Use in Millimeter-Wave Sources**",** IRMMW-THz 39th International Conference on Infrared, Millimeter and Terahertz Waves, The University of Arizona, Tucson, Arizona, USA

A. J. MacLachlan, A. R. Phipps, C. W. Robertson, A. W. Cross, I. V. Konoplev and A. D. R. Phelps, "PSL Modelling and Experiments", UCMMT 2015, 8th UK, Europe, China conference on Millimeter Waves and Terahertz Technologies, National Museum of Wales, Cardiff, UK, 14-16 September.

Mahmoud, S. F. (1991). Electromagnetic waveguides : theory and applications, Peregrinus, London

Maier, S. A., S. R. Andrews, L. Martín-Moreno and F. J. García-Vidal (2006). "Terahertz Surface Plasmon-Polariton Propagation and Focusing on Periodically Corrugated Metal Wires." Physical Review Letters **97**(17) 176805.

McIver, P. (2007). "Approximations to wave propagation through doubly-periodic arrays of scatterers." Waves in Random and Complex Media **17**(4) 439-453.

Mittleman, D (2008). "Metamaterials - A tunable terahertz response", Nature Photon **(2)** 267-268

Mizrahi, A. and L. Schächter (2006). "Electromagnetic forces on the dielectric layers of the planar optical Bragg acceleration structure." Physical Review E **74**(3) 036504.

Noginov, M. A., G. Zhu, A. M. Belgrave, R. Bakker, V. M. Shalaev, E. E. Narimanov, S. Stout, E. Herz, T. Suteewong and U. Wiesner (2009). "Demonstration of a spaser-based nanolaser." Nature **460**(7259) 1110-1112.

Ouseph P. J., K. Driver and J. Conklin (2001) “Polarization of light by reflection and the Brewster angle”, American Journal of Physics. **69**(11) 1166-1168

Pendry, J. B., A. J. Holden, W. J. Stewart and I. Youngs (1996). "Extremely low frequency plasmons in metallic mesostructures." Physical Review Letters **76**(25) 4773-4776.

Pendry J. B., A. J. Holden, D. J. Robbins and W. J. Stewart (1998) "Low frequency plasmons in thin-wire structures", Journal of Physics: Condensed matter **10**(22) 4785-4809.

Pendry J. B (2000) " Negative refraction makes a perfect lens " Physical Review Letters **85**(18) 3966-3969

Phipps, A. R., A. J. MacLachlan, C. W. Robertson, I. V. Konoplev, A. D. R. Phelps and A. W. Cross (2014). Numerical analysis and experimental design of a 103 GHz Cherenkov maser. Infrared, Millimeter, and Terahertz waves (IRMMW-THz), 2014 39th International Conference on.

Renger, J., S. Grafström and L. M. Eng (2007). "Direct excitation of surface plasmon polaritons in nanopatterned metal surfaces and thin films." Physical Review B - Condensed Matter and Materials Physics **76**(4) 045431

Riley, K. F. (2006). Mathematical methods for physics and engineering, Cambridge University Press, Cambridge

Scalzi, G. J, Slobodnik,A. J. and G. A. Roberts (1988) “Network analyzer calibration using offset shorts,” IEEE Transactions On Microwave Theory and Technology, **36**(6) 1097-1100

Schächter, L. and A. Ron (1989). "Smith-Purcell free-electron laser." Physical Review A **40**(2) 876-896

Seco-Martorell, C., V. López-Domínguez, G. Arauz-Garofalo, A. Redo-Sanchez, J. Palacios and J. Tejada (2013). "Goya's artwork imaging with Terahertz waves." Optics Express **21**(15) 17800-17805

Shapiro, M. A., K. R. Samokhvalova, J. R. Sirigiri, R. J. Temkin and G. Shvets (2008). "Simulation of the bulk and surface modes supported by a diamond lattice of metal wires." Journal of Applied Physics **104**(10) 103107

Shchegolkov, D. Y., A. K. Azad, J. F. O'Hara and E. I. Simakov (2010). "Perfect subwavelength fishnetlike metamaterial-based film terahertz absorbers." Physical Review B - Condensed Matter and Materials Physics **82**(20) 205117

Shelby, R. A., D. R. Smith and S. Schultz (2001). "Experimental Verification of a Negative Index of Refraction." Science **292**(5514) 77-79

Shen, J. T., P. B. Catrysse and S. Fan (2005). "Mechanism for designing metallic metamaterials with a high index of refraction." Physical Review Letters **94**(19) 197401

D. Schurig, J. J. Mock, B. J. Justice, S. A. Cummer, J. B. Pendry, A. F. Starr and D. R. Smith (2006)"Metamaterial Electromagnetic Cloak at Microwave Frequencies", Science, **314** (5801) 977-980

Sievenpiper, D (1999) "High- Impedance Electromagnetic Surfaces", PhD Thesis, University of California

Sievenpiper, D., L. Zhang, R. F. Jimenez Broas, N. G. Alexöpolous and E. Yablonovitch (1999). "High-impedance electromagnetic surfaces with a forbidden frequency band." IEEE Transactions on Microwave Theory and Techniques **47**(11) 2059-2074

Silver, S (1949) *Microwave Antenna Theory and Design*, volume 12 of *MIT Radiation Laboratory Series*. McGraw-Hill, New York.

Sirigiri, J. R., K. E. Kreischer, J. Machuzak, I. Mastovsky, M. A. Shapiro and R. J. Temkin (2001). "Photonic-Band-Gap Resonator Gyrotron." Physical Review Letters **86**(24) 5628-5631

Smirnova, E. I., A. S. Kesar, I. Mastovsky, M. A. Shapiro and R. J. Temkin (2005). "Demonstration of a 17-GHz, High-Gradient Accelerator with a Photonic-Band-Gap Structure." Physical Review Letters **95**(7) 074801

Stockman, M. I. (2008). "Spasers explained." Nature Photonics **2**(6) 327-329

Stockman, M. I. (2010). "The spaser as a nanoscale quantum generator and ultrafast amplifier." Journal of Optics A: Pure and Applied Optics **12**(2) 024004

Tymis, N. and I. Thompson (2014). "Scattering by a semi-infinite lattice and the excitation of Bloch waves." Quarterly Journal of Mechanics and Applied Mathematics **67**(3) 469-503

Ulrich, R. (1968). "Interference Filters for the Far Infrared." Applied Optics **7**(10) 1987-1996

Ulrich, R. (1976), "Far-Infrared Properties of Metallic Mesh and its Complimentary Structure", Infrared Physics **7** (1) 37-55

Urzhumov, Y. A. and D. R. Smith (2010). "Transformation Optics with Photonic Band Gap Media." Physical Review Letters **105**(16) 163901

Urzhumov, Y. A. and D. R. Smith (2010). "Transformation Optics with Photonic Band Gap Media." Physical Review Letters **105**(16) 163901

Worthing, P. T. and W. L. Barnes (2001). "Efficient coupling of surface plasmon polaritons to radiation using a bi-grating." Applied Physics Letters **79**(19) 3035-3037

Yablonovitch, E., T. J. Gmitter and K. M. Leung (1991). "Photonic band structure: The face-centered-cubic case employing nonspherical atoms." Physical Review Letters **67**(17) 2295-2298

Yin H., G. R. M. Robb, W. He, A. D. R. Phelps, A. W. Cross and K. Ronald (2000) “Pseudospark-based electron beam and Cherenkov maser experiments”, Physics of Plasmas (**7**) 5195-5205

Yariv, A. and M. Nakamura (1977). "Periodic structures for integrated optics." Quantum Electronics, IEEE Journal of **13**(4) 233-253.

York, A. G., H. M. Milchberg, J. P. Palastro and T. M. Antonsen (2008). "Direct Acceleration of Electrons in a Corrugated Plasma Waveguide." Physical Review Letters **100**(19) 195001

Zayats, A. V., I. I. Smolyaninov and A. A. Maradudin (2005). "Nano-optics of surface plasmon polaritons." Physics Reports **408**(3–4)131-314

Author's Publications

Conference Proceedings

I. V. Konoplev, A. R. Phipps, A. J. MacLachlan, A. W. Cross, C. W. Robertson, A. R. Young and A. D. R. Phelps, "W-band two-dimensional periodic surface lattice for a surface field Cherenkov maser**",** IRMMW-THz 2011 - 36th International Conference on Infrared, Millimeter and Terahertz Waves, Houston, Texas, USA, 2-7th October 2011.

I. V. Konoplev, , A. W. Cross, A. J. MacLachlan, A. R. Phipps, C. W. Robertson, A. R. Young, A. D. R. Phelps and M. Thumm, "Study of two-dimensional periodic surface lattices for high-power mm and sub-mm wave Cherenkov devices**",** IRMMW-THz 2011 - 36th International Conference on Infrared, Millimeter and Terahertz Waves, Houston, Texas, USA, 2-7th October 2011.

I. V. Konoplev, A. MacLachlan, C. W. Robertson, A. W. Cross and A. D. R. Phelps, "Concept of passive devices based on low-contrast periodic structures**",** IET Seminar Digest 2011, 49-56

A. J. MacLachlan, I. V. Konoplev, C. W. Robertson, A. W. Cross and A. D. R. Phelps, "Concept of Cherenkov Oscillator Based on a Cylindrical, Periodic Surface Lattice Metamaterial", IoP Annual Plasma Physics Conference**,** St Hughes College, University of Oxford, Oxford, 2-5th April, 2012 (Student paper prize winner)

A. J. MacLachlan, I. V. Konoplev, C. W. Robertson, A. W. Cross and A. D. R. Phelps, "Concept of Cherenkov Oscillator Based on a Cylindrical, Periodic Surface Lattice", NVEC 2012 National Vacuum Electronics Conference, John Adams Institute, Department of Physics, University of Oxford, Oxford, 25th June 2012.

A. J. MacLachlan, I. V. Konoplev, C. W. Robertson, A. W. Cross and A. D. R. Phelps, "Cylindrical, Periodic-Surface Lattice Cavity for a mm-wave Cherenkov Source**",** IRMMW-THz 2012 37th International Conference on Infrared, Millimeter and Terahertz Waves, University of Wollongong, Wollongong, Australia, 23-28th September 2012.

A. J. MacLachlan, C. W. Robertson, A. W. Cross, A. D. R. Phelps and I. V. Konoplev, "Cylindrical, Periodic-Surface Lattice Cherenkov Source**",** 2012 IEEE 13th International Vacuum Electronics Conference, Monterey, California, 24-26th April 2012.

A. J. MacLachlan, I. V. Konoplev, C. W. Robertson, A. R. Phipps, A. D. R. Phelps and A. W. Cross, "Periodic-Surface-Lattice Cavities for MM-Wave Vacuum Electronic Sources**",** 2013 IEEE 14th International Vacuum Electronics Conference, Paris, France, 21-23 May 2013.

A. J. MacLachlan, A. R. Phipps, C. W. Robertson, I. V. Konoplev, , A. W. Cross and A. D. R. Phelps, "MM-wave Cylindrical, Periodic-Surface Lattice Cavities for Cherenkov Sources**",** IRMMW-THz 2013 38th International Conference on Infrared, Millimeter and Terahertz Waves, Congress Center Mainz, Mainz, Germany, 1-6th September 2013.

A. J. MacLachlan, A. R. Phipps, C. W. Robertson, I. V. Konoplev, , A. W. Cross and A. D. R. Phelps, "Periodic-Surface-Lattice Cavities for Millimetre-wave Cherenkov Sources**",** UCMMT 2013, 6th UK, Europe, China conference on Millimeter Waves and Terahertz Technologies, National Roman Museum, Rome, Italy 9-11 September 2013.

A. R. Phipps, A. J. MacLachlan, C. W. Robertson, I. V. Konoplev, A. D. R. Phelps and A. W. Cross, " PIC Simulations And Experimental Design Of A Cherenkov Millimetre-Wave Source", IRMMW-THz 2013 38th International Conference on Infrared, Millimeter and Terahertz Waves, Congress Center Mainz, Mainz, Germany, 1-6th September 2013.

C. W. Robertson, A. R. Phipps, A. J. MacLachlan, I. V. Konoplev, C. G. Whyte, A. D. R. Phelps, A. R. Young, K. Ronald and A. W. Cross, "W-Band Cherenkov Maser Based on a Periodic Surface Field Structure", IEEE Pulsed Power and Plasma Science Conference, 16-21 June, 2013, San Francisco, USA.

A. J. MacLachlan, "Periodic Surface Lattices for MM-Wave Cherenkov Sources", 1st Annual Active and Passive RF Devices Seminar, Teacher Building, Glasgow, 30th October 2013.

A. J. MacLachlan, A. R. Phipps, C. W. Robertson, I. V. Konoplev, , A. W. Cross and A. D. R. Phelps, "Planar Periodic Surface Lattices for Use in Millimeter-Wave Sources**",** IRMMW-THz 2014 39th International Conference on Infrared, Millimeter and Terahertz Waves, The University of Arizona, Tucson, Arizona, USA, 14-20th September 2014.

A. R. Phipps, A. J. MacLachlan, C. W. Robertson, I. V. Konoplev, , A. W. Cross and A. D. R. Phelps, "Numerical Analysis and Experimental Design of a 103 GHz Cherenkov Maser**",** IRMMW-THz 2014 39th International Conference on Infrared, Millimeter and Terahertz Waves, The University of Arizona, Tucson, Arizona, USA, 14-20th September 2014.

A. J. MacLachlan, A. R. Phipps, C. W. Robertson, A. W. Cross, I. V. Konoplev and A. D. R. Phelps, “PSL Modelling and Experiments”, UCMMT 2015, 8th UK, Europe, China conference on Millimeter Waves and Terahertz Technologies, National Museum of Wales, Cardiff, UK, 14-16 September.

A. J. MacLachlan, A. R. Phipps, C. W. Robertson, I. V. Konoplev, A. W. Cross, and A. D. R. Phelps, “Periodic Surface Lattice Experiments”, NVEC 2015 National Vacuum Electronics Conference, Atoms Beams and Plasmas Group, Department of Physics, University of Strathclyde, Glasgow, 18th November 2015.

Journal Publications

Konoplev, I. V., A. J. MacLachlan, C. W. Robertson, A. W. Cross and A. D. R. Phelps (2011). "Cylindrical periodic surface lattice as a metadielectric: Concept of a surface-field Cherenkov source of coherent radiation." Physical Review A - Atomic, Molecular, and Optical Physics **84**(1) 013826

Konoplev, I. V., A. J. MacLachlan, C. W. Robertson, A. W. Cross and A. D. R. Phelps (2012). "Cylindrical, periodic surface lattice-theory, dispersion analysis, and experiment." Applied Physics Letters **101**(12) 121111

Cylindrical periodic surface lattice as a metadielectric: Concept of a surface-field Cherenkov source of coherent radiation

I. V. Konoplev,* A. J. MacLachlan, C. W. Robertson, A. W. Cross, and A. D. R. Phelps
SUPA, Department of Physics, University of Strathclyde, Glasgow G4 0NG, United Kingdom
(Received 8 April 2011; published 25 July 2011)

A two-dimensional (2D), cylindrical, periodic surface lattice (PSL) forming a surface field cavity is considered. The lattice is created by introducing 2D periodic perturbations on the inner surface of a cylindrical waveguide. The PSL facilitates a resonant coupling of the surface and near cutoff volume fields, leading to the formation of a high-Q cavity eigenmode. The cavity eigenmode is described and investigated using a modal approach, considering the model of a cylindrical waveguide partially loaded with a metadielectric. By using a PSL-based cavity, the concept of a high-power, 0.2-THz Cherenkov source is developed. It is shown that if the PSL satisfies certain defined conditions, single-mode operation is observed.

DOI: 10.1103/PhysRevA.84.013826 PACS number(s): 42.25.Fx, 42.60.Da, 78.67.Pt, 73.20.Mf

I. INTRODUCTION

Electromagnetic (EM) field excitation and evolution inside and on the surface of periodic structures facilitate interaction between active media and the fields and thus are important and challenging problems in plasma physics and electronics [1–10] as well as optics and photonics [11–17]. Extensive study of the electromagnetic wave propagation and control in periodic structures has already led to many technological breakthroughs and is a driving force behind many interesting concepts such as plasmonic devices [11–15], particle acceleration [3,4], and signal transformers [10,15–17]. Bridging the terahertz (THz) gap and realization of compact, high-power sources operating in the GHz-THz [1,2,5–8] and x-ray [1,11], frequency ranges are also strongly linked to the ability to control the EM fields inside and on the surface of periodic lattices. In recent years, a large amount of research has been carried out using periodic lattices and deals with both propagating volume (bulk) waves and surface waves. For many conventional active devices, such as lasers, localized surface waves are rather inconvenient due to their strong localization at the surface accompanied by large thermal losses and weak coupling with bulk active media resulting from the rapid exponential decay inside the active media. However, it has been suggested recently that such fields can be used either in very small nano-oscillators [14] or in high-power [5,6] active devices. The research has been further propelled [15–17] by the exponential development of nanofabrication and nanotechnology. The current stage is one of the rapidly growing areas of research, promising groundbreaking results in signal processing, communication [18], and spectroscopy [16]. The lattices (metamaterials) are normally based on fundamental cells (scatterers) (e.g., split-ring resonators or nanoparticles covered with dielectrics) having dimensions much smaller than the operating wavelength λ [19]. Conventionally, both theory and experiments have been developed for these structures with overall transverse dimensions comparable with the operating wavelength, which allows synchronization of the radiation from individual scatterers. However, there are a number of challenges associated with the interaction region's small size, including manufacture of the lattices and their output power limitations. A simple scaling up of the interaction region's dimensions (i.e., making the total surface area $S \gg \lambda^2$ or total volume $V \gg \lambda^3$) results in disruption of the coherent emission or scattering due to problems associated with synchronization of the individual scatterers that form the metamaterial. The synchronization of the individual scatterers is needed, for example, because of the spatial detuning (caused by finite tolerances of manufacturing) and temporal detuning (caused by nonuniform heating of the metamaterial) of the scatterers' eigenfrequencies and lack of "cross talk" and feedback between them. If the synchronization is not provided, the temporal and spatial coherence of such devices can be questionable. Overcoming these difficulties is especially important for applications where high-power, coherent radiation is required, for instance, in THz active devices for pollution monitoring (atmospheric dust clouds and space debris), security (active control and detection), chemistry, and bioscience. In this paper, we discuss one of the ways to synchronize the radiation from individual scatterers or radiators assembled into a large-area structure. The structure discussed is based on a cylindrical conducting waveguide having an area $S = 2\pi r_0 L \gg \lambda^2$ and manufactured using electroforming techniques. The periodic two-dimensional (2D) perturbations on the inner surface of the waveguide have amplitudes much smaller than the operating wavelength (λ) and form the 2D periodic surface lattice (2D PSL) of cylindrical topology. The photograph and numerical model of the 2D periodic structure are shown in Figs. 1(a) and 1(b). Each individual element of the lattice [Fig. 1(c)] has dimensions smaller but comparable with the operating wavelength ($\sim\lambda/2$), and each fundamental cell of the lattice is an individual scatterer that supports an individual localized surface field. The surface currents excited along the boundaries of the cells [Fig. 1(c)] allows "cross talk" between fundamental cells and coupling of the surface and near cutoff volume fields. These lead to synchronization of the scatterers' oscillations from different parts of the oversized structure. The structure studied [Figs. 1(a) and 1(b)] is low contrast (small amplitude perturbations) and oversized, allowing the "square wave" approximation (also known as the "chessboard" model) [5,7], to be used [Fig. 1(b)]. Further, in this paper, all numerical simulations are carried out using the "square wave" model. Figure 1(c) demonstrates the excitation of synchronized

*ivan.Konoplev@strath.ac.uk

surface currents I_n around a single cell C_n formed by square wave perturbations. The contour plot [observed using the three-dimensional (3D) software package CST MICROWAVE STUDIO] demonstrates the current distributions on the surface of the individual cells C_n, while the arrows indicate the currents' flow directions. To study the eigenmodes of the structure (Fig. 1), the lattice, consisting of the discrete, distributed scatterers, is substituted with a cylindrical waveguide partially loaded with continuous "metadielectric" [19]. The parameters and the properties of the "metadielectric" such as its geometry and refractive index are discussed. We note that the introduction of the metadielectric allows us to consider the localized surface fields supported by the scatterers as eigenmodes of a partially loaded waveguide [20]. Such modes, being eigensolutions of the wave equation, can only be observed in a waveguide with resistive walls or partially loaded with dielectric. One of the features of such fields is an imaginary transverse wave number in free space, leading to localization of the surface modes inside the metal skin layer or the dielectric and decaying rapidly outside. Also, when increasing the field frequency toward the optical range and the metal plasma frequency, the surface fields become known as surface plasmons. In this work, the field structure is studied and a surface field (SF) Cherenkov source based on such a SF cavity will be designed. The results of numerical studies of the Cherenkov source driven by an oversized, mildly relativistic electron beam are presented and discussed.

The paper's structure is as follows. In Secs. II and III, the basic model and equations are described and shown. The model is analyzed and the results are discussed. In these sections, the results of the numerical studies which have been conducted using the 3D code MAGIC are presented and compared with analytical data. By substituting the periodic lattice with a metadielectric and combining this approach with direct 3D numerical modeling of the lattice, the understanding of the field evolution and formation of the cavity's eigenfield structure is developed. Section IV is dedicated to the concept of Cherenkov sources based on a 2D cylindrical lattice, and it is shown that such sources can produce spatially coherent high-power radiation in the high-GHz to THz frequency ranges. The basic principles of the SF Cherenkov source and its design are discussed. In the conclusion, we summarize the results obtained.

II. CYLINDRICAL STRUCTURE BASED ON 2D LATTICE: ANALYTICAL AND NUMERICAL MODELS

The 2D lattice of cylindrical topology [Fig. 1(a)] can be observed by machining small periodic perturbations ($\Delta r << \lambda$, where Δr is the amplitude of the perturbations) on the inner surface of the cylindrical waveguide: $r = r_0 + \Delta r \cos(\bar{k}_z z) \cos(\bar{m}\varphi)$. Here, r_0 is the mean radius of the unperturbed waveguide, $\bar{k}_z = 2\pi/d_z$ and d_z is the lattice longitudinal period, and $\bar{m}$ is the lattice number of azimuthal variations. The structure made from copper [Fig. 1(a)] has a large diameter $2r_0 = 79$ mm ($r_0 \gg d_z = 8$ mm, $r_0 \gg \lambda$, $\lambda \sim 8$ mm) and $\bar{m} = 28$. Let us note that $\bar{m}$ is smaller than $M = 2\pi r_0/d_z \sim 31$; that is, the cells forming the lattice are slightly asymmetric. Such a structure has already

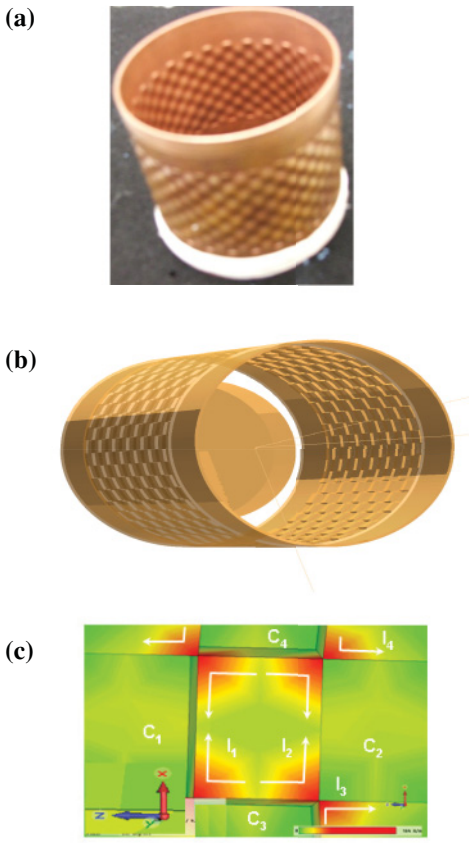

FIG. 1. (Color online) (a) Photograph of the 2D periodic lattice of length $L = 48$ mm machined on the inner surface of copper cylindrical waveguide of mean diameter 80 mm. The lattice has longitudinal period $d_z = 8$ mm and number of azimuthal variations $\bar{m} = 28$ azimuthal. (b) The chessboard model [5,7], of the 2D cylindrical lattice studied via numerical simulations and illustrated using 3D code MAGIC. (c) The excitation of surface currents on the lattice fundamental cell boundaries observed using 3D code CST MICROWAVE STUDIO.

been used in a number of experiments [5,7,10], and thus it is chosen here for theoretical consideration. The conditions of low-contrast (small) perturbations of the waveguide wall allow us to apply a modal approximation. We assume that the transverse structure of the excited eigenfield is a superposition of the transverse structures of eigenmodes of the unperturbed cylindrical waveguide partially loaded with a metadielectric. The substitution of the corrugation with a thin metadielectric (Fig. 2) allows us to define the field's complex structure at the lattice interface and include the surface fields in the study. One notes that the surface fields do not exist in a smooth cylindrical waveguide machined from an ideal conductor, and they were ignored in [7]. The electric field will be described as a superposition of volume (subscript v) and surface (subscript s) fields:

$$\vec{E} = \vec{A}_s + \vec{B}_v. \tag{1}$$

Such a description is different from the one used in [7], which is based on defining the structure's eigenmodes as a superposition of partial volume waves structurally coinciding with the eigenmode of the unperturbed waveguide. In this

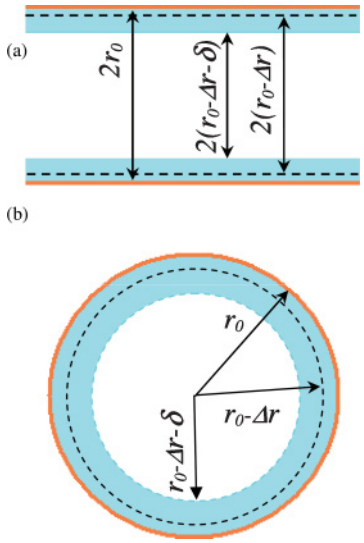

FIG. 2. (Color online) The schematics of the (a) r-z and (b) r-φ cross sections of partially loaded cylindrical waveguide.

work, we consider that the surface field is bound to the lattice-vacuum interface, is therefore localized, and decays towards the structure's axis (i.e., it has an imaginary transverse wave number, while the volume (bulk) field with a real transverse wave number occupies the bulk of the structure. We note that the coupling of otherwise independent fields is mediated by the "soft" boundary (i.e., the 2D lattice). The volume field will be considered as having a transverse structure coinciding with the structure of a near cutoff azimuthally symmetric eigenmode of the unperturbed cylindrical waveguide of radius r. The thin dielectric insert does not affect the transverse structure of this partial field, as the near cutoff wave that forms this field has $\lambda_z \sim L$ (where L is the length of the lattice) and $\lambda_z \gg d_z$. Taking into account the amplitude of the perturbation Δr, one finds an approximate expression for the waveguide radius $r = r_0 - \Delta r$ (Fig. 2). The surface fields (SFs) are described as eigenmodes of the partially loaded cylindrical waveguide. The surface fields will have a real transverse wave number inside the dielectric and an imaginary transverse wave number outside it. The effective dielectric used in the substitution has a refractive index and thickness defined by the lattice parameters, as well as the field's structure and frequency.

Let us consider the stationary regime (i.e., when cavity's eigenmode is established). In this case, the azimuthally nonsymmetric ($m_s \neq 0$) surface field can be described as a superposition of E and H modes of the partially loaded cylindrical waveguide (EH hybrid mode). By taking into account the cylindrical topology of the lattice (i.e., periodicities along azimuthal φ and longitudinal z coordinates), the Fourier decomposition of the surface field can be applied:

$$\begin{aligned} E_z &= \sum_{m_s} F^e_{m_s}(k_{\perp s} r)\sin(m_s\varphi) \sum_{q=-\infty}^{\infty} E_q(z) e^{iq\bar{k}_z z}; \\ H_z &= \sum_{m_s} F^h_{m_s}(k_{\perp s} r)\cos(m_s\varphi) \sum_{q=-\infty}^{\infty} H_q(z) e^{iq\bar{k}_z z}, \end{aligned} \tag{2a}$$

where E_z and H_z are the longitudinal field components which define the hybrid EH mode, q is the harmonic number due to the lattice periodicity along z, and m_s is the number of azimuthal variations of the field. The surface field's transverse wave number is $k_{\perp s}$, the angular frequency is $\omega = k v_{\text{ph}}$, k is the wave vector, and v_{ph} is the phase velocity ($v_{\text{ph}} = c/n$, where c is speed of light in vacuum and n is the refractive index of the dielectric). The amplitudes $E_q(z)$ and $H_q(z)$ are the slowly varying amplitudes of the field harmonics, and $F^{e,h}_m(x)$ are the cylindrical functions of order m. Let us note that outside the metadielectric the functions $F^{e,h}_m(x)$ are combinations of modified Bessel functions (x is imaginary) [8] defining the field decay toward the central axis of the cylindrical structure, while inside the dielectric the field is defined by the ordinary Bessel functions that have an oscillating nature. It is important to note that in general, the boundary of the metadielectric may not coincide with the corrugation boundary (Fig. 2). The surface and volume fields are coupled on the metadielectric-vacuum interface, and the radius of the interface can be found from the impedance matching condition, which is discussed below. The matching condition on the boundary follows also from the two-stage scattering model via surface current excitation (i.e., as the two fields excite the same surface currents, their impedances on the boundary should be equal). The transverse structure of the near cutoff volume field (in the stationary regime) is close to the structure of a TM_{0l} mode of cylindrical waveguide and is defined by an ordinary Bessel function $J_0(x)$: $E_z = J_0(k_{\perp v} r)\sum_{q=-\infty}^{\infty} E^v_q(z) e^{iq\bar{k}_z z}$, where l is the radial variation number and $k_{\perp v}$ is the transverse wave number. To illustrate the applicability of the model, numerical studies of the eigenfields' distributions inside the 2D structure [Fig. 1(b)] have been carried out using the three-dimensional (3D) code MAGIC. The structure studied and shown has square-wave periodic perturbations on the inner surface of the waveguide. The total length of the lattice is 48 mm and the mean diameter is 79 mm, while the lattice has the following parameters: $\bar{m} = 28$, $\Delta r = 0.5$ mm, and $d_z = 8$ mm. To simulate the excitation of the EM field inside the structure, the coaxial launcher tested in the real experiments and based on the coaxial line termination [5] has been modeled [Fig. 1(b)]. In this case, the Transverse Electromagnetic (TEM) wave is formed in a coaxial line before the termination point. In the vicinity of the periodic structure's input, the line is terminated, resulting in excitation of the whole spectrum of the azimuthally symmetric waveguide modes. Figures 3 and 4 illustrate the dependence of the structure eigenfield excited by a narrow band (35–40 GHz) pulse. In Fig. 3, the dependencies of the transverse structures of the electric [Fig. 3(a), bold lines] and magnetic [Fig. 3(b), bold lines] fields on the radial coordinate are shown and compared with the transverse structure of the field associated with the TM near the cutoff wave (broken lines) of the conventional smooth waveguide of the same dimensions. It is evident that the volume fields observed inside the 2D lattice and smooth cylindrical waveguide coincide well and that the differences are due to the surface fields excited at the cavity wall (see $H_{r,z}$ and E_ϕ field components). The TM near the cutoff, azimuthally symmetric field has zero $H_{r,z}$ and E_ϕ field components, while the eigenfield structure of the 2D PSL-based cavity has all six nonzero field components, including both longitudinal electric and magnetic fields. This is similar to the hybrid mode of an unperturbed partially dielectric-loaded waveguide, which indirectly confirms the model described above. In spite of

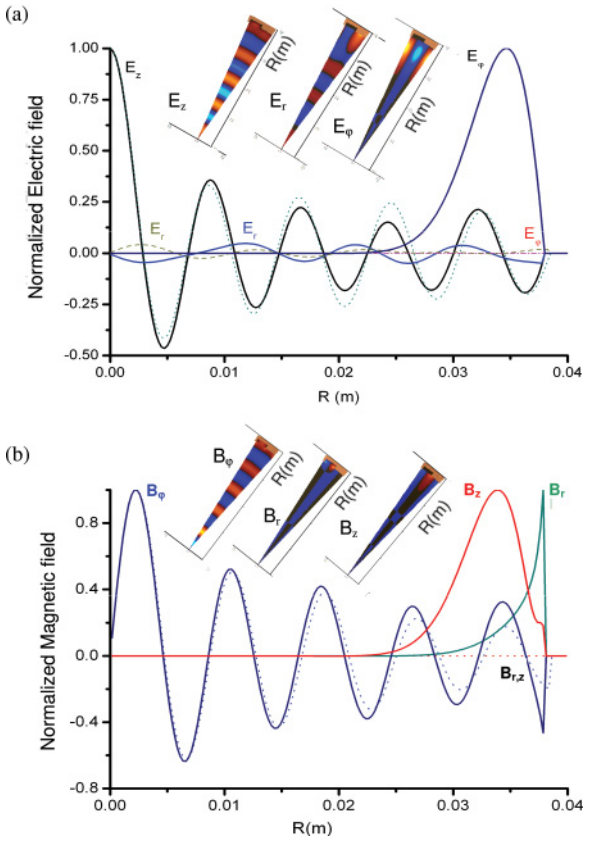

FIG. 3. (Color online) The comparison of the transverse structures of the (a) electric $E_{z,r,\phi}$ and (b) magnetic $B_{z,r,\phi}$ fields observed (3D code MAGIC) inside the SF cavity (solid lines) and smooth cylindrical waveguide (SCW) cavity (broken lines). The SCW cavity eigenmode's transverse structure coincides with the structure of the near cutoff $TM_{0,10}$ wave. The inserts (contour diagrams) illustrate (a) electric and (b) magnetic fields inside the SF cavity (the 1/28th section of the structure).

the fact that the fields H_z and E_ϕ have structures similar to those of a whispering-gallery mode, the $H_{r,\phi}$ components are exponentially decaying toward the center, underlining surface field behavior. The inserts to Figs. 3(a) and 3(b) are the partial contour plots (showing one azimuthal period of the lattice) illustrating the transverse dependence of the periodic structure's eigenmode in the r-φ cross sections. In Fig. 4, a full set of contour plots along r-z [Fig. 4(a)] and r-φ [Fig. 4(b)] are shown. The coupling between the surface and volume fields can be clearly seen. Also, one may note that the decay of the surface fields starts outside the lattice-vacuum interface (the maximum of the field is slightly elevated above the metal surface), allowing us to define the boundary of the metadielectric as the field's caustic radius.

Let us look closely on a field structure excited inside the 2D SF cavity (Fig. 4). We note that each fundamental cell or scatterer supports an individual uncoupled localized field, and the cavity's eigenmode is formed only if such fundamental cells are synchronized [19]. It is known that the resonant coupling of the surface and volume fields on the SP lattice takes place only if the Bragg resonance condition $\vec{\bar{k}} = \vec{k}_s - \vec{k}_v$ is satisfied, where $\vec{\bar{k}}$ is the lattice reciprocal vector and $\vec{k}_{s,v}$ are the wave vectors. The number of the field's azimuthal variations, as well as the longitudinal wave numbers, are linked with the lattice parameters such that $\bar{m} = m_s + m_v$ and $\bar{k}_z = k_{zs} - k_{zv}$. If the eigenmode is formed, and the volume field is azimuthally symmetric $m_v = 0$, the SF number of azimuthal variations is $m_s = \bar{m}$ and one can write $A_s(\varphi)e^{i\varphi_{\bar{m}}\bar{m}} = A_s(\varphi + \varphi_{\bar{m}})$ where $\varphi_{\bar{m}} = 2\pi/\bar{m}$ (Fig. 4). The lattice also defines the localized SF periodicity along the z coordinate [i.e., $A_s(z)e^{i\bar{k}_z d_z} = A_s(z + d_z)$], leading to a strong presence of spatial harmonics in the stationary regime. As a result, taking into account that the volume field is represented by a fundamental harmonic of a near cutoff ($k_{zv} \cong 0$; see Figs. 3 and 4) wave with $m_v = 0$ (azimuthally symmetric field, Fig. 4), it is clear that the coupling takes place with the ± 1 spatial harmonics of the SF $|k_{zs}| = |\bar{k}_z|$, having $m_s = \bar{m}$. At this stage, for clarity, the coupling between the higher harmonics of the volume and surface fields are overlooked; however, all these discussions are still valid for higher harmonics as well. Further, we deal with the cavity fundamental eigenmode, which is defined as a superposition of the azimuthally symmetric, near cutoff, volume partial field and surface partial field having $m_s = \bar{m}$ and one radial variation. No doubt, more complex modes can also be observed, for instance if the volume wave is not azimuthally symmetric. Considering the fundamental mode, we can rewrite the expressions (2a):

$$\begin{aligned} E_z^s &= F_{\bar{m}}(k_{\perp s}r)E(z)\sin(\bar{k}_z z)\sin(\bar{m}\varphi); \\ H_z^s &= F_{\bar{m}}(k_{\perp s}r)H(z)\cos(\bar{k}_z z)\cos(\bar{m}\varphi); \\ E_z^v &= J_0(k_{\perp v}r). \end{aligned} \tag{2b}$$

The surface modes with $m \neq 0$, unlike whispering-gallery modes, are always hybrid (i.e., having both E_z and H_z (see below) field components). Due to coupling to a near cutoff $TM_{0,10}$ mode, which is defined by $E_{z,r}$ and H_ϕ with $|E_r|/|E_z| = k_z/k_{\perp v} \approx d_z/L$, the coupling between the surface and volume fields takes place via the H_ϕ field [7], leading to excitation and strong modification of the transverse structures of the surface H_ϕ and E_z field components. The peculiarity of the eigenmode structures observed is due to a combination of ordinary and modified Bessel functions, which "elevates" the maximum amplitude of the surface fields above the lattice-vacuum interface, making it look like a whispering-gallery mode. However, if the whispering-gallery mode having $m = \bar{m} = 28$ would be excited, the E_z and E_ϕ should be comparable, while the E_ϕ observed in modeling is nearly 100 times smaller than E_z. Let us note that "elevation" of the SF above the interface makes it more effective for interaction with the active media located outside the lattice.

To identify the fields bound to the lattice, one can also analyze the partial fields' dispersions at the frequency of the interest. The fundamental expressions for the dispersions (in the cylindrical waveguide partially loaded with a metadielectric) for volume and surface fields are $k^2 = k_{\perp v}^2 + k_z^2$ and $k^2 = k_z^2 - k_{\perp s}^2$, respectively. It is known that under the assumption of the perturbations' amplitudes tending to zero, any complex dispersion relation that describes coupling of the partial fields should split into fundamental dispersions of the fields existing in the unperturbed system. In the case considered, the partial fields' dispersion diagrams should coincide with the dispersions of the unperturbed waveguide eigenmodes; however, due to the

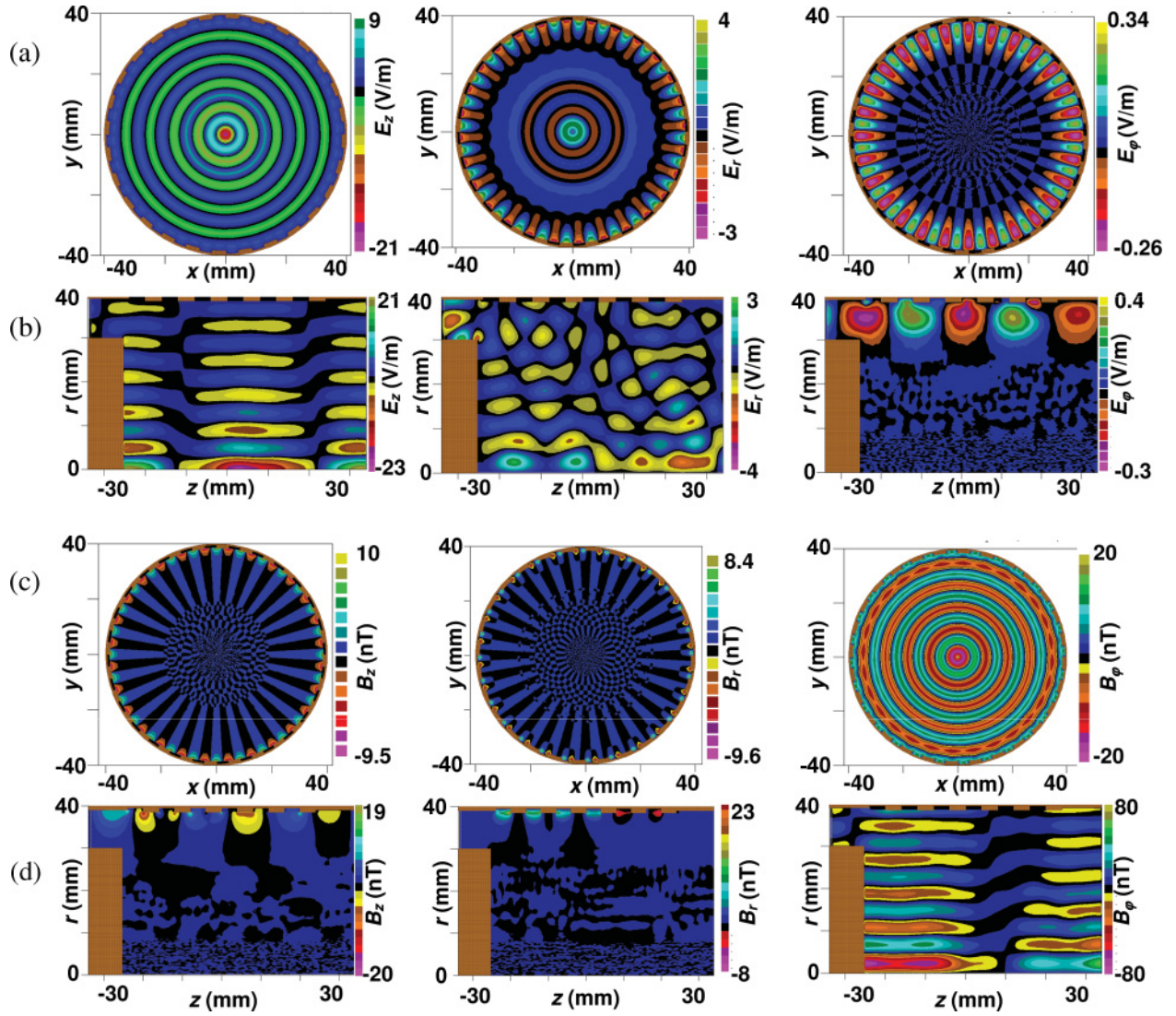

FIG. 4. (Color online) The contour plots of (a,b) electric (E) field's components and (c,d) magnetic (B) field's components in (a,d) r-z and (b,d) r-φ cross sections. The contours indicate the field strength and polarity. The figures observed using full 3D code MAGIC when the structure is irradiated by the narrow-band (35–40 GHz), flat-top-spectrum pulse.

periodicity along the longitudinal coordinate, the formation of the spatial harmonics should be taken into account. Though the modifications of the diagrams, such as splitting and kink formation, will take place in the immediate vicinity of the crossings of the dispersions' branches, it will only slightly affect the diagram's overall appearance. Therefore, analyzing the unperturbed dispersions may give a good first inspection and fundamental understanding of the properties and positions of the eigenmodes. Such an analysis can also show which partial fields can be coupled in the frequency region of interest. In Figs. 5, the dispersion diagrams associated with different partial fields are shown. The graphs are for the structure having a 40-mm mean radius, 8-mm longitudinal period, and 28 azimuthal variations. To observe coupling between the partial fields in the vicinity of the cutoff frequency of the TM_{0l} mode associated with the volume partial field, it is important that the second partial field has an imaginary transverse wave number. If alternatively the partial fields are those of a whispering-gallery mode, either $TM_{28,1}$ or $TE_{28,1}$ having $m_s \cong 2\pi r_0/\lambda$ and real transverse wave number, the crossing with the TM_{0l} mode takes place at higher frequencies above the region of interest, that is, $f > 40$ GHz [Fig. 5(a)]. However, if the second partial field is the surface field, it is possible to observe the intersection in the frequency interval between the cutoff frequencies ~37.5 and 40 GHz [Figs. 5(b)–5(d)]. Let us note that in Figs. 5(a) and 5(d) the case ($\bar{k}_z^2 = k_{\perp s}^2 + k_{\perp v}^2$ and $\bar{k}_z = \sqrt{2}k_{\perp v}$) when the branches of the surface and the volume fields' dispersions cross each other at the precise cutoff frequency is also shown. Figures 5(b), 5(c), 5(e), and 5(f) show the dispersions observed for the cases $\bar{k}_z^2 < (k_{\perp s}^2 + k_{\perp v}^2)$ if $\bar{k}_z = k_{\perp v}/1.1$ (b); $\bar{k}_z = k_{\perp v}/1.5$ (c); and $\bar{k}_z^2 > (k_{\perp s}^2 + k_{\perp v}^2)$ if $\bar{k}_z = 1.5k_{\perp v}$ (e), $\bar{k}_z = 2k_{\perp v}$ (f). The arrows indicate the shifts of the branches of the surface field's dispersion with variation of the lattice period d_z. In Figs. 5(b) and 5(c), the branches "move" toward each other, while in Figs. 5(e) and 5(f), the branches "move" outward. If $\bar{k}_z^2 = k_{\perp s}^2 + k_{\perp v}^2$ [Fig. 5(d)],

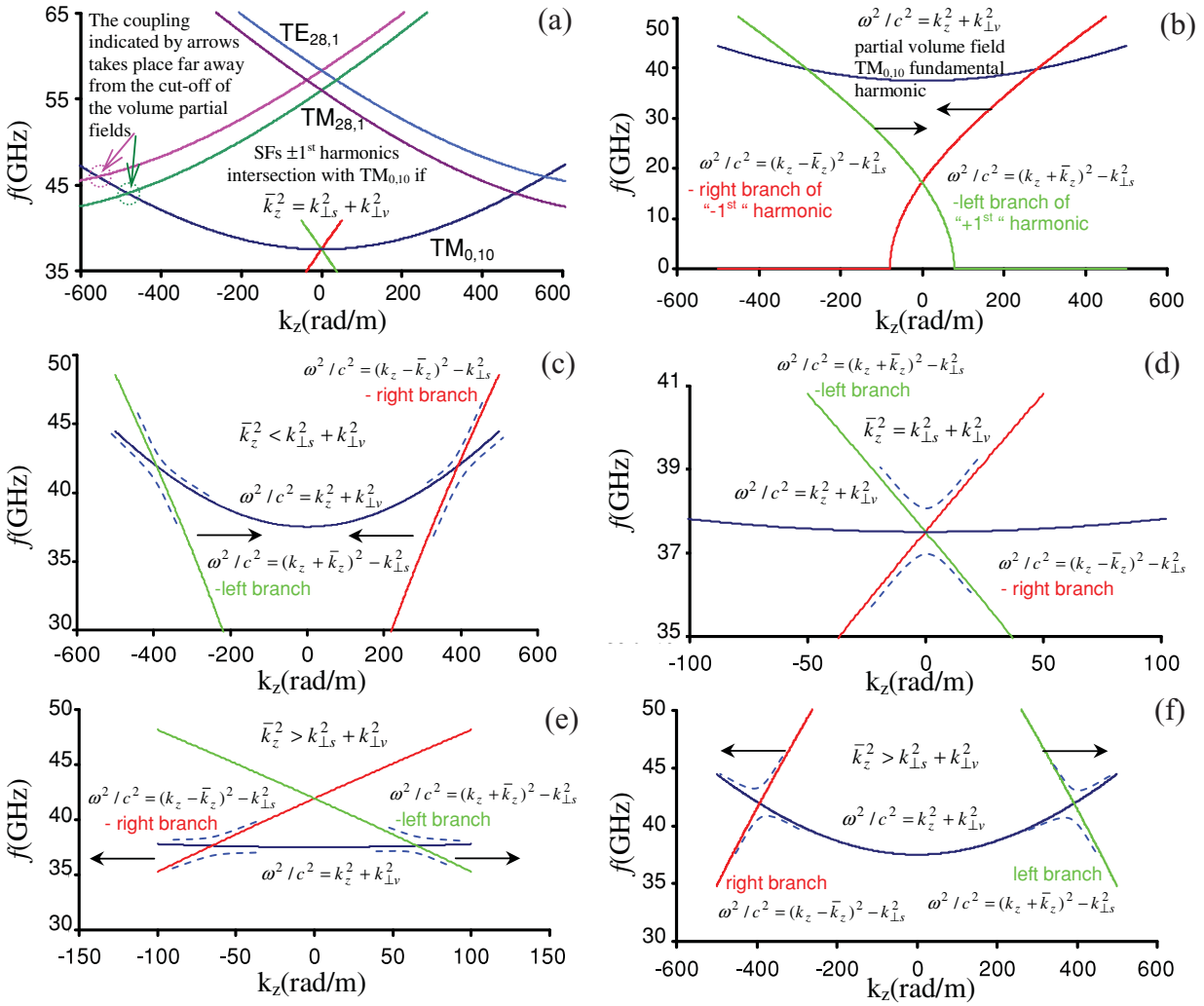

FIG. 5. (Color online) The unperturbed dispersions of the fundamental volume and ±1 harmonics surface partial fields observed inside the 2D cylindrical PSL of 80 mm mean diameter, $\bar{m} = 28$, and amplitude of the perturbations tending to zero. The volume field is associated with the $TM_{0,10}$ mode of the cylindrical waveguide, while the second partial field is associated with (a) whispering-gallery mode ($TM_{28,1}$-$TE_{28,1}$) and (b,c,d,e,f) surface field having an imaginary transverse wave number. The crossing between volume and surface field at exact cutoff frequency ($\bar{k}_z^2 = k_{\perp s}^2 + k_{\perp v}^2$) is shown in (a) and (d). The figures (b) and (c) are observed if $\bar{k}_z^2 < k_{\perp s}^2 + k_{\perp v}^2$, while (e) and (f) if $\bar{k}_z^2 > k_{\perp s}^2 + k_{\perp v}^2$. The arrows indicate the displacement of the surface field dispersions with increase of $\bar{k}_z$. The dashed lines indicate schematically the splitting of the dispersions with increase of the lattice contrast.

one observes a bifurcated state. The dispersion splitting is schematically illustrated by dashed lines on these graphs. The topology of the dispersion splittings are different, illustrating the possibilities of observing instabilities of different types, either convective [Figs. 5(b), 5(c)] or absolute [Figs. 5(e), 5(f)] instabilities, if the lattice forms an interaction region of an active device driven, for example, by an electron beam. This can be beneficial for devices operating in different regimes and using different types of interactions.

The number of the radial variations of the field excited inside the low-contrast structure is not controlled by the lattice in the same way as it maintains the field's number of azimuthal variations. The number of radial variations only depends on the radius of the unperturbed cylindrical waveguide. Thus, the volume field inside the structure will have l radial variations such that $k_{\perp v} = \chi_l^v / r$, where χ_l^v is the lth root of the Bessel function of zero order. As we deal with the fundamental mode of the structure, inside the frequency interval, which is associated only with the fundamental mode, the number of radial variations of the surface field will be considered to be equal to unity. Increasing the operating frequency will lead to an increase of the surface and volume fields' numbers of radial variations, affecting for instance the inner boundary of the metadielectric (the surface field's radial variations exist only inside the metamedia). The numerical modeling illustrating such eigenfield dependence on the operating frequency and eigenmode excitation has been carried out using the full 3D code MAGIC in the following frequency regions: from 30 to 40 GHz (Fig. 6) and from 65 to 70 GHz. Let us note that the first band is well below the whispering-gallery modes' ($TE_{28,1}$ and $TM_{28,1}$) cutoff frequencies (44.6 and 41.6 GHz respectively), while the second band was chosen to illustrate

the concept discussed and to demonstrate the high-order modes' excitation. To observe the cavity eigenmodes having different radial indices, a broad-band pulse has been used. In Fig. 6(a), the eigenmodes excited (solid line) by the pulse with a flat spectrum (dotted line) in the region between 30 and 40 GHz are shown. The spectrum maxima are associated with the eigenmodes having different radial $l\in$ [8–10] and the same azimuthal indices, $m = \bar{m} = 28$. An excitation of a specific mode with $l = 9$ [Figs. 4 and 6(b), solid line] has been observed using a narrow-band, flat-top-spectrum pulse in the interval from 35 to 40 GHz [Fig. 6(b), dotted line]. The contour plots of the eigenfields' components observed in this case are shown in Fig. 4. In Fig. 7, the contour plots of the eigenfield structure inside the cavity observed as a result of the cavity excitation with a narrow-band, flat-top-spectrum pulse similar to the one shown in Fig. 6(b) (dotted line) in the interval from 65 to 70 GHz are presented. It can be seen from these figures that the surface field's components of high-order eigenmodes are also localized inside a specific region. The number of radial variations is increased, as discussed, while the azimuthal variation number of the eigenmode is maintained constant. The increase of the radial variation number results in a shift of the surface field caustic radius from the lattice toward the center. The dotted lines in Fig. 7 indicate the position of the field caustic radius, which coincides with the metadielectric boundary.

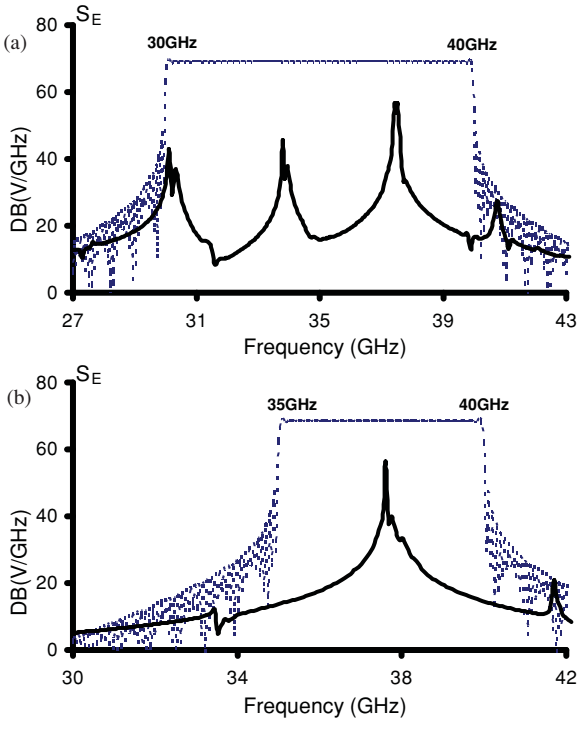

FIG. 6. (Color online) The spectra of the structure's eigenmodes excited (solid lines) if the input signal used to irradiate the lattice has a flat-top spectrum in the frequency ranges (a) 30–40 GHz and (b) 35–40 GHz.

III. SURFACE FIELD INSIDE WAVEGUIDE PARTIALLY LOADED WITH A METADIELECTRIC

Let us consider the SF structure observed inside the 2D periodic lattice by substituting the periodic lattice with an effective imaginary dielectric (metadielectric) [18], the thickness $2\Delta r - \delta$ and refractive index $n = \sqrt{\varepsilon\mu}$ of which are functions of the EM field frequency, structure, and lattice parameters (Fig. 2). The inner and outer radii of the metadielectric insert can be defined as $r_d = r_0 - \Delta r - \delta$ and $r_+ = r_0 + \Delta r$ respectively. The surface field is localized (having a real wave number) inside the dielectric ($r_d < r \leqslant r_+$) and decaying (imaginary transverse wave number) outside ($r \leqslant r_d$). At the boundary of the metadielectric, the field's continuity conditions for its tangential components (i.e., $E_{z,\phi}$ and $H_{z,\phi}$) should be met. The field is described as a standing (to observe localization) wave having both E_z and H_z field components and defined using the vector potential $\Psi_{e,h}$ as follows:

$$(E_z; H_z) = \left(\frac{\partial^2}{\partial z^2} + k^2\varepsilon\mu\right)(\Psi_e; \Psi_h), \tag{3}$$

where the vector potentials inside the dielectric are

$$\begin{aligned}\Psi_e &= C_1 F_e(\kappa_s r)\sin(\bar{m}\varphi)\sin(\bar{k}z),\\ \Psi_h &= C_2 F_h(\kappa_s r)\cos(\bar{m}\varphi)\cos(\bar{k}z)\end{aligned} \tag{4a}$$

and those outside the dielectric are

$$\begin{aligned}\Psi_e &= C_3 \widehat{F}_e(p_s r)\sin(\bar{m}\varphi)\sin(\bar{k}z),\\ \Psi_h &= C_4 \widehat{F}_h(p_s r)\cos(\bar{m}\varphi)\cos(\bar{k}z)\end{aligned} \tag{4b}$$

and

$$\kappa_s^2 = k^2 n^2 - \bar{k}_z^2, \quad p_s^2 = \bar{k}_z^2 - k^2. \tag{5}$$

The $C_{1,2,3,4}$ are arbitrary constants and

$$\begin{aligned}F_e(\kappa_s r) &= J_{\bar{m}}(\kappa_s r)N_{\bar{m}}(\kappa_s r_+) - J_{\bar{m}}(\kappa_s r_+)N_{\bar{m}}(\kappa_s r),\\ F_h(\kappa_s r) &= J_{\bar{m}}(\kappa_s r)N'_{\bar{m}}(\kappa_s r_+) - J'_{\bar{m}}(\kappa_s r_+)N_{\bar{m}}(\kappa_s r),\\ \widehat{F}_e(p_s r) &= \widehat{F}_h(p_s r) = I_{\bar{m}}(p_s r).\end{aligned} \tag{6}$$

The approach is synonymous with including only the first positive and negative harmonics (observed in the periodic structure), manifesting itself as $\cos(\bar{k}z)$ and $\sin(\bar{k}z)$ dependences of the Ψ_e and Ψ_h potentials. By expressing the tangential fields using (4) and applying the continuity conditions at the dielectric-vacuum interface, the characteristic equation that links the transverse wave numbers can be observed:

$$p_s^4\kappa_s^4 r_d^4(\varepsilon f_e - \widehat{f}_e)(\mu f_h - \widehat{f}_h) = \bar{m}^2\bar{k}_z^2 k^2(n^2-1)^2, \tag{7}$$

where $\widehat{f}_e = \widehat{f}_h = \widehat{f} = -I'_{\bar{m}}(y)/(yI_{\bar{m}}(y))$, $y = p_s r_d$, $f_e = \frac{1}{x_d}\frac{J'_{\bar{m}}(x_d)N_{\bar{m}}(x_+) - J_{\bar{m}}(x_+)N'_{\bar{m}}(x_d)}{J_{\bar{m}}(x_d)N_{\bar{m}}(x_+) - J_{\bar{m}}(x_+)N_{\bar{m}}(x_d)}$, $f_h = \frac{1}{x_d}\frac{J'_{\bar{m}}(x_d)N'_{\bar{m}}(x_+) - J'_{\bar{m}}(x_+)N'_{\bar{m}}(x_d)}{J_{\bar{m}}(x_d)N'_{\bar{m}}(x_+) - J'_{\bar{m}}(x_+)N_{\bar{m}}(x_d)}$, and $x_{d,+} = \kappa_s r_{d,+}$. The dispersion equation (7) shows that the EM fields with nonzero azimuthal variation numbers are always hybrid (i.e., have E_z and H_z field components), while the azimuthally symmetric fields are either E or H polarized. It also indicates that far from the resonance, where the effective refractive index is equal to 1 (no interaction), no hybrid modes can be observed; that is, the partially loaded

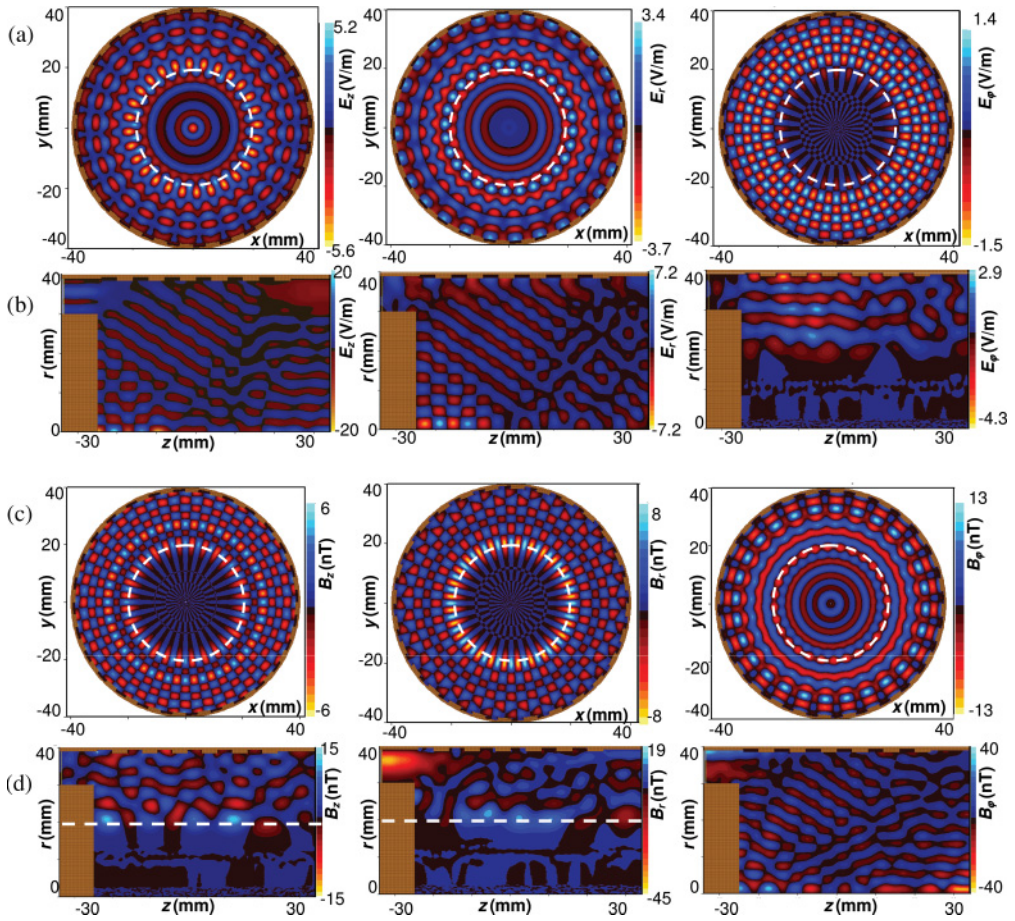

FIG. 7. (Color online) The contour plots of (a,b) electric (E) field's components and (c,d) magnetic (B) field's components in (a,d) r-z and (b,d) r-φ cross sections. The contours indicate the field strength and polarity. The figures were observed using full 3D code MAGIC when the structure was irradiated by the narrow-band (65–70 GHz), flat-top-spectrum pulse. The dotted line shows schematically the boundary of the imaginary metadielectric, whose radius coincides with caustic radius.

waveguide turns into a conventional cylindrical waveguide. Taking into account (5), one finds that

$$\kappa_s^2 + p_s^2 = k^2(n^2 - 1), \tag{8}$$

which together with (7) allows the evaluation of the transverse wave numbers and dispersion analysis. To define fully the dispersion relation, the refractive index and dielectric inner boundary have to be found. Assuming that the metadielectric has $\mu = 1$, the refractive index n, where $n^2 = \varepsilon\mu$, can be defined from the following consideration: The system which includes the lattice and EM fields (the lattice manifests itself in the appearance of the field's harmonics) has been substituted with a waveguide partially loaded with a metadielectric and the EM field. Thus, taking into account that the localized field, which is nonpropagating and exists only inside the metadielectric, is coupled to the cutoff volume wave, we require the absolute value of κ_s (the transverse wave number inside the metadielectric) to be equal to the wave number k. One can also regard this as phase matching of the fundamental harmonics of the surface and volume fields. Taking (5) into account leads to the following expression: $k^2n^2 = \kappa_s^2 + (l\bar{k}_z)^2 = k^2 + (l\bar{k}_z)^2$, where l is an integer indicating the harmonic's number. Considering only the surface field's ± 1 harmonics, the expression for the refractive index in the vicinity of the resonance frequency takes the following form:

$$n = \sqrt{1 + \frac{\bar{k}_z^2}{k^2}}. \tag{9}$$

At this stage, the only unknown parameter is the inner radius r_d of the metadielectric. We define it from the following consideration. At the caustic boundary, the two partial fields (the surface and volume fields) have to be matched, yielding the following condition:

$$p_s \frac{I_{\bar{m}}(p_s r_d)}{I'_{\bar{m}}(p_s r_d)} = k_{\perp v} \frac{J_0(k_{\perp v} r_d)}{J'_0(k_{\perp v} r_d)} \quad \text{and}$$
$$\omega/c = \sqrt{(k_{\perp v})^2 + k_{zv}^2} \cong k_{\perp v}, \tag{10}$$

which defines the inner radius. Its analytical solution can be found under the assumptions that the structure is oversized in comparison with an operating wavelength, the amplitude of the corrugations, and the deviation δ ($r_d = r_- + \delta$) of the metadielectric boundary from the lattice interface (Fig. 2), which are small in comparison with the operating wavelength

($\delta/r_0 \ll 1$ and $\delta/\lambda \ll 1$). The solution for δ can be found by applying Taylor's expansions to the above expression (10):

$$\delta \cong \frac{p_s^2}{\left(k_{\perp v}^2 - p_s^2\right)} \frac{r_-}{(p_s r_- - \bar{m})}. \tag{11}$$

The expression (11) allows estimation of the field caustic radius, that is, the boundary at which the surface field starts to decay exponentially. One notes that if $k_{\perp v} \cong k = \omega/c$ and considering only the surface field's ± 1 harmonics, it follows from (11) and (5) that $\delta = 0$ if $\bar{k}_z = k = \omega/c$ and $\delta \sim -\varepsilon/k$, where ε is the detuning $\varepsilon = (\bar{k}_z/k)^2 - 1$. Also, if an interaction between an electron beam and the EM field is considered in order to observe high-power lasing, the electron beam should propagate outside the lattice while still inside the region defined by the shift δ (i.e., $\delta < 0$). Thus, expression (11) imposes conditions on the electron beam, accelerating voltage, EM field, and lattice parameters. By optimizing these parameters, a steady-state, single-mode, high-power source operating in the low-THz frequency range can be created.

IV. CHERENKOV OSCILLATOR BASED ON CYLINDRICAL 2D SURFACE PERIODIC LATTICE

Let us consider the interaction between an electron beam and the electromagnetic fields mediated by the cylindrical 2D PSL. Inside the cavity defined by the lattice, the partial surface and volume fields form the cavity eigenmode. Electrons interact with the synchronous harmonic of the cavity eigenmode's partial SF at the lattice interface. The near cutoff partial volume field synchronizes the individual scatterers forming the lattice and ensures that the different parts of the oversized electron beam interact with the coherent SF. The condition required for the electron beam–EM wave interaction has the following general form:

$$\omega = k_z v_z + \frac{2\pi}{d_z} v_z, \tag{12a}$$

where v_z is the electron beam longitudinal velocity and k_z is the wave's longitudinal wave number. Taking into account that the electrons interact with the localized surface field ($k_z \cong 0$), (12a) can be rewritten as $f = \frac{c}{d_z}\sqrt{1-\gamma^{-2}}$, where $\gamma = 1 + \frac{eU}{m_0 c^2} \cong 1 + \frac{W\,(\mathrm{keV})}{511\,\mathrm{keV}}$ is the relativistic Lorentz factor and f is the wave frequency. By rearranging the last expression, the formula linking the longitudinal period of the lattice with the wave frequency and the electron beam accelerating voltage U can be found:

$$U\,(\mathrm{kV}) \cong 511\ \mathrm{kV} \times \left[\frac{\lambda}{\sqrt{\lambda^2 - d_z^2}} - 1\right]. \tag{12b}$$

To study the interaction between an electron beam and the cavity eigenmode, it is important to define correctly the radial position of the annular electron beam (i.e., the mean radius). We have to locate the electron beam outside the lattice to avoid its interception with the structure. Such an interception may affect the lifetime of the oscillator as well as limit the level of output power. To optimize the beam radius, the relations (11) and (12b) can be used, and as discussed above, to observe an effective interaction between the electron beam and the EM field the electron beam should be inside the following region (Fig. 2):

$$r_0 - \Delta r = r_+ > R > r_d = r_0 - \Delta r + \delta.$$

To avoid the electron beam interception, it is important that $\delta < 0$. This can be achieved if either

$$k_{\perp v}^2 - p_s^2 > 0, \quad \text{while} \quad p_s r_0 - \bar{m} < 0 \tag{13a}$$

or

$$k_{\perp v}^2 - p_s^2 < 0, \quad \text{while} \quad p_s r_0 - \bar{m} > 0. \tag{13b}$$

By looking at the conditions (13) and linking them to the expression (12b), two distinctive cases can be identified. It is possible to show that the first condition (13a) is associated with high-voltage (relativistic) electron beams, while the condition (13b) is linked to low-voltage (mildly relativistic) electron beams. Indeed, taking into account that $k_{\perp v} = \omega/c$, $p_s = \sqrt{\bar{k}_z^2 - (\omega/c)^2}$, $d_z = \frac{\lambda}{a}\sqrt{a^2-1}$, and $a^2 = (\frac{U\,(\mathrm{kV})}{511\ \mathrm{kV}} + 1)^2 > 1$ and substituting them into (11), we find that $k_{\perp v}^2 - p_s^2 > 0$ if $\lambda/d_z < \sqrt{2}$, leading to $a > \sqrt{2}$ (i.e., if the beam accelerating voltage is above $U_0 = 212$ kV). In this case, $\delta < 0$ if $p_s r_0 - \bar{m} < 0$, which is achieved when

$$\frac{2\pi r_0}{\lambda a} < \bar{m} \quad \text{and} \quad a > \sqrt{2}. \tag{14a}$$

This shows that for a specific mean radius of the lattice and operating wavelength, the number of the lattice azimuthal variations should be larger than the number of wavelengths along the unperturbed circumference of the waveguide. In the low-voltage regime for which $k_{\perp v}^2 - p_s^2 < 0$ and the electron beam accelerating voltage is less than U_0, then $\delta < 0$ if

$$\frac{2\pi r_0}{\lambda a} > \bar{m} \quad \text{and} \quad a \sim 1, \tag{14b}$$

indicating that the number of azimuthal variations should be less than the number of wavelengths along the unperturbed circumference of the waveguide. If the conditions (14) are not satisfied, the coupling between the electron beam and electromagnetic fields will be significantly weaker, resulting in the necessity to either increase the length of the interaction region or the electron beam current and propagate the electron beam inside the periodic structure. The electron beam accelerating voltage defines also the topology of the lattice's single cell. If γ is large (relativistic electron beam), the cell has rectangular geometry, with the longest side codirected with the electron beam drift velocity, while if γ is low (mildly relativistic electron beam), the cells have elongated geometry with the longest side perpendicular to the electron beam drift velocity. One also notes that there is overlap $\Delta \sim (1 - 1/a)$ between (14a) and (14b), allowing the maser's operating frequency to be maintained if the accelerating voltage is varied by adjusting only the structure's longitudinal period.

Numerical studies of a 200-GHz Cherenkov oscillator based on the PSL and driven by an annular ($r_b = 5$ mm), thin-wall ($\delta r = 0.5$ mm) electron beam immersed in a guiding magnetic field of 2 T have been carried out using the 3D code MAGIC. In Fig. 8, the results illustrating the scaling relation (12b) are shown. The graphs presented were observed under the condition that the system's only variable parameters are

the electron beam accelerating voltage and the longitudinal period of the structure. The rest of the parameters, including the number of lattice periods along z, have been maintained constant. The oscillator's parameters were chosen to satisfy the relations (11) and (14) for the range of the electron beam voltages (overlapping region is from 100 to 300 kV). It can be seen from Fig. 8 that by changing the electron beam accelerating voltage and scaling the lattice period d_z using (12b), the operating frequency is maintained constant. However, as one would expect, the operating regime as well as the output efficiency of the oscillator varies with the change of the accelerating voltage. In Fig. 8(b), the steady-state single-mode operation of a 0.2-THz Cherenkov oscillator is observed. The device is driven by a 250-kV, 20-A annular electron beam and the efficiency observed is around 2.5%, yielding ~120 kW output power. However, taking into account the possibility of highly efficient electron beam energy recovery, which is routinely carried out, an overall efficiency above 40% (after energy recovery) can be expected. By optimizing the interaction region parameters, a further increase of the energy extraction efficiency and thus an increase of output power can be observed. For instance, an efficiency of 10% is achieved when a 100-kV electron beam is used [Fig. 8(c)]. However, for the parameters used, output power modulation can be seen, indicating mode competition due to the excitation of high-order eigenmodes. The number of the lattice azimuthal variation $\bar{m}$ should also affect the behavior of the Cherenkov oscillator [see (14)]. The numerical modeling of the Cherenkov oscillator driven by a low-voltage (50-kV), 40-A electron beam was carried out, and the results of the investigation of the dependence of the oscillator operation on $\bar{m}$ are shown in Fig. 9. In these studies, the lattice longitudinal period d_z = 0.58 mm was changed in accordance with (12b) to maintain the operating frequency range of ~0.2 THz. The rest of the lattice parameters are the same as listed in Fig. 8. One notes that if the number of the structure's azimuthal variations are maintained ($\bar{m} = 20$ as in Fig. 8), a drop of the output power [Fig. 9(a)] and a frequency jump to 207.3 GHz [Fig. 9(b)] [which follows from (14b) take place (operating with higher order radial mode). Taking into account that $r_0 = 5.5$ mm, $U = 50$ kV ($a \sim 1.1$), $\lambda = 1.53$ mm (~195 GHz), one finds that in accordance with condition (14b) $\bar{m} < 20$ is required to observe an effective interaction below 195 GHz. The variation of transient times observed [Fig. 9(a)] from approximately 4 ns (for $\bar{m} = 18$) to above 10 ns (for $\bar{m} = 21$) indicates also the dependence of coupling between the electron beam and the EM field on the azimuthal index $\bar{m}$. It is clear that changing $\bar{m}$ results in variation of the oscillation evolution [Fig. 9(a)] and the operating frequency [Fig. 9(b)]. One notes that in all cases observed (14b) has been satisfied. Thus with the change of the number of azimuthal variations, the operating frequency upshift from 182 GHz ($\bar{m} = 18$) to 214 GHz ($\bar{m} = 21$) has been observed. Further increase of $\bar{m}$ led to continuous increase of the transient time, and at $\bar{m} = 24$ the startup of the oscillations did not take place. We note that for $\bar{m} = 21$ the transition time to observe steady-state single-mode operation has increased from ~7 ns (for $\bar{m} \in [18; 20]$) to 30 ns. However, one also notes that the output power has

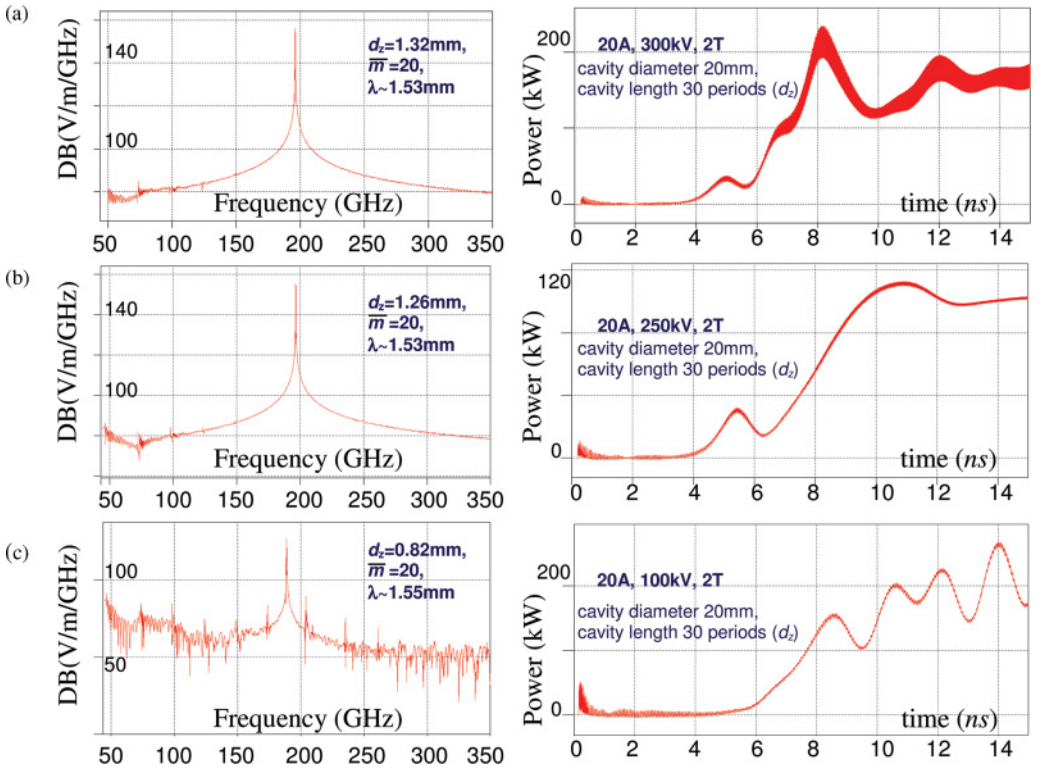

FIG. 8. (Color online) The spectrum of the output radiation (first column) and output power (second column) from Cherenkov oscillator driven by a 20-A, thin, annular electron beam with interaction region formed by cylindrical 2D PSL of 11 mm diameter with $\bar{m} = 20$ and 30 longitudinal periods. The lattice's longitudinal period and beam accelerating voltage was (a) $d_z = 1.32$ mm, $U = 300$ kV; (b) $d_z = 1.26$ mm, $U = 250$ kV; and (c) $d_z = 0.82$ mm, $U = 100$ kV.

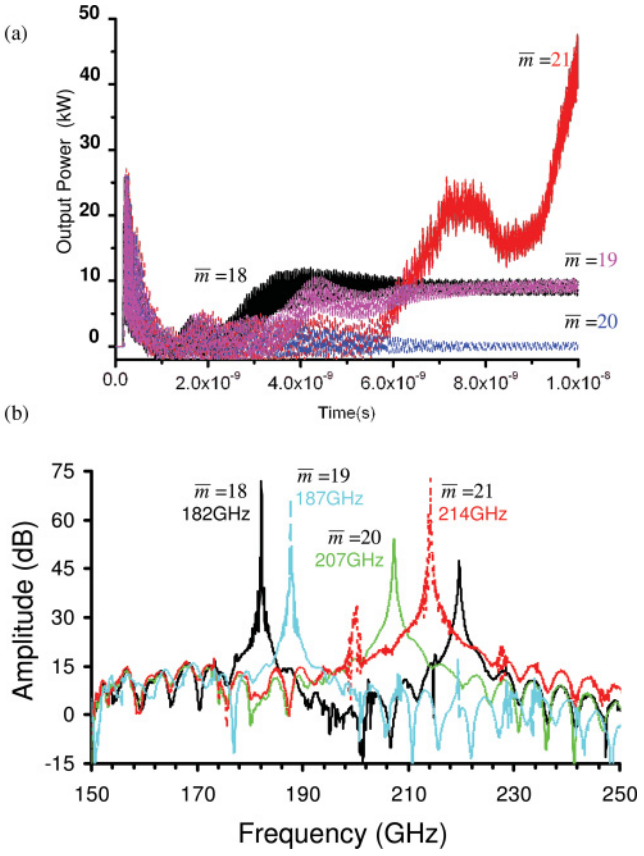

FIG. 9. (Color online) (a) The output power and (b) the spectrum of the output radiation observed from the Cherenkov maser driven by a thin, annular, 40-A, 50-kV electron beam and based on a 2D PSL of 11 mm mean diameter and 17.4 mm length (30 longitudinal periods) and having $\bar{m} = [18;21]$.

also increased by a factor of 4, indicating significant potential for further improvement of the oscillator performance. The excitation of up- and down-shifted satellite modes associated with fields having different radial variation numbers has been observed for $\bar{m} \in [18; 21]$. The field amplitudes of these modes are 30 dB less than the operating mode but still would be measurable if experimental studies are conducted with such a device.

V. CONCLUSION

In this paper, we presented the model describing the fundamental eigenmode structure inside the cavity formed by a 2D periodic surface lattice of cylindrical topology. We demonstrated that the eigenmode structure can be considered as a superposition of partial surface and volume fields, which are coupled on the lattice-vacuum interface. We discussed the structures of the volume and surface partial fields, and it was shown that the surface field excited is different from a whispering-gallery mode and has all the features of a surface mode. To define the structure of the eigenfield, the cylindrical lattice was substituted with a smooth cylindrical waveguide, partially loaded with a metadielectric. It was found that the properties of the metadielectric depend on the lattice and radiation parameters, and the conditions required to observe the elevation of the surface field above the lattice were discussed. Contour plots of the cavity eigenfield structures were demonstrated. By analyzing the dispersion of the weakly coupled partial fields, we illustrated that to observe coupling at a near cutoff frequency of the volume field, the surface field has to decay toward the center (i.e., it should have an imaginary transverse wave number), thus making its structure different from the whispering-gallery modes. Using the observed results, numerical studies of a Cherenkov oscillator based on a 2D PSL cavity and driven by an annular, electron beam were carried out. The dependence of the lattice parameters on the electron beam accelerating voltage was discussed and the required lattice parameters' scaling (to maintain the operation of the Cherenkov oscillator) with variation of the electron beam voltage was shown. Using the 3D numerical code MAGIC, we demonstrated that single-mode steady-state operation of a high-power 200-GHz Cherenkov maser can be achieved.

Let us note that the results observed in the paper have a fundamental impact as they illustrate coupling on a "soft" boundary of two different electromagnetic fields, which without the lattice would be uncoupled. The model developed shows that the set of discrete synchronized scatterers (oscillators) assembled into the 2D cylindrical lattice allows coupling between an azimuthally nonsymmetric, localized surface field and an azimuthally symmetric volume field. The nature of the scatterers as well as the fields coupled can be different from the ones considered, as the mathematical apparatus and concepts used here can be applied to different systems. For instance, similar results showing the evolution of Bose-Einstein condensate density waves in atomic quantum corrals have been recently observed in [21]. Such coupling can also be expected inside the structures formed by dust particles in plasma and other cylindrical systems based on periodic discrete oscillators or scatterers. We also presented the fundamental concept of substituting the PSL with a continuous metadielectric and have shown the possibility of using surface waves for high-power sources of coherent radiation.

[1] N. E. Glass, Phys. Rev. A **36**, 5235 (1987); L. Schächter and A. Ron, *ibid.* **40**, 876 (1989); S. E. Korbly, A. S. Kesar, J. R. Sirigiri, and R. J. Temkin, Phys. Rev. Lett. **94**, 054803 (2005); B.-I. Wu, J. Lu, J. A. Kong, and M. Chen, J. Appl. Phys. **102**, 114907 (2007).

[2] A. Halperin, A. Gover, and A. Yariv, Phys. Rev. A **50**, 3316 (1994); J. Urata, M. Goldshtein, M. F. Kimmitt, A. Naumov, C. Platt, and J. E. Walsh, Phys. Rev. Lett. **80**, 516 (1998).

[3] A. G. York, H. M. Milchberg, J. P. Palastro, and T. M. Antonsen, Phys. Rev. Lett. **100**, 195001 (2008); A. Mizrahi and L. Schächter, Phys. Rev. E **74**, 036504 (2006).

[4] M. A. Shapiro, K. R. Samokhvalova, J. R. Sirigiri, R. J. Temkin, and G. Shvets, J. Appl. Phys. **104**, 103107 (2008); E. I. Smirnova, A. S. Kesar, I. Mastovsky, M. A. Shapiro, and R. J. Temkin, Phys. Rev. Lett. **95**, 074801 (2005).

[5] I. V. Konoplev, L. Fisher, K. Ronald, A. W. Cross, A. D. R. Phelps, and M. Thumm, Appl. Phys. Lett. **97**, 261102 (2010).

[6] V. L. Bratman, B. S. Dumesh, A. E. Fedotov, P. B. Makhalov, B. Z. Movshevich, and F. S. Rusin, IEEE Trans. Plasma Sci. **38**, 1466 (2010); Yu. A. Grishin, M. R. Fuchs, A. Schnegg, A. A. Dubinskii, B. S. Dumesh, F. S. Rusin, V. L. Bratman, and K. Möbius, Rev. Sci. Instrum. **75**, 2926 (2004); V. L. Bratman, G. G. Denisov, M. M. Ofitserov, S. D. Korovin, S. D. Polevin, and V. V. Rostov, IEEE Trans. Plasma Sci. **15**, 2 (1987).

[7] N. S. Ginzburg, I. V. Konoplev, and A. S. Sergeev, Tech. Phys. **41**, 465 (1996); I. V. Konoplev, A. W. Cross, W. He, A. D. R. Phelps, K. Ronald, G. R. M. Robb, C. G. Whyte, N. S. Ginzburg, N. Yu. Peskov, and A. S. Sergeev, Nucl. Instrum. Methods Phys. Res. Sect. A **445**, 236 (2000); A. W. Cross, I. V. Konoplev, A. D. R. Phelps, and K. Ronald, J. Appl. Phys. **93**, 2208 (2003); I. V. Konoplev, A. W. Cross, P. MacInnes, W. He, C. G. Whyte, A. D. R. Phelps, C. W. Robertson, K. Ronald, and A. R. Young, Appl. Phys. Lett. **89**, 171503 (2006); I. V. Konoplev, A. W. Cross, A. D. R. Phelps, W. He, K. Ronald, C. G. Whyte, C. W. Robertson, P. MacInnes, N. S. Ginzburg, N. Y. Peskov, A. S. Sergeev, V. Y. Zaslavsky, and M. Thumm, Phys. Rev. E **76**, 056406 (2007); I. V. Konoplev, A. W. Cross, P. MacInnes, W. He, A. D. R. Phelps, C. G. Whyte, K. Ronald, and C. W. Robertson, Appl. Phys. Lett. **92**, 211501 (2008).

[8] A. M. Cook, R. Tikhoplav, S. Y. Tochitsky, G. Travish, O. B. Williams, and J. B. Rosenzweig, Phys. Rev. Lett. **103**, 095003 (2009); G. Adamo, K. F. MacDonald, Y. H. Fu, C.-M. Wang, D. P. Tsai, F. J. Garcia de Abajo, and N. I. Zheludev, *ibid.* **103**, 113901 (2009).

[9] J. C. Ashley, T. L. Ferrell, and R. H. Ritchie, Phys. Rev. B **10**, 554 (1974); V. Karagodsky, D. Schieber, and L. Schächter, Phys. Rev. Lett. **104**, 024801 (2010).

[10] G. Burt, S. V. Samsonov, K. Ronald, G. G. Denisov, A. R. Young, V. L. Bratman, A. D. R. Phelps, A. W. Cross, I. V. Konoplev, W. He, J. Thomson, and C. G. Whyte, Phys. Rev. E **70**, 046402 (2004); I. V. Konoplev, A. D. R. Phelps, A. W. Cross, and K. Ronald, *ibid.* **68**, 066613 (2003); I. V. Konoplev, P. MacInnes, A. W. Cross, A. D. R. Phelps, L. Fisher, and K. Ronald, Appl. Phys. Lett. **93**, 231110 (2008).

[11] J. B. Pendry, L. Martin-Moreno, and F. J. Garcia-Vidal, Science **305**, 847 (2004); K. Ishizaki and S. Noda, Nature (London) **460**, 367 (2009); P. T. Worthing and W. L. Barnes, Appl. Phys. Lett. **79**, 3035 (2001).

[12] J. B. Pendry, A. J. Holden, W. J. Stewart, and I. Youngs, Phys. Rev. Lett. **76**, 4773 (1996); M. C. K. Wiltshire, J. B. Pendry, I. R. Young, D. J. Larkman, D. J. Gilberdale, and J. V. Hajnal, Science **291**, 849 (2001).

[13] R. A. Shelby, D. R. Smith, and S. Schultz, Science **292**, 77 (2001); Y. A. Urzhumov and D. R. Smith, Phys. Rev. Lett. **105**, 163901 (2010).

[14] D. J. Bergman and M. I. Stockman, Phys. Rev. Lett. **90**, 027402 (2003); M. I. Stockman, Nature Photonics **2**, 327 (2008); C. Luo, M. Ibanesco, S. G. Johnson, and J. D. Joannopoulos, Science **299**, 368 (2003); M. A. Noginov, G. Zhu, A. M. Belgrave, R. Bakker, V. M. Shalaev, E. E. Narimanov, S. Stout, E. Herz, T. Suteewong, and U. Wiesner, Nature (London) **460**, 1110 (2009).

[15] N. Aközbek and S. John, Phys. Rev. E **57**, 2287 (1998); P. Colman, C. Husko, S. Combre, I. Sagnes, C. W. Wong, and A. De Rossi, Nature Photonics **4**, 862 (2010); S. A. Maier, S. R. Andrews, L. Martin-Moreno, and F. J. Garcia-Vidal, Phys. Rev. Lett. **97**, 176805 (2006).

[16] F. J. Garcia-Vidal and J. B. Pendry, Phys. Rev. Lett. **77**, 1163 (1996); F. Benabid, J. C. Knight, G. Antonopoulos, P. St. J. Russell, Science **298**, 399 (2002); J. T. Hugall, J. J. Baumberg, and S. Mahajan, Appl. Phys. Lett. **95**, 141111 (2009).

[17] A. Babuty, A. Bousseksou, J.-P. Tetienne, I. Moldovan Doyen, C. Sirtori, G. Beaudoin, I. Sagnes, Y. De Wilde, and R. Colombelli, Phys. Rev. Lett. **104**, 226806 (2010); T. Dufaux, J. Dorfmuller, R. Vogelgesang, M. Burghard, and K. Kern, Appl. Phys. Lett. **97**, 161110 (2010); A. Schneider. A. Shuvaev, S. Engelbrecht, S. O. Demokritov, and A. Pimenov, Phys. Rev. Lett. **103**, 103907 (2009).

[18] E. Lier, D. H. Werner, C. P. Scarborough, Q. Wu, and J. A. Bossard, Nat. Mater. 2950 (2011).

[19] V. A. Fedotov, N. Papasinakis, E. Plum, A. Bitzer, M. Walther, P. Kuo, D. P. Tsai, and N. I. Zheludev, Phys. Rev. Lett. **104**, 223901 (2010); V. G. Kravets, F. Schedin, and A. N. Grigorenko, Phys. Rev. Lett. **101**, 087403 (2008); R. Singh, C. Rockstuhl, and W. Zhang, Appl. Phys. Lett. **97**, 241108 (2010).

[20] J. D. Jackson, *Classical Electrodynamics*, 3rd ed. (John Wiley & Sons, New York (1999); A. V. Zayats, I. I. Smolyaninov, and A. A. Maradudin, Phys. Rep. **408**, 131 (2005).

[21] H. Xiong and B. Wu, Phys. Rev. A **82**, 053634 (2010).

Cylindrical, periodic surface lattice—Theory, dispersion analysis, and experiment

I. V. Konoplev,[1,a)] A. J. MacLachlan,[2] C. W. Robertson,[2] A. W. Cross,[2] and A. D. R. Phelps[2]
[1]*JAI, Department of Physics, University of Oxford, Keble Road, Oxford OX1 3RH, United Kingdom*
[2]*Department of Physics, SUPA, University of Strathclyde, Glasgow G4 0NG, United Kingdom*

(Received 6 August 2012; accepted 10 September 2012; published online 20 September 2012)

A two-dimensional surface lattice of cylindrical topology obtained via perturbing the inner surface of a cylinder is considered. Periodic perturbations of the surface lead to observation of high-impedance, dielectric-like media and resonant coupling of surface and non-propagating volume fields. This allows synthesis of tailored-for-purpose "coating" material with dispersion suitable, for instance, to mediate a Cherenkov type interaction. An analytical model of the lattice is discussed and coupled-wave equations are derived. Variations of the lattice dispersive properties with variation of parameters are shown, illustrating the tailoring of the structure's electromagnetic properties. Experimental results are presented showing agreement with the theoretical model. © *2012 American Institute of Physics*. [http://dx.doi.org/10.1063/1.4754572]

One of the important and challenging problems is to understand the phenomena associated with excitation and evolution of electromagnetic (EM) fields on the surface of artificial periodic structures.[1–4] The studies of surface lattices, which mediate the interaction between active media and EM fields, are an active and exciting research field, recently boosted by development of nanotechnology and understanding of utilizing surface fields (SFs) for compact sources of coherent radiation (CSCR) such as the SPASAR.[4] Here, we consider the hollow cylindrical structure made from a perfect conductor with the inner surface having two-dimensional (2D) chessboard patterns (periodic perturbations).[2,5–7] The periodic perturbations manufactured via machining of the smooth surface of the conductor form the square lattice, which geometrically results in localization of the free electrons inside areas which were not machined (scatterers). Thus, electrons move freely inside the scatterers but electron transmission through the whole lattice is terminated, with no electron transport across the lattice in the azimuthal and longitudinal directions, for some range of frequencies. The structure at these frequencies can be considered as a cylindrical waveguide lined with a thin (2D) dielectric[8] or a high-impedance surface,[9,10] inside which the excitation of SFs and resonance coupling between surface and near cut-off volume fields (VFs) take place. Also, the topology of the structure is perfect for a number of applications including CSCR and wake-field acceleration. The lattice has a large surface area (in comparison with λ^2, where λ is the operating wavelength) and formed by the ensemble of individual scatters which has to be synchronized to observe a coherent state. To resolve the problem, feedback (realized in the set-up (Fig. 1) similar to a Fabry-Perot (FP) cavity with a periodic surface lattice (PSL) playing the role of one of the mirrors) can be used.[11] In Figure 1, conformal mapping is required to observe a cylindrical system from a planar system as shown. The cut-off wave of the cylindrical waveguide (standing wave in a planar system) ensures the feedback and synchronization of the individual scatterers while the surface fields can be used to interact with active media to observe a CSCR.[2,4–8,10–14] In this letter, we present an analytical model of PSL eigenmodes defined via coupling of the partial localized SFs with the azimuthally symmetric, near cut-off VFs and comparing the experimental data observed with our understanding of the phenomena. We show that dispersive properties of the structures can be tailored to mediate different phenomena including a Cherenkov instability.[8,10] The model is defined using a modal approach and a set of coupled wave equations describing the eigenfields' distribution inside the lattice. The eigenfield is considered as a superposition of partial localized SFs and VFs of the unperturbed, partially loaded with a thin dielectric, cylindrical waveguide. Using coupled wave equations derived from the Maxwell equations, the eigenfields' dispersion relations are derived. We note that without the 2D patterns the SF will not be formed; a change of the perfect conductor surface into a high-impedance (dielectric-like) surface can only be observed under specific conditions (see Refs. 1, 8–10 and 12), which is outside the scope of this paper.

Let us consider a 2D cylindrical structure formed by a chessboard,[6,8] surface lattice on the inner wall of a hollow, cylindrical, copper waveguide. The pattern's depth, i.e., the individual element amplitude is smaller than the operating wavelength. The resonant coupling (scattering) and cavity eigenmode formation take place if the resonance conditions are satisfied.[2,6,8,12–14] The discussion and experiments were carried out in the GHz frequency range[6] but as will be clear, the equations observed are applicable to THz and infrared frequencies.

Starting with $curl\vec{E} = ik\vec{H} - (4\pi\vec{J}_m/c)$; $curl\vec{H} = -ik\vec{E}$, where c is the speed of light, $\vec{k} = \omega/c$ is the wave vector, ω is the angular frequency, $\vec{J}_m$ is the surface magnetic current,[12–14] we present the fields as a superposition of partial modes whose transverse structure coincides with eigenmodes of a cylindrical waveguide having a high surface impedance (partially loaded with dielectric). The field's components are $\vec{H} = \sum_q C_q(z)\vec{H}_q; \vec{E} = \sum_q C_q(z)\vec{E}_q$ (see Refs. 12–14), the

a)Email: ivan.konoplev@physics.ox.ac.uk. Tel.: +44(0)-1865-273456.

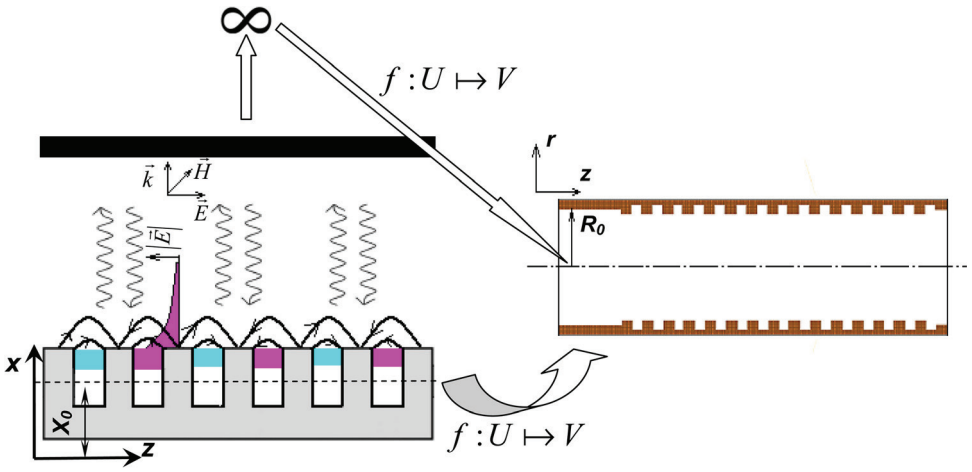

FIG. 1. Schematic showing a planar Fabry-Perot like cavity with one of the mirrors having a high-impedance surface which allows coupling of surface fields and volume fields. The arrows indicate the mathematical steps required to move from planar geometry to a cylindrical cavity with a high-impedance surface similar to a dielectric layer.

C_q(z) are the slowly varying amplitudes along the z coordinate and the wave equations are

$$\sum_q \Delta_z C_q(z) + \sum_q \left(\frac{\omega^2 \mp (\omega_0^q)^2}{c^2} \right) C_q(z) = i \frac{1}{N_q} \int_\sigma \vec{J}_m \vec{H}_{-q}|_{r_0} d\sigma. \tag{1}$$

The contour integral taken along the unperturbed cylinder cross-section, $N_q^{-1} = 4\pi k/(c\int_\sigma \vec{H}_q \vec{H}_{-q} d\sigma)$ is the wave norm[12–14] and $d\sigma$ defines the integration surface while the lattice is substituted with the set of surface currents, which exist on the waveguide wall ($r = r_0$). Equation (1) was obtained taking into account: $k^2 = \omega^2/c^2$; $\Delta = \Delta_z + \Delta_\perp$ and $\left(\Delta_\perp \pm \frac{(\omega_0^q)^2}{c^2} \right) H_q = 0$, where "+" corresponds to the volume ($\omega_0^q = \omega_0^v = k_\perp^v c$, $k^2 = k_z^2 + k_\perp^2$) and "−" to the surface ($k^2 = k_z^2 + (ip)^2$, $\omega_0^q = \omega_0^s = pc$) localized modes. Introducing $\Omega^2 = (|\omega_0^v|^2 + |\omega_0^s|^2)/2$, $\Phi^2 = (|\omega_0^s|^2 - |\omega_0^v|^2)/2$, $\delta = \omega - \Omega$ and considering $\Phi^2/\Omega^2 \ll 1$ (partial fields coupling with $k_z \to 0$ inside a long lattice), using Fourier decomposition (structure is periodic along z), the set of equations defining the coupling of the surface field's spatial harmonic with an index n and the fundamental harmonic of the VF can be obtained

$$\left(\frac{\partial^2}{\partial z^2} + 2\bar{K}^2 \left(\frac{\bar{\delta}}{\bar{K}} + \frac{\bar{\delta}^2}{2\bar{K}^2} + \frac{\Delta^2}{2\bar{K}^2} \right) \right) A(z) = i \frac{1}{N_v} \int_\sigma \vec{J}_m \vec{H}^v_{-q} \Big|_{r_0} d\sigma, \tag{2a}$$

$$\left(\frac{\partial^2}{\partial z^2} + 2in\bar{k}_z \frac{\partial}{\partial z} + 2\bar{K}^2 \left(1 - \frac{n^2 \bar{k}_z^2}{2\bar{K}^2} + \frac{\bar{\delta}}{\bar{K}} + \frac{\Delta^2}{2\bar{K}^2} + \frac{\bar{\delta}^2}{2\bar{K}^2} \right) \right) \times B_n(z) = \frac{i}{N_s} \int \vec{J}_m \vec{H}^s_{-q}|_{r_0} e^{-in\bar{k}_z z} d\sigma, \tag{2b}$$

where "s" and "v" indicate the norms of the surface and volume fields, A(z) and B_n(z) are the slowly varying amplitudes, $\bar{K} = \Omega/c$, $\Delta = \Phi/c$, and $\bar{\delta} = \delta/c$. The right-hand sides of Eqs. (2a) and (2b) can be rewritten as $\alpha_{v,s}^2 F_{s,v}$,[12–14] where $\alpha_{v,s}$ are the coupling coefficients and $F_{s,v}$ are functions of the amplitudes A(z) and B_n(z)[12–14] (i.e., Eqs. (2a) and (2b) are coupled only if $\alpha_{v,s}^2 F_{s,v} \neq 0$). Here, we will treat $\alpha_{s,v}$ as variable parameters, the strict definition of which is outside the scope of this letter and can be found using the technique discussed in Refs. 12–14. The coupling between the near cutoff, VF fundamental harmonic, and SF takes place if the SF harmonic's number n coincides with the harmonic of the lattice $\bar{n}$. Assuming that the lattice is sinusoidal ($n = \pm 1$), introducing $Z = \bar{K}z$, $\hat{A}_0(Z) = A_0(Z)/\alpha_v$, $\hat{B}_\pm(Z) = B_\pm(Z)/\alpha_s$, $\alpha^2 = \alpha_v \alpha_s/\bar{K}^2$, $\Gamma = \bar{k}_z/\bar{K}$, $\tilde{\delta} = \bar{\delta}/\bar{K} = (\omega - \Omega)/\Omega$; $\tilde{\Delta} = \Delta/\bar{K} \ll 1$, $\omega_e^2 = 2\tilde{\delta} + (\tilde{\delta}^2 + \tilde{\Delta}^2)$ and assuming that $\hat{A}_0$, $\hat{B}_\pm$ are proportional to $e^{i\Lambda Z}$, the dispersion relation can be found

$$(\omega_e^2 - \Lambda^2)[\Lambda^4 - 2\Lambda^2(2 + \Gamma^2 + \omega_e^2) + (2 - \Gamma^2 + \omega_e^2)^2] = 2\alpha^4(2 - \Gamma^2 + \omega_e^2 - \Lambda^2). \tag{3}$$

The detuning parameter Γ is a function of the structure's geometry (for a specific mode) as it links the periodicity of the lattice and $\omega_0^s = pc$ and $\omega_0^v = k_\perp^v c$. One notes that if $\alpha \to 0$, no coupling is observed (Fig. 2, broken lines) while large α such as $\alpha = 1$ is associated with strong coupling and the whole dispersion is affected (right insets of Fig. 2). For clarity reasons only, the dispersions (Fig. 2) were observed for the structure having the same mean diameter as used in experiments reported[6] under the assumption that $\Delta = 0$ and $\alpha \ll 1$ (weak coupling, solid lines). If $\alpha \ll 1$, then the eigenmode dispersion deviates from the unperturbed values in the vicinity of the crossing points where the split between branches takes place (main case). In Figure 2, eigenmodes' dispersions are presented for the set of structure detuning parameter $\Gamma = 1, \sqrt{2}$, and 2.3, respectively. With increase of Γ from 1 to 2.3, the crossing points are moving towards the vertex of the parabola[8] and at $\Gamma = \sqrt{2}$ and $\alpha = 0.25$ (Fig. 2(b)), the crossing points merge at the center of the parabola. Also, the gap in this case (as expected) is larger as compared with $\alpha = 0.1$. Assuming now a Cherenkov interaction between an electron beam and the eigenfield formed, the synchronism condition required for the interaction to take place is $\omega = 2\pi v_z l/d_z$ ($k_z = 0$, $l = 1$ here l is the electron beam harmonic) leading to an electron beam velocity condition $1/\sqrt{2} \leq v_z/c < 1$. At $\Gamma = 2.3$ and $\alpha = 0.1$, the eigenmodes' dispersions (Fig. 2(c)) change further and now the interaction between the electron beam and the EM fields can be observed even at lower beam velocities $1/\Gamma \leq v_z/c$,[8] thus making an increase of Γ synonymous with increasing effective dielectric refractive index. On the right-side insets

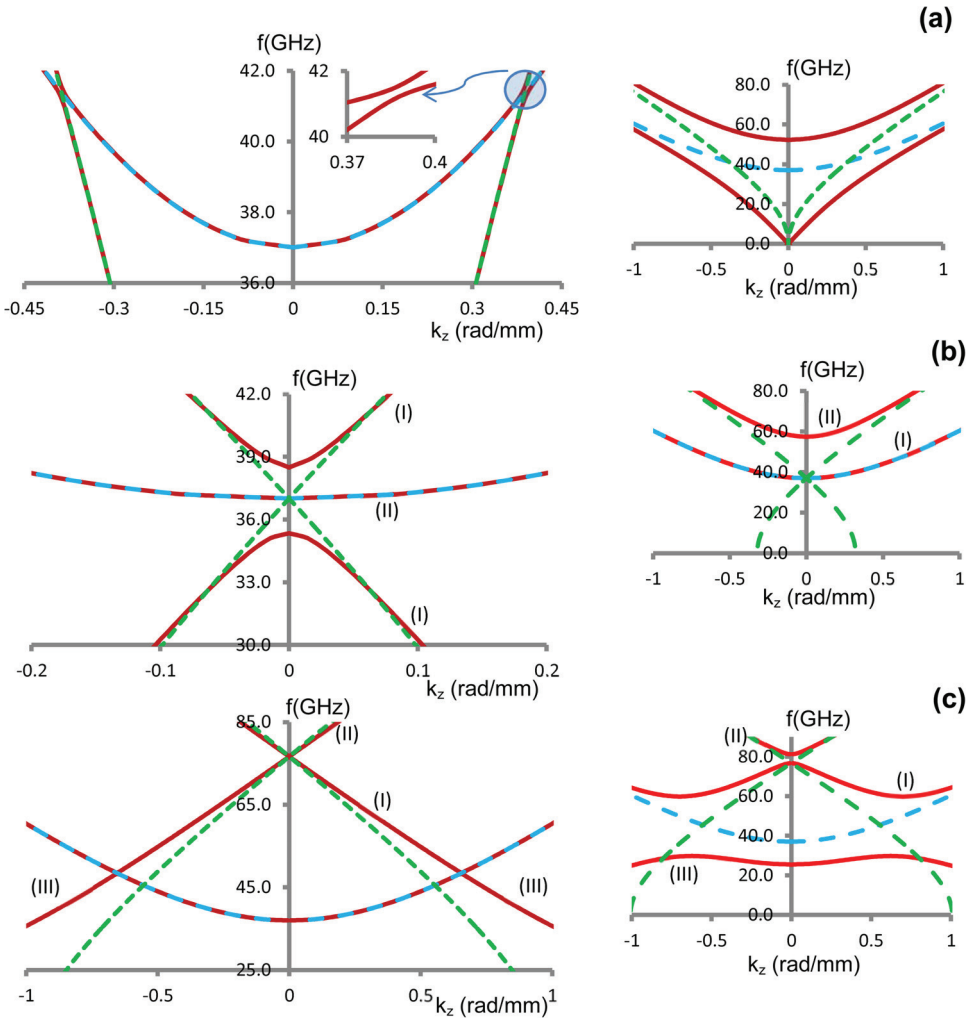

FIG. 2. Dispersion diagrams observed from Eq. (3) for a structure having: mean diameter 7.9 cm, number of azimuthal variation 28 illustrating the coupling between partial volume $TM_{0,10}$ and surface $EH_{28,1}$ fields when λ_c/d_z and α coupling coefficient ($\alpha = 1$ for all right hand-side insets) are: (a) 1 and 0.1; (b) $\sqrt{2}$ and 0.25; (c) 2.3 and 0.1, respectively. In all figures, the dashed lines indicate the dispersion of the unperturbed partial fields, i.e., when $\alpha = 0$.

(Fig. 2), the dispersion diagrams for $\alpha = 1$ are shown and it is clear that these are formed via an increasing gap between branches at the crossings. Analyzing the graphs we see that the positions of the extrema points ($\partial f/\partial k_z = 0$), indicating the positions of the cavity eigenmodes, are different from the unperturbed waveguide cut-off frequencies and having $f/k_z < c$ and $\partial f/\partial k_z$ with sign variation illustrates the possibility for observing slow forward and backward waves, required for a Cherenkov interaction to take place.

The experiments, for which the set-ups were discussed in Refs. 3 and 6, have been conducted to link theoretical understanding with experimental measurements. The first set of experiments is based on excitation of the structure's eigenmode inside the lattice via resonant scattering of the near cut-off VFs to the SFs. To observe the near cut-off VF, a coaxial line was used and it was terminated at the lattice, resulting in excitation of the near cut-off, azimuthally symmetric mode. The resonant coupling between the fields manifests itself as two gaps (Fig. 3(a)) in the signal transmission observed at small observation angles with respect to the structure's axis of symmetry. The gaps are shifting in the frequency domain with variation of the observation angle. Each minima correspond to a point on the dispersion and the frequency shift corresponds to the move of the point along the dispersions' branches. A specific angle corresponds to a longitudinal wavenumber (ratio k and $k_\perp$, $k_\perp^2/k^2 = \varepsilon^2$). Thus, measuring the frequency shift of the minima and knowing the observation angle one can recover the dispersion. The technique works for small observation angles, corresponding to small variations of k_z around 0, as at larger angles the appearance of other minima can be expected due to non-coherent scattering[3] of propagating waves. In Figure 3(a) and the inset of this figure, the results of the transmission measurements for the observation angles [0°;6°] and the shift of the observed minima are shown. There is correlation between the theory and the predictions, while differences come from the fact that the structure studied in the experiment is of finite size (4.8 cm long and 7.9 cm in diameter), while the theory is developed for an infinitely long structure. In the second set of experiments, we illustrate the high-Q mode excitation[6,8] at a frequency different from the cut-off frequency of the non-perturbed waveguide. For this purpose, the cavity was driven by short 50 ns pulses having 5 ns rise and fall times and formed via amplitude modulation of the high-frequency wave. The structure is based on the waveguide with an unperturbed radius of 3.95 cm ($TM_{0,10}$ mode cut-off frequency, i.e., $\partial f/\partial k_z = 0$ is $\sim$37 GHz), while from the previous experiment it was expected that the cavity eigenmode should be observed at $\sim$37.7 GHz, i.e., $\partial f/\partial k_z = 0$ is above the cut off frequency of the conventional waveguide. The results shown in Fig. 3(b) illustrate the pulse propagation through the structure and cavity

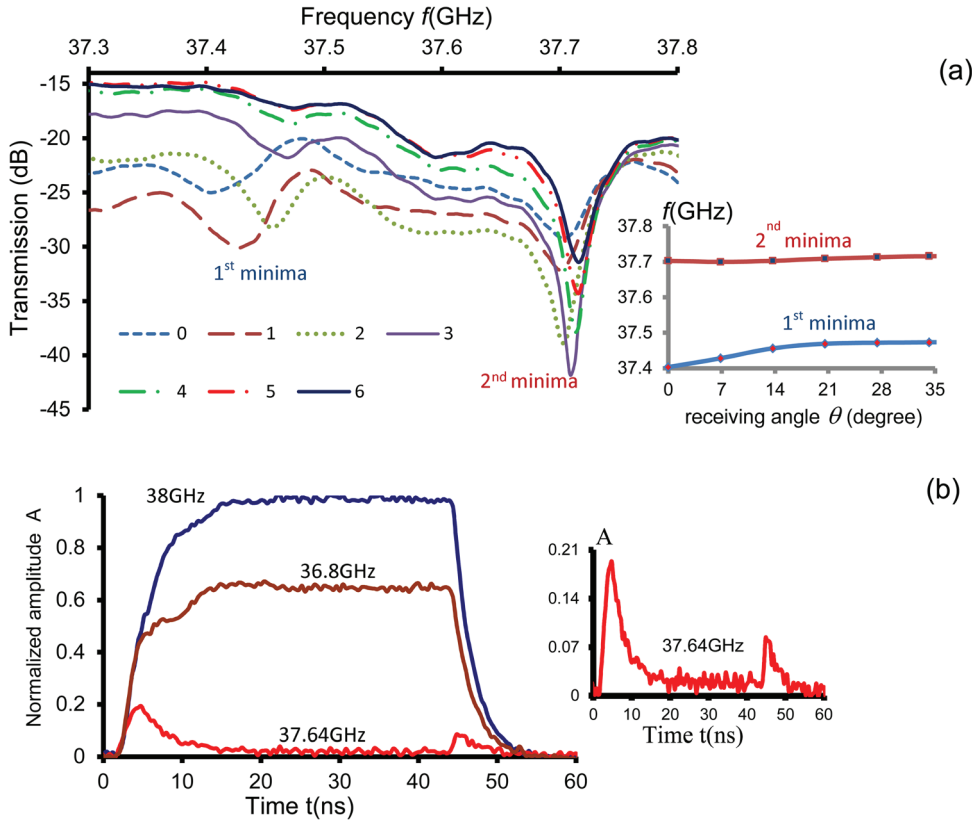

FIG. 3. The experimental studies of (a) frequency dependence of signal transmission through the cylindrical 2D PSL measured at the set of angles $\theta \in [0°;6°]$ with right hand side insets illustrating the shifts of the minima measured with variation of observation angle θ, (b) pulse propagation through the 2D PSL measured having carrier frequencies 38.0 GHz, 37.64 GHz, and 36.8 GHz, with the right hand-side insets magnifying the results observed for pulses formed with the 37.64 GHz carrier frequency.

excitation at 37.64 GHz (inset of Fig. 3(b)). Tuning the signal carrier frequency to 37.64 GHz results in a visible change of the pulse profile, similar to those observed during excitation of critically coupled cavities, confirming our understanding of the structure's dispersion and phenomena observed. The cavity Q-factor can also be estimated from the exponential time-decay observed in Fig. 3(b) and is found to be approximately 600.

To summarize, in this paper, we have developed an analytical theory of the coupling of partial fields inside a 2D cylindrical periodic structure formed by small periodic perturbations. The surface lattice is described as a high-impedance thin material (dielectric layer) allowing SFs to be taken into consideration as partial fields forming the lattice eigenmode. The dispersion relation describing the EM property of the lattice has been derived and dispersion diagrams were analyzed for different sets of parameters. We have discussed the possibility to excite the structure with a relativistic electron beam to observe Cherenkov interaction. The theory developed was linked to the previous works and analysis was carried out taking into account the parameters of the experimental set-up. We have measured the dependence of the spectra of the transmission coefficient versus angle of observation and discussed the method of deriving the dispersion from the data obtained. The structure has been considered as a cavity and eigenmode excitation using a short pulse has been carried out. We have shown that in spite of the complexity of the measurements a good agreement, between theoretical understanding and experimental measurements, has been observed. We would like to note that the theory developed is applicable for a broad range of frequencies including THz and infrared frequencies.

The support of the UK EPSRC is gratefully acknowledged.

[1]J. B. Pendry, A. J. Holden, W. J. Stewart, and I. Youngs, Phys. Rev. Lett. **76**, 4773 (1996); F. J. Garcia-Vidal and J. B. Pendry, *ibid.* **77**, 1163 (1996); N. Papasimakis, V. A. Fedotov, Y. H. Fu, D. P. Tsai, and N. I. Zheludev, Phys. Rev. B **80**, 041102 (2009); D. Yu. Shchegolkov, A. K. Azad, J. F. O'Hara, and E. I. Simakov, *ibid.* **82**, 205117 (2010); V. A. Fedotov, M. Rose, S. L. Prosvirnin, N. Papasimakis, and N. I. Zheludev, Phys. Rev. Lett. **99**, 147401 (2007).
[2]I. V. Konoplev, A. D. R. Phelps, A. W. Cross, and K. Ronald, Phys. Rev. E **68**, 066613 (2003); I. V. Konoplev, P. McGrane, W. He, A. W. Cross, A. D. R. Phelps, C. G. Whyte, K. Ronald, and C. W. Robertson, Phys. Rev. Lett. **96**, 035002 (2006); I. V. Konoplev, L. Fisher, A. W. Cross, A. D. R. Phelps, K. Ronald, and C. W. Robertson, Appl. Phys. Lett. **96**, 261101 (2010); I. V. Konoplev, A. W. Cross, and A. D. R. Phelps, IEEE Trans. Plasma Sci. **39**, 2610 (2011).
[3]W. L. Barnes, A. Dereux, and T. W. Ebbesen, Nature **424**, 824 (2003); N. Papasimakis, V. A. Fedotov, N. I. Zheludev, and S. L. Prosvirnin, Phys. Rev. Lett. **101**, 253903 (2008); J. Renger, S. Grafström, and L. M. Eng, Phys. Rev. B **76**, 045431 (2007); S. A. Maier, S. R. Andrews, L. Martín-Moreno, and F. J. García-Vidal, Phys. Rev Lett. **97**, 176805 (2006).
[4]D. J. Bergman and M. I. Stockman, Phys. Rev. Lett. **90**, 027402 (2003); M. I. Stockman, Nature Photon. **2**, 327 (2008); M. I. Stockman, J. Opt. **12**, 024004 (2010).
[5]N. S. Ginzburg, I. V. Konoplev, and A. S. Sergeev, Zh. Tech. Fiziki (J. Tech. Phys. (ZhTP)) **66**, 108 (1996); I. V. Konoplev, A. W. Cross, W. He, A. D. R. Phelps, K. Ronald, G. R. M. Robb, C. G. Whyte, N. S. Ginzburg, N. Y. Peskov, and A. S. Sergeev, Nucl. Instrum. Methods Phys. Res. A **445**, 236 (2000).
[6]I. V. Konoplev, L. Fisher, K. Ronald, A. W. Cross, A. D. R. Phelps, C. W. Robertson, and M. Thumm, Appl. Phys. Lett. **96**, 231111 (2010); I. V. Konoplev, L. Fisher, A. W. Cross, A. D. R. Phelps, K. Ronald, and M. Thumm, *ibid.* **97**, 261102 (2010); A. W. Cross, I. V. Konoplev, K. Ronald, A. D. R. Phelps, W. He, C. G. Whyte, N. S. Ginzburg, N. Yu. Peskov, and A. S. Sergeev, *ibid.* **80**, 1517 (2002).
[7]N. E. Glass, Phys. Rev. A **36**, 5235 (1987); P. T. Worthing and W. L. Barnes, Appl. Phys. Lett. **79**, 3035 (2001); S. Riechel, C. Kallinger, U. Lemmer, J. Feldmann, A. Gombert, V. Wittwer, and U. Scherf, *ibid.* **77**, 2310 (2000).

[8]I. V. Konoplev, A. J. MacLachlan, C. W. Robertson, A. W. Cross, and A. D. R. Phelps, Phys. Rev. A **84**, 013826 (2011).
[9]D. F. Sievenpiper, E. Yablonovitch, J. N. Winn, S. Fan, P. R. Villeneuve, and J. D. Joannopoulos, Phys. Rev. Lett. **80**, 2829 (1998); E. Lier, D. H. Werner, C. P. Scarborough, Q. Wu, and J. A. Bossard, Nature Mater. **10**, 252 (2011).
[10]J. T. Shen, P. B. Catrysse, and S. Fan, Phys. Rev. Lett. **94**, 197401 (2005); P. B. Catrysse, G. Veronis, H. Shin, J.-T. Shen, and S. Fan, Appl. Phys. Lett. **88**, 031101 (2006); M. J. Lockyear, M. J. Lockyear, A. P. Hibbins, and J. R. Sambles, Phys. Rev. Lett. **102**, 073901 (2009).
[11]V. L. Bratman, B. S. Dumesh, A. E. Fedotov, P. B. Makhalov, B. Z. Movshevich, and F. S. Rusin, IEEE Trans. Plasma Sci. **38**, 1466 (2010); Yu. A. Grishin, M. R. Fuchs, A. Schnegg, A. A. Dubinskii, B. S. Dumesh, F. S. Rusin, V. L. Bratman, and K. Möbius, Rev. Sci. Instrum. **75**, 2926 (2004).
[12]A. W. Cross, I. V. Konoplev, A. D. R. Phelps, and K. Ronald, J. Appl. Phys. **93**, 2208 (2003).
[13]N. F. Kovalev, I. M. Orlova, and M. I. Petelin, Izv. Vyssh. Uchebn. Zaved., Radiofiz. **11**, 783 (1968); I. V. Konoplev, P. McGrane, A. W. Cross, K. Ronald, and A. D. R. Phelps, J. Appl. Phys. **97**, 073101 (2005); G. Burt, S. V. Samsonov, A. D. R. Phelps, V. L. Bratman, K. Ronald, G. G. Denisov, W. He, A. R. Young, A. W. Cross, and I. V. Konoplev, IEEE Trans. Plasma Sci. **33**, 661 (2005).
[14]G. Burt, S. V. Samsonov, K. Ronald, G. G. Denisov, A. R. Young, V. L. Bratman, A. D. R. Phelps, A. W. Cross, I. V. Konoplev, W. He, J. Thomson, and C. G. Whyte, Phys. Rev. E **70**, 046402 (2004); I. V. Konoplev, P. McGrane, A. D. R. Phelps, A. W. Cross, and K. Ronald, Appl. Phys. Lett. **87**, 121104 (2005); I. V. Konoplev, G. Doherty, A. W. Cross, A. D. R. Phelps, and K. Ronald, *ibid.* **88**, 111108 (2006).